JULY-SEPTEMBER 2019 VOL. 11 № 3 (42)

ISSN 2075-8251

ActaNaturae

Surgical Simulation of a Posttraumatic Spinal Cord Glial Scar in Rats

THE MOLECULAR MECHANISMS OF GAMETIC INCOMPATIBILITY IN INVERTEBRATES
P. 4

THE MECHANISMS OF ACTION OF TRIINDOLYLMETHANE DERIVATIVES ON LIPID MEMBRANES
P. 38

MERCK

Comprehensive solutions for cell analysis

- Cell lines and primary cells
- Traditional and specialized culture media
- Sterilizing filtration
- Biochemical reagents
- Water purification systems
- Cell counting and analysis
- Cryopreservation

An extensive range and top quality of cell lines from our partner, the European Collection of Authenticated Cell Cultures (ECACC):

- 4000 animal and human cell lines;
- Cells of 45 animal species and 50 tissue types;
- 370 B-lymphoblastoid cell lines for which human leukocyte antigen (HLA) typing data are available;
- 480 hybridoma cell lines secreting monoclonal antibodies;
- DNA, RNA, and cDNA extracted from the cell lines from our collection;

SIGMAaldrich.com/ECACC

LLC Merck
Valovaya Str., 35, Moscow, 115054, Russia;
Tel. +7 (495) 937-33-04
E-mail: mm.russia@merckgroup.com, ruorder@sial.com

SIGMAaldrich.com/cellculture
MERCKmillipore.com/cellculture

SIGMA-ALDRICH® is now MERCK

The Effect of a Lipopolysaccharide from *Rhodobacter capsulatus* PG on Inflammation Caused by Various Influenza Strains

S. V. Zubova, M. F. Vorovich, A. S. Gambaryan,
A. A. Ishmukhametov, S. V. Grachev, I. R. Prokhorenko

The development of a specific inflammation in mice that had been infected by two influenza virus strains, A/chicken/Kurgan/5/2005 (H5N1) and A/Hamburg/2009 MA (H1N1), was studied. We investigated the effect of a non-toxic lipopolysaccharide from *Rhodobacter capsulatus* PG on the survival and body weight of the mice, production of IgG antibodies, and the induction of pro- and anti-inflammatory cytokines in blood serum. The administration of the *R. capsulatus* PG lipopolysaccharide was shown to induce interferon-β synthesis, both in healthy and influenza A virus-infected mice, and to promote production of antiviral antibodies in the blood of the influenza-infected animals.

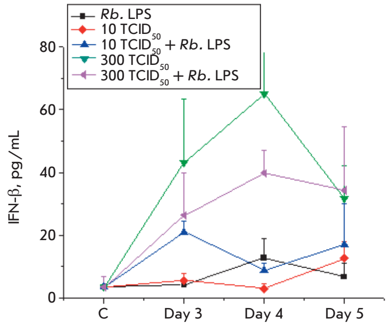

Dynamics of cytokine levels in response to the administration of the *Rb.* LPS, H1N1 influenza virus, and both factors simultaneously

---

An Abnormally High Closing Potential of the OMPF Porin Channel from *Yersinia Ruckeri*: The Role of Charged Residues and Intramolecular Bonds

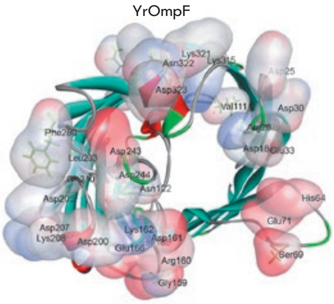

Distribution of basic and acidic amino acid residues in the variable regions of the porins

D. K. Chistyulin, O. D. Novikova, E. A. Zelepuga, V. A. Khomenko,
G. N. Likhatskaya, O. Yu. Portnyagina, Y. N. Antonenko

Electrophysiological experiments on bilayer lipid membranes showed that the isolated outer membrane major porin of *Yersinia ruckeri* (YrOmpF) exhibits activity typical of porins from Gram-negative bacteria, forming channels with a mean conductance of 230 pS and slight asymmetry with respect to the applied voltage. The studied channel significantly differed from the porins of other bacteria by high values of its critical closing potential (Vc): Vc = 232 mV at pH = 7.0 and Vc = 164 mV at pH = 5.0. A theoretical model of the YrOmpF spatial structure was used for the analysis of the charge distribution in the mouth and inside the channel to explain these properties and quantitatively assess the bonds between the amino acid residues in the L3 loop and on the inner wall of the barrel.

The Structural and Immunological Properties of Chimeric Proteins Containing HIV-1 MPER Sites

A. P. Rudometov, N. B. Rudometova, D. N. Shcherbakov, A. A. Lomzov, O. N. Kaplina, N. S. Shcherbakova,
A. A. Ilyichev, A. Yu. Bakulina, L. I. Karpenko

The objective of this study was to develop immunogens capable of targeting an immune response to MPER, one of the regions of bNAb binding in Env. Two immunogens carrying MPER fragments on their scaffolds (protein YkuJ *Bacillus subtilis* and artificial polypeptide TBI) were constructed. The antigenic structure of the MPER-TBI and YkuJ-MPER proteins was characterized using bNAbs that recognize HIV-1 MPER. The rabbit model made it possible to show the immunogenicity of the constructed recombinant proteins. The resulting serum was found to be cross-reactive with immunogens carrying MPER.

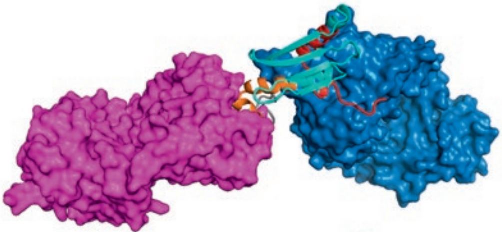

The model of interactions of YkuJ with the Fab fragments of mAbs 2F5 and 4E10

ActaNaturae
JULY-SEPTEMBER 2019 VOL. 11 № 3 (42)
since april 2009, 4 times a year

Founders
Acta Naturae, Ltd,
National Research University
Higher School of Economics

Editorial Council
Chairman: A.I. Grigoriev
Editors-in-Chief: A.G. Gabibov, S.N. Kochetkov

V.V. Vlassov, P.G. Georgiev, M.P. Kirpichnikov,
A.A. Makarov, A.I. Miroshnikov, V.A. Tkachuk,
M.V. Ugryumov

Editorial Board
Managing Editor: V.D. Knorre

K.V. Anokhin (Moscow, Russia)
I. Bezprozvanny (Dallas, Texas, USA)
I.P. Bilenkina (Moscow, Russia)
M. Blackburn (Sheffield, England)
S.M. Deyev (Moscow, Russia)
V.M. Govorun (Moscow, Russia)
O.A. Dontsova (Moscow, Russia)
K. Drauz (Hanau-Wolfgang, Germany)
A. Friboulet (Paris, France)
M. Issagouliants (Stockholm, Sweden)
A.L. Konov (Moscow, Russia)
M. Lukic (Abu Dhabi, United Arab Emirates)
P. Masson (La Tronche, France)
V.O. Popov (Moscow, Russia)
I.A. Tikhonovich (Moscow, Russia)
A. Tramontano (Davis, California, USA)
V.K. Švedas (Moscow, Russia)
J.-R. Wu (Shanghai, China)
N.K. Yankovsky (Moscow, Russia)
M. Zouali (Paris, France)

Project Head: N.V. Soboleva
Editor: N.Yu. Deeva
Designer: K.K. Oparin
Art and Layout: K. Shnaider
Copy Chief: Daniel M. Medjo

Phone/Fax: +7 (495) 727 38 60
E-mail: vera.knorre@gmail.com, actanaturae@gmail.com

Reprinting is by permission only.

© ACTA NATURAE, 2019

Номер подписан в печать 30 сентября 2019 г.
Тираж 100 экз. Цена свободная.
Отпечатано в типографии: ООО «Вариант»,
115054, Москва, ул. Дубининская, 40-59
E-mail: a1605@mail.ru

Indexed in Pubmed, Web of Science, Scopus, and RISC

CONTENTS

REVIEWS

RESEARCH ARTICLES

SHORT REPORTS

IMAGE ON THE COVER PAGE
(see the article by *G. B. Telegin et al.*)

The Molecular Mechanisms of Gametic Incompatibility in Invertebrates

A. A. Lobov[1,2]*, A. L. Maltseva[1], N. A. Mikhailova[3], A. I. Granovitch[1]
[1]Department of Invertebrate Zoology, Faculty of Biology, St Petersburg State University, Universitetskaya Emb. 7/9, St. Petersburg, 199034, Russia
[2]Laboratory of Regenerative Biomedicine, Institute of Cytology of the Russian Academy of Sciences, Tikhoretsky Ave. 4, St. Petersburg, 194064, Russia
[3]Centre of Cell Technologies, Institute of Cytology of the Russian Academy of Sciences, Tikhoretsky Ave. 4, St. Petersburg, 194064, Russia
*E-mail: arseniylobov@gmail.com

Received June 03, 2019; in final form, September 09, 2019
DOI: 10.32607/20758251-2019-11-3-4-15

Copyright © 2019 National Research University Higher School of Economics. This is an open access article distributed under the Creative Commons Attribution License,which permits unrestricted use, distribution, and reproduction in any medium, provided the original work is properly cited.

ABSTRACT **Fertilization (gamete fusion followed by zygote formation) is a multistage process. Each stage is mediated by ligand-receptor recognition of gamete interaction molecules. This recognition includes the movement of sperm in the gradient of egg chemoattractants, destruction of the egg envelope by acrosomal proteins, etc. Gametic incompatibility is one of the mechanisms of reproductive isolation. It is based on species-specific molecular interactions that prevent heterospecific fertilization. Although gametic incompatibility may occur in any sexually reproducing organism, it has been studied only in a few model species. Gamete interactions in different taxa involve generally similar processes, but they often employ non-homologous molecules. Gamete recognition proteins evolve rapidly, like immunity proteins, and include many taxon-specific families. In fact, recently appeared proteins particularly contribute to reproductive isolation via gametic incompatibility. Thus, we can assume a multiple, independent origin of this type of reproductive isolation throughout animal evolution. Gametic incompatibility can be achieved at any fertilization stage and entails different consequences at different taxonomic levels and ranges, from complete incompatibility between closely related species to partial incompatibility between distantly related taxa.**

KEYWORDS **gamete recognition proteins; gametic incompatibility; gametic isolation; reproductive isolation; speciation; invertebrates.**

ABBREVIATIONS **GRM/P – gamete recognition molecules/proteins; GI – gametic isolation; AR – acrosome reaction; FCC – female cryptic choice; SC – sperm competition; RI – reproductive isolation; PCPZ – post-copulatory prezygotic reproductive barriers.**

INTRODUCTION

The modern interpretation of species identity is based on the idea of unity of the species gene pool [1–3]. The hypotheses describing the mechanisms of speciation (microevolution) refer to the potential mechanisms of species subdivision into either partially or completely reproductively isolated groups [3]. Reproductive isolation (RI) is an essential stage of speciation and, at the same time, the key species criterion [1–3].

RI is realized via prezygotic and postzygotic mechanisms that are triggered at the stages that precede and follow zygote formation, respectively [3]. Their biological roles differ: the prezygotic and reproductive barriers form and function at early stages of speciation; postzygotic – at the late stages [4–7]. For example, it took at least 22 million years of divergence for the postzygotic RI between closely related bird species to form [3]. On the contrary, the prezygotic reproductive barriers between the *Drosophila* species can form within less than ten generations [8]. Gametic incompatibility (GI) is one of the prezygotic reproductive barriers that might emerge rather quickly [3].

GI is based on interactions between highly specialized gamete-recognition molecules. Gamete recognition proteins (GRPs) are expressed in reproductive tissues and are typically uninvolved in other functions [9, 10].

Even single amino acid substitutions in GRPs influence the efficiency and/or species specificity of gamete recognition [9, 10]. For example, it is considered that as few as 10 amino acid changes in the sea urchins acrosomal protein bindin can lead to RI between two species

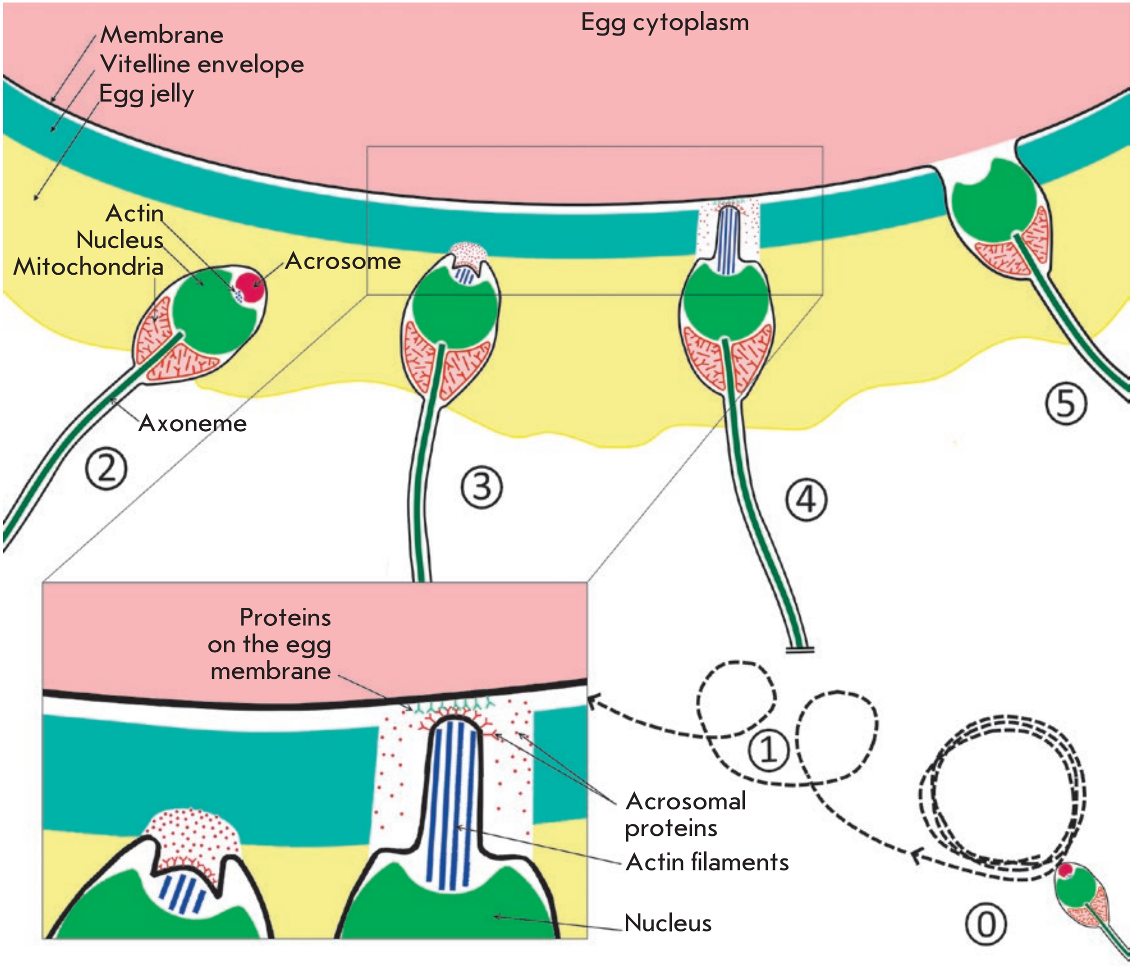

Fig. 1. Stages of gamete recognition in sea urchins. Numbers denote the steps of gamete recognition, with the description provided in the main text

[11]. Remarkably, the GRP structure is modified by some forms of natural selection, leading to an adaptive high level of GRP polymorphism; along with the immunity proteins, GRPs are among the most rapidly evolving traits [9–20].

Investigation of the individual mechanisms of RI at the molecular level has now become possible: the post-genomic era offers novel tools for studying the genomes and proteomes of many organisms. However, many of the proteins involved in RI belong to novel families and their secondary structure and/or functions cannot be adequately predicted using the available bioinformatic resources.

Sea urchins and marine mollusks (genus *Haliotis*) are the model objects routinely used for GI studies in externally fertilizing species [9, 10]. In some other invertebrates, only distinct stages of gamete recognition were studied (this will be discussed below). In many high-level invertebrate taxa, no molecular mediators of gamete recognition have been detected yet. For example, the recently described paraspermal protein LOSP became the first identified potential GRP in caenogastropods [21, 22].

GAMETE RECOGNITION

Gametic incompatibility is based on the structural changes that take place in GRM to ensure their specific interaction. The principal mechanisms of gamete recognition are similar in different organisms (with a few exceptions, such as *Nematoda*) and involve five stages (*Fig. 1*, exemplified by the sea urchin) [9, 23].

Stage 1: sperm guidance (steps 0–1)

At the start of this stage, after a period of spontaneous movement of a spermatozoon (usually following a wide loop without linear sections) (*Fig. 1*, step 0), a sperm guidance program is initiated (*Fig. 1*, step 1; [24]). The action of egg chemoattractants forces the sperm to move linearly with sharp loop-shaped turns [24]. This sperm movement pattern has been demonstrated for many phylogenetically distant taxa, such as echinoderms, chitons [25], cnidaria [25, 26], and polychaete

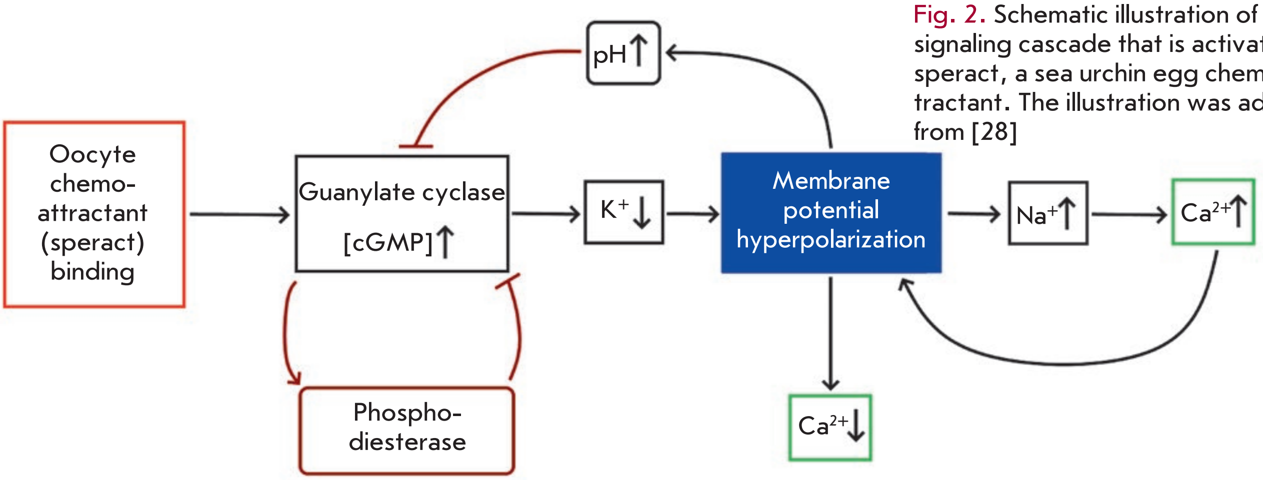

Fig. 2. Schematic illustration of the signaling cascade that is activated by speract, a sea urchin egg chemoattractant. The illustration was adapted from [28]

A list of egg chemoattractants detected in invertebrates and protists

Taxon	Species	Chemoattractant	Reference
Cnidaria	*Montipora digitata; Lobophytum crassum*	Unsaturated fatty alcohols; macrocyclic diterpene alcohols	[30, 31]
Echinodermata		Peptides	[32, 33]
Mollusca	*Octopus vulgaris; Sepia officinalis*		[34, 35]
	Haliotis	*L*-tryptophan	[36]
Ascidia	*Ciona intestinalis*	Sulfated steroids	[37]
Nematoda	*Caenorhabditis elegans*	Polyunsaturated fatty alcohols (PUFAs)	[38]
Brown algae	*Fucus vesiculosus*	Unsaturated carbohydrates (fucoserratins)	[39, 40]
Infusoria	*Euplotes*	Proteins	[41]

Arenicola marina [27]. It is made possible by molecular mechanisms similar to those in the sea urchins *Strongylocentrotus purpuratus* (*Fig. 2*) [28].

In sea urchins, the egg chemoattractant (speract) activates the guanylate cyclase receptor on the sperm membrane, resulting in the emergence of cGMP opening of the cGMP-dependent K^+ channels (Sp-tetraKCNG). Opening of these channels causes membrane hyperpolarization and activates the signaling cascade that drives calcium concentration oscillations [28]. The oscillating pattern of the signal results in an alternation of the individual phases of sperm movement: the spermatozoon moves linearly at low Ca^{2+} concentrations while assuming a sharp loop-shaped turn at high Ca^{2+} concentrations [29].

The structure of egg chemoattractants is unique in all the studied taxa (*Table*) [30–41]. It is possible that different sperm guidance systems form independently based on the fundamental mechanism of sperm motility [42].

Stage 2–3: the acrosome reaction and destruction of the egg envelope (steps 2–4)

The key stage of fertilization is the penetration of a spermatozoon through the egg envelope ensured by acrosomal proteins. These specialized proteins reside in the acrosome, a vesicle in the apex of the sperm [43]. In most animals, spermatozoa have a relatively large acrosome; however, the acrosome can also be rather small (e.g., in filiform spermatozoa of *Littorina* mollusks and *Lepisma* insects) [44, 45].

Acrosomal proteins are released upon acrosomal exocytosis during the acrosome reaction (AR; step 2). Also in many animals, such as sea urchins, pH-dependent actin polymerization occurs and an acrosomal rod forms (*Fig. 1*, 3–4) [46, 47]. AR is triggered by the interaction between specific sperm receptors and their ligands in the egg envelope.

Among invertebrates, the molecular basis of these processes has been studied only in echinoderms. Yet, they probably differ among invertebrate taxa. For

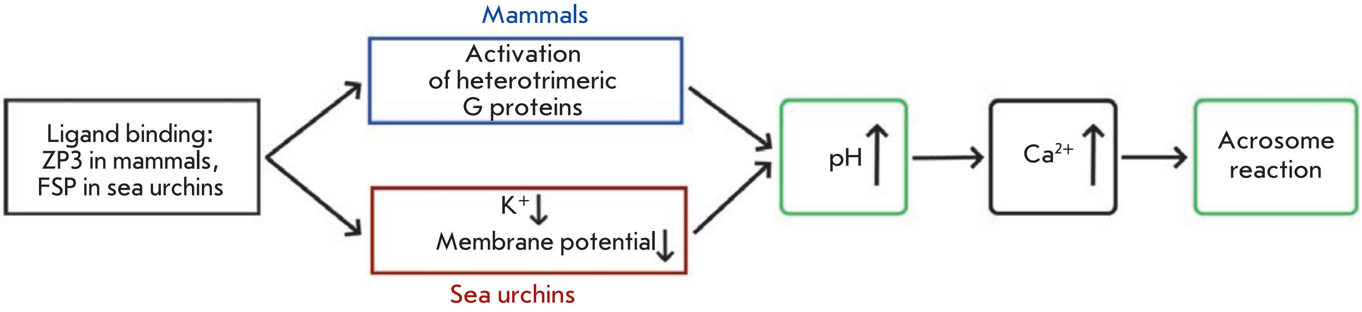

Fig. 3. Schematic illustration of the signaling cascades inducing the acrosome reaction in sea urchins and mammals. The illustration was adapted from [48]

example, these processes vary even within deuterostomes. In sea urchins and mammalians, AR is induced by different classes of molecules: sulfated polysaccharides and glycoproteins ZP3, respectively [46, 48]. As a result, non-homologous proteins are responsible for the recognition of these compounds: the 210 kDa membrane glycoprotein (REJ) acts as a receptor in sea urchins; PKDREJ and β-galactosyl transferase act as receptors in mice [46, 48].

In humans, the acrosome reaction can be induced not only by glycoprotein ZP3, but also by ZP1 and ZP4; additional receptors also seem to be involved [49]. Unlike the activation of AR via the ZP3 pathway, activation via the ZP1 and ZP4 does not involve G-protein signaling cascades and activates the L- and T-type voltage-gated calcium channels [49]. Hence, the signaling cascades inducing AR significantly differ within mammals; furthermore, they seem to use several independent pathways for their activation.

However, there also are fundamental similarities between the signaling cascades that induce AR in mammals and sea urchins (*Fig. 3*) [48]. Although their receptors belong to different classes, they induce the opening of calcium channels and those that cause a local increase in pH. These factors activate phospholipase C. The emergence of IP3 causes the release of intracellular calcium, the opening of the calcium channels controlled by the Ca^{2+} release (SOCs), and induction of AR.

Further, the course of fertilization depends on the activity of acrosomal proteins. In the organisms studied so far, these proteins are non-homologous but can be clearly subdivided into three functional groups.

(1) Components that degrade the egg envelope. These components usually are proteases or other enzymes [9, 10,50], but the integrity of the egg envelope can be lost even without the rupture of covalent bonds.

The acrosome of abalones (genus *Haliotis*) contains the 16 kDa lysin protein that degrades the egg envelope via the non-enzymatic mechanism. Lysin contains five α-helices that form two surfaces: a hydrophobic surface on one side and a cationic surface on the other. Lysin exists in the form of dimers noncovalently bound due to hydrophobic surfaces. The cationic surface sticks outside the dimer and is responsible for the interaction with VERL.

The vitelline envelope of abalones eggs consists of dense fibers that contain 6–10 VERL glycoprotein molecules, each; its structure is stabilized by hydrogen bonds. The interaction between the lysin dimer and VERL repeats causes lysin monomerization and binding to VERL. This specific recognition replaces the hydrogen bonds between VERL molecules with VERL-lysin hydrogen bonds, causing local degradation of the egg envelope [51–53].

(2) Components that ensure sperm adhesion to the egg envelope. Bindin discovered in sea urchin sperm was the first protein known to have this function [13]. In different sea urchin species, the size of mature bindin ranges from 193 to 418 amino acids. It consists of a 55-amino-acid-conserved core, which is involved in gamete fusion (stage 4), and two flanking regions responsible for species-specific adhesion to the egg envelope [13]. Non-homologous proteins with a similar function were detected in the echiuran (spoon worm) *Urechis* sp. [54]. Five highly homologous lectins serve this function in oysters [55].

(3) Components that affect the cell physiology. For example, the acrosomal proteins M3, M6, and M7 in bivalve mollusks of the genus *Mytilus* induce completion of oocyte meiosis [56] while bindin in spoon worm activates the oocyte [54].

Stage 4: membrane fusion (step 5)

After local degradation of the outer envelope of the egg, the membranes of interacting gametes approach each other and fuse. The lipid composition of these membranes, especially the cholesterol concentration [57], may affect the fusion process [58]. However, the key role is played by specialized proteins. It is assumed that HAP2, a homologue of the class II viral fusion protein, is involved in gamete fusion in eukaryotes [59]. It was demonstrated experimentally that this protein participates in gamete fusion in sea anemones *Nematostella vectensis* [60], in angiosperms belonging to the genus *Arabidopsis* [61], and protists *Chlamydomonas*, *Tetrahymena*, and *Plasmodium* [62, 63]; the orthologous genes of protein HAP2 were detected in the genomes of almost all metazoans [64]. In addition to HAP2, there are data on the involvement of group-specific proteins in membrane fusion (e.g., bindin from sea urchins, which has already been mentioned) [65–67].

Gamete recognition is based on conserved processes controlled by second messengers (primarily by calcium ions). However, a large number of non-homologous proteins are involved in gamete recognition in distantly related taxa. Its complexity has increased multiple times throughout the evolution of individual taxa.

THE MECHANISMS OF GAMETE INCOMPATIBILITY IN EXTERNALLY FERTILIZING INVERTEBRATES

GI is studied in detail in a model of closely related sea urchin species. For other taxa, data exists only for individual stages; unfortunately, the reasons why GI evolves at specific stages of gamete recognition have been elucidated in none of the models.

Peptide chemoattractants (*Fig. 1*, steps 0–1) in sea urchins often display species-specific differences in their amino acid sequences [68]. The species specificity of sperm guidance was confirmed by experimental data collected on 17 species from several sea urchin genera [69]. For example, the chemoattractant of *Arbacia punctulata* has no effect on *S. purpuratus* or *Lytechinu spictus* sperm [70–72].

A similar phenomenon has been observed in several holothurian species belonging to the *Bohadschia* genus and 22 ophiuroid species [73]. However, there are a number of examples when chemoattractants exhibit no species-specific activity. In a number of holothurian species (e.g., *Cucumaria piperata*), spermatozoa respond not only to the egg chemoattractants of closely related species, but also to starfish eggs [74, 75]. In echinoderms, the specificity of sperm guidance varies from the species level to the absence of specificity within the class. The reason for these observed differences remains unknown.

Total extracts of the reproductive tissues of the bivalve mollusks *Dreissena polymorpha* and *D. bugensis* can guide both homo- and heterospecific sperm, but the chemoattractant concentration has to be 100-fold higher in order to guide heterospecific gametes [75]. A similar situation is typical for sea anemones of the genus *Montipora*: experiments with three synthetic analogues of chemoattractants demonstrated that the spermatozoa of different species vary in their response to different concentrations of these substances [30]. Finally, it has also been reported that, sometimes, the chemical structure of egg chemoattractant can be identical in the groups that are being studied, since it is involved in basic physiological processes. For instance, this is true for *L*-tryptophan (a chemoattractant in *Haliotis*), which is considered to release in its intact form [36].

Induction of AR (*Fig. 1*, steps 2–3) in sea urchins may also be species-specific. This is made possible by the differences in the position and number of sulfate groups in the polysaccharide chains of the sulfated polysaccharides of the egg envelope [15].

In starfish, specificity of AR induction exists only at the subfamily level (e.g., between the species belonging to the genera *Asterias* and *Aphelasterias* (*Asteriinae* subfamily)) [76]. Furthermore, in most species AR can be induced by many nonspecific interactions, such as mechanical contact with a microscope slide.

Enzymatic degradation of the egg envelope (*Fig. 1*, step 4) in sea urchins appears to be not species-specific [77]. It is believed that in most cases of heterospecific fertilization between closely related species, sperm adhesion to the egg envelope is disrupted [78–82]. For example, in experiments on heterospecific gamete interactions among 11 sea urchin species AR induction occurred in nine combinations, but heterospecific adhesion was observed in none of the cases [80, 81]. It has been confirmed that the variability in bindin plays a crucial role in the species specificity of these processes in sea urchin species that dwell in the same habitat (genera *Echinometra*, *Heliocidaris*, and *Strongylocentrotus*) [83–85]. Species specificity is achieved through structural matching between the flanking regions of bindin and its receptor, EBR1. Alleles characterized by different interaction efficiencies have been revealed in the sea urchin population; however, a model that interprets the matching between them has not yet been developed.

Species-specific egg-envelope degradation has been revealed only in abalones (*Haliotis* spp.), but not in other animal taxa. As mentioned above, acrosomal protein lysin degrades the egg envelope via specific interactions with VERL. The lysin protein either does not dissolve the envelope of heterospecific eggs at all or is inefficient in *in vitro* experiments with the eggs of three abalone species (*H. rufescens*, *H. cracherodii*, and *H. corrugata*) [86]. This specificity is due to the respec-

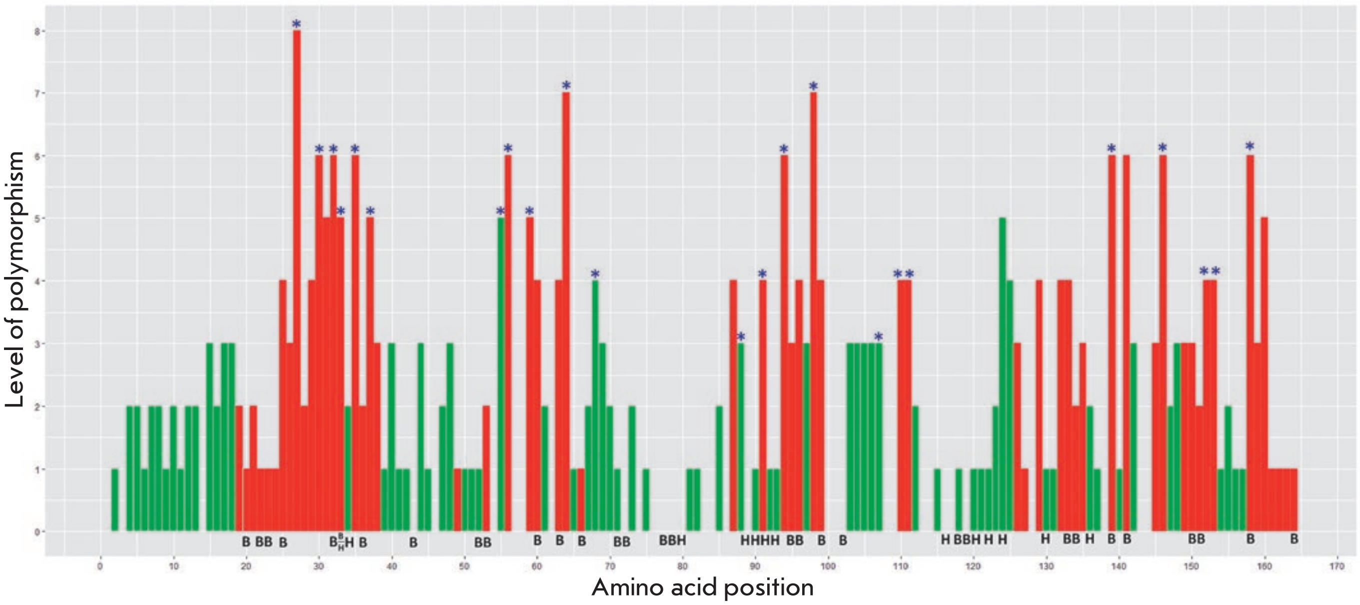

Fig. 4. Diagram showing the variability of the primary structure of the lysin protein. The analysis included the lysin sequences of 25 species from two families (Trochidae and Haliotidae, [53]). The amino acid position in the molecule is plotted against the X axis; the number of detected substitutions is plotted along the Y axis. The sites of radical substitutions (replacement of a hydrophobic amino acid with a hydrophilic one, a cationic amino acid with an anionic one, or deletions) are marked in red. * – sites influenced by positive selection. H – hydrophobic amino acids forming a hydrophobic surface; B – basic amino acids that interact with VERL

tive mutations in VERL repeats and in the positively charged lysin region that carries 24 cationic amino acid residues, of which only seven are conserved (*Fig. 4*).

Finally, there are data showing species-specific differences in the acrosomal proteins in oysters and mussels: it has been hypothesized that the polymorphism in acrosomal proteins maintains the reproductive barriers that exist between the closely related species *Crassostrea* [54, 87] and *Mytilus* [88].

The species specificity of **membrane fusion** (*Fig. 1*, step 5) has been reported (e.g., upon heterospecific fertilization of gametes in the sea urchins *Echinometra mathaei* and *E. oblonga* [78]). However, this species specificity appears to be related to some unknown factors, rather than to the structural differences in protein HAP2, which controls gamete fusion in all eukaryotes [58, 59].

Therefore, the variability of individual gamete recognition proteins can reduce fertilization efficiency and even cause GI. GI can occur at any stage of gamete interaction.

In invertebrates, GI is implemented at different taxonomic levels. In a number of studied taxa, it is inefficient at the species level [30, 68, 69, 73–75]. Unequivocal examples of GI between closely related species have been reported only for complexes of closely related species: in the mollusk genera *Haliotis* and *Tegula* and the sea urchin genera *Echinometra*, *Heliocidaris*, and *Strongylocentrotus*. Heterospecific fertilization is often possible but is not as efficient as the interactions between homospecific gametes; in particular, this was demonstrated in no-choice experiments [52, 75, 77, 89–91]. It is possible that in a number of the studied taxa, GI between closely related species is achieved only upon competition between homo- and heterospecific gametes.

It is expected that genome-wide sequencing and whole-genome annotation of many species listed in this section, as well as advances in bioinformatic methods for predicting the secondary structures of sought-after proteins, will lead to some breakthrough in this field.

GAMETIC INCOMPATIBILITY IN INTERNALLY FERTILIZING SPECIES

In internally fertilizing species, gamete interaction largely depends on the physiological state of a female. For example, oocyte maturation in insects is induced by the synthesis of vitellogenin, whose secretion is regulated by a juvenile hormone, ecdysosteroid, and a number of nutritional signals [92]. The female immune status also plays an important role as it affects sperm storage and survival. The more active the female immune system is, the shorter the sperm storage period will be (see review [93]). This phenomenon is clearly visible in insects that mate only once in their life. A high activity of the immune system of an *Atta colombica* ant queen has a negative effect on sperm survival; in order to ensure long-term sperm storage, special mechanisms that suppress immunity are activated in the female's organism [94]. To gauge the activity of the immune system, Baer et al. measured the efficiency of encapsulation response: small pieces of nylon were inserted into a female's body at equal time periods, and the number of melanized haemocytes encapsulating this extraneous object was counted [94]. This method provides only indirect evidence to the correlation between insects' immune systems and sperm storage, and it still remains to be elucidated what specific molecular cascades are involved in these processes.

In internally fertilizing animals, it would be more accurate to use the term "post-copulatory pre-zygotic reproductive barriers (PCPZ)" instead of GI. This concept involves a number of mechanisms of reproductive isolation that have similar manifestations but are based on different molecular cascades.

PCPZ is often based on a male ability to affect a female physiology. For example, in *Anastrepha suspensa* flies, male presence increases the rate of female ovarian development [95]. Another example is the phenomenon of nuptial gift transfer to females, which affects their physiology and the mating rate (see review [96]). Seminal fluid proteins transferred by the male during internal fertilization play an important role. For instance, the seminal fluid components of the moth *Heliothis virescens* stimulate the female to produce oocytes [97]; the specific protein inducing oocyte production in homospecific females is also known in the cricket *Allonemobius* [98, 99]. We believe that, despite their functional similarity, these proteins are non-homologous.

It has been demonstrated that seminal fluid proteins are rather diverse in terms of their functions and structure. For example, at least 127 proteins were found in the seminal fluid of the beetle *Callosobruchus maculatus* [100]. Seminal fluid proteins may affect oocyte production and changes in the shape of reproductive ducts; they also ensure antimicrobial activity and female receptivity. The proteins can determine the period of sperm storage and modulate the activity of spermatozoa, thus influencing potential sperm competition (SC). Finally, these proteins were shown to be involved in the blocking of the spermatheca (via the formation of mating plugs, see review [101]). A proteomic analysis of seminal fluid components is quite relevant, since many seminal fluid proteins belong to novel families with unknown functions. The available data do not allow one to perform a comparative structural analysis and thoroughly evaluate their role in reproduction. For example, 19 previously not-annotated proteins with unknown functions were discovered in 2009 by proteomic analysis of the seminal fluid of the fruit fly (one of the most commonly used model organisms), followed by a bioinformatic analysis of the whole-genome data [102]. This problem is likely to find a solution as bioinformatic algorithms for predicting protein structure and function based on their primary structure are developed.

Nonetheless, the PCPZ strategy involves the same principles of ligand–receptor interactions. Like in gamete incompatibility, PCPZ species specificity is caused by the coevolution of individual pairs of molecules. These mechanisms may be classified into two groups: female cryptic choice and sperm competition.

Sperm competition (SC)

Polyandry (multi paternity) is a phenomenon that materializes when spermatozoa from several homospecific or sometimes heterospecific partners enter a female reproductive system. Seminal fluid is involved in the formation/sustaining of the active state of the spermatozoa; its components can determine the probability of oocyte fertilization. When sperm from heterospecific males comes into contact, seminal fluid components may be responsible for the outcome of sperm competition (see reviews [103, 104]). This competition may result in conspecific sperm precedence. For example, single mating between individuals from closely related *Drosophila* species may result in interspecific hybridization. However, when a female mates with a hetero- and a homospecific males, most of the progeny will come from the homospecific male [105]. It has been demonstrated experimentally that this effect is connected with seminal fluid proteins [105]. These mechanisms have been extensively studied in a pair of closely related species: *Drosophila simulans* and *D. mauritiana*. PCPZ between them is based on two mechanisms that depend on the copulation order. (1) If homospecific copulation is the first to occur, the seminal fluid components inactivate the heterospecific sperm subsequently entering the female reproductive system. (2) If heterospecific copulation is the first to occur, subsequent homospecific mating results in physical displacement of heterospecific sperm from the sperm storage organs [106]. A similar phenomenon has been demonstrated in flour beetles [107], crickets [108], beetles *Callosobruchus* [109], dragonflies [110], and ladybugs [111].

Female cryptic choice

Female cryptic choice (FCC) is a combination of behavioral, anatomical, and physiological features that allow a female to control efficiency in the process of reproductive products transferring (precopulative FCC) or fertilization (postcopulative FCC; see review [112]). For example, upon the mating of the yellow dung flies *Scathophaga stercoraria*, the probability of egg fertilization depends on which spermatheca the sperm has entered. The female controls sperm distribution, thus rendering the contributions of males to the progeny unequal [113]. Furthermore, the components of female accessory reproductive glands affect sperm survival, which varies in males with different genotypes [113].

Identically to SC, FCC is responsible for conspecific sperm precedence [112]. For example, after the mating of crickets belonging to two species *Allonemobius fasciatus* and *A. socius*, heterospecific sperm loses its motility in the female reproductive system [108].

It is clear that the SC and FCC strategies are phenomenologically similar: so, it is challenging to pinpoint the specific mechanisms that are responsible for reproductive isolation. For example, a female of *L. saxatilis* belonging to the currently being studied group of promiscuous, closely related species of the genus *Littorina* stores sperm and can simultaneously carry progeny from 20 or even more males. However, the distribution of embryonic genotypes in that case is quite abnormal: most of the progeny would originate from one to several males [114]. This phenomenon is considered to result from SC [114]. We presume that it could be related to the recently revealed paraspermal (i.e., residing in “paraspermatozoa”, type of sperm cells that are incapable of fertilization but are present in the sperm) protein LOSP and seminal fluid proteins [21, 22]. However, we possess no direct evidence of this yet.

THE EVOLUTIONARY INTERPRETATION OF GAMETIC INCOMPATIBILITY

GRP polymorphism limits panmixia (random mating) in populations of externally and internally fertilizing invertebrates. Thus, coevolution of individual protein pairs has a direct effect on speciation. The phenomenon of rapid GRP evolution, which has been widely discussed in reviews published since 2002, warrants special attention [9, 10, 12]. The observed level of GRP polymorphism in a number of organisms, ranging from protists to metazoans, is much higher than the expected. Nonsynonymous substitutions in the genes encoding these proteins within the population occur more often than the synonymous ones ($dN/dS > 1$). This means that selection acts on the analyzed loci and the level of polymorphism in the respective proteins is potentially high [9, 10, 115]. For instance, this is true for pheromones of *Euplotes* and Basidiomycota, acrosomal proteins lysin in mollusks *Tegula* and *Haliotida*, and bindin in sea urchins [9, 10, 12]. The evolutionary significance of this phenomenon may be interpreted from two perspectives: explaining the reasons for the high level of GRP polymorphism and analyzing the role of GRP polymorphism and GI in speciation.

The reasons for the high level of GRP polymorphism

Although modifications in GRPs significantly reduce fertilization efficiency, there probably are some factors that form/maintain a high level of polymorphism.

Sympatry (coexistence of species in habitats overlapping either completely or partially) is tightly associated with a rapid rate of GRP evolution. Thus, GI and dN/dS GRP > 1 are observed only between the sympatric sea urchin species of the genera *Echinometra*, *Heliocidaris*, and *Strongylocentrotus* [11, 13–15]. A similar situation is also typical of most of the other taxa mentioned in this article in which GI was demonstrated at the species level. In insects, the condition for GI is not just sympatry, but also polygamy (a reproductive strategy when a female can mate with several males, sometimes as many as a few dozen).

Reinforcement is a special form of selection driving reproductive isolation between spatially subdivided subpopulations within one species, which are adapted to different microniches. We have found only one published experimental confirmation that GI and reinforcement are linked. Under conditions of experimental sympatry in *D. yakuba* and *D. santomea* from allopatric populations (sympatric populations are also known for these species), ethological isolation and PCPZ become significantly stronger within four generations [8].

The discovered polymorphism in protein LOSP, which is potentially involved in RI in closely related sympatric species of the genus *Littorina*, probably serves as additional evidence of a connection between GI and reinforcement [21, 22]. According to our preliminary data, LOSP polymorphism is maximal in populations of *L. saxatilis*. This species exhibits a strong potential to forming races and local ecotypes [115–119] and exists sympatrically with the genetically closely related cryptic species *L. arcana* and *L. compressa* [120–122]. By contrast, this protein is virtually monomorphic in *L. obtusata* populations that exist sympatrically with *L. fabalis* but form no ecotypes in the analyzed populations.

One can assume that the high likelihood of a contact between heterospecific gametes or hybridogenesis between closely related subspecific groups makes the high level of GRP polymorphism and GI formation adaptive [8, 122–126].

Interspecific sexual conflict can also increase the level of GRP polymorphism in a population [18, 19, 127–129]. This model is based on simple stochastic principles: the likelihood of fertilization of the passive partner (the egg) by a spermatozoon is always high, while the spermatozoa compete for the fertilization of a specific egg. For an egg, the highest risk is polyspermia: so, it is adaptive to reduce the efficiency of gamete interaction. For a spermatozoon, the highest risk is competition with other spermatozoa: so, it is adaptive to an increase in the efficiency of gamete interaction. This conflict may result in high GRP polymorphism in the population [18, 19, 127–129], and it may also imply a molecular arms race between a spermatozoon and an egg.

Relationship between the GRP polymorphism and speciation

Taking into account the aforedescribed effect of single amino acid substitutions in GRP for GI, the high level of GRP polymorphism maintained in a population will inevitably partially limit random mating (panmixia).

Speciation is primary. The assumption that selection against hybrids directly influences the GRP polymorphism correlates well with one of the first definitions given for this form of selection by E. Mayr (1970): formation of reproductive isolation between two taxa would be adaptive if the hybrids are less well adapted than their parents [124]. The GRP genes are among the few loci whose products are either predominantly or exclusively related to fertilization: this very part of the genome can be the most "sensitive" to selection against hybrids [8, 125–127]. This point of view significantly contributes to our conventional model of ecological speciation. The phenomenon of high GRP polymorphism as a direct result of selection against hybrids explains the mechanisms of formation of reproductively isolated taxa and confirms the mere possibility of ecological speciation in sympatric populations.

Limitation of panmixia is primary. The data on the potential association between the GRP polymorphism and speciation can also be interpreted in the opposite direction. The subdivision of gene pools may be caused by "background" processes that are not directly involved in speciation. Sexual conflict can be such a factor. In this case, the intraspecific competition will form the primary genetic subdivision. This interpretation is supported by the fact that formation of intra- and interspecific SC in fruit flies is accompanied by similar genomic changes in the same loci [130].

Although the opinions presented in this review seem contradictory, they are in fact largely complementary. On the one hand, sexual conflict reduces the stability of the gene pool of species due to a high level of GRP polymorphism. On the other hand, selection against hybrids may lead to a "targeted" formation of reproductively isolated groups. According to the ecological speciation concept, any form of RI is adaptive and GI in particular arises given certain prerequisites – biological characteristics of individual taxa, such as polyandry.

Verification of these concepts is quite challenging and requires the development of novel model systems. The closely related, internally fertilizing species of marine mollusks from the genus *Littorina* (Mollusca: Caenogastropoda) may serve as such a model. This group has been comprehensively studied in respect to ecological speciation, local adaptation, reproductive behavior, parasite–host interactions, etc. [116–122, 131–133]. Potential effectors of gamete recognition (e.g. paraspermal protein LOSP involved in RI between closely related species via one of the mechanisms described above, such as SC) are currently being actively researched [21, 22, 118]. At least several dozen novel seminal fluid proteins, potentially involved in the formation of interspecific reproductive barriers, have already been discovered, and we plan to report on them in the near future.

CONCLUSIONS

In all studied species, gamete recognition goes through the same stages; however, the stages are based on non-homologous proteins in phylogenetically distant taxa. GI can emerge at any step of gamete recognition, due to structural changes in the respective molecules, and can be observed at various taxonomic levels: between members of different classes, at the genus level, between closely related species, and even at the intraspecific level.

Despite the wide use of whole-genome sequencing, studying novel, highly variable protein families is a challenging task; therefore, the data on GRPs is still fragmentary.

The key trends in this field are related to (1) developing new model systems belonging to different taxonomic groups and manually annotating novel protein families and (2) improving our bioinformatics algorithms for automated annotation and prediction of protein structure and function. ●

This work was supported by the Russian Foundation for Basic Research (grant No. 18-34-00873 (AAL)) and the Russian Science Foundation (grant No. 19-14-00321 (ALM, NAM, and AIG)).

REFERENCES

1. De Queiroz K. // Systematic Biol. 2007. V. 56. № 6. P. 879–886.
2. Mallet J. // Biol. Philosophy. 2010. V. 25. № 4. P. 497–527.
3. Coyne J.A., Orr H.A. Speciation. Sunderland: Sinauer Associates, 2004. 545 c.
4. Turissini D.A., McGirr J.A., Patel S.S., David J.R., Matute D.R. // Mol. Biol. Evol. 2017. V. 35. № 2. P. 312–334.
5. Servedio M.R., Noor M.A. // Annu. Rev. Ecol. Evol. Systemat. 2003. V. 34. № 1. P. 339–364.
6. Schluter D. // Trends Ecol. Evol. 2001. V. 16. № 7. P. 372–380.
7. Coyne J.A., Orr H.A. // Evolution. 1997. V. 51. № 1. P. 295–303.
8. Matute D.R. // PLoS Biol. 2010. V. 8. № 3. P. e1000341.
9. Swanson W.J., Vacquier V.D. // Nat. Rev. Genet. 2002. V. 3. № 2. P. 137.
10. Wilburn D.B., Swanson W.J. // J. Proteomics. 2016. V. 135. P. 12–25.
11. Zigler K.S., McCartney M.A., Levitan D.R., Lessios H.A. // Evolution. 2005. V. 59. № 11. P. 2399–2404.
12. Clark N.L., Aagaard J.E., Swanson W.J. // Reproduction. 2006. V. 131. № 1. P. 11–22.
13. Zigler K.S. // Internat. J. Dev. Biol. 2004. V. 52. № 5–6. P. 791–796.
14. Lessios H.A., Zigler K.S. // Rates of sea urchin bindin evolution. Oxford: Oxford Univ. Press, 2012. P. 136–143.
15. Pomin V.H. // Glycoconjugate J. 2015. V. 32. № 1–2. P. 9–15.
16. Kvarnemo C., Simmons L.W. // Philosoph. Transact. Royal Society B: Biol. Sci. 2013. V. 368. № 1613. P. 20120042.
17. Dorus S., Evans P.D., Wyckoff G.J., Choi S.S., Lahn B.T. // Nat. Genet. 2004. V. 36. № 12. P. 1326.
18. Parker G.A. // Biol. Rev. 1970. V. 45. № 4. P. 525–567.
19. Levitan D.R., Stapper A.P. // Evol. Internat. J. Organic Evol. 2010. V. 64. № 3. P. 785–797.
20. Levitan D.R., Ferrell D.L. // Science. 2006. V. 312. № 5771. P. 267–269.
21. Lobov A.A., Maltseva A.L., Starunov V.V., Babkina I.Y., Ivanov V.A., Mikhailova N.A., Granovitch A.I. // J. Exp. Zool. Part B: Mol. Dev. Evol. 2018. V. 330. № 4. P. 193–201.
22. Lobov A.A., Maltseva A.L., Mikhailova N.A., Granovitch A.I. // J. Molluscan Studies. 2015. V. 81. № 4. P. 512–515.
23. Vacquier V.D. // Science. 1998. V. 281. № 5385. P. 1995–1998.
24. Wood C.D., Nishigaki T., Furuta T., Baba S.A., Darszon A. // J. Cell Biol. 2005. V. 169. № 5. P. 725–731.
25. Miller R.L. // J. Exp. Zool. 1977. V. 202. № 2. P. 203–211.
26. Miller R.L. // Marine Biol. 1979. V. 53. № 2. P. 99–113.
27. Pacey A., Cosson J., Bentley M. // J. Exp. Biol. 1994. V. 195. № 1. P. 259–280.
28. Espinal J., Aldana M., Guerrero A., Wood C., Darszon A., Martínez-Mekler G. // PLoS One. 2011. V. 6. № 8. P. e22619.
29. Guerrero A., Nishigaki T., Carneiro J., Tatsu Y., Wood C.D., Darszon A. // Dev. Biol. 2010. V. 344. № 1. P. 52–65.
30. Coll J.C., Bowden B.F., Meehan G.V., Konig G.M., Carroll A.R., Tapiolas D.M., Aliño P.M., Heaton A., De Nys R., Leone P.A., et al. // Marine Biol. 1994. V. 118. № 2. P. 177–182.
31. Coll J.C., Leone P.A., Bowden B.F., Carroll A.R., König G.M., Heaton A., De Nys R., Maida M., Aliño P.M., Willis R.H., et al. // Marine Biol. 1995. V. 123. № 1. P. 137–143.
32. Hansbrough J.R., Garbers D.L. // J. Biol. Chem. 1981. V. 256. № 3. P. 1447–1452.
33. Suzuki N., Garbers, D.L. // Biol. Reprod. 1984. V. 30. № 5. P. 1167–1174.
34. Zatylny C., Marvin L., Gagnon J., Henry J. // Biochem. Biophys. Res. Commun. 2002. V. 296. № 5. P. 1186–1193.
35. De Lisa E., Salzano A.M., Moccia F., Scaloni A., Di Cosmo A. // J. Exp. Biol. 2013. V. 216. № 12. P. 2229–2237.
36. Riffell J.A., Krug P.J., Zimmer R.K. // J. Exp. Biol. 2002. V. 205. № 10. P. 1439–1450.
37. Yoshida M., Murata M., Inaba K., Morisawa M. // Proc. Natl. Acad. Sci. USA. 2002. V. 99. № 23. P. 14831–14836.
38. Kubagawa H.M., Watts J.L., Corrigan C., Edmonds J.W., Sztul E., Browse J., Miller M.A. // Nat. Cell Biol. 2006. V. 8. № 10. P. 1143.
39. Derenbach J.B., Gereck M.V. // Marine Biol. Ecol. 1980. V. 44. № 1. P. 61–65.
40. Hombeck M., Boland W. // Tetrahedron. 1998. V. 54. № 37. P. 11033–11042.
41. Vallesi A., Giuli G., Bradshaw R.A., Luporini P. // Nature. 1995. V. 376. № 6540. P. 522.
42. Kaupp U.B., Strünker T. // Trends Cell Biol. 2017. V. 27. № 2. P. 101–109.
43. Pitnick S., Hosken D.J., Birkhead T.R. // Sperm biology. Cambridge: Acad. Press, 2009. P. 69–149.
44. Reid D.G. Systematics and evolution of Littorina. London: The Ray Society, 1996. 463 c.
45. Wingstrand K.G. // Acta Zoologica. 1973. V. 54. № 1. P. 31–52.
46. Moy G.W., Mendoza L.M., Schulz J.R., Swanson W.J., Glabe C.G., Vacquier V.D. // J. Cell Biol. 1996. V. 133. № 4. P. 809–817.
47. Dan J.C. // Internat. Rev. Cytol. Cambridge: Acad. Press, 1965.V. 5. P. 365–393.
48. Darszon A., Espinosa F., Galindo B., Sánchez D., Beltrán C. Fertilization. Cambridge: Acad. Press, 2002. P. 225–264.
49. Gupta S.K., Bhandari B. // Asian J. Androl. 2011. V. 13. № 1. P. 97.
50. Talbot P., Chanmanon P. // J. Ultrastruct. Res. 1980. V. 70. № 3. P. 287–297.
51. Vacquier V.D., Lee Y.H. // Zygote. 1993. V. 1. № 3. P. 181–196.
52. Galindo B.E., Moy G.W., Swanson W.J., Vacquier V.D. // Gene. 2002. V. 288. № 1–2. P. 111–117.
53. Kresge N., Vacquier V.D., Stout C.D. // Bioessays. 2001. V. 23. № 1. P. 95–103.
54. Gould M., Stephano J., Holland L.Z. // Dev. Biol. 1986. V. 117. № 1. P. 306–318.
55. Wu Q., Li L., Zhang G. // Marine Biotechnol. 2011. V. 13. № 2. P. 327–335.
56. Takagi T., Nakamura A., Deguchi R., Kyozuka K.I. // J. Biochem. 1994. V. 116. № 3. P. 598–605.
57. Yang S.T., Kreutzberger A.J., Lee J., Kiessling V., Tamm L.K. // Chem. Phys. Lipids. 2016. V. 199. P. 136–143.
58. Chernomordik L., Kozlov M.M., Zimmerberg J. // J. Membrane Biol. 1995. V. 146. № 1. P. 1–14.
59. Fedry J., Forcina J., Legrand P., Péhau-Arnaudet G., Haouz A., Johnson M., Rey F.A., Krey T. // PLoS Biol. 2018. V. 16. № 8. P. e2006357.
60. Ebchuqin E., Yokota N., Yamada L., Yasuoka Y., Akasaka M., Arakawa M., Deguchid R., Mori T., Sawada H. // Biochem. Biophys. Res. Commun. 2014. V. 451. № 4. P. 522–528.
61. von Besser K., Frank A.C., Johnson M.A., Preuss D. // Development. 2006. V. 133. № 23. P. 4761–4769.
62. Liu Y., Tewari R., Ning J., Blagborough A.M., Garbom

S., Pei J., Grishin N.V., Steele R.E., Sinden R.E., Snell W.J., Billker O. // Genes Dev. 2008. V. 22. № 8. P. 1051–1068.
63. Cole E.S., Cassidy-Hanley D., Pinello J.F., Zeng H., Hsueh M., Kolbin D., Ozzello C., Giddings T., Winey M.J., Clark T.G. // Curr. Biol. 2014. V. 24. № 18. P. 2168–2173.
64. Steele R.E., Dana C.E. // PLoS One. 2009. V. 4. № 11. P. e7680.
65. Moy G.W., Vacquier V.D. // Curr. Topics Dev. Biol. 1979. V. 13. P. 31–44.
66. Rufas O., Fisch B., Ziv S., Shalgi R. // Mol. Hum. Reprod. 2000. V. 6. № 2. P. 163–169.
67. Ulrich A.S., Otter M., Glabe C.G., Hoekstra D. // J. Biol. Chem. 1998. V. 273. № 27. P. 16748–16755.
68. Suzuki N., Yoshino K.I. // Comp. Biochem. Physiol. Part B: Comp. Biochem. 1992. V. 102. № 4. P. 679–690.
69. Suzuki N. // Zool. Sci. 1995. V. 12. № 1. P. 13–28.
70. Hathaway R.R. // Biol. Bull. 1963. V. 125. № 3. P. 486–498.
71. Suzuki N., Garbers D.L. // Biol. Reprod. 1984. V. 30. № 5. P. 1167–1174.
72. Ward G.E., Brokaw C.J., Garbers D.L., Vacquier V.D. // J. Cell Biol. 1985. V. 101. № 6. P. 2324–2329.
73. Miller R.L. // J. Exp. Zool. 1997. V. 279. № 2. P. 189–200.
74. Miller R.L. Biology of fertilization. London: Elsevier, 1985. 496 c.
75. Miller R.L., Mojares J.J., Ram J.L. // Canad. J. Zool. 1994. V. 72. № 10. P. 1764–1770.
76. Nakachi M., Moriyama H., Hoshi M., Matsumoto M. // Dev. Biol. 2006. V. 298. № 2. P. 597–604.
77. Yokota N., Sawada H. // Dev. Biol. 2007. V. 308. № 1. P. 222–231.
78. Metz E.C., Kane R.E., Yanagimachi H., Palumbi S.R. // Biol. Bull. 1994. V. 187. № 1. P. 23–34.
79. Glabe C.G., Vacquier V.D. // Nature. 1977. V. 267. № 5614. P. 836.
80. Summers R.G., Hylander B.L. // Exp. Cell Res. 1975. V. 96. № 1. P. 63–68.
81. Summers R.G., Hylander B.L. // Exp. Cell Res. 1976. V. 100. № 1. P. 190–194.
82. Palumbi S.R., Metz E.C. // Mol. Biol. Evol. 1991. V. 8. № 2. P. 227–239.
83. Zigler K.S., McCartney M.A., Levitan D.R., Lessios H.A. // Evolution. 2005. V. 59. № 11. P. 2399–2404.
84. Zigler K.S. // Internat. J. Dev. Biol. 2004. V. 52. № 5–6. P. 791–796.
85. Vacquier V.D., Swanson W.J., Hellberg M.E. // Dev. Growth Differ. 1995. V. 37. № 1. P. 1–10.
86. Vacquier V.D., Lee Y.H. // Zygote. 1993. V. 1. № 3. P. 181–196.
87. Moy G.W., Springer S.A., Adams S.L., Swanson W.J., Vacquier V.D. // Proc. Natl. Acad. Sci. USA. 2008. V. 105. № 6. P. 1993–1998.
88. Riginos C., McDonald J.H. // Mol. Biol. Evol. 2003. V. 20. № 2. P. 200–207.
89. Geyer L.B., Palumbi S.R. // Evolution. 2005. V. 59. № 1. P. 97–105.
90. Levitan D.R. // Evolution. 2002. V. 56. № 8. P. 1599–1689
91. Evans J.P., Garcia-Gonzalez F., Almbro M., Robinson O., Fitzpatrick J.L. // Proc. Royal Soc. B: Biol. Sci. 2012. V. 279. № 1739. P. 2855–2861.
92. Roy S., Saha T.T., Zou Z., Raikhel A.S. // Annu. Rev. Entomol. 2018. V. 63. P. 489–511.
93. Lawniczak M.K., Barnes A.I., Linklater J.R., Boone J.M., Wigby S., Chapman T. // Trends Ecol. Evol. 2007. V. 22. № 1. P. 48–55.
94. Baer B., Armitage S.A., Boomsma J.J. // Nature. 2006. V. 441. № 7095. P. 872.
95. Pereira R., Teal P.E., Sivinski J., Dueben B.D. // J. Insect Behav. 2006. V. 19. № 1. P. 31–43.
96. Gwynne D.T. // Annu. Rev. Entomol. 2008. V. 53. P. 83–101.
97. Park Y.I., Ramaswamy S.B., Srinivasan A. // J. Insect Physiol. 1998. V. 44. № 10. P. 903–908.
98. Marshall J.L., DiRienzo N. // Internat. J. Evol. Biol. 2012. V. 2012. P. 7.
99. Marshall J.L., Huestis D.L., Hiromasa Y., Wheeler S., Oppert C., Marshall S.A., Tomich J.M., Oppert B. // PLoS One. 2009. V. 4. № 10. P. e7537.
100. Goenaga J., Yamane T., Rönn J., Arnqvist G. // BMC Evol. Biol. 2015. V. 15. № 1. P. 266.
101. Avila F.W., Sirot L.K., LaFlamme B.A., Rubinstein C.D., Wolfner M.F. // Annu. Rev. Entomol. 2011. V. 56. P. 21–40.
102. Findlay G.D., MacCoss M.J., Swanson W.J. // Genome Res. 2009. V. 19. № 5. P. 886–896.
103. Parker G.A. // Biol. Rev. 1970. V. 45. № 4. P. 525–567.
104. Smith R.L. Sperm competition and the evolution of animal mating systems. Cambridge: Acad. Press, 1984. 710 c.
105. Price C.S. // Nature. 1997. V. 388. № 6643. P. 663.
106. Price C.S., Kim C.H., Posluszny J., Coyne J.A. // Evolution. 2000. V. 54. № 6. P. 2028–2037.
107. Wade M.J., Patterson H., Chang N.W., Johnson N.A. // Heredity. 1994. V. 72. № 2. P. 163.
108. Gregory P.G., Howard D.J. // Evolution. 1994. V. 48. № 3. P. 705–710.
109. Rugman-Jones P.F., Eady P.E. // Proc. Royal Soc. B: Biol. Sci. 2007. V. 274. № 1612. P. 983–988.
110. Sánchez-Guillén R.A., Córdoba-Aguilar A., Cordero-Rivera A. // Internat. J. Odonatol. 2013. V. 16. № 3. P. 259–267.
111. Katakura H. // Zool. Sci. 1997. V. 14. № 6. P. 869–882.
112. Firman R.C., Gasparini C., Manier M.K., Pizzari T. // Trends Ecol. Evol. 2017. V. 32. № 5. P. 368–382.
113. Ward P.I. // Adv. Study Behav. 2007. V. 37. P. 343–369.
114. Johannesson K., Saltin S.H., Charrier G., Ring A.K., Kvarnemo C., André C., Panova M. // Behav. Ecol. Sociobiol. 2016. V. 70. № 8. P. 1357–1366.
115. Kryazhimskiy S., Plotkin J.B. // PLoS Genet. 2008. V. 4. № 12. P. e1000304.
116. Ravinet M., Westram A., Johannesson K., Butlin R., André C., Panova M. // Mol. Ecol. 2016. V. 25. № 1. P. 287–305.
117. Grahame J.W., Wilding C.S., Butlin R.K. // Evolution. 2006. V. 60. № 2. P. 268–278.
118. Johannesson K. // J. Sea Res. 2003. V. 49. № 2. P. 107–117.
119. Rolán-Alvarez E. // J. Molluscan Studies. 2007. V. 73. № 1. P. 1–10.
120. Mikhailova N.A., Gracheva Y.A., Backeljau T., Granovitch A.I. // Genetica. 2009. V. 137. № 3. P. 333.
121. Small M.P., Gosling E.M. // Heredity. 2000. V. 84. № 6. P. 692.
122. Granovitch A.I., Sokolova I.M. // Sarsia. 2001. V. 86. № 3. P. 241–243.
123. Lukhtanov V.A. // Zhurnal obshchei biologii. 2010. V. 71. № 5. P. 372-385.
124. Mayr E. Populations, species, and evolution: an abridgment of animal species and evolution. Cambridge: Harvard Univ. Press, 1970. 453 c.
125. Lorch P.D., Servedio M.R. // J. Evol. Biol. 2007. V. 20. № 3. P. 937–949.
126. Matute D.R. // Am. Naturalist. 2015. V. 185. № 2. P. 253–269.
127. Albrecht T., Opletalová K., Reif J., Janoušek V., Piálek L., Cramer E.R., Johnsen A., Reifová R. // Evolution. 2019. V. 73. № 2. P. 202–213.

128. Ting J.J., Woodruff G.C., Leung G., Shin N.R., Cutter A.D., Haag E.S. // PLoS Biol. 2014. V. 12. № 7. P. e1001915.
129. Levitan D.R., TerHorst C.P., Fogarty N.D. // Evolution. 2007. V. 61. № 8. P. 2007–2014.
130. Civetta A., Finn S. // G3: Genes, Genomes, Genetics. 2014. V. 4. № 9. P. 1701–1707.
131. Maltseva A.L., Varfolomeeva M.A., Lobov A.A., Mikhailova N.A., Renaud P.E., Grishankov A.V., Volovik K.Y., Granovitch A.I. // Marine Ecol. Prog. Ser. 2016. V. 552. P. 177–193.
132. Granovitch A., Johannesson K. // Ophelia. 2000. V. 53. № 1. P. 55–65.
133. Granovitch A.I., Sergievsky S.O., Sokolova I.M. // Dis. Aquatic Organisms. 2000. V. 41. № 1. P. 53–64.

Cold Physical Plasma Decreases the Viability of Lung Adenocarcinoma Cells

E. A. Golubitskaya[1,2#], O. S. Troitskaya[1#], E. V. Yelak[3], P. P. Gugin[4], V. A. Richter[1],
I. V. Schweigert[5], D. E. Zakrevsky[3,4], O. A. Koval[1,2*]
[1]Institute of Chemical Biology and Fundamental Medicine, Siberian Branch of the Russian Academy of Sciences, Akad. Lavrentiev Ave. 8, Novosibirsk, 630090, Russia
[2]Novosibirsk State University, Pirogova Str. 1, Novosibirsk, 630090, Russia
[3]Novosibirsk State Technical University, K. Marx Ave. 20, Novosibirsk, 630073, Russia
[4]Rzhanov Institute of Semiconductor Physic, Siberian Branch of the Russian Academy of Sciences, Akad. Lavrentiev Ave. 13, Novosibirsk, 630090, Russia
[5]Khristianovich Institute of Theoretical and Applied Mechanics, Siberian Branch of the Russian Academy of Sciences, Institutskaya Str. 4/1, Novosibirsk, 630090, Russia
[*]E-mail: o.koval@niboch.nsc.ru
[#]The authors have contributed equally

Received June 17, 2019; in final form, September 13, 2019
DOI: 10.32607/20758251-2019-11-3-16-19

Copyright © 2019 National Research University Higher School of Economics. This is an open access article distributed under the Creative Commons Attribution License,which permits unrestricted use, distribution, and reproduction in any medium, provided the original work is properly cited.

ABSTRACT **The high mortality rate that accompanies cancer spurs the search for new methods that can be used to treat malignant neoplasms. In addition to chemotherapy, electrophysical techniques for tumor treatment appear rather promising. The results of *in vitro* exposure of A549 human lung adenocarcinoma cells to cold atmospheric plasma (CAP) are hereby presented. A gas-discharge device that generates a sequence of streamers propagating along a stream of inert gas in the ambient air was used. In the zone where the plasma jet came into contact with the target object, there were high-intensity electric fields and high plasma concentrations, while the gas temperature changed by less than a degree. In this study, we compared the cytotoxic effect of CAP in helium and argon. Direct irradiation of cells by CAP with $U = 4.2$ kV for 30–120 s was shown to reduce cell viability by 25%. Variation of the amplitude of the AC voltage in the plasma device in argon within a range of 3.8–5.6 kV did not significantly alter the cell death rate. Further optimization of the modes of CAP generation in gas-discharge devices with various geometries for the treatment of a tumor cell and animal tumor models can underlie the development of antitumor plasma medicine.**

KEYWORDS **cold atmospheric plasma, antitumor therapy, reactive oxygen species, lung adenocarcinoma.**

ABBREVIATIONS **CAP – cold atmospheric plasma; FBS – fetal bovine serum; MTT – 3-(4,5-dimethylthiazol-2-yl)-2,5-diphenyltetrazolium bromide; RNS – reactive nitrogen species; ROS – reactive oxygen species.**

INTRODUCTION

Along with the development of efficacious chemotherapeutic agents to treat malignant neoplasms, much attention is currently being focused on physical methods such as radiotherapy (including photon radiation therapy, proton beam therapy, and boron neutron capture therapy) [1, 2]. The application of cold atmospheric plasma (CAP) is among the promising novel biophysical approaches to the treatment of a number of malignancies [3]. The potential risk factors associated with the use of CAP on humans include the risk that some amount of current may flow through tissue, thermal damage, and exposure to UV radiation. However, all these drawbacks can be eliminated at the stage of selection of gas composition, radiation intensity, and duration. CAP has been shown to be safe in patients with chronic skin ulcers [4, 5]. CAP is a sequence of streamers that are generated in inert gases in the dielectric channel of a plasma jet device and propagate along the gas stream in ambient air under atmospheric pressure. A gas mixture consisting of an inert gas, nitrogen, oxygen, and water vapor is excited and ionized thanks to high-energy electrons and the high plasma concentration in the steamer head, where the electric field intensity can go as high as 10–20 kV/cm. Various oxygen- and nitrogen-containing compounds, such as H_2O_2, HNO_2, HNO_3, N_2O, NO_2, NO, and N_2O_3, form in plasma-stimulated chemical reactions. Inert gases are commonly used as a working gas in plasma jet devices, since air breakdown voltage is much higher. The low temperature in the zone where cold plasma comes into contact with a biological object is an attractive feature

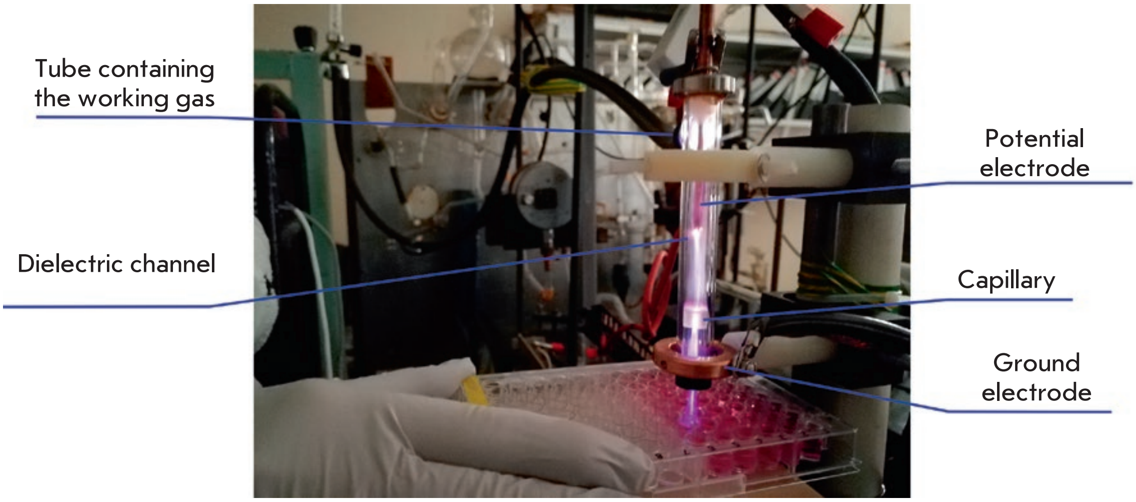

Fig. 1. The plasma jet device for the irradiation of cultured cells

of the technique of using a plasma jet in antitumor approaches [3]. Cold atmospheric plasma was shown to exhibit cytotoxic activity against more than 20 lines of tumor cells of different histogenesis and in experimental *in vivo* models in animals carrying tumors [6]. Reactive oxygen (ROS) and reactive nitrogen species (RNS) were identified as the key molecules that trigger cell death upon exposure to CAP. H_2O_2 molecules are believed to play a crucial role among ROS as they can induce mitochondrial and DNA damage [7]. It was shown experimentally that cells undergo a synergistic effect of H_2O_2, NO_2^- and NO_3^- upon exposure to CAP, but the cytotoxicity of RNS is much lower than that of ROS [8]. Not only does CAP treatment induce cytotoxic effects, but it also may restore the susceptibility of resistant tumor cells to cytostatics (e.g., in case of temozolomide-resistant glioblastoma) [9].

In this study, we used an original device that generates a plasma jet, which allows one to widely vary the modes of streamer breakdown in the dielectric channel and the dynamics of streamer sequence propagation along an inert gas jet (*Fig. 1*). The effects of the exposure of human tumor cells to CAP in helium and argon were compared. The reason for using two working gases was that argon and helium have different physical properties (namely, argon atoms are tenfold heavier than helium atoms, while the threshold ionization and excitation energies are lower for argon), which eventually influences the physical properties of the plasma jet (electron concentration, electric field intensity, etc.) and the near-surface plasma chemistry.

EXPERIMENTAL

Our gas-discharge device consisted of a dielectric coaxial channel (100 mm long) with an inside diameter of 8 mm. A metal (copper) electrode (50mm long and 2 mm in diameter) and a capillary (6 mm long; inside diameter, 2.6 mm) were coaxially inserted into the channel and immobilized with a quartz bushing (23 mm long; inside diameter, 5 mm). The quartz channel was surrounded by an annular copper electrode. The discharge zone consisted of an inner (recording) and outer (ground) electrode. A sinusoidal voltage (frequency, ~ 25 kHz and amplitude < 6 kV) produced by a high-voltage pulse generator was applied to the recording electrode. The gas system ensured a flow rate of working gases of up to 15 l/min at an excessive pressure in the gas line of 1 atm. The experiments were conducted using helium and argon as working gases.

As the working gas is fed and the sinusoidal voltage U applied, a breakdown is observed during the positive half-wave between the recording and ground electrodes. As the voltage U is further increased to $> 1–3$ kV (depending on the gas and gas flow rate), a plasma jet is formed. This jet leaves the dielectric channel and propagates in free space. Depending on the excitation parameters, a typical jet length is 5–50 mm (in helium) and 5–20 mm (in argon).

A549 human lung adenocarcinoma cells (Russian Collection of Cell Cultures Vertebrate, Institute of Cytology, St. Petersburg, Russia) were used in this study. The cells were cultured in DMEM (GIBCO, USA) supplemented with 2 mM *L*-glutamine (Sigma-Aldrich, USA), 10% FBS (GIBCO, USA), and an antibiotic-antimycotic solution (100 U/ml penicillin, 100 mg/ml streptomycin sulfate, 0.25 μg/ml amphotericin; GIBCO, USA) at 37.0 ± 1.0°C under an atmosphere of 5.0 ± 0.5% CO_2.

The cells to be further exposed to CAP were cultured in 96-well plates (4×10^3 cells per well) in 100 μL.

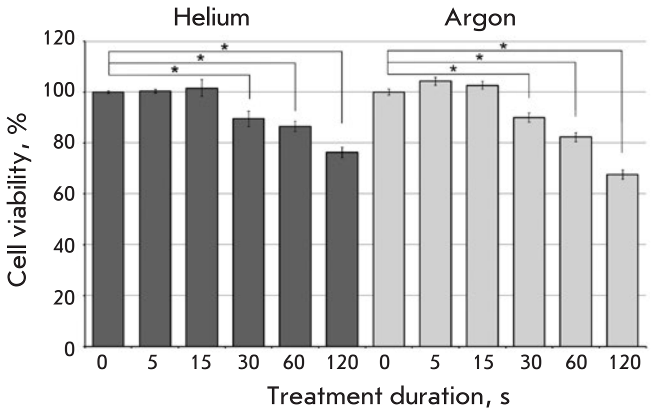

Fig. 2. The effect of cold physical plasma on the viability of A549 adenocarcinoma cells. Voltage, 4.2 kV. The viability of the control (untreated) cells was 100%. The MTT assay data are presented as a mean of three independent experiments ± SD, $^*p < 0.05$

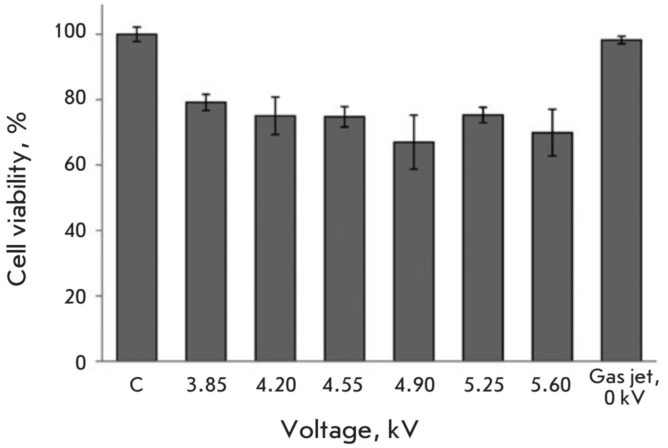

Fig. 3. Voltage-dependent cytotoxicity of CAP irradiation of A549 cells in argon. The MTT assay data 48h post-irradiation. C – control (untreated) cells. The data are presented as a mean of three independent experiments ± SD

Once the cell monolayer had reached 70–80% confluence, the cells were exposed to cold atmospheric plasma treatment. The cells were cultured under standard conditions for 24 days. The medium was then replaced with a serum-free RPMI medium supplemented with 0.25 mg/ml MTT (3-(4,5-dimethylthiazol-2-yl)-2,5-diphenyltetrazolium bromide) (Sigma, USA), and the cells were incubated for 4 h at 37°C. Next, the medium was removed from the wells and formazan crystals were dissolved in DMSO. The optical density of the solution in the wells was measured on a multichannel spectrophotometer (Berthold Technologies, Germany) at $\lambda = 570$ nm.

RESULTS AND DISCUSSION

The effect of a cold atmospheric plasma on the survival of tumor cells was studied using the A549 human lung adenocarcinoma cell line. It was demonstrated by MTT assay that cell viability decreases as treatment duration is increased from 5 s to 2 min. Short-term (< 30 s) CAP treatment of the cells had virtually no effect on cell survival (*Fig. 2*). The maximum reduction of cell viability was attained after a 2-min treatment phase, both for helium and for argon.

Cell death was visualized using propidium iodide (PI), a low-molecular-weight fluorescent dye that is capable of intercalating into the DNA of dying cells with the damaged membrane but does not penetrate into living cells. It was found that the percentage of stained cells increases with CAP treatment duration (the data are not shown). Hence, it was demonstrated that CAP treatment induces cell death.

When using a plasma jet, the loaded electrode voltage is one of the key parameters responsible for plasma jet dynamics and the plasma–surface interaction. The energy of the electrons in the plasma jet, as well as the rates of ionization, dissociation, and excitation of molecules due to electron impact, depends on the applied pressure, which may have a significant effect on the induced plasma-chemical processes and, therefore, the biological effect of a plasma jet. Direct irradiation at various AC voltage amplitudes was employed to analyze the effect of the voltage applied to the loaded electrode in a plasma jet device generating CAP on cytotoxic activity against A549 cells. It was found experimentally that changes in the voltage amplitude of argon within a range of 3.8–5.6 kV have no effect on the level of cell death (*Fig. 3*). Additional studies focused on the impact of an inert gas flow without a plasma jet on cells and studies at zero voltage demonstrated that both the argon and helium flows did not affect the viability of the irradiated cells.

CONCLUSIONS

Hence, it has been demonstrated for A549 lung adenocarcinoma cells that direct exposure to cold atmospheric plasma causes tumor cell death. Variation of the modes of the irradiating inert gases (including their mixtures with molecular gases) in the gas-discharge device allows one to generate a cold plasma jet with a wide range of energy parameters and compositions, which certainly is an advantage of this study. Further optimization of devices based on dielectric channels of different geometries, as well as the mediated treatment of cells through the pre-irradiated culture medium, will make it possible to choose the optimal conditions for the impact of cold atmospheric plasma on human tumor cells. The safety of CAP treatment as relates to human tissue has already been demonstrated; therefore, it is beyond any doubt that this method can potentially be used in clinical practice to treat certain malignant neoplasms. ●

This study was supported by the Russian Science Foundation (grant No. 19-19-00255) and by State Budget Program (0245-2019-0001).

REFERENCES

1. Hideghéty K., Brunner S., Cheesman A., Szabó E.R., Polanek R., Margarone D., Tőkés T., Mogyorósi K. // Anticancer Res. 2019. V. 39. № 5. P. 2265–2276.
2. Laprie A., Hu Y., Alapetite C., Carrie C., Habrand J.-L., Bolle S., Bondiau P.-Y., Ducassou A., Huchet A., Bertozzi A.-I., et al. // Cancer/Radiothérapie. 2015. V. 19. № 8. P. 775–789.
3. Utsumi F., Kajiyama H., Nakamura K., Tanaka H., Mizuno M., Ishikawa K., Kondo H., Kano H., Hori M., Kikkawa F. // PLoS One. 2013. V. 8. № 12. P. e81576.
4. Isbary G., Heinlin J., Shimizu T., Zimmermann J., Morfill G., Schmidt H., Monetti R., Steffes B., Bunk W., Li Y., Klaempfl T., Karrer S., Landthaler M., Stolz W. // Br. J. Dermatol. 2012. V. 167. № 2. P. 404–410.
5. Ulrich C., Kluschke F., Patzelt A., Vandersee S., Czaika V., Richter H., Bob A., Hutten Jv., Painsi C., Hüge R., Kramer A., Assadian O., Lademann J., Lange-Asschenfeldt B. // J. Wound Care. 2015. V. 24. № 5. P. 198–200.
6. Keidar M. // Plasma Sources Sci. Technol. 2015. V. 24. № 3. P. 033001.
7. Bekeschus S., Iseni S., Reuter S., Masur K., Weltmann K.D. // IEEE Trans. Plasma Sci. 2015. V. 43. № 3. P. 776–781.
8. Wende K., Williams P., Dalluge J., van Gaens W., Aboubakr H., Bischof J., von Woedtke T., Goyal S.M., Weltmann K.-D., Bogaerts A., et al. // Biointerphases. 2015. V. 10. № 2. P. 029518.
9. Köritzer J., Boxhammer V., Schäfer A., Shimizu T., Klämpfl T.G., Li Y.-F., Welz C., Schwenk-Zieger S., Morfill G.E., Zimmermann J.L., et al. // PLoS One. 2013. V. 8. № 5. P. e64498.

A Novel Sulfonated Derivative of β-Cyclodextrin Effectively Inhibits Influenza A Virus Infection *in vitro* and *in vivo*

E. P. Goncharova[1*], Y. A. Kostyro[2], A. V. Ivanov[2], M. A. Zenkova[1]
[1]Institute of Chemical Biology and Fundamental Medicine, Siberian Branch of Russian Academy of Sciences, Lavrentiev Ave. 8, Novosibirsk, 630090, Russia
[2]A.E. Favorsky Irkutsk Institute of Chemistry, Siberian Branch of Russian Academy of Sciences, Lermontov Str. 134, Irkutsk, 664033, Russia
*Email: egn@niboch.nsc.ru

Received April 25, 2019; in final form, July 15, 2019
DOI: 10.32607/20758251-2019-11-3-20-30

Copyright © 2019 National Research University Higher School of Economics. This is an open access article distributed under the Creative Commons Attribution License,which permits unrestricted use, distribution, and reproduction in any medium, provided the original work is properly cited.

ABSTRACT **The development of novel drugs against the influenza virus with high efficiency and low toxicity is an urgent and important task. Previous reports have demonstrated that compounds based on sulfo derivatives of oligo- and polysaccharides possess high antiviral activity. In this study, we have examined the ability of a novel sulfonated derivative of β-cyclodextrin (KS-6469) to inhibit the influenza virus A/WSN/33 (H1N1) infection *in vitro* and *in vivo*. The antiviral potential of KS-6469 against the influenza virus was evaluated in Madin-Darby Canine Kidney epithelial cells treated with serially diluted KS-6469. We found out that KS-6469 completely inhibited viral reproduction after treatment of the infected cells with the compound for 48 h. Our data show that double intranasal treatment of mice with KS-6469 fully protected the animals from a lethal infection and significantly decreased the viral titers in the lungs of the infected animals. Thus, the novel sulfonated β-cyclodextrin derivative KS-6469 is a promising candidate for the development of antiviral drugs for preventing and treating the influenza infection.**

KEYWORDS **influenza virus, antiviral activity, sulfonated derivative of β-cyclodextrin.**

ABBREVIATIONS **IAV – influenza A virus; PBS – phosphate-buffered saline; MDCK – Madin-Darby canine kidney cells; IMDM – Iscove's Modified Dulbecco's Medium; MOI – multiplicity of infection; IC_{50} – compound concentration that produces 50% cell growth inhibition; CI – cell index; FFA – focus-forming assay; FFU – focus-forming unit; NA – neuraminidase; MUNANA – 2'-(4-methylumbelliferyl)-α-D-N-acetylneuraminic acid; HA – hemagglutination activity; p.i. – post-infection; MBCD – methyl-β-cyclodextrin; mAbs – monoclonal antibodies.**

INTRODUCTION

The influenza virus causes respiratory diseases that are responsible for the death of up to 650,000 people each year worldwide [1]. The emergence of new drug-resistant strains of influenza and the limited effectiveness of existing vaccines mean that the development of new, more effective antiviral compounds is critical in order to fight the virus. To this end, sulfonated polysaccharides are among the most promising antiviral compounds. This group of compounds includes sulfo derivatives of oligo- and polysaccharides containing O-sulfate and/or N-sulfamate moieties. The antiviral properties of sulfonated polysaccharides have been known for a long time. Ginsberg et al. investigated the antiviral properties of the capsular polysaccharide of *Klebsiella pneumoniae* and showed that this polysaccharide effectively suppresses the replication of the mumps virus [2]. It has previously been reported that sulfonated polysaccharides, including β-cyclodextrin, display antiviral activity against a number of enveloped viruses [3–7]. There is evidence that a number of sulfonated polysaccharides–in particular, sulfo derivatives of oligo- and polysaccharides containing O-sulfate groups–possess high antiviral activity [8–11]. Synthetic polymers of the N-sulfonate derivatives of poly(allylamine hydrochloride) have been shown to effectively inhibit the influenza A virus *in vitro* and *ex vivo*, mainly in the late stages of the infection [12]. It is noteworthy that i-carrageenan, a sulfated polysaccharide, has been clinically tested, authorized for release, and sold in some countries for intranasal treatment of an influenza infection [13]. However, no data on the antiviral activity of the sulfo derivatives of carbohydrates containing sulfonate groups (C-sulfates) are available.

In this study, we investigated the antiviral properties of a sulfonated (C-sulfate) oligosaccharide (a bisulfite derivative of oxidized β-cyclodextrin KS-6469) against the influenza A/WSN/33 (H1N1) (IAV) virus *in vitro* and *in vivo*. The results revealed that KS-6469 effectively inhibits the replication of IAV in MDCK cells by acting in the late stages of the viral infection, and that it possesses virucidal properties. The results obtained on a mouse model of lethal influenza infection *in vivo* confirmed the high antiviral potential of this compound.

EXPERIMENTAL

Synthesis of the KS-6469 compound

The KS-6469 compound was developed and synthesized at the A.E. Favorsky Irkutsk Institute of Chemistry (Siberian Branch of the Russian Academy of Sciences) based on commercially available β-cyclodextrin (KLEPTOSE®, Belgium). A detailed description of the synthetic procedure and the physicochemical properties of KS-6469 will be published separately. Oseltamivir (Tamiflu®, Switzerland) was prepared as a solution in phosphate-buffered saline (PBS) for oral gavage administration.

Cytotoxicity of KS-6469 in MDCK cells

The MTT assay. The cytotoxicity of KS-6469 was evaluated using the 3-(4,5-dimethylthiazol-2-yl)-2,5-diphenyltetrazolium bromide (MTT) test as described previously [14]. Madin-Darby Canine Kidney (MDCK) cells were received from the Bank of Cell Cultures (Institute of Cytology, St. Petersburg, Russia). The cells were maintained in Iscove's Modified Dulbecco's Medium (IMDM; Sigma, USA) supplemented with 5% fetal bovine serum (Sigma, USA), 100 units/L penicillin, 100 mg/mL streptomycin, and 0.25 mg/mL amphotericin (antibiotic-antimycotic solution, Sigma, USA) at 37°C in a humidified atmosphere containing 5% CO_2 (from here on referred to as "standard conditions"). Briefly, MDCK cells were seeded into 96-well plates and grown to confluence under standard conditions. The medium was replaced with a fresh medium containing serially diluted KS-6469, and the cells were incubated for another 24 h under standard conditions. Aliquots of the MTT solution were added to each well, and incubation was continued for an additional 3 h. The dark blue formazan crystals formed within live cells were solubilized with dimethyl sulfoxide (DMSO); absorbance was measured at 570 nm in a Multiskan™ FC plate reader (Thermo LabSystems, Finland). The IC_{50} was determined as the compound concentration required to decrease the A_{570} to 50% of the control (DMSO alone) and was determined by interpolation from the dose-response curves.

Real-time cell analysis. The cytotoxic effects of KS-6469 on the MDCK cells were measured on an xCELLigence real-time cell analyzer (ACEA Biosciences Inc., USA), which is based on the microelectronic biosensor technology. The electrode impedance displayed as the cell index (CI) value was measured to compare the status of treated and untreated cells. The cells were plated in 16-well plates (ACEA Bioscience Inc., USA) in IMDM supplemented with 10% FBS and a antibiotic-antimycotic solution and incubated overnight (20 h) under standard conditions. The growth medium was then removed, the cells were washed with PBS, and 150 μL of IMDM either containing different concentrations of KS-6469 or without the compound was added to each well. The cells were then incubated under standard conditions for 65 h with cell viability monitored every 15 min using the xCELLigence real-time cell analyzer. The points were run in duplicate, and the IC_{50} value was calculated using the xCELLigence real-time cell analyzer software. The concentration of KS-6469 at which the diagram of CI for the treated cells coincided with that of CI for the untreated cells was defined as the maximum tolerated concentration (MTC).

Determination of the antiviral activity of KS-6469 in MDCK cells

The influenza virus strain A/WSN/33 (H1N1) was obtained from the Ivanovsky Institute of Virology (Moscow, Russia). MDCK cells were grown to confluence in 24-well plates under standard conditions. The cells were then infected with IAV at MOI 0.1 in a medium supplemented with KS-6469 (70–600 μg/mL) and incubated at 37°C for 24 or 48 h under standard conditions. Twenty-four or 48 h post-infection (p.i.), the cells were subjected to one freeze/thaw cycle (-20/20°C) and then the viral titer was determined by FFA as described previously [15].

The index of virus yield reduction (KI, %) and the chemotherapeutic index (CTI) were used as basic criteria for evaluating the efficacy of KS-6469 *in vitro*. The index of virus yield reduction was determined as:

$$KI = (T_c - T_o)/T_c \times 100\%,$$

where T_c is the viral titer in the medium without KS-6469, and T_o is the viral titer in the medium supplemented with KS-6469 [16]. CTI of the compound was defined as the ratio:

$$CTI = MTC / MEC,$$

where MTC is the maximum tolerated concentration, and MEC is the minimum concentration of the compound producing a 100-fold reduction in virus titer [17].

Time-of-addition assay

To determine the steps of the IAV life cycle that proved sensitive to the KS-6469 treatment, the MDCK cells were grown to confluence in 24-well plates and infected with IAV (MOI 0.1) for 1 h under standard conditions. The KS-6469 compound was added at a concentration of 5 mg/mL before, during, or after the IAV infection. After each period of incubation with the virus, the cells were washed with PBS and incubated with a fresh infection medium at 37°C. Forty-eight h p.i., the cells were subjected to one freeze/thaw cycle and the viral titer was determined by FFA.

The NA-Fluor™ Influenza Neuraminidase Assay

Neuraminidase (NA) activity was measured using the NA-Fluor™ Influenza Neuraminidase Assay kit (Applied Biosystems, USA), according to the manufacturer's protocol. The assay is based on the NA enzyme cleaving the 2'-(4-methylumbelliferyl)-α-D-N-acetylneuraminic acid (MUNANA) substrate to release the fluorescent product, 4-methylumbelliferone. The fluorescent signal was measured using a CLARIOstar® fluorescence plate reader (BMG LABTECH, Germany). The assays were performed in triplicate.

Hemagglutination assay

The antiviral activity of KS-64649 was estimated using hemagglutination assay (HA). Viral suspensions were incubated with an equal volume of the medium with or without KS-6469. In this assay, a 0.5% suspension of chicken erythrocytes was used. The viral titer of the sample was calculated as the inverse value of the dilution at which the last agglutinated appearance was detected.

Analysis of the cholesterol level in the viral envelope

The cholesterol level in the viral envelopes was determined using the Amplex Red Cholesterol assay kit (Molecular Probes, USA), according to the manufacturer's instructions. Briefly, the viruses were incubated with different concentrations of KS-646 for 6 h at 37°C then pelleted and re-suspended in Amplex Red reaction buffer. Methyl-β-cyclodextrin was used as a positive control. Fluorescence was then analyzed on a CLARIOstar® plate reader at an excitation wavelength of 550 nm and an emission wavelength of 590 nm. The assays were performed in triplicate.

Virucidal activity of KS-6469

Viral suspensions were incubated with an equal volume of the medium with or without KS-6469 for 3 or 6 h at 4, 20 or 37°C. The viral titer was estimated using the FFA. The assays were performed in triplicate.

Enzyme-linked immunosorbent assay

Enzyme-linked immunosorbent assays were performed using commercially available monoclonal antibodies against influenza virus hemagglutinin [IVC102], [1.B.408] and [B219M] (Abcam) as described previously [18].

Antiviral activity of KS-6469 on the mouse model of lethal influenza infection

Animals. Female 4- to 6-week-old BALB/c mice were purchased from the State Research Center of Virology and Biotechnology Vector (Koltsovo, Russian Federation). The animals were kept in the vivarium of the Institute of Chemical Biology and Fundamental Medicine, SB RAS, with a natural light regime on a standard diet for laboratory animals (GOST [State Standard] R 5025892) in compliance with the international recommendations of the European Convention for the Protection of Vertebrate Animals used for Experimental and Other Scientific Purposes [19], as well as the rules of laboratory practice in the performance of pre-clinical studies in the Russian State Standards (R 51000.3-96 and 51000.4-96). The experimental protocols were approved by the Inter-Institute Bioethics Commission of SB RAS (22.11 dated May 30, 2014).

In vivo toxicity analysis. To evaluate the toxicity of KS-6469, the mice were treated by intraperitoneal or intranasal administration of varying amounts of the compound. Each of the experimental groups contained six BALB/c mice. The animals received KS-6469 in different doses intraperitoneally in 0.2 mL of PBS, or 250 mg/kg twice daily intranasally in 40 μL of PBS. The mice from the control groups received the same volume of PBS. After the treatment, signs of intoxication including general condition, weight, and depression of the central nervous system were assessed daily for 14 days.

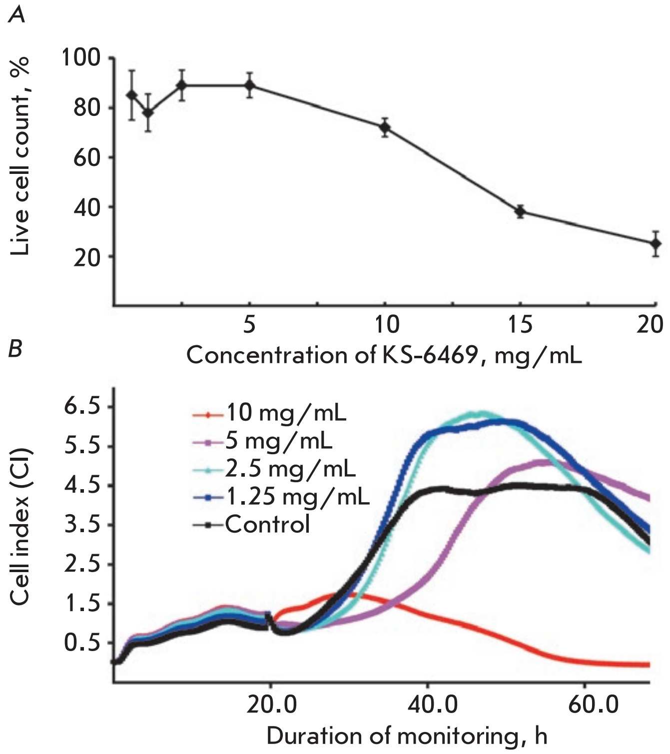

Fig. 1. Cytotoxicity of KS-6469 with respect to MDCK cells. MDCK cells were exposed to different concentrations of KS-6469 and incubated at 37°C, followed by cell viability measurement by MTT assay (*A*); the viability of MDCK cells treated with KS-6469 was monitored by Real-Time Cell Analysis (*B*). Cells incubated in IMDM without KS-6469 were used as control

Protective efficacy in mice. To test the protective efficacy of KS-6469, we evaluated weight changes, the survival rate, and viral titer in the lungs of the infected mice. BALB/c mice with an average weight of 14 to 16 g were divided into groups of six animals. The mice were anesthetized by intraperitoneal injection of tribromoethanol (Avertin®) and infected intranasally with 3 LD_{50} being equal to ~$1.2 \times 10^4 \pm 0.7 \times 10^4$ FFU of IAV immediately after intranasal administration of KS-6469 at a dose of 250 mg/kg. The following day, the mice received a second dose of KS-6469 intranasally. The study included a positive control group that received oseltamivir daily (7.5 mg/kg) for 5 days. The control mice received PBS instead of KS-6469. The animals were inspected daily and weighed for 14 days after infection. The degree of protection was estimated according to the reduction in the mortality rate. To assess the viral titer in the lungs, BALB/c mice were divided into groups of six animals. The mice were infected intranasally with 3 LD_{50} of IAV immediately after intranasal administration of KS-6469 at various doses. The following day, the mice received a second dose of KS-6469 intranasally. The control mice received PBS instead of KS-6469. The mice in each group were euthanized on day 3 p.i., and the lung tissue was harvested. The lungs were weighed and the medium was added at a ratio between the lung tissue and the medium of 1 : 10 (v/v). The homogenates were prepared using a Sonopuls HD 2070 ultrasonic homogenizer (Bandelin, Germany). The viral titers of the lung homogenates were determined using FFA.

Statistical analysis

The data are expressed as the mean ± SD. The statistical analysis was performed using the two-tailed unpaired t-test. P-values of less than 0.05 were deemed statistically significant.

RESULTS

Characterization of KS-6469

The compound KS-6469 is a bisulfite derivative of oxidized β-cyclodextrin. The sulfonate moieties of bisulfite derivatives are bound directly to a carbon atom with the general formula $(Glu_{ox})_7\text{-}C_x\text{-}(SO_3Na)_x$, where $(Glu_{ox})_7\text{-}C_x$ is oxidized β-cyclodextrin, x is the number of sulfonated carbon atoms, and SO_3R is the bisulfite (sulfonate) group. The detailed structure and physicochemical properties of KS-6469 are the subject of ongoing research and will be published later.

Cytotoxicity of KS-6469

The cytotoxicity of KS-6469 toward the MDCK cells was examined. The half maximal inhibitory concentration (IC_{50}) value (the concentration of KS-6469 that caused 50% cell lethality) was 15 ± 3.3 mg/mL, as determined by MTT assay after 24 h incubation with the compound (*Fig. 1A*). An analysis of the cytotoxic effect of KS-6469 on the cells following 65 h exposure to KS-6469 was measured using real-time cell analysis. The IC_{50} value obtained by this method was found to be 8.9 ± 1.3 mg/mL after 65 h exposure (*Fig. 1B*). These results confirmed the low cytotoxicity of KS-6469 toward eukaryotic cells, which reached 15 and 8.9 mg/mL for the 24 and 65 h exposure durations, respectively. Based on the data from these experiments, we can conclude that KS-6469 possesses low toxicity toward MDCK cells.

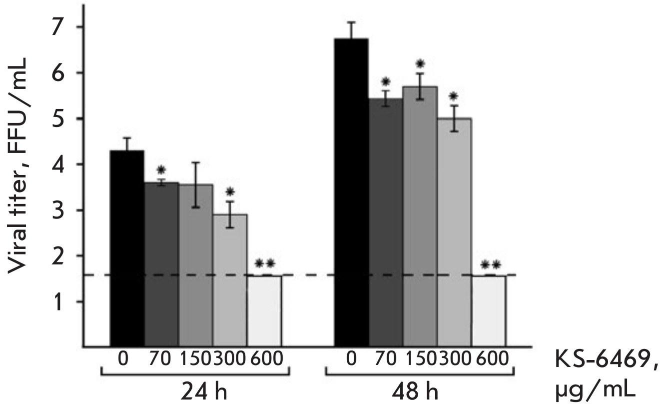

Fig. 2. The replication of the influenza virus A/WSN/33 (H1N1) is effectively inhibited in MDCK cells by treatment with KS-6469. Various concentrations of KS-6469 were used to treat MDCK cells. The production of infectious viruses was determined by FFA 24 and 48 h p.i. The limit of detection for the FFA is 1.7 lg FFU/mL and is shown by a dotted line. Significance: $^*p < 0.05$, $^{**}p < 0.01$ vs. virus only (0)

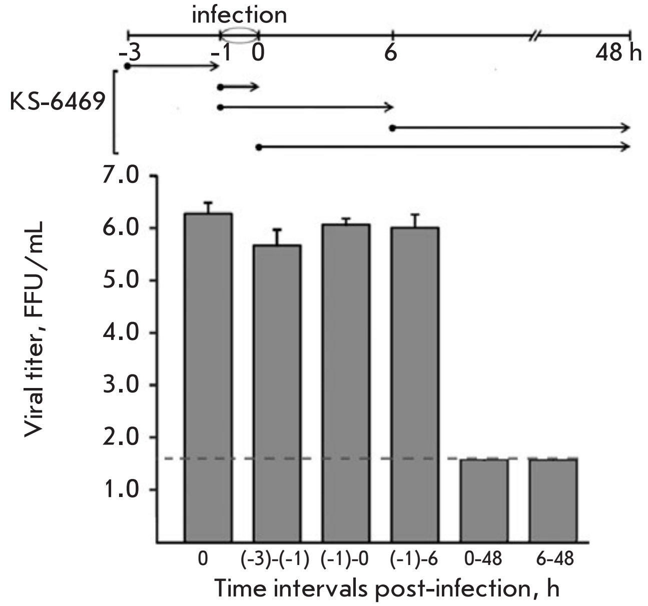

Fig. 3. Time-of-addition experiment showing the mechanism of influenza virus inactivation by KS-6469. Cells were infected with IAV at MOI 0.1 for 1 h (from time point (-1) to 0 h); 5 mg/mL KS-6469 was then added to the cells at the indicated time points (·). After each incubation period (shown with arrows), the medium containing KS-6469 was replaced with a compound-free medium. At 48 h p.i., the supernatants were collected and the viral titers were evaluated by FFA. The data are presented as mean ± SD ($n = 3$). The limit of detection for FFA (1.7 lg FFU/mL) is shown with a dashed line

Antiviral properties of KS-6469

The antiviral activity of KS-6469 was tested *in vitro* in the MDCK cells/IAV model of the influenza infection. The MDCK cells were simultaneously treated with different doses of KS-6469 and IAV (MOI 0.1). Virus quantification (*Fig. 2*) showed that replication was severely affected by KS-6469. Dose-dependent inhibition of viral replication was observed at KS-6469 concentrations of 70–600 µg/mL. At 70 µg/mL KS-6469, the viral titer was significantly reduced: KI = 75% (60.0–80.2%) ($p < 0.05$). It should be noted that when the virus was incubated with 600 µg/mL KS-6469, viral replication was entirely suppressed by KS-6469 because the virus levels were undetectable in the culture medium at 48 h post-infection. Hence, the sulfonated derivative of β-cyclodextrin investigated in this study could significantly reduce the virus titer when used at a concentration > 70 µg/mL and entirely suppressed viral replication at 600 µg/mL.

To gain insight into the mechanism of KS-6469 inhibition of IAV replication, we determined the step of the viral life cycle that was affected by the compound using time-of-addition assay. First, we investigated whether KS-6469 added to the cells prior to virus adsorption could protect the cells against infection. The cells were treated with KS-6469 2 h prior to IAV infection ((-3) to (-1) h) (*Fig. 3*). The viral yield showed no difference when compared with the virus-only control. Similarly, no antiviral activity was observed when KS-6469 was introduced into the well during infection ((-1) to 0 h) or during the early stages of viral replication ((−1 h) to 6 h p.i.). These results indicate that the compound directly affects neither the binding nor virus entry into the target cells, or its early release. Inhibition of viral replication was only observed either when KS-6469 was continuously present in the medium from the post-infection period (0 to 48 h) or when it was added 6 h after infection (*Fig. 3*).

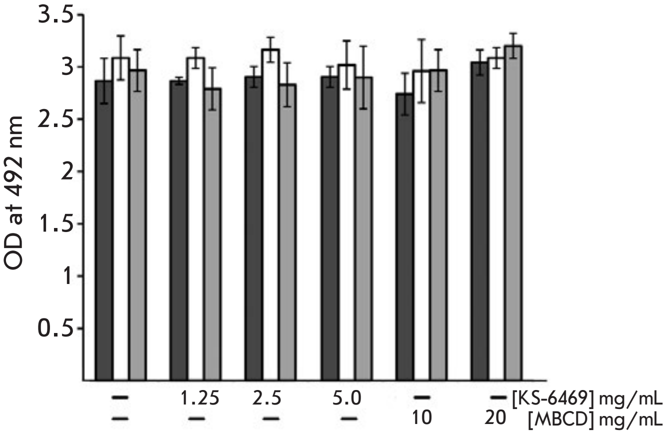

Fig. 4. The effect of treatment with KS-6469 on the binding of virus hemagglutinin to specific monoclonal antibodies. The data are presented as mean OD ± SD ($n = 3$). OD is the optical density. The experiment was conducted in triplicate

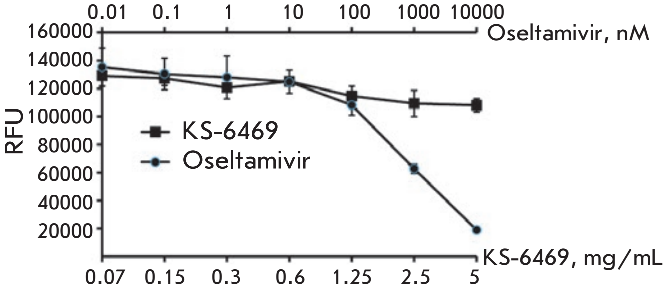

Fig. 5. Neuraminidase activity assay. The influenza virus A/WSN/33 was incubated with KS-6469 or Oseltamivir for 6 h before addition of a MUNANA substrate and then incubated for 1 h at 37°C. The results are presented in RFU ± SD ($n = 3$). RFU stands for relative fluorescence units. The experiment was conducted in triplicate

Table 1. HA titer of the virus after incubation with KS-6469

Compound	HA titer of the virus and incubation conditions			
	4°C		37°C	
	1 h	6 h	1 h	6 h
KS-6469, 5 mg/mL	64	32	16	4
PBS	64	64	64	64

Effect of KS-6469 on the functional activity of influenza virus surface proteins.

Functional balance between influenza virus hemagglutinin (HA) and neuraminidase (NA) was found to be very important for successful viral replication and fitness. In order to determine whether KS-6469 affected the structure of viral hemagglutinin, we investigated virus attachment to erythrocytes. The influenza virus was treated with KS-6469 (5 mg/mL) for 1 or 6 h at 37 or 4°C, and the viral HA titer was evaluated using HA assay (*Table 1*). Virus co-incubation with KS-6469 for 1 h at 37°C caused a fourfold reduction in the HA titer, and after 6 h of incubation HA was reduced 16-fold (*Table 1*). Interestingly, the HA titer did not change significantly after incubation for 6 h at 4°C in the presence of KS-6469 at the same concentration. The reduction in hemagglutinin binding suggests that KS-6469 could induce changes in the conformation of the surface epitopes of the protein.

The ability of KS-6469 to affect the structure of the surface epitope of viral hemagglutinin was analyzed using a set of monoclonal antibodies specific to hemagglutinin of IAV. The treatment of IAV with KS-6469 (5 mg/mL) at 37°C, which resulted in a 16-fold decrease in HA titer, changed neither the structure of virus hemagglutinin nor the efficacy of its binding to specific monoclonal antibodies (*Fig. 4*). It should be noted that the process of inhibiting HA of virus glycoproteins and, therefore, the infectivity of the virus particle, require a sufficiently long incubation with KS-6469 at a temperature of at least 37°C; so, we observed only a partial decrease in HA activity following incubation of the virus with the compound for 1 h.

In order to gain an understanding of the mechanism by which K-6469 inhibits viral replication, we examined the inhibition of viral neuraminidase (NA), which mediates the release of viral progeny from infected cells and promotes viral transmission. The results (*Fig. 5*) indicated that KS-6469 (5 mg/mL) did not change the NA activity, suggesting that NA is not targeted by KS-6469. Given that the mechanism of the antiviral effect of another derivative of β-cyclodextrin, methyl β-cyclodextrin (MBCD), is associated with cholesterol removal from the viral envelope [20], we examined the cholesterol level of virus particles with and without KS-6469 or MBCD treatment. IAV was

Table 2. Virus titer (lg FFU/mL) after treatment of the influenza virus with KS-6469

KS-6469 (mg/mL)	Incubation conditions					
	4°C		20°C		37°C	
	3 h	6 h	3 h	6 h	3 h	6 h
0.3	n.d.	5.4 ± 0.1	n.d.	4.9 ± 0.1	n.d.	4.8 ± 0.3
0.6	5.4 ± 0.1	4.9 ± 0.1	5.3 ± 0.1	4.9 ± 0.2	3.9 ± 0.1	1.9 ± 0.3
1.25	4.7 ± 0.3	5.1 ± 0.1	4.8 ± 0.2	4.6 ± 0.2	2.4 ± 0.2	< 1.7
2.5	5.0 ± 0.2	5.3 ± 0.3	4.5 ± 0.2	4.3 ± 0.2	< 1.7	< 1.7
5.0	n.d.	4.9 ± 0.4	n.d.	4.3 ± 0.4	< 1.7	< 1.7
PBS	5.1 ± 0.1	5.2 ± 0.2	5.1 ± 0.1	5.0 ± 0.3	4.4 ± 0.3	4.6 ± 0.1

n.d. – not determined.

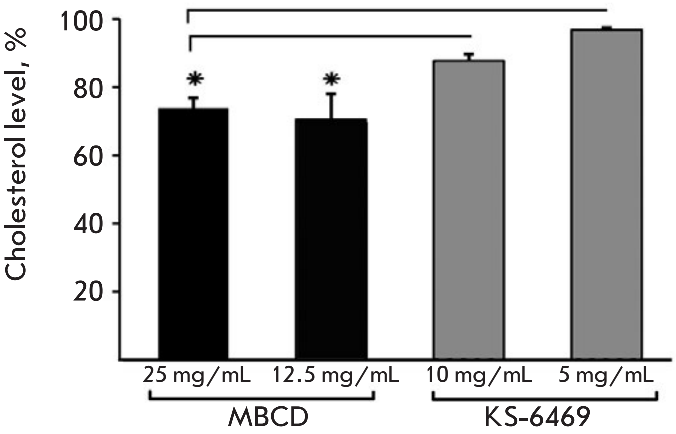

Fig. 6. Cholesterol level in the IAV envelope following treatment with KS-6469 or MBCD. IAV was incubated with different concentrations of KS-6469 or MBCD for 6 h at 37°C, and cholesterol levels were detected using the Amplex Red Cholesterol assay kit ($n = 3$). The cholesterol level in the untreated virus was set as 100%. Significance: $^*p < 0.05$. The experiment was conducted in triplicate

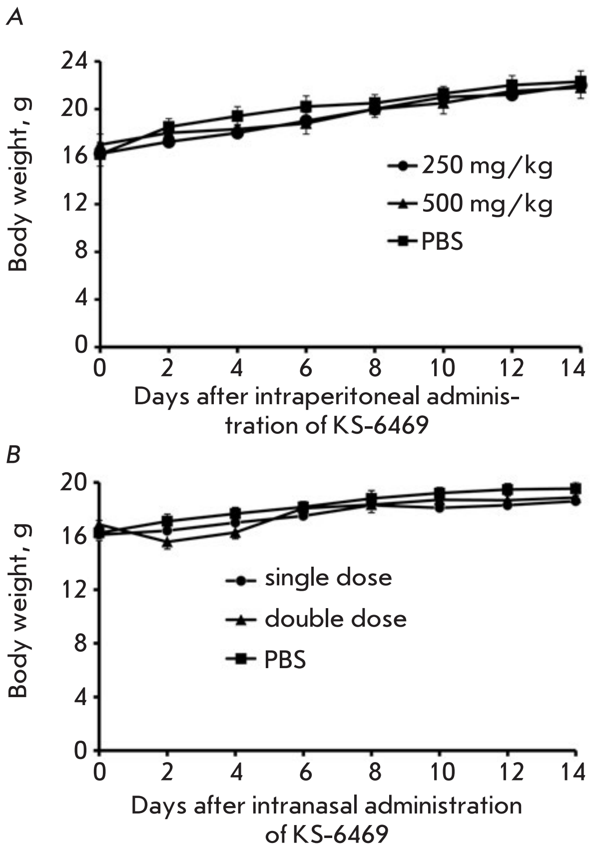

Fig. 7. Effects of KS-6469 treatment on the body weight of healthy mice. BALB/c mice ($n = 6$) received KS-6469 at doses of 500 and 250 mg/kg once as an intraperitoneal injection in 200 μL of PBS (*A*), or once or twice intranasally at a dose of 250 mg/kg in 40 μL of PBS (*B*). Mean values ± SD are shown at each time point

pretreated with various concentrations of KS-6469 and MBCD or left untreated (*Fig. 6*). A relative depletion of viral envelope cholesterol was observed after treatment with MBCD but not following treatment with KS-6469. Unlike MBCD, the antiviral effect of KS-6469 is, therefore, not associated with changes in the cholesterol content in the viral envelope. Taking into account these findings, a conclusion can be drawn that treatment with KS-6469 partially decreases the HA activity of the virus but does not change the NA activity and cholesterol content in the viral envelope.

Virucidal properties of KS-6469

It has been previously shown that sulfated polysaccharides possess virucidal activity [21, 22]. In the present study, a series of experiments was conducted to examine the ability of KS-6469 to directly inactivate influenza virus particles. The incubation of IAV with 5 or 2.5 mg/mL KS-6469 at 37°C for 3 h resulted in complete inactivation of virus infectivity. Treatment with 1.25 mg/mL KS-6469 followed by 3 h incubation at 37°C resulted in a ~2 lg reduction of viral titer, and no infectious virus particles were detected by FFA after 6-h incubation (*Table 2*). Incubation with 0.3 mg/mL KS-6469 at 37°C for 6 h did not affect viral infectivity. The lower incubation temperature resulted in significantly decreased virucidal properties for KS-6469. When virus particles were incubated with the compound at 4 or 20 °C, no effect on infectivity was observed. We hypothesized that the virucidal effect of KS-6469 might be mediated by the formation of aggregates of virus particles and the compound, and that a lower incubation temperature might drastically reduce the formation of such aggregates, thus diminishing the virucidal activity of the compound.

Antiviral activity of KS-6469 in the mouse model of influenza

In vivo cytotoxicity of KS-6469. BALB/c mice were subjected to a single intraperitoneal injection of different doses of KS-6469 (250 mg/kg or 500 mg/kg) in PBS. The physical parameters and body weights of the animals were monitored daily (*Fig*. 7). A single injection of the compound at a maximum dose of 500 mg/kg did not cause any weight loss or changes in the general condition, or death, thus indicating that KS-6469 exhibits low toxicity (*Fig*. 7*A*). Mice treated twice with KS-6469 intranasally (dose 250 mg/kg) had minimal weight loss and no signs of toxic side effects during the entire observation period (*Figs*. 7*A* and 7*B*).

Treatment of mice with KS-6469 confers protection against a lethal challenge of the influenza virus. The efficacy of KS-6469 against a lethal challenge of IAV was tested in the mouse model of influenza. To assess whether the compound could inhibit viral replication *in vivo*, we estimated the pulmonary viral titer in animals challenged with a lethal dose of 3 LD_{50} of

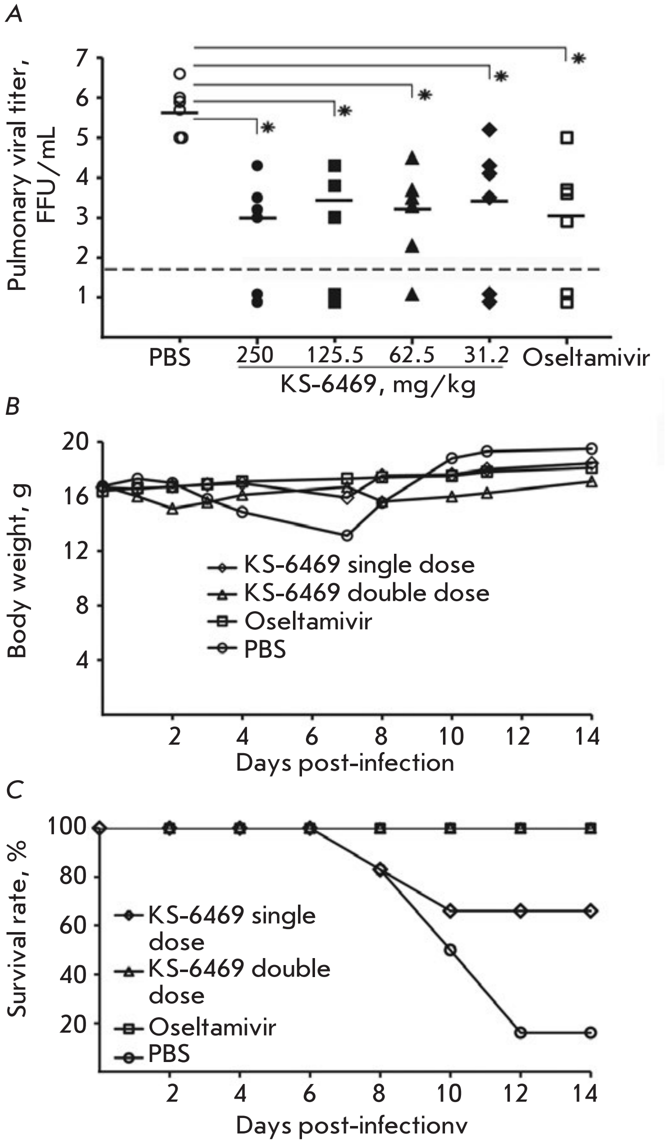

Fig. 8. Protective efficacy of KS-6469 in a lethal challenge of IAV: *A* – BALB/c mice ($n = 6$/group) were treated intranasally with KS-6469 at the indicated doses and infected with 3 LD_{50} of IAV. The following day, the mice received a second dose of KS-6469 intranasally. The data show the pulmonary viral titers on day 3 p.i. by FFA. *B* – The average body weight of mice treated intranasally with KS-6469 at the indicated doses, oseltamivir (7.5 mg/kg) or PBS and infected with 3 LD_{50} of IAV. *C* – The survival rate of BALB/c mice ($n = 6$) treated intranasally with KS-6469 at the indicated doses, oseltamivir (7.5 mg/kg) or PBS and infected with 3 LD_{50} of IAV. Significance: $^*p < 0.05$ vs. control group (without treatment)

IAV after the administration of different doses of KS-6469 via intranasal instillation. On day 2 p.i., the mice received a second dose of KS-6469 intranasally. The study included a positive control group that received oseltamivir daily (7.5 mg/kg), starting 30 min prior to viral challenge. On day 3 p.i., six animals per group were sacrificed and lung tissue extracts were analyzed by FFA (*Fig. 8A*). Viral titers were significantly reduced in the lungs of the animals treated with KS-6469 compared with those in the untreated group ($p < 0.05$), suggesting that intranasal therapy with KS-6469 inhibits influenza replication in mouse lungs (*Fig. 8A*). On day 3 p.i., the mock-treated mice had ~2.5 lg higher viral lung titers than the KS-6469- and oseltamivir-treated mice ($p < 0.05$). We suppose that the dose-independent antiviral activity of KS-6469 may be related to the mechanism of action of the compound.

To compare the protective effect of KS-6469, two groups of mice were treated intranasally with KS-6469 at a dose of 250 mg/kg, followed by challenge with a lethal dose of 3 LD_{50} IAV. On day 2 p.i., one of the two groups received a second dose of KS-6469 intranasally. Mice in the positive control group were treated orally with oseltamivir at a dose of 7.5 mg/kg. The control animals were treated intranasally with PBS on the same schedule. The daily weight loss and survival rate were evaluated within 14 days. *Figure 8B, C* shows that two doses of KS-6469 or treatment with oseltamivir led to minimal body weight loss with a 100% survival rate, which is significantly different than the untreated group (20% survival rate). The survival rate among mice treated with KS-6469 only once was 66%, and weight loss was minimal. Taken together, these data show that KS-6469 protects mice against a lethal infection of the influenza virus.

DISCUSSION

Influenza remains one of the most dangerous viral diseases in existence. To date, only two classes of drugs have been approved for the treatment of influenza: M2 ion channel blockers (adamantanes) and NA inhibitors [23, 24]. Vaccination is a reliable way to control an influenza infection [25], but the emergence of mutated viruses has resulted in a low effectiveness of the influenza vaccine and antiviral therapeutic agents. Thus, there is an urgent need to develop new approaches to combat influenza. One of the possible solutions is to develop antiviral compounds based on sulfo derivatives of oligo- and polysaccharides derived from either synthetic or natural products. Although the antiviral studies are generally performed with enveloped viruses that are more susceptible to these compounds [3–7]; sulfated polysaccharides from marine microalgae have been shown to be active against non-enveloped viruses [26]. It is believed that sulfated polysaccharides target certain stages of the influenza replication cycle, such as binding of virus particles to the cell surface receptors of the host [27], internalization [28], mRNA and protein expression, and viral release [12, 29]. However, due to the manifold activities of sulfated polysaccharides, additional studies are required to elucidate the specific molecular mechanisms of their antiviral action. In the present study, we investigated the antiviral properties of a novel sulfonated derivative of β-cyclodextrin: KS-6469. We found that viral replication was completely suppressed after incubation of infected cells with 600 μg/mL of KS-6469 for 24 h, indicating that the compound exhibits a high antiviral potential. To elucidate the mechanism of antiviral activity of KS-6469, we evaluated the effectiveness of inhibition at different stages of the virus replicative cycle (*Fig. 3*). Co-incubation of MDSK cells with KS-6469 did not affect the early stages of viral replication; however, the viral titer was significantly reduced when infected cells were co-incubated with KS-6469 for a long period of time. Based on these data, we hypothesized that KS-6469 affects the late stages of the influenza infection. The inhibitory effect of KS-6469 in the late stages of the infection might be related to the suppression of NA activity. We did not detect any changes in NA activity after incubation with KS-6469 (*Fig. 5*), but the activity of another viral envelope protein, hemagglutinin, decreased significantly under these conditions. After incubation of IAV with KS-6469 for 1 h at 37°C, the HA decreased fourfold compared with that in the untreated control, which did not lead to inhibition of the binding of viral hemagglutinin to sialic acid-containing receptors on cell surfaces (*Table 1*) and did not reduce virus reproduction. It should be noted that treatment with KS-6469 did not decrease the ability of viral hemagglutinin to interact with specific monoclonal antibodies (mAbs), suggesting that the structure of the hemagglutinin (the mAb target) remained intact (*Fig. 4*). Our results revealed that KS-6469 has pronounced virucidal activity, being able to cause complete loss of viral infectivity (*Table 2*). The virucidal activity of the compound was at its highest at 37°C but required a longer incubation period, which in turn explains the absence of KS-6469-induced inhibition during the early stages of viral replication. Treatment of the virus with KS-6469 during the first 6 hours p.i. resulted only in a partial loss of infectivity and did not inactivate a sufficient number of virus particles to prevent infection. We hypothesize that viral inactivation occurs due to the interaction between KS-6469 and viral particles with the concomitant formation of aggregates, leading to a significant reduction in infectivity. Previously, it was suggested [21] that the virucidal activity of antiviral drugs observed *in vitro* would produce much more pronounced therapeutic effects *in vivo*. This assumption has been confirmed by the data presented in this study. We have demonstrated the antiviral efficacy of KS-6469 over a wide dose range in mice infected with IAV (*Fig. 8*). Intranasal treatment of influenza-infected mice with KS-6469 reduced the mortality rate in mice. Single application of KS-6469 increased the survival rate to 66%, while double application of the compound provided complete protection to the animals. The placebo-treated group showed only a 16% survival rate. Intranasal treatment of influenza-infected mice with KS-6469 markedly decreased the pulmonary viral titer even at the lowest dose used (62.5 mg/kg (*Fig. 8*)).

CONCLUSIONS

Our study has shown that KS-6469 is a low-toxicity and safe agent that effectively inhibits the development of the infectious disease caused by the influenza virus. Intranasal application of KS-6469 had anti-IAV effects comparable to those of oseltamivir. Hence, KS-6469 is a promising candidate for developing an effective antiviral drug for the prevention and treatment of influenza infections. ●

This research was supported in part by the Russian state-funded budget project under the Program of Fundamental Research for State Academies of Sciences for 2013-2020 No. AAAA-A17-117020210024-8.

REFERENCES

1. Iuliano D., Roguski K.M., Chang H.H., Muscatello D.J., Palekar R., Tempia S., Cohen C., Gran J.M., Schanzer D., Cowling B.J., et al. // Lancet. 2018. V. 391. P. 1285–1300.
2. Ginsberg H.S., Goebel W.F., Horsfall F.J. // J. Exp. Med. 1948. V. 87. P. 385–410.
3. Moriya T., Saito K., Kurita H., Matsumoto K., Otake T., Mori H., Morimoto M., Ueba N., Kunita N. // J. Med. Chem. 1993. V. 36. P. 1674–1677.
4. Ying C., van Pelt J.F., van Lommel A., van Ranst M., Leyssen P., De Clercq E., Neyts J. // Antivir. Chem. Chemother. 2002. V. 13. P. 157–164.
5. Cardozo F.T., Camelini C.M., Leal P.C., Kratz J.M., Nunes R.J., Mendonça M.M., Simões C.M. // Intervirology. 2014. V. 57. P. 375–383. doi: 10.1159/000365194.
6. Hidari K.I., Takahashi N., Arihara M., Nagaoka M., Morita K., Suzuki T. // Biochem. Biophys. Res. Commun. 2008. V. 376. P. 91–95. doi: 10.1016/j.bbrc.2008.08.100.
7. Novetsky A.P., Keller M.J., Gradissimo A., Chen Z., Morgan S.L., Xue X., Strickler H.D., Fernández-Romero J.A., Burk R., Einstein M.H. // Gynecol. Oncol. 2016. V. 143. P. 313–318. doi: 10.1016/j.ygyno.2016.09.003.
8. Ikeda S., Neyts J., Verma S., Wickramasinghe A., Mohan P., De Clercq E. // Antimicrob. Agents Chemother. 1994. V. 38. P. 256–259.
9. Fitton J.H. // Mar. Drugs. 2011. V. 9. P. 1731–1760.
10. Tang F., Chen F., Li F. // J. Appl. Polym. Sci. 2012. V. 127. P. 2110–2115.
11. Kim M., Yim J.H., Kim S.Y., Kim H.S., Lee W.G., Kim S.J., Kang P.S., Lee C.K. // Antiviral Res. 2012. V. 93. P. 253–259. doi: 10.1016/j.antiviral.2011.12.006.
12. Ciejka J., Milewska A., Wytrwal M., Wojarski J., Golda A., Ochman M., Nowakowska M., Szczubialka K., Pyrc K. // Antimicrob. Agents Chemother. 2016. V. 60. P. 1955–1966. doi: 10.1128/AAC.02183-15.
13. Eccles R., Winther B., Johnston S.L., Robinson P., Trampisch M., Koelsch S. // Respir. Res. 2015. V. 16. P. 121. doi: 10.1186/s12931-015-0281-8.
14. Carmihael J., DeGraff W.G., Gazdar A.F., Minna J.D., Mitchell J.B. // Cancer Res. 1987. V. 47. P. 936–942.
15. Brien J.D., Lazear H.M., Diamond M.S. // Curr. Protoc. Microbiol. 2013. doi:10.1002/9780471729259.mc15d03s31.
16. Krylova N. V., Leonova G.N. // Problem of Virology. 2016. V. 61. P. 139 – 144. (in Russian). (in Russian).
17. Khabriev R.U. A Manual on Experimental (preclinical) Studies of Pharmacological Substances [Rukovodstvo po eksperimental'nomu (doklinicheskomu) izuchenieu novykx farmakologicheskikh veshestv. M.: Medicine, 2005. 832 p. (in Russian).
18. Goncharova E.P., Koroleva L.S., Silnikov V.N., Ternovoy V.A., Vlassov V.V., Zenkova M.A. // J. Mol. Genet. Med. 2011. V. 5. P. 266–272.
19. European Convention for the Protection of Vertebrate Animals used for Experimental and Other Scientific Purposes. European Treaty Series. 1986. No. 123.
20. Sun X., Whittaker G.R. // J. Virol. 2003. V. 77. P. 12543–12551.
21. Harden E.A., Falshaw R., Carnachan S.M., Kern E.R., Prichard M.N. // Antiviral Res. 2009. V. 83. №. 3. P. 282–289. doi: 10.1016/j.antiviral.2009.06.007.
22. Leibbrandt A., Meier C., König-Schuster M., Weinmüllner R., Kalthoff D., Pflugfelder B., Graf P., Frank-Gehrke B., Beer M., Fazekas T., et al. // PLoS One. 2010. V. 5. № 12. E. 14320. doi: 10.1371/journal.pone.0014320.
23. Yen H.L. // Curr. Opin. Virol. 2016. V. 18. P. 126–134.
24. Nakamura S., Miyazaki T., Izumikawa K., Kakeya H., Saisho Y., Yanagihara K., Miyazaki Y., Mukae H., Kohno S. // Open Forum Infect. Dis. 2017. V. 4. ofx129. doi: 10.1093/ofid/ofx129.
25. Lewnard J.A., Cobey S. // Vaccines (Basel). 2018. doi:

10.3390/vaccines6020028.
26. Yim J.H., Kim S.J., Ahn S.H., Lee C.K., Rhie K.T., Lee H.K. // Mar. Biotechnol (NY). 2004. V. 6. P. 17–25.
27. Vives R.R., Imberty A., Sattentau Q.J., Lortat-Jacob H.J. // J. Biol. Chem. 2005. V. 280. P. 21353–21357.
28. Hashimoto K., Kodama E., Mori S., Watanabe J., Baba M., Okutani K., Matsuda M., Shigeta S. // Antiviral Chem. Chemother. 1996. V. 7. P. 189–196.
29. Wang W., Wu J., Zhang X., Hao C., Zhao X., Jiao G. Shan X., Tai W., Yu G. // Sci. Rep. 2017. V. 7. P. 40760. doi: 10.1038/srep40760.

A Nerve Growth Factor Dipeptide Mimetic Stimulates Neurogenesis and Synaptogenesis in the Hippocampus and Striatum of Adult Rats with Focal Cerebral Ischemia

T. A. Gudasheva*, P. Yu. Povarnina, A. A. Volkova, S. V. Kruglov, T. A. Antipova, S. B. Seredenin
Federal State Budgetary Institution "Zakusov Research Institute of Pharmacology", Baltiyskay Str. 8, Moscow, 125315, Russia
*E-mail: gudasheva@academpharm.ru

Received April 05, 2019; in final form, June 06, 2019
DOI: 10.32607/20758251-2019-11-3-31-37

Copyright © 2019 National Research University Higher School of Economics. This is an open access article distributed under the Creative Commons Attribution License,which permits unrestricted use, distribution, and reproduction in any medium, provided the original work is properly cited.

ABSTRACT **The nerve growth factor (NGF) and its mimetics, which have neuroprotective and neuroregenerative properties, are attractive candidates for developing new drugs for brain injury therapy. A dipeptide mimetic of NGF loop 4, bis(N-succinyl-*L*-glutamyl-*L*-lysine) hexamethylenediamide (GK-2), developed at the Zakusov Research Institute of Pharmacology, has the NGF-like ability to activate TrkA receptors, but unlike NGF, GK-2 activates mainly the PI3K/AKT pathway associated with neuroprotection and has no effect on the MAPK cascade associated with hyperalgesia, the main side effect of NGF. That GK-2 possesses neuroprotective activity has been observed in various models of cerebral ischemia. GK-2 was found to statistically significantly reduce the cerebral infarct volume in experimental stroke, even at treatment onset 24 h after injury. This suggests that GK-2 possesses neuroregenerative properties, which may be associated with the activation of neurogenesis and/or synaptogenesis. We studied the effect of GK-2 on neurogenesis and synaptogenesis in experimental ischemic stroke caused by transient occlusion of the middle cerebral artery in rats. GK-2 was administered 6 or 24 h after surgery and then once a day for 7 days. One day after the last administration, proliferative activity in the hippocampus and striatum of the affected hemisphere was assessed using Ki67 and synaptogenesis in the striatum was evaluated using synaptophysin and PSD-95. Ki67 immunoreactivity, both in the striatum and in the hippocampus of the ischemic rats, was found to have dropped by approximately 30% compared to that in the sham-operated controls. Synaptic markers - synaptophysin and PSD-95 - were also statistically significantly reduced, by 14 and 29%, respectively. GK-2 in both administration schedules completely restored the level of Ki67 immunoreactivity in the hippocampus and promoted its increase in the striatum. In addition, GK-2 restored the level of the postsynaptic marker PSD-95, with the therapeutic effect amounting to 70% at the start of its administration after 6 h, and promoted restoration of the level of this marker at the start of administration 24 h after an experimental stroke. GK-2 had no effect on the synaptophysin level. These findings suggest that the neurotrophin mimetic GK-2, which mainly activates one of the main Trk receptor signaling pathways PI3K/AKT, has a stimulating effect on neurogenesis (and, probably, gliogenesis) and synaptogenesis in experimental cerebral ischemia. This effect may explain the protective effect observed at the start of dipeptide administration 24 h after stroke simulation.**

KEYWORDS **NGF, GK-2 dipeptide mimetic, stroke, neurogenesis, synaptogenesis, Ki67, PSD-95, synaptophysin.**

INTRODUCTION

The development of pathogenic treatments for an ischemic stroke after reperfusion remains a challenge in modern medicine.

The nerve growth factor (NGF) is an attractive neuroprotective agent capable of affecting the main mechanisms of ischemic neuronal injury: glutamate toxicity mediating excessive calcium entry into the cell [1]; oxidative stress [2]. NGF reduces the expression of pro-apoptotic proteins and activates the synthesis of anti-apoptotic proteins [3, 4]. NGF was experimentally proven to be involved in neurogenesis in the adult brains of rodents. NGF enhances the proliferation of neuronal stem cells, promotes the survival of progenitor cells, and stimulates the differentiation of neuroblasts in both major neurogenic zones: the subventricular zone and the dentate gyrus of the hippocampus [5–9]. The efficacy of intracerebral and intranasal administration of NGF has been proven in various cerebral ischemia models in rodents. It is extremely important that the neurotrophin remains active upon delayed administration – 24 h after a simulated stroke [6, 10]. Applications of NGF in clinical practice are limited not only due to its unsatisfactory pharmacokinetic properties, but also due to serious pleiotropic side effects, such as hyperalgesia, catastrophic weight loss, excessive neuritogenesis, and angiogenesis [11]. Probably, the disadvantages of the full-length NGF protein may be obviated through the development of related low-molecular-weight mimetics with a selective pharmacological activity [12].

At the Zakusov Research Institute of Pharmacology, a hypothesis has been developed, holding that receptor recognition and binding are controlled by the most exposed portions of neurotrophin loops, usually by the central parts of their beta-turns, with mimetics of beta-turns from different loops imitating different functions of the neurotrophin [13]. This hypothesis was the basis for the development of a dimeric dipeptide mimetic of NGF loop 4, bis(N-monosuccinyl-*L*-glutamyl-*L*-lysine) hexamethylenediamide, that received the laboratory code GK-2 [RF Patent No. 2410392, 2010; US patent US 9,683,014, 2017; Chinese Patent CN 102365294 B, 2016]. GK-2 was found to have the NGF-like ability to activate TrkA receptors, but unlike the full-length protein, GK-2 primarily activates the PI3K/AKT pathway associated with neuroprotection and has no effect on the MAPK cascade that mediates hyperalgesia [14].

In vitro studies have shown that GK-2 in micro-nanomolar amounts, like NGF, has a neuroprotective effect on both immortalized and primary neuron cultures under oxidative stress and glutamate toxicity [15]. The neuroprotective activity of GK-2 was also demonstrated *in vivo* upon systemic administration in Alzheimer and Parkinson models, as well as in various cerebral ischemia models [16]. In support of the *in vitro* data, GK-2, unlike the full-length protein, did not cause hyperalgesia and weight loss in *in vivo* experiments [14]. A study of the neuroprotective effect of GK-2 in a model of ischemic stroke caused by transient occlusion of the middle cerebral artery in rats showed that the dipeptide statistically significantly reduced the amount of brain injury if the onset of therapeutic administration started between 4 and 24 h, with the strongest effect (60%) being observed if the first administration occured 6 h after surgery [17]. Preservation of the GK-2 activity when its first administration occurs 24 h after a simulated ischemic stroke is probably not explained by its neuroprotective properties, because the infarction area has fully formed by that time [18]. Therefore, the protective effect of GK-2 administered 24 h after an ischemic stroke may be associated with the regenerative properties of the mimetic.

To shed light on this issue, we studied the effect of GK-2 on neurogenesis and synaptogenesis in an experimental ischemic stroke using antibodies to the Ki67 proliferation marker and synaptogenesis markers (synaptophysin and PSD-95). Neurogenesis and synaptogenesis parameters were assessed in the hippocampus and striatum. These structures were chosen because one of the main neurogenic zones in the adult brain (subgranular zone) is located in the hippocampus, and the striatum is the most affected structure during occlusion of the middle cerebral artery [6]. The effects of GK-2 were studied when its administration occurred 6 and 24 h after a simulated stroke.

EXPERIMENTAL

Animals

We used 34 male Wistar rats weighing between 220 and 250 g and 8–9 weeks of age at the beginning of the experiment. The animals originated from the Andreevka Branch of the Scientific Center of Biomedical Technologies of the FMBA, Russia. The animals were kept in a vivarium under natural circadian light/dark cycles with free access to standard granular feed and water. The study complied with the requirements of Order of the Ministry of Health of the Russian Federation No. 199 “On Approval of the Rules of Good Laboratory Practice” and Decision of the Council of the Eurasian Economic Commission No. 81 “On Approval of the Rules of Good Laboratory Practice of the Eurasian Economic Union in the Area of Circulation of Medicines.” All manipulations with the animals were approved by the Bioethical Commission of the Zakusov Research Institute of Pharmacology.

Simulation of ischemic stroke

Ischemic stroke was simulated by intravascular thread occlusion of the middle cerebral artery [19]. All surgical procedures were performed using titanium microsurgical tools. The rats were anesthetized with a 5% chloral hydrate solution (350 mg/kg, ip). Following a midline incision in the neck, the right carotid triangle was identified, which is bounded superiorly by the digastric muscle, laterally by the sternocleidomastoid muscle, and medially by the sternohyoid muscle. In the carotid triangle, the carotid neurovascular bundle formed by the common carotid artery and the vagus nerve was identified. The vagus nerve was carefully isolated, and a microsurgical vascular titanium clip was placed on the common carotid artery 1.5 cm below its bifurcation. The external and internal carotid arteries were carefully isolated from adhesions. The external carotid artery was tightly tied with a cotton suture. The internal carotid artery was loosely tied with a vicryl suture, and then the external carotid artery was cut proximal to the suture. A 0.25-mm heparinized nylon filament was inserted through the stump of the external carotid artery into the internal carotid artery to a depth of 19–21 mm (until the middle cerebral artery was occluded) and fixed with a microvascular clip. The circulation was occluded for 60 min; then, the filament was removed from the vessel, restoring blood supply in the middle cerebral artery territory. After filament removal, the stump of the external carotid artery was tightly sealed by electrocautery coagulation. Sham-operated animals underwent the same procedures, except for vascular transection and filament insertion. The midline incision in the neck was sutured with a cotton thread and treated with streptocide. In our experiments, the ischemic injury volume on day 7 after the simulated stroke was 700–800 mm^3 (according to the morphometry of brain sections stained with 2,3,5-triphenyltetrazolium chloride) [17].

Study design

Operated animals were randomly divided into three groups: the "stroke" group (operated untreated animals; $n = 9$) and two groups receiving GK-2 (1 mg/kg, ip) diluted in water for injection. GK-2 was administered in a volume of 2 mL per kilogram of body weight, starting 6 ($n = 10$) or 24 h ($n = 7$) after surgery, and then once a day, with the end of administration on day 6 after surgery. Animals from the groups "stroke" and "sham surgery" ($n = 8$) received water for injection according to the same schedule. On day 7 after surgery, the rats were decapitated; the brain was removed at a temperature of 0–4°C; and the striatum and hippocampus were removed from the affected hemisphere, frozen in liquid nitrogen, and stored at −70°C. The experimental design is shown in *Fig. 1*.

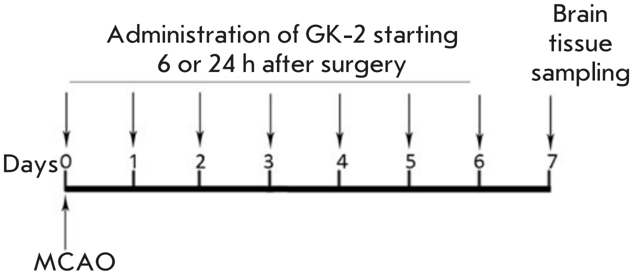

Fig. 1. Experimental design. MCAO – middle cerebral artery occlusion

Assessment of the proliferative activity and synaptogenesis

The effect of GK-2 on the proliferative activity and synaptogenesis in the striatum and hippocampus was evaluated using a Western blot analysis [20]. After thawing, animal tissue samples from one group were combined to prepare at least three samples. Then, the samples were homogenized at 4°C in a glass homogenizer with lysis buffer (50 mM Tris-HCl, 5 mM EDTA, 1 mM dithiothreitol, 1% Triton X-100, pH 7.5) containing a cocktail of protease inhibitors (pepstatin, bestatin, leupeptin, and aprotinin; Sigma-Aldrich, USA), at a tissue : buffer ratio of 1 : 10 (weight/volume). Then, the samples were incubated at 4°C for 20 min and centrifuged (15,000 rpm for 20 min; Allegra® X-12R centrifuge; BeckmanCoulter Inc., USA) at the same temperature. The protein concentration in the supernatant was determined according to the Folin–Lowry method [21]. Supernatant proteins were separated on a 12% polyacrylamide gel and transferred onto a polyvinylidene fluoride membrane by electroelution. The membranes were then incubated in Tris-HCl buffer (200 mM, pH 7.5) containing 1% Tween-20 (TBST) and 5% (w/v) skim milk at room temperature for 1 h. Then, the membranes were incubated with primary monoclonal antibodies against synaptophysin (BD Biosciences, Great Britain) at a 1 : 5,000 dilution, primary monoclonal antibodies against PSD-95 (Thermo Fisher Scientific, USA) at a 1 : 1,000 dilution, and primary polyclonal antibodies against Ki67 (Thermo Fisher Scientific) at a 1 : 5,000 dilution at room temperature for 1.5 h; excess antibodies were removed with TBST containing 0.5% (w/v) skim milk. The membranes were incubated with secondary goat antibodies against rabbit IgG (Santa Cruz Biotechnology, USA; 1 : 2,000) conjugated to horseradish peroxidase at room temperature for 1 h. After the removal of secondary antibodies with TBST, the proteins were detected by a reaction with enhanced chemiluminescence reagents (ECL reagents, Santa Cruz Biotechnology) using the Alliance Q9 gel documentation system (UVITEC, UK). Images were analyzed using the GIMP2 software.

Statistical processing

Intergroup differences were evaluated using a Mann–Whitney U test. Differences were considered statistically significant at $p < 0.05$. Data was presented as a mean and a standard error of the mean.

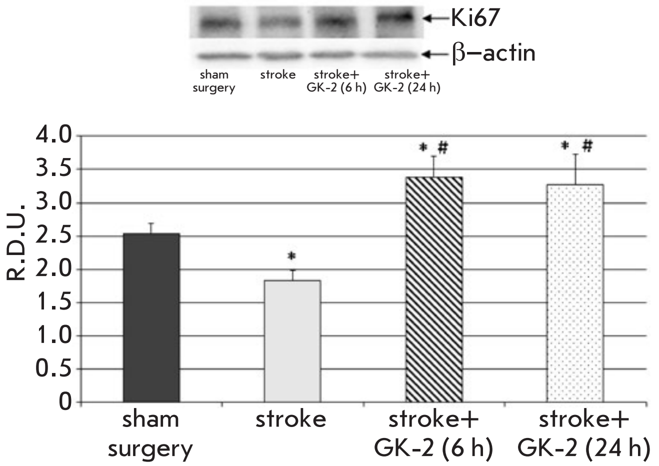

Fig. 2. Effect of GK-2 on Ki67 proliferation marker levels in the hippocampus upon subchronic (7 days) administration (1 mg/kg, ip) after an experimental ischemic stroke caused by transient occlusion of the middle cerebral artery in rats, in a 6 or 24 h therapeutic window (the time between surgery and the first injection of the agent). R.D.U. – relative densitometric units. * – $p < 0.05$ compared to the sham-operated group, # – $p < 0.05$ compared to the stroke group (Mann–Whitney U test)

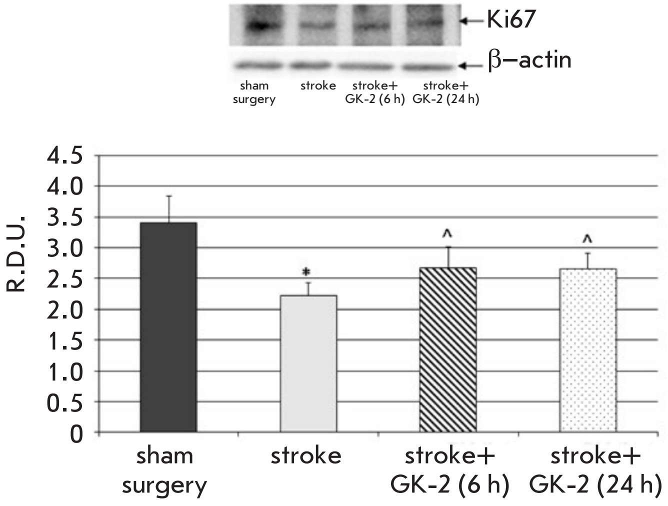

Fig. 3. Effect of GK-2 on Ki67 proliferation marker levels in the striatum upon subchronic (7 days) administration (1 mg/kg, ip) after an experimental ischemic stroke caused by transient occlusion of the middle cerebral artery in rats, in a 6 or 24 h therapeutic window (the time between surgery and the first injection of the agent). R.D.U. – relative densitometric units. * – $p < 0.05$ compared to the sham-operated group; ˆ – $p < 0.1$ compared to the stroke group (Mann-Whitney U test)

RESULTS AND DISCUSSION

Seven days after surgery, the immunoreactivity for the Ki67 proliferation marker, both in the striatum and in the hippocampus of the ischemic brain of rats untreated with GK-2, was reduced by about 30% compared to that in the sham-operated controls (*Fig. 2, 3*). Administration of GK-2 to ischemic animals for seven days led not only to a restoration of the Ki67 immunoreactivity level in the hippocampus, but also to an excess of its baseline values by 35 and 36% for a 6- and 24-hour interval between surgery and the first peptide administration, respectively (*Fig. 2*). These findings indicate the ability of the NGF mimetic to stimulate a proliferative activity in the hippocampus of the ischemic brain. Based on previously obtained data on the improvement in the neurological status of rats receiving GK-2 (administration starting 6 and 24 h after surgery) under the same conditions as in this experiment [17], we suggest that dipeptide-induced stimulation of proliferative activity leads, at least predominantly, to neurogenesis. This is also supported by published data indicating that the full-length NGF stimulates hippocampal neurogenesis, increasing the proliferative activity and promoting the survival of neuroblasts in the dentate gyrus of the hippocampus [5, 9].

Therefore, we may draw a preliminary conclusion that GK-2 reproduces the effects of NGF, increasing hippocampal neurogenesis in cerebral ischemia. An effect of GK-2 on gliogenesis is less likely, because even full-length neurotrophin primarily stimulates neuroblast formation.

In the striatum, GK-2 administered in both schedules increased the level of Ki67 immunoreactivity about 1.2-fold compared to that in the untreated animals (which corresponds to a therapeutic effect of 36–37% ($p = 0.08$)) (*Fig. 3*). During middle cerebral artery occlusion, NGF is known to stimulate the proliferative activity and increase the survival of neuroblasts in the subventricular zone and striatum of rats [6, 10]. In the same brain ischemia model, by using the BrdU proliferation marker, intranasal administration of NGF was shown to increase the survival rate of progenitor cells in the striatum about 1.5-fold after 4 weeks [6]. By using another proliferation marker, Ki67, NGF expressed in the rat brain using a lentiviral vector was found [10] to stimulate neurogenesis in the injured striatum, increasing the number of neuroblasts about 2-fold compared to that in untreated animals 3 weeks after a simulated stroke.

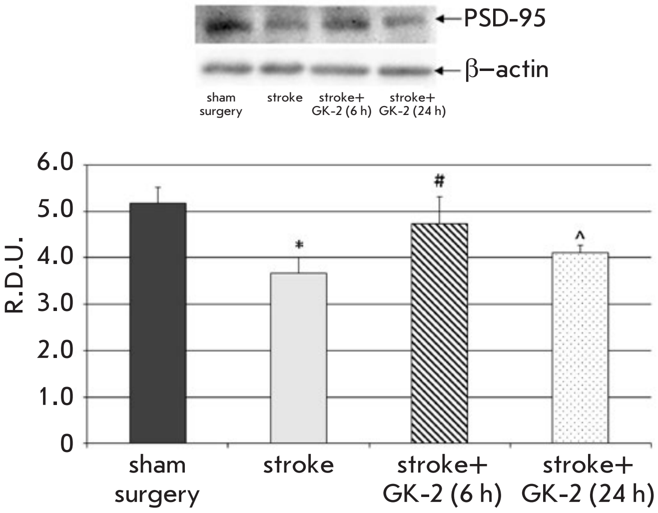

Fig. 4. Effect of GK-2 on PSD-95 levels in the striatum upon subchronic (7 days) administration (1 mg/kg, ip) after an experimental ischemic stroke caused by transient occlusion of the middle cerebral artery in rats. Administration of GK-2 was begun 6 or 24 h after surgery. R.D.U. – relative densitometric units. * – $p < 0.05$ compared to the sham-operated group; # – $p < 0.05$ compared to the stroke group; ˆ – $p < 0.1$ compared to the stroke group (Mann-Whitney U test)

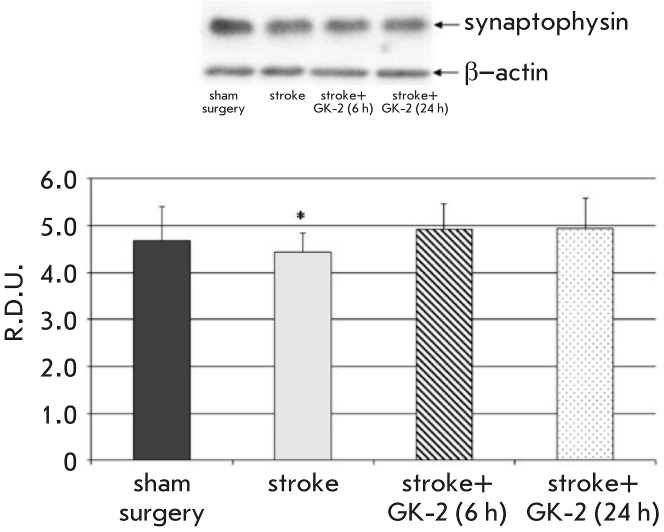

Fig. 5. Effect of GK-2 on synaptophisin presynaptic marker levels in the striatum upon subchronic (7 days) administration (1 mg/kg, ip) after an experimental ischemic stroke caused by transient occlusion of the middle cerebral artery in rats. Administration of GK-2 was started 6 or 24 h after surgery. R.D.U. – relative densitometric units. * – $p < 0.05$ compared to the sham-operated group (Mann-Whitney U test)

Therefore, systemically administered GK-2 apparently has an effect on neurogenesis in the striatum of ischemic rats, which is similar to that of NGF introduced in the brain intranasally or by gene therapy.

To date, a large amount of experimental data has been accumulated indicating a compensatory role for neurogenesis in the subventricular and subgranular zones in cerebral ischemia [22]. According to the published data, neurogenesis is activated in pathological conditions; in this case, newly formed neuroblasts migrate to injured brain areas, where they replace dead neurons [23]. Therefore, it may be assumed that the stimulating effect of GK-2 on the proliferative activity in the hippocampus leads to the activation of neuroregenerative processes in the ischemic injury area due to the migration of a larger amount of survived neuronal progenitor cells into this area and, ultimately, to their integration. Probably, the GK-2-induced increase in the Ki67 proliferation marker level in the striatum is related to the migration of neuroblasts from neurogenic zones to this region.

Assessment of the synaptic marker levels in the striatum of the injured hemisphere in ischemic rats showed that the levels of both the PSD-95 postsynaptic density protein and the presynaptic synaptophysin protein were statistically significantly lower compared to those in sham-operated animals (29 and 14%, respectively) (*Fig. 4, 5*). These results confirm the presence of an ischemic injury in this area, which is associated with a loss of neurons and synapses. GK-2 restored the PSD-95 level with a therapeutic effect of 70% when its administration started 6 h after surgery; however, administration of GK-2 starting 24 h after surgery caused only a tendency ($p = 0.08$) to restore the level of this marker (*Fig. 4*).

At the same time, GK-2 had no statistically significant effect on the synaptophysin level in the striatum (*Fig. 5*).

A possible explanation for the lack of changes in the presynaptic synaptophysin protein upon administration of GK-2 is the formation of presynaptic terminals at the final stages of neurogenesis, which completes in at least 3 weeks. On the other hand, the postsynaptic density protein PSD-95 is a component of the dendritic spines that form in a shorter time [24]. On the basis of these findings, we may suggest that GK-2 stimulated striatal synaptogenesis in terms of dendritic spine formation 7 days after an experimental stroke.

Neuroprotective and neuroregenerative effects of GK-2 (1 mg/kg, 7 days) in a model of ischemic stroke caused by transient occlusion of the middle cerebral artery in rats

First administration after surgery, h	Reduction in the ischemic injury volume [17], %	Stimulation of neurogenesis (based on the Ki67 proliferation marker), therapeutic effect,%		Stimulation of synaptogenesis in the striatum (based on the postsynaptic marker PSD-95), therapeutic effect, %
		hippocampus	striatum	
6	60*	220*	37ˆ	72*
24	24*	205*	36ˆ	30ˆ

Note. The therapeutic effect was calculated using the formula: [(protein level in the stroke + GK-2 group – protein level in the stroke group)/(protein level in the sham-surgery group – protein level in the stroke group)] × 100%.
* – $p < 0.05$; ˆ – $p < 0.1$ compared to the stroke group (Mann–Whitney U-test).

To assess the contribution of neuroregeneration to the protective effects of GK-2 in an experimental stroke, we compared our biochemical data with the results of a previous morphological study [17] on the role of GK-2 in reducing the volume of an ischemic brain injury. All dipeptide effects were evaluated on the 7th day after surgery (see *Table*).

As seen from *Table*, GK-2 reduced the volume of the ischemic injury by 60% and 24% when administration started 6 and 24 h after surgery, respectively. According to [18], a significant amount of penumbra neurons are preserved 6 h after a stroke, which may survive thanks to the neuroprotective effect of GK-2. Probably, recovery in the brain occurs partially due to neurogenesis. In the absence of a penumbra, restoration of injured brain tissue (by 24%) after 24 h may occur only due to regenerative processes. These findings suggest that regeneration associated with the proliferation and migration of new cells does not depend on the penumbra volume, which is evidenced by similar indicators of Ki67 immunoreactivity upon GK-2 administration starting 6 and 24 h after surgery.

However, given the PSD-95 postsynaptic marker levels, synaptogenesis may depend on the total amount of intact neurons, both survived and newly formed. Changes in the density of this marker in the presence of GK-2 are proportional to the degree of neuronal volume recovery in the ischemic injury area (72/60 and 30/24, respectively).

Therefore, our findings suggest that the effect of GK-2 administered shortly after a simulated stroke is associated with both neuroprotective and reparative processes; while the effect of GK-2 administered after 24 h is associated with the stimulation of reparative processes, including both neurogenesis (and, probably, gliogenesis) and synaptogenesis.

CONCLUSION

The dimeric dipeptide mimetic of nerve growth factor loop 4, GK-2, administered subchronically and starting 6 and 24 h after surgery statistically significantly restores the reduced proliferation of neuronal stem cells in the hippocampus and increases the proliferative activity in the striatum, according to the Ki67 marker, in an experimental ischemic stroke caused by transient occlusion of the middle cerebral artery. Based on the previously obtained data on the improvement in the neurological status of rats receiving GK-2 under conditions similar to those of the present experiment [17], we may suggest that stimulation of proliferative activity by the dipeptide leads, at least primarily, to neurogenesis. The effect of GK-2 increases the number of synaptic contacts being reduced after surgery, which was assessed using the postsynaptic marker PSD-95, upon administration starting 6 h after surgery and increases this indicator when the first administration occurrs 24 h after surgery. These findings demonstrate the stimulating effect of GK-2 on neurogenesis (and, probably, gliogenesis) and synaptogenesis in experimental cerebral ischemia. ●

This work was supported by the Russian Science Foundation (project No. 18-15-00381) and the Russian Foundation for Basic Research (project No. 18-015-00228).

REFERENCES

1. Jiang H., Tian S., Zeng Y., Shi J. // J. Huazhong Univ. Sci. Technol. - Med. Sci. 2008. V. 28. № 4. P. 379–382.
2. Hassanzadeh P., Arbabi E., Atyabi F., Dinarvand R. // Life Sci. 2017. V. 179. P. 15–22.
3. Park J.H., Kang S.S., Kim J.Y., Tchah H. // Investig. Ophthalmol. Vis. Sci. 2016. V. 57. № 15. P. 6767–6775.
4. Yang J.P., Liu H.J., Yang H., Feng P.Y. // Neurol. Sci. 2011. V. 32. № 3. P. 433–441.
5. Frielingsdorf H., Simpson D.R., Thal L.J., Pizzo D.P. //

Neurobiol. Dis. 2007. V. 26. № 1. P. 47–55.

6. Zhu W., Cheng S., Xu G., Ma M., Zhou Z., Liu D., Liu X. // Drug Deliv. 2011. V. 18. № 5. P. 338–343.
7. Tirassa P., Maccarone M., Carito V., De Nicolò S., Fiore M. // Eur. J. Neurosci. 2015. V. 41. № 9. P. 1207–1218.
8. Tirasa P. // Arch. Ital. Biol. 2011. V. 149. № 2. P. 205–213.
9. Zhang H., Petit G.H., Gaughwin P.M., Hansen C., Ranganathan S., Zuo X., Smith R., Roybon L., Brundin P., Mobley W.C., et al. // J. Huntingtons. Dis. 2013. V. 2. № 1. P. 69–82.
10. Cao J.-Y., Lin Y., Han Y.-F., Ding S.-H., Fan Y.-L., Pan Y.-H., Zhao B., Guo Q.-H., Sun W.-H., Wan J.-Q., et al. // CNS Neurosci. Ther. 2018. V. 24. № 6. P. 508–518.
11. Aloe L., Rocco M.L., Bianchi P., Manni L. // J. Transl. Med. 2012. V. 10. № 1. P. 239.
12. Price R.D., Milne S.A., Sharkey J., Matsuoka N. // Pharmacol. Ther. 2007. V. 115. № 2. P. 292–306.
13. Gudasheva T.A., Antipova T.A., Seredenin S.B. // Dokl. Biochem. Biophys. 2010. V. 434. P. 262–265.
14. Gudasheva T.A., Povarnina P.Y., Antipova T.A., Firsova Y.N., Konstantinopolsky M.A., Seredenin S.B. // J. Biomed. Sci. 2015. V. 22. P. 106.
15. Antipova T.A., Gudasheva T.A., Seredenin S.B. Bull Exp Biol Med. 2011. V. 150. № 5. P. 607–609.
16. Seredenin S.B., Gudasheva T.A. Zh Nevrol Psikhiatr Im S S Korsakova. 2015. V. 115. № 6. P. 63–70.
17. Seredenin S.B., Povarnina P.Y., Gudasheva T.A. Zh Nevrol Psikhiatr Im S S Korsakova. 2018. V. 118. № 7. P. 49–53.
18. McCullough L.D., Liu F. // J. Biomed. Biotechnol. 2011. V. 2011. P. 464701–464701.
19. Longa E.Z., Weinstein P.R., Carlson S., Cummins R. // Stroke. 1989. V. 20. № 1. P. 84–91.
20. Towbin H., Staehelin T., Gordon J. // Proc. Natl. Acad. Sci. USA. 1979. V. 76. № 9. P. 4350–4354.
21. Lowery O.H., Rosebrough N.J., Farr A.L., Randall R.J. // J. Biol. Chem. 1951. V. 193. № 1. P. 265–275.
22. Lindvall O., Kokaia Z. // Cold Spring Harb. Perspect. Biol. 2015. V. 7. № 11. P. a019034.
23. Christie K.J., Turnley A.M. // Front. Cell. Neurosci. 2013. V. 6. P. 70.
24. Lippman J., Dunaevsky A. // J. Neurobiol. 2005. V. 64. № 1. P. 47–57.

The Mechanisms of Action of Triindolylmethane Derivatives on Lipid Membranes

S. S. Efimova[1,*], T. E. Tertychnaya[1], S. N. Lavrenov[2], O. S. Ostroumova[1]
[1]Institute of Cytology, Russian Academy of Sciences, Tikhoretsky Ave. 4, St. Petersburg, 194064, Russia
[2]Gause Institute of New Antibiotics, Russian Academy of Medical Sciences, Bolshaya Pirogovskaya Str. 11, Moscow, 119021, Russia
[*]E-mail: efimova@incras.ru

Received April 12, 2019; in final form, July 18, 2019
DOI: 10.32607/20758251-2019-11-3-38-45

Copyright © 2019 National Research University Higher School of Economics. This is an open access article distributed under the Creative Commons Attribution License,which permits unrestricted use, distribution, and reproduction in any medium, provided the original work is properly cited.

ABSTRACT The effects of new synthetic antibacterial agents – *tris*(1-pentyl-1*H*-indol-3-yl)methylium chloride (LCTA-1975) and (1-(4-(dimethylamino)-2,5-dioxo-2,5-dihydro-1*H*-pyrrol-3-yl)-1*H*-indol-3-yl)*bis*(1-propyl-1*H*-indol-3-yl)methylium chloride (LCTA-2701 – on model lipid membranes were studied. The ability of the tested agents to form ion-conductive transmembrane pores, influence the electrical stability of lipid bilayers and the phase transition of membrane lipids, and cause the deformation and fusion of lipid vesicles was investigated. It was established that both compounds exert a strong detergent effect on model membranes. The results of differential scanning microcalorimetry and measuring of the threshold transmembrane voltage that caused membrane breakdown before and after adsorption of LCTA-1975 and LCTA-2701 indicated that both agents cause disordering of membrane lipids. Synergism of the uncoupling action of antibiotics and the alkaloid capsaicin on model lipid membranes was shown. The threshold concentration of the antibiotic that caused an increase in the ion permeability of the lipid bilayer depended on the membrane lipid composition. It was lower by an order of magnitude in the case of negatively charged lipid bilayers than for the uncharged membranes. This can be explained by the positive charge of the tested agents. At the same time, LCTA-2701 was characterized by greater efficiency than LCTA-1975. In addition to its detergent action, LCTA-2701 can induce ion-permeable transmembrane pores: step-like current fluctuations corresponding to the opening and closing of individual ion channels were observed. The difference in the mechanisms of action might be related to the structural features of the antibiotic molecules: in the LCTA-1975 molecule, all three substituents at the nitrogen atoms of the indole rings are identical and represent *n*-alkyl (pentyl) groups, while LCTA-2701 contains a maleimide group, along with two alkyl substituents (*n*-propyl). The obtained results might be relevant to our understanding of the mechanism of action of new antibacterial agents, explaining the difference in the selectivity of action of the tested agents on the target microorganisms and their toxicity to human cells. Model lipid membranes should be used in further studies of the trends in the modification and improvement of the structures of new antibacterial agents.

KEYWORDS antimicrobial agents, antibiotics, turbomycin A, lipid bilayers, liposomes, ion-permeable nanopores.

ABBREVIATIONS LCTA-1975 – *tris*(1-pentyl-1*H*-indol-3-yl)methylium chloride; LCTA-2701 – (1-(4-(dimethylamino)-2,5-dioxo-2,5-dihydro-1*H*-pyrrol-3-yl)-1*H*-indol-3-yl)*bis*(1-propyl-1*H*-indol-3-yl)methylium chloride; DOPS – 1,2-dioleoyl-*sn*-glycero-3-phospho-L-serine; DOPE – 1,2-dioleoyl-*sn*-glycero-3-phosphoethanolamine; DPhPC – 1,2-diphytanoyl-*sn*-glycero-3-phosphocholine; POPC – 1-palmitoyl-2-oleoyl-*sn*-glycero-3-phosphocholine; DPPC – 1,2-dipalmitoyl-*sn*-glycero-3-phosphocholine.

INTRODUCTION

The main challenge of modern antibiotic therapy is the side effects of antibacterial agents and the growing resistance of pathogenic bacteria to them, which results in the loss of their clinical potency by a number of drugs. One of the promising ways to overcoming these difficulties is to modify natural antibiotic compounds in order to create semisynthetic derivatives, which not only exhibit pronounced activity against resistant microorganisms, but also exert an extended spectrum of action, compared to their original versions.

The antibiotic turbomycin A, first isolated as a metabolic product of *Saccharomyces cerevisiae*, exhibits relatively low activity against Gram-positive bacteria [1] and presents a salt of *tris*(indol-3-yl)methylium [2]. Introduction of alkyl substituents at nitrogen atoms of the indole rings of the antibiotic was shown to significantly increase the antibacterial effect, expand the antibacterial spectrum, and induce the antitumor activity of the drug [3, 4].

Of great interest are the novel homologs of turbomycin A, namely, *tris*(1-pentyl-1*H*-indol-3-yl) methylium chloride (LCTA-1975) and (1-(4-(dimethylamino)-2,5-dioxo-2.5-dihydro-1*H*-pyrrol-3-yl)-1*H*-indol-3-yl)*bis*(1-propyl-1*H*-indol-3-yl)methylium chloride (LCTA-2701), which were synthesized at the Gause Institute of New Antibiotics. In addition to its high antibacterial activity against multidrug-resistant Gram-positive bacteria, LCTA-1975 also induces the apoptosis of tumor cells via the NF-kB signaling pathway [3, 5, 6]. LCTA-2701, which exhibits approximately the same level of antibacterial activity as LCTA-1975, is significantly less toxic to human cells (donor fibroblasts) [7]. This work presents a study of the mechanisms of interaction of LCTA-1975 and LCTA-2701 with lipid bilayers, including those that simulate the membranes of target cells.

EXPERIMENTAL

The following compounds were used in the study: 1,2-dioleoyl-*sn*-glycero-3-phospho-L-serine (DOPS), 1,2-dioleoyl-*sn*-glycero-3-phosphoethanolamine (DOPE), 1,2-diphytanoyl-*sn*-glycero-3-phosphocholine (DPhPC), 1-palmitoyl-2-oleoyl-*sn*-glycero-3-phosphocholine (POPC), and 1,2-dipalmitoyl-*sn*-glycero-3-phosphocholine (DPPC) (Avanti Polar Lipids, USA); KCl, KOH, HEPES, pentane, ethanol, hexadecane, dimethyl sulfoxide, capsaicin, caffeine (Sigma, USA). The chemical structures of the triindolylmethane derivatives LCTA-1975 and LCTA-2701 synthesized at the Gause Institute of New Antibiotics are presented in *Fig. 1*.

Preparation of planar lipid bilayers and recording of the transmembrane currents

Bilayer lipid membranes were formed according to the Montal and Müller technique [8], by mixing condensed lipid monolayers over a hole in a Teflon film dividing the experimental chamber into two (the *cis* and *trans*) compartments. The volume of each compartment was 1.5 ml, the thickness of the Teflon film was 10 μm, and the hole diameter was about 50 μm. The hole in the Teflon film was treated with hexadecane prior to membrane formation. Planar lipid bilayers were formed from DPhPC or POPC, as well as from an equimolar mixture of DOPS and DOPE. The experiments were carried out using aqueous electrolyte solutions (0.1 M KCl, pH 7.4) with an identical ionic composition separated by a membrane. The acidity of the solutions (pH 7.4) was maintained using a 5 mM HEPES/KOH buffer.

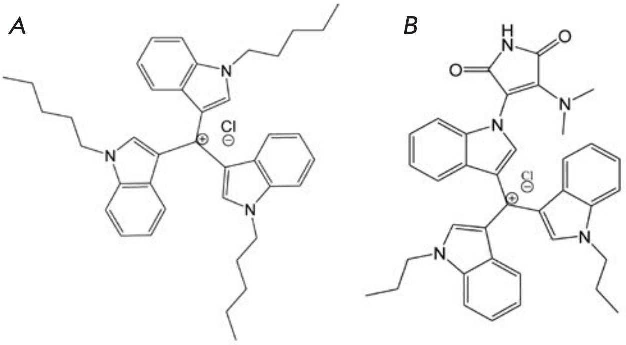

Fig. 1. The chemical structure of triindolylmethane derivatives: LCTA-1975 (*A*) and LCTA-2701 (*B*)

The tested substances, LCTA-1975 and LCTA-2701, were added from a 10 mg/ml solution in dimethyl sulfoxide and H_2O (1 : 1) to the *cis* compartment of the chamber to the final concentration as indicated in *Table 1*. At least four independent experiments (repeats) were performed for each agent-lipid bilayer system.

Silver/silver chloride electrodes connected to the chamber solutions through 1.5% agarose bridges containing 2 M KCl were used to apply the transmembrane potential and record the transmembrane current. The potential of the current flow of cations from the *cis* to the *trans* compartment of the chamber was considered positive.

Transmembrane currents were measured and digitized in the voltage clamp mode using an Axopatch 200B and Digidata 1440A systems (Axon Instruments, USA). The data were processed using an eight-pole Bessel filter (Model 9002, Frequency Devices) at a filtering frequency of 1 kHz.

Transmembrane current recordings were processed using the Clampfit 9.0 software package (Axon Instruments). Statistical analysis of the data was performed using the Origin 8.0 software (Origin Lab., USA).

The conductance of the pore was determined as the ratio of the current flowing through a single pore to the transmembrane voltage. Histograms of current fluctuations were obtained for the values of the transmembrane currents determined by the changes in the

Table 1. The dependence between the membrane activity and concentration of triindolylmethane derivatives in the membrane-bathing solutions (C, µM)

Activity type	LCTA-1975			LCTA-2701		
	DOPS : DOPE (50 : 50 mol%)	DPhPC	POPC	DOPS : DOPE (50 : 50 mol%)	DPhPC	POPS
No activity	< 15	< 315	< 200	< 8	< 55	< 30
Ion-permeable pores	–	–	–	8–25	55–135	30–130
Detergent effect	> 15	> 315	> 200	> 25	> 135	> 130

Note: The concentration error is ≤ 10%.

current amplitude upon opening or closing of individual channels. Records of current fluctuations through membranes with a single integrated channel were used to determine the channel lifetime (the open state time). For each of the experimental systems, the conductance and pore lifetime values were presented as an arithmetic mean and a standard error (mean ± SE).

The threshold values of the transmembrane voltage *Vbd*, which causes the destruction of the DPhPC membranes before and after the addition of triindolylmethane derivatives to the membrane-bathing solutions, were measured by applying a voltage in the range of 0 to ± *Vbd* to the membrane. No differences were found between the positive and negative transmembrane potentials.

Determination of changes in the electric potential at the membrane/aqueous solution interface upon introduction of the test derivatives

The nonactin ionophore was added to the bathing solutions on both sides of the membrane to a final concentration of 10^{-7}–10^{-6} M. Lipid membranes were formed from DPhPC in 0.1 M KCl, 5 mM HEPES/KOH buffer, pH 7.4, according to the procedure described above.

Bilayer conductance (G) was determined as the ratio of the steady-state transmembrane current to the transmembrane potential, which equaled 50 mV. Changes in the electric potential at the membrane/aqueous solution interface caused by the introduction of the test derivatives ($\Delta\varphi_d$) were determined as

$$\frac{G_m}{G_m^0} = \exp\left(\frac{e\Delta\phi_d}{kT}\right),$$

where G^0_m and G_m are the values of the steady-state K^+ conductance of the bilayer induced by nonactin before and after the introduction of the test agent.

The studied compounds LCTA-1975 and LCTA-2701 were added to the *cis* compartment of the experimental chamber from a 1 : 1 dimethyl sulfoxide-to-H_2O solution to a final concentration of 300 and 150 µM, respectively.

Confocal fluorescence microscopy of liposomes

Giant unilamellar liposomes were formed from POPC in an electric field using a commercial Nanion vesicle *prep pro* setup (Germany) on a pair of glasses coated with a conductive mixture of indium oxide and tin oxide with a standard protocol (alternating voltage with an amplitude of 3 V, 10 Hz frequency, 1 h, 25°C) according to [9].

The resulting suspension of liposomes was divided into aliquots. Triindolylmethane derivatives were added into the experimental samples at a lipid-to-agent ratio of 10 : 1. Aliquots were equilibrated for 30 min at room temperature, and 10 µl of the obtained liposome suspension was placed between the slide and cover glasses. Liposomes were observed in transmitted light on an Olympus FV3000 confocal microscope (Germany). Independent experiments (3 to 5) were carried out, and the average liposome diameter was determined for each of the experimental systems (mean ± SE).

Differential scanning microcalorimetry of liposomes

Giant unilamellar liposomes were formed from DPPC in an electric field as described above. The resulting liposome suspension was adjusted to 800 µl with a buffer solution (5 mM HEPES, pH 7.4). The final lipid concentration was 5 mM. LCTA-1975 and LCTA-2701 were introduced into the experimental samples at a lipid-to-agent ratio of 10 : 1 or 5 : 1. The control samples remained unmodified. Thermograms of liposome suspensions were obtained using a µDSC7 differential scanning microcalorimeter (Setaram, France). The required amount of suspension was placed in a cell and heated at a constant rate of 0.2 K/min; an equivalent volume of the buffer solution was placed in the second cell. The reproducibility of the temperature depend-

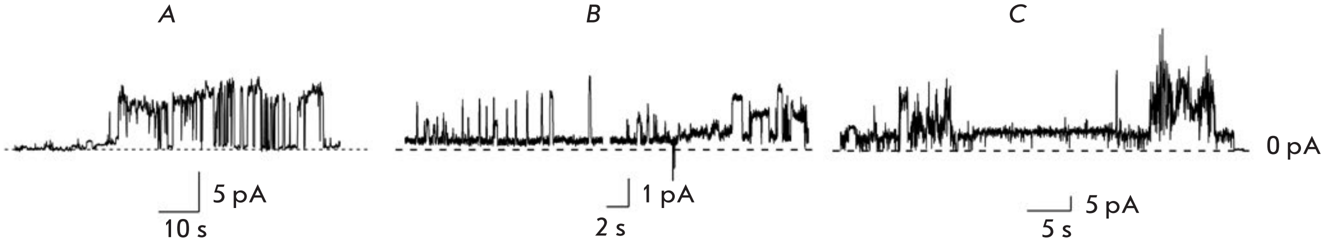

Fig. 2. Current fluctuations corresponding to the opening and closing of individual pores induced by LCTA-2701 in the planar lipid bilayer at antibiotic concentrations of 10 (*A*), 70 (*B*), and 100 (*C*) µM. Membranes were formed from the DOPS:DOPE (50 : 50 mol%) (*A*), DPhPC (*B*) and POPC (*C*) and bathed in 0.1 M KCl, 5 mM HEPES, pH 7.4. The transmembrane voltage was equal to 100 mV

ence of the heat capacity was achieved by reheating the sample immediately after cooling. Thermogram peaks were characterized by the temperatures of the pre-transition (T_p) and the main transition (T_m), and the width at half-maximum of the main peak ($T_{1/2}$), which characterizes the cooperativity of the transition of DPPC from gel phase to liquid phase, as well as the change in the enthalpy of the main phase transition (ΔH).

RESULTS AND DISCUSSION

The membrane activity of the synthetic homologs of turbomycin A, namely LCTA-1975 and LCTA-2701, has been studied. *Table 1* presents the characteristics of the action of the tested agents on lipid bilayers. Introduction of LCTA-1975 to membranes made from an equimolar mixture of DOPS and DOPE to a final concentration of 15 µM does not cause any noticeable fluctuations in the transmembrane current. An increase in the agent concentration disturbs the bilayer, with its subsequent breakdown. Addition of LCTA-2701 to a concentration of 8 µM does not affect the ionic permeability of negatively charged membranes. Introduction of LCTA-2701 to a concentration of 8–25 µM into the *cis* compartment solution increases the membrane conductance through the formation of ion-permeable pores. *Figure 2A* shows examples of recordings of step-like current fluctuations for DOPS : DOPE (50 : 50 mol%) membranes in the presence of LCTA-2701. It can be seen from *Fig. 2A* that the pores have differing conductance. Pore conductance varies from 5 to 100 pS, and their lifetime ranges from 0.1 to 5 s. A further increase in LCTA-2701 concentration results in the disintegration of the lipid bilayer.

Unlike for negatively charged membranes, including DOPS, the tested agents exert a detergent effect with respect to the bilayers composed of neutral lipids, DPhPC or POPC, at concentrations higher by an order of magnitude (*Table 1*). An increase in the concentrations of LCTA-1975 and LCTA-2701 to 200 and 130 µM, respectively, disturbs the stability of uncharged membranes and causes their breakdown. LCTA-2701 at a concentration of 30–130 µM also demonstrates pore-forming ability. Recordings of current fluctuations corresponding to the opening and closing of the transmembrane pores induced by this substance in the DPhPC or POPC bilayer are shown in *Fig. 2B,C*.

The obtained results allow us to conclude that the test compounds act differently on the model lipid membranes: both agents exhibit detergent activity, while LCTA-2701 is also capable of inducing transmembrane pores. It should be noted that the type of membrane activity for these substances does not depend on the membrane composition. The threshold concentration at which the destructive effect of the tested agents is manifested is determined by the surface charge of the bilayer. A possible explanation for this may be the positive charge of the tested compounds, which contributes to their sorption on the negatively charged membranes composed of DOPS and DOPE. In addition, the membrane activity of the tested derivatives is virtually independent of the shape of the membrane-forming lipids. The effect of the tested substances on the membranes of cone-shaped DPhPC and cylindrical POPC molecules [10, 11] manifests itself at similar concentrations. The threshold concentration that causes an increase in the ionic permeability of the lipid bilayer also depends on the type of agent. LCTA-2701 is more effective than LCTA-1975 with respect to both negatively charged and neutral membranes.

The planar lipid bilayers formed from DPhPC exhibit the highest electrical stability in the absence of any modifiers. The threshold value of the transmembrane voltage (*Vbd*) that causes a disruption of DPhPC membranes is 450 ± 30 mV. Introduction of LCTA-1975 or LCTA-2701 to a concentration of 100 µM leads to a drop in *Vbd* to 310 ± 30 mV and 370 ± 30 mV, respectively. This indicates that the electrical stability

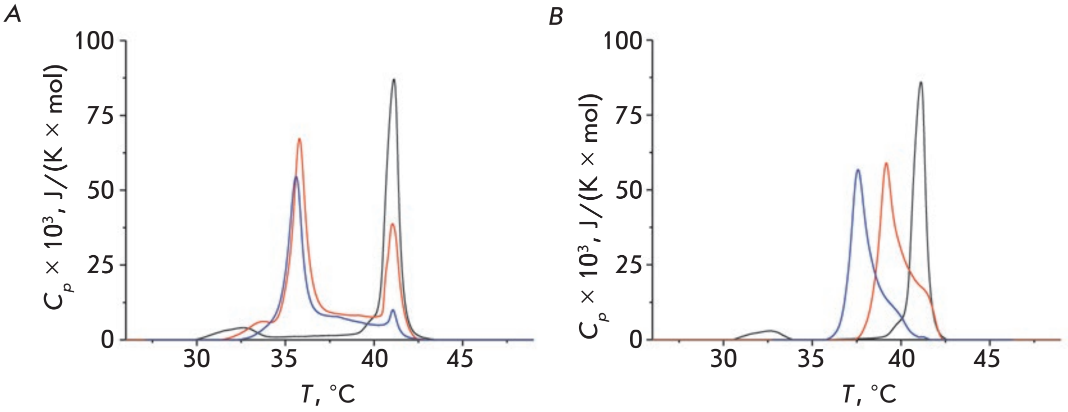

Fig. 3. The thermograms of DPPC melting in the absence (control, *black line*) and presence of LCTA-1975 (*A*) and LCTA-2701 (*B*). The lipid : antibiotic ratio was equal to 10 : 1 (*red lines*) and 5 : 1 (*blue lines*)

of the membrane decreases in the presence of these substances. The results suggest that the tested agents exhibit a disordering effect on the lipids in the bilayer.

The proposed assumption is independently confirmed by the results of a study focused on the effect of alkaloids on the membrane activity of LCTA-1975 or LCTA-2701. Comprehensive studies using such methods as differential scanning microcalorimetry, X-ray diffraction, fluorescence probe spectroscopy, and NMR demonstrated the significant effect of capsaicin, an alkaloid from chili pepper, on the phase transitions of membrane lipids [12, 13]. Capsaicin significantly reduces the melting temperature and cooperativity of dimyristoylphosphatidylcholine [14] and dipalmitoylphosphocholine [12]. Significant deconvolution of the peak corresponding to the main phase transition is observed in the thermogram at relatively high concentrations of the alkaloid, which is an indication that several mixed alkaloid–lipid phases coexist. Moreover, capsaicin enhances the ability of phosphoethanolamine to form non-lamellar inverted hexagonal phases. Capsaicin adsorption is believed to increase the negative spontaneous curvature of lipid monolayers [12, 15]. In palmitoyl–oleoyl–phosphocholine membranes, capsaicin is located between the lipid–water interphase and the plane of the double bond of the unsaturated acyl lipid chain [13]. A decrease in membrane stiffness in the presence of capsaicin was found to be responsible for the modulation of ion currents induced by the antibiotic gramicidin A [16, 17]. According to the reported data on the disordering effect of capsaicin, one can expect that the tested compounds would exhibit an enhanced detergent action in its presence. Indeed, the introduction of 0.4 mM capsaicin into the solutions bathing the DOPS : DOPE (50 : 50 mol%) membranes modified by LCTA-1975 or LCTA-2701 reduces the concentrations of the substances by 20–30%, thus causing a destabilization of the bilayer.

Table 2. Thermodynamic characteristics of DPPC liposomes in the absence and presence of triindolylmethane derivatives

Experimental system	Lipid : agent ratio	Peak No.	T_m, °C	$T_{1/2}$, °C	ΔH, kcal/mol
Control	–	1	41.2	0.6	13.3
LCTA-1975	10 : 1	1	41.0	0.9	12.3
		2	38.7		
		3	35.8		
		4	33.7		
	5 : 1	1	41.0	0.9	11.2
		2	37.8		
		3	35.5		
		4	34.4		
LCTA-2701	10 : 1	1	41.1	2.4	10.6
		2	39.1		
	5 : 1	1	41.2	1.8	9.6
		2	39.1		
		3	37.6		

Note. T_m is the temperature at the local maximum of heat capacity; $T_{1/2}$ is the width at half -maximum of the main peak; Δ*H* is the enthalpy change of the main phase transition.

Interaction of another plant alkaloid, caffeine, with water molecules bound to neighboring lipids leads to a local increase in hydration and membrane thickness, while reducing its fluidity [18]. These results are consistent with calorimetry and molecular dynamics data

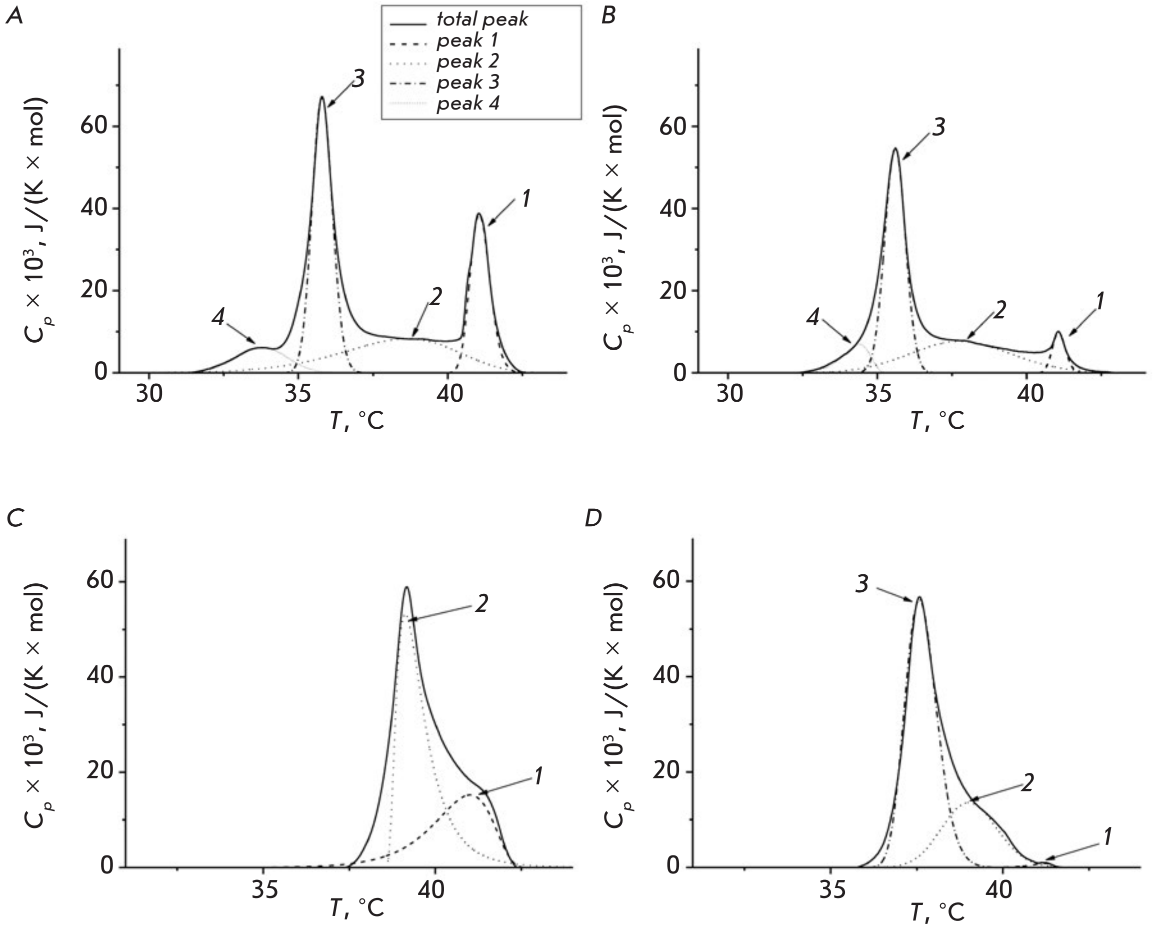

Fig. 4. Deconvolution analysis of the main transition peak of DPPC in the presence of LCTA-1975 (*A*, *B*) and LCTA-2701 (*C*, *D*). The lipid : antibiotic ratio was equal to 10 : 1 (*A*, *C*) and 5 : 1 (*B*, *D*). Peak parameters are presented in *Table 2*

according to which caffeine significantly compensates for the uncoupling effect of the local anesthetic tetracaine [19]. The effect is absent in the case of LCTA-1975 and LCTA-2701. The non-specific interaction of caffeine with DOPS : DOPE (50 : 50 mol%) bilayers has almost no effect on the membrane activity of the tested substances. The inability of caffeine to compensate for the uncoupling effect of LCTA-1975 or LCTA-2701 may indicate a significant difference between the localization of these substances and caffeine in the membrane. According to [18, 20], xanthine molecules are located at the boundary between the regions of lipid "heads" and "tails." LCTA molecules are more likely to be able to immerse in the hydrophobic region of the membrane due to their alkyl substituents, which results in an increase in the lateral pressure in this region and its expansion. The proximity of the location of the tested antibacterial agents and capsaicin in the membrane may explain the synergism of their disordering effect.

Figure 3 presents the thermograms for the DPPC liposomes in the absence (control, *black lines*) and in the presence of LCTA-1975 or LCTA-2701 in the suspension at the lipid-to-agent molar ratio of 10 : 1 (*red lines*) and 5 : 1 (*blue lines*). In the absence of LCTA derivatives, the pre-transition temperature T_p is 32.6°C; the temperature of the main phase transition T_m is 41.2°C; and the width at half-maximum of the main peak $T_{1/2}$, which characterizes the cooperativity of the transition of DPPC from gel phase to liquid phase, does not exceed 0.6°C. Both tested agents significantly affect the DPPC melting process. In both cases, pre-transition is eliminated. *Table 2* presents the T_m and $T_{1/2}$ values for the lipid-to-agent ratio used in this study. Deconvolution of the peak corresponding to the main phase transition of DPPC should be noted, since its degree depends on the lipid-to-agent ratio observed in the presence of the tested compounds (*Fig. 3*). *Figure 4* shows the result of deconvolution of the peak corresponding to the main phase transition of DPPC into separate components in the presence of the tested agents. The presence of several peaks indicates the coexistence of different phases. The number 1 peak in the thermograms (*Fig. 4A–D*) can be associated with the melting of pure DPPC, while the two remaining peaks are associated with the presence of different phases, including both DPPC and LCTA (peak *2* and(or) *3* in *Fig. 4A–D*). The drop in the temperature and cooperativity of DPPC transition in the presence of test substances can be associated with their immersion in the hydrophobic region of the bilayer, resulting in an increase in the area per lipid molecule and, consequently, an increase in the mobility of the lipid acyl tails. The obtained results also demonstrate that an increase in the LCTA-1975 and LCTA-2701 concentrations leads to a decrease in the change of the main phase transition enthalpy (ΔH): an approximately 10% decrease in ΔH is observed with a 2-fold increase in concentration. A decrease in ΔH can be due to the transition of part of the lipid to the non-lamellar phase [21–23]. In particular, the appearance of a pronounced peak at 34°C after the introduction of LCTA-1975 at all tested concentrations may indicate a significant change in the distribution of the lateral pressure in the membrane and appearance of non-layer lipid formations in the presence of this agent (peak *4* in *Fig. 4A,B*).

The effect of antibacterial substances on the boundary potential of the planar lipid bilayers formed of DOPS : DOPE (50 : 50 mol%) has been also studied. LCTA-1975 and LCTA-2701 do not affect the steady-state transmembrane current induced by the complex of nonactin ionophore with the potassium ion ($\Delta\varphi_d = 1 \pm 1$ mV). This indicates the invariance of the distribution of the electric potential at the membrane/aqueous solution interface during adsorption of the tested compounds.

POPC vesicles were studied using confocal microscopy before and after the introduction of LCTA derivatives into the suspension. The addition of LCTA-1975 or LCTA-2701 to POPC liposomes at a lipid-to-agent ratio of 10 : 1 does not change the spherical shape of lipid vesicles. The identical average liposome diameter before (15 ± 6 μm) and after (15 ± 7 μm) addition indicates that the tested agents do not cause fusion or division of the lipid vesicles.

CONCLUSION

It has been established that the tested compounds act differently on model lipid membranes: LCTA-1975 demonstrates detergent properties, while LCTA-2701, in addition to its detergent activity, is also capable of inducing pores in phospholipid membranes. The differences in their mechanisms of action are due to their structural features: all three substituents at the nitrogen atoms of the indole rings in LCTA-1975 are identical and present *n*-alkyl (pentyl) groups, while LCTA-2701 contains, along with the two alkyl substituents (*n*-propyl), a maleimide group. The obtained results might be relevant to our understanding of the mechanism of action of new antibacterial agents, explaining the difference in the selectivity of their action on microorganisms and their cytotoxicity to human cells. Model lipid membranes should be used in further studies on the trends in the modification and improvement of the structures of new antibacterial agents. ●

This work was financially supported by the grants of the Russian Foundation for Basic Research No. 18-34-20047 (studies of the effect on membranes), the Russian Science Foundation No. 16-15-10300 (design and synthesis of test substances) and the Scholarship of the President of the Russian Federation awarded to. S.S. Efimova (SP-484.2018.4).

REFERENCES

1. Palchaudhuri R., Nesterenko V., Hergenrother P.J. // J. Am. Chem. Soc. 2008. V. 130. № 31. P. 10274–10281.
2. Budzikiwicz H., Eckau H., Ehrenberg M. // Tetrahedron Lett. 1972. V. 36. P. 3807.
3. Lavrenov S.N., Luzikov Y.N., Bykov E.E., Reznikova M.I., Stepanova E.V., Glazunova V.A., Volodina Y.L., Tatarsky V.V., Shtil A.A., Preobrazhenskaya M.N. // Bioorg. Med. Chem. 2010. V. 18. № 18. P. 6905–6913.
4. Stepanova E.V., Shtil' A.A., Lavrenov S.N., Bukhman V.M., Inshakov A.N., Mirchink E.P., Trenin A.S., Preobrazhenskaya M.N. // Russ. Chem. Bull. 2010. V. 59. № 12. P. 2259–2267.
5. Isakova E.B., Treshchalin I..D.., Bodyagin D.A., Lavrenov S.N., Preobrazhenskaya M.N., Pereverzeva E.R. // Russian Biotherapeutic Journal. 2012. V. 11. No. 2. P. 22.
6. Solomko E.Sh., Lavrenov S.N., Inshakov A.N., Abramov M.E., Preobrazhenskaya M.N., Stepanova E.V. // Sarcomas of bones, soft tissues and skin tumors. 2012. № 3. P. 48–53.
7. Lavrenov S.N., Simonov A.Yu., Panov A.A., Lakatosh S.A., Isakova Ye.B., Tsvigun Ye.A., Bychkova O.P., Tatarsky V.V., Ivanova E.S., Mirchink, E.P., Korolev A.M., Trenin, A.S. // Antibiotics and chemotherapy. 2018. V. 63. № 7-8. P. 3-9.
8. Montal M., Mueller P. // Proc. Natl. Acad. Sci. USA. 1972. V. 69. № 12. P. 3561–3566.
9. Efimova S.S., Ostroumova O.S. // Acta Naturae. 2017. T. 9. № 2. C. 67–74.
10. Bezrukov S.M. // Curr. Opin. Colloid. Interface Sci. 2000. V. 5. P. 237–243.
11. Sakuma Y., Taniguchi T., Imai M. // Biophys. J. 2010. V. 99. P. 472–479.
12. Aranda F.J., Villalaín J., Gómez-Fernández J.C. // Biochim. Biophys. Acta. 1995. V. 1234. № 2. P. 225–234.
13. Torrecillas A., Schneider M., Fernández-Martínez A.M., Ausili A., de Godos A.M., Corbalán-García S., Gómez-Fernández J.C. // ACS Chem. Neurosci. 2015. V. 6. № 10. P. 1741–1750.
14. Swain J., Kumar Mishra A. // J. Phys. Chem. B. 2015.

V. 119. № 36. P. 12086–12093.
15. Ingólfsson H.I., Andersen O.S. // Assay Drug Dev. Technol. 2010. V. 8. № 4. P. 427–436.
16. Lundbaek J.A., Birn P., Tape S.E., Toombes G.E., Søgaard R., Koeppe R.E., Gruner S.M., Hansen A.J., Andersen O.S. // Mol. Pharmacol. 2005. V. 68. № 3. P. 680–689.
17. Søgaard R., Werge T.M., Bertelsen C., Lundbye C., Madsen K.L., Nielsen C.H., Lundbaek J.A. // Biochem. 2006. V. 45. № 43. P. 13118–13129.
18. Khondker A., Dhaliwal A., Alsop R.J., Tang J., Backholm M., Shi A.C., Rheinstädter M.C. // Phys. Chem. Chem. Phys. 2017. V. 19. № 10. P. 7101–7111.
19. Sierra-Valdez F.J., Forero-Quintero L.S., Zapata-Morin P.A., Costas M., Chavez-Reyes A., Ruiz-Suárez J.C. // PLoS One. 2013. V. 8. № 4. P. e59364.
20. Paloncýová M., Berka K., Otyepka M. // J. Phys. Chem. B. 2013. V. 117. № 8. P. 2403–2410.
21. Maruyama S., Hata T., Matsuki H., Kneshina S. // Biochim. Biophys. Acta. 1997. V. 1325. P. 272–280.
22. Hata T., Matsuki H., Kaneshina S. // Biophys. Chem. 2000. V. 87. P. 25–36.
23. Takeda K., Okuno H., Hata T., Nishimoto M., Matsuki H., Kaneshina S. // Colloids Surf. B Biointerf. 2009. V. 72. P. 135–140.

The Effect of a Lipopolysaccharide from *Rhodobacter capsulatus* PG on Inflammation Caused by Various Influenza Strains

S. V. Zubova[1*], M. F. Vorovich[2,3], A. S. Gambaryan[2], A. A. Ishmukhametov[2,3], S. V. Grachev[1,3], I. R. Prokhorenko[1]
[1]Institute of Basic Biological Problems of RAS, FRC PSCBR RAS, Science Ave. 3, Pushchino, Moscow, 142290, Russia
[2]FGBNU Federal Scientific Center of Research and Development of Immunobiological Preparations named M.P. Chumakov of RAS, pos. Institute of Poliomyelitis, Kievskoye Highway, 27th km, 8/1, Moscow Region, 142782, Russia
[3]GAOUVO First Moscow State Medical University named I.M. Sechenov of Russia Health Ministry, Trubetskaya Str. 8, Moscow, 119811, Russia
*E-mail: zusvet@rambler.ru

Received December 5, 2018; in final form, May 15, 2019
DOI: 10.32607/20758251-2019-11-3-46-55

Copyright © 2019 National Research University Higher School of Economics. This is an open access article distributed under the Creative Commons Attribution License,which permits unrestricted use, distribution, and reproduction in any medium, provided the original work is properly cited.

ABSTRACT **The development of a specific inflammation in mice that had been infected by two influenza virus strains, A/chicken/Kurgan/5/2005 (H5N1) and A/Hamburg/2009 MA (H1N1), was studied. We investigated the effect of a non-toxic lipopolysaccharide from *Rhodobacter capsulatus* PG on the survival and body weight of the mice, production of IgG antibodies, and the induction of pro- and anti-inflammatory cytokines in blood serum. The administration of the *R. capsulatus* PG lipopolysaccharide was shown to induce interferon-β synthesis, both in healthy and influenza A virus-infected mice, and to promote production of antiviral antibodies in the blood of the influenza-infected animals.**

KEYWORDS **influenza virus, H5N1, H1N1, *Rhodobacter capsulatus* PG lipopolysaccharide, mice, antiviral antibodies, cytokines.**

ABBREVIATIONS **DAMP – damage-associated molecular pattern; HA – hemagglutinin; HMGB1 – high mobility group box 1 protein/amphoterin; IFN – interferon; Ig – immunoglobulin; IL – interleukin; MD-2 – myeloid differentiation protein 2; MDCK cells – Madin-Darby canine kidney cells; MyD88 – myeloid differentiation protein 88; NP – nucleoprotein; PA, PB1 – polymerase complex proteins; TLR – Toll-like receptor; TNF – tumor necrosis factor; TRAF6 – TNF receptor-associated factor 6; ELISA – enzyme-linked immunosorbent assay; LPS – lipopolysaccharide.**

INTRODUCTION

Influenza epidemics have, to date, affected millions of people across the world despite the use of recommended vaccines, whose effectiveness proves lower than expected [1, 2]. Influenza A viruses have a high degree of genomic variation and produce resistant strains that can be controlled by vaccines or antiviral systemic medication for some time. The development of safe and effective vaccines remains an important public health goal.

The interaction of viral components with various receptors activates the intracellular pathways responsible for the secretion of type I IFN, pro-inflammatory cytokines, and chemokines. The key factors involved in the recognition of viral ligands are the Toll-like receptors (TLRs) of innate immune cells. TLR2 and TLR4, situated on the cell surface, recognize viral envelope glyco/lipoproteins, while intracellular endosomal TLR3, TLR7, TLR8, and TLR9 recognize nucleic acids [3, 4]. Toll-like receptors can interact with other receptors, thereby stimulating the response of innate immune cells to pathogens, including influenza viruses [4]. TLR4 can be activated by damage-associated molecular patterns (DAMPs), which are molecular structures released by virus-infected cells [5]. Different influenza strains activate cells through various mechanisms, which lead to the synthesis of various cytokines and chemokines [6, 7].

Compound E5564 (Eritoran), a synthetic analogue of the non-toxic lipid A from *Rhodobacter sphaeroides*, when administered in a certain regimen to C57BL/6J mice, was shown to protect mice from death caused by the mouse-adapted H1N1 influenza virus [8]. The nuclear non-histone high mobility group box 1 (HMGB1) protein/amphoterin, which is a DAMP, is known to be released relatively late after the infection onset and is involved in the development of both gram-negative sepsis and influenza complications, interacting with MD-2 and activating TLR4 [5, 9, 10]. TLR4 activation leads to a cytokine storm with an accentuated release of pro-inflammatory cytokines, including interferons, tumor necrosis factors, interleukins, and chemokines [11]. Pharmacological blockade of TLR4 by Eritoran can significantly reduce mouse mortality from avian influenza [8]. A lipopolysaccharide (LPS) from a phototrophic bacterium *R. capsulatus* PG (*Rb.*) strain [12], with a lipid A structure similar to that of lipid A from *R. sphaeroides*, is an endotoxin antagonist that inhibits activation of the synthesis of numerous pro-inflammatory cytokines by human blood cells [13], an indication of its ability to block TLR4.

Mice are the main tools used for studying the human immune system and immune responses. However, there are significant differences between the innate and adaptive immune systems of mice and those of humans, which reside in the blood cell ratio, plasma composition, surface receptors, the expression levels of various cytokines and chemokines, etc. [14, 15]. This should be considered when using mice as human disease models.

In this paper, we studied the effect of a non-toxic *Rb.* LPS on the induction of pro- and anti-inflammatory cytokines and survival rates of mice infected with various influenza A strains. The study aim was to investigate the features of the inflammatory processes caused by H1N1 and H5N1 influenza viruses.

EXPERIMENTAL

The following ELISA kits were used: mouse TNF alpha platinum ELISA, mouse IL-6 platinum ELISA, mouse IL-10 platinum ELISA, and mouse INF gamma platinum ELISA (eBioscience, USA), as well as a mouse IFN beta ELISA kit (PBL Assay Science, USA).

The *Rb.* LPS was produced in a laboratory of the Institute of Basic Biological Problems, according to the procedure described previously [16].

Viruses

We used the following influenza A virus strains: chicken/Kurgan/5/2005 (H5N1) and mouse-adapted Hamburg/2009 MA (H1N1). Viruses were cultured in chicken embryos. The virus median tissue culture infectious dose ($TCID_{50}$) was determined by titration in a Madin-Darby canine kidney (MDCK) cell culture. The median lethal dose (LD_{50}) was determined by titration in mice. Experiments with the highly pathogenic A/chicken/Kurgan/5/2005 virus were performed in boxes with the BSL-3 safety level.

Mice

We used 10–14 g Balb/c mice, 36–38 days of age, regardless of gender. The animals originated in the nursery of the Scientific Center for Biomedical Technology of the Federal Medical and Biological Agency. All manipulations with the animals were performed according to the Rules of Laboratory Practice in the Russian Federation [17], in compliance with biological ethics in experiments on laboratory animals.

Experimental influenza infection in mice infected with the influenza virus strain H5N1

Mice were divided into six groups depending on the received drugs. Each group included at least 12 animals. The animals in the five groups were infected, under light ether anesthesia, intranasally (50 μL each) with the highly pathogenic avian influenza virus H5N1 at doses of 10 to 10^5 $TCID_{50}$ per mouse, which amounted to 10^{-1} to 10^3 LD_{50}. The sixth control group remained uninfected. After 24 h, all groups were divided in half. One half of the animals was injected intraperitoneally with 500 μL/mouse of saline daily for the following 4 days, and the other half was injected with the *Rb.* LPS at a dose of 400 μg/500 μL/mouse. Mice not injected with any agents were the controls. The experimental design is shown in *Fig. 1.* Blood was sampled from the animals that survived by the end of the experiment (day 14), after euthanasia in a CO_2 chamber; blood cells were precipitated; and the resulting serum was frozen at −20°C until the H5N1 influenza virus antibody titer in the serum was determined by ELISA.

Experimental influenza infection in mice infected with the mouse adapted influenza virus strain H1N1

The mice-adapted pandemic virus H1N1 used in the study was passed serially 20 times in a mouse lungs and differed from the parent A/Hamburg/2009 (H1N1) strain by a deletion in neuraminidase (NA) and mutations in the HA, NP, PA, and PB1 proteins (*Table*). The H1N1 influenza virus is 10^5–fold more pathogenic for mice compared to the initial parent strain.

The mice were divided into three groups depending on the received drugs. Each group included at least 12 animals. Two groups of mice were infected, under mild ether anesthesia, intranasally (50 μL each) with the

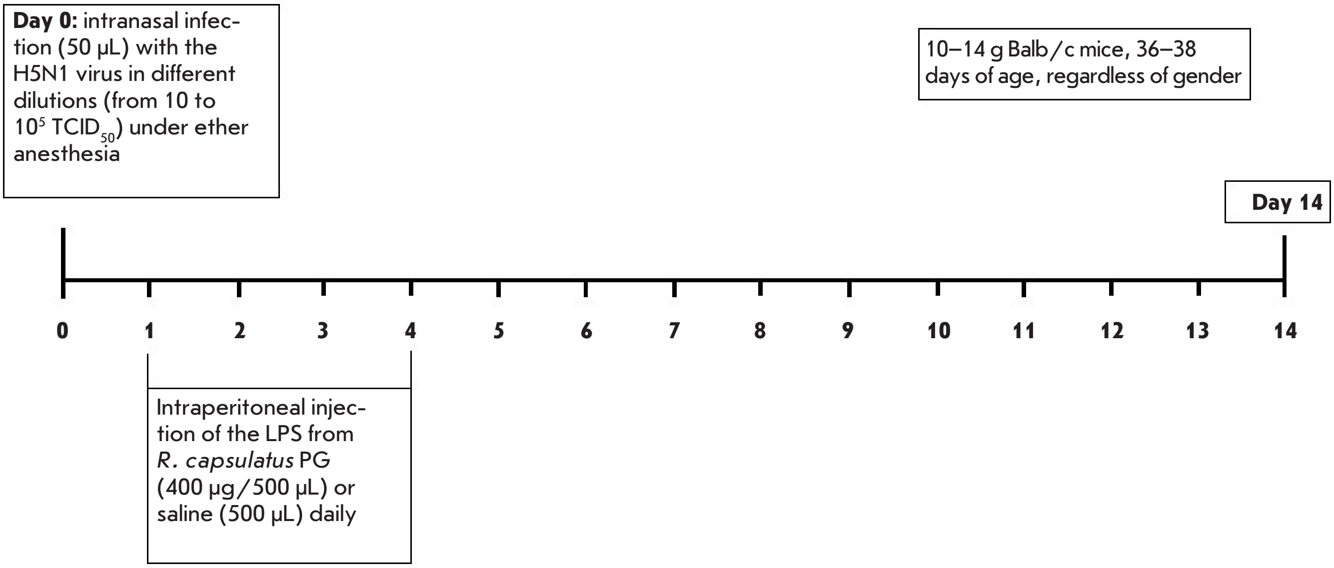

Day 0: intranasal infection (50 µL) with the H5N1 virus in different dilutions (from 10 to 10^5 $TCID_{50}$) under ether anesthesia

10–14 g Balb/c mice, 36–38 days of age, regardless of gender

Day 14

Intraperitoneal injection of the LPS from *R. capsulatus* PG (400 µg/500 µL) or saline (500 µL) daily

Fig. 1. Design of the experiment on the infection of mice with the A/chicken/Kurgan/5/2005 (H5N1) influenza virus strain

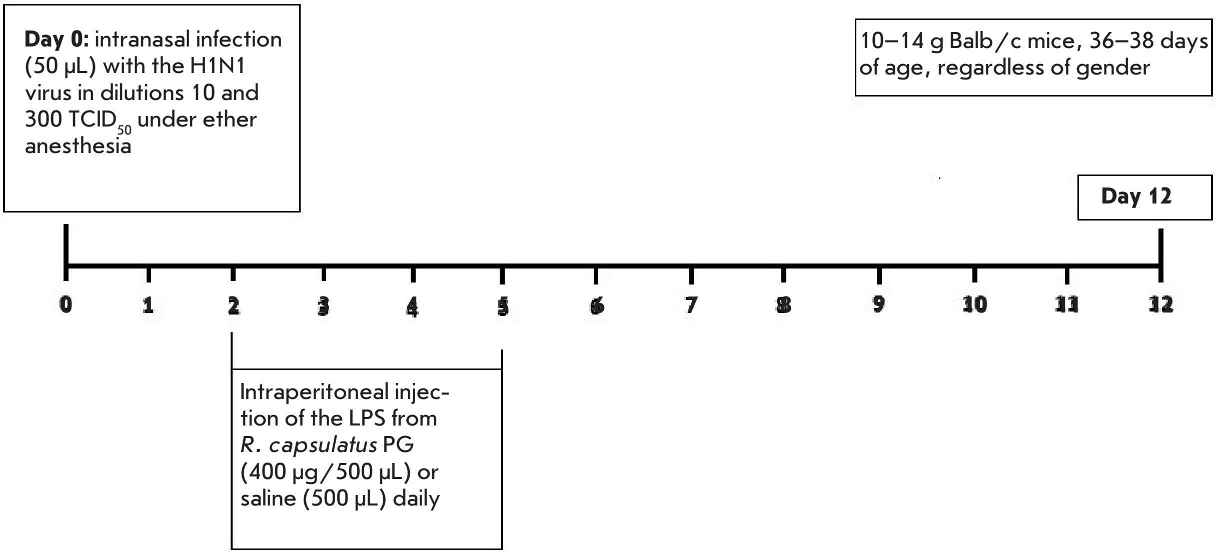

Day 0: intranasal infection (50 µL) with the H1N1 virus in dilutions 10 and 300 $TCID_{50}$ under ether anesthesia

10–14 g Balb/c mice, 36–38 days of age, regardless of gender

Day 12

Intraperitoneal injection of the LPS from *R. capsulatus* PG (400 µg/500 µL) or saline (500 µL) daily

Fig. 2. Design of the experiment on the infection of mice with the A/Hamburg/2009 MA (H1N1) influenza virus strain

Substitutions in the A/Hamburg/2009 virus during adaptation to mice

Viral strain	Viral protein, amino acid sequence						
	NA	HA			NP	PA	PB1
	56–67	158	224	225	289	92	317
Hamburg/2009		G	R	D	H	N	M
Hamburg/2009 MA	Del 56-67	E	K	G	Y	S	V

mouse-adapted H1N1 influenza virus at doses of 10 and 300 $TCID_{50}$ per mouse. The control group included uninfected mice. Two days after infection, all groups were divided in half. One half of the animals was injected intraperitoneally with 500 μL/mouse of saline daily for the following 4 days, and the other half was injected with the *Rb*. LPS at a dose of 400 μg/500 μL/mouse. Mice not injected with any agents were the controls. The experimental design is shown in *Fig. 2*. Five hours after administration of the *Rb*. LPS, blood was sampled in three mice from each group, after euthanasia in a CO_2 chamber, on days 3, 4, and 5. The blood was centrifuged, and the resulting serum was frozen at −20 °C until the cytokine levels were determined by ELISA. Blood was sampled from the animals that had survived by the end of the experiment (day 14), after euthanasia in a CO_2 chamber; blood cells were precipitated, and the resulting serum was frozen at −20 °C until the serum levels of the H1N1 influenza virus IgG1 and IgG2a antibodies were determined by ELISA.

Determining Cytokine Levels

Levels of TNF-α, IL-6, IL-10, IFN-γ, and IFN-β cytokines in the blood serum of mice infected with the H1N1 influenza virus were determined using ELISA kits according to the manufacturer's recommended procedure. The optical density of the samples was measured using a STAT FAX 3200 immunoassay analyzer (Awareness, USA) at a wavelength of 450 nm.

Determining influenza virus antibody levels

To determine the levels of antibodies to hemagglutinin (HA) of the H5N1 and H1N1 influenza viruses in the serum of the mice, allantoic fluid containing 64 HA units of one of the viruses was added to a plate sensitized with fetuin, kept at 40°C overnight, washed with phosphate-buffered saline (PBS) pH 7.4 with 0.1% Tween-20, and blocked with buffer A (0.1% Tween-20, 0.2% BSA in PBS) for 1 h. To determine the IgG1 and IgG2a antibodies, each serum sample was titrated on two different plates. The blocking solution was removed, and wells were added with 100 μL of the serum from H5N1-infected mice at 1 : 40 to 1 : 2,560 dilutions or from H1N1-infected mice at 1 : 50 to 1 : 3,200 dilutions in buffer A. Plates were incubated at 40°C for 4 h, washed with PBS, added with horseradish peroxidase-labeled rabbit antibodies against mouse immunoglobulins (Sigma, USA) or against mouse IgG1 or IgG2a, and incubated at 40°C for 2 h. Then, the plates were washed with PBS and stained with ortho-phenylenediamine. The optical density of the samples was measured using an AIFR-01 Uniplan immunoassay analyzer (Picon, Russia) at a wavelength of 492 nm. Control wells without viral particles were used to exclude nonspecific binding. The antibody level in the samples was expressed as serum dilution enabling a signal exceeding twice the background value.

Statistical analysis

Microsoft Office Excel 2010 (AtteStat plugin) and OriginPro 7.5 were used for statistical analysis and graphical presentation of our data. Statistically significant differences between the results were evaluated using a nonparametric Mann–Whitney U-test. Differences were considered significant at a significance level $p < 0.05$.

RESULTS AND DISCUSSION

The condition of the experimental animals was evaluated based on survival and body weight changes. The administration of the *Rb*. LPS into the control mice, as well as infection with a minimum dose of 10 $TCID_{50}$ of the H5N1 virus, regardless of *Rb*. LPS administration, did not affect the survival rates of the animals up to the end of the experiment (day 14) (*Fig. 3*). Deaths of animals in the groups infected with doses of $10^2/10^3$ and $10^4/10^5 TCID_{50}$ of the H5N1 virus began on days 8 and 6 after infection, respectively. All mice that had received 10^3, 10^4, and 10^5 $TCID_{50}$ of the influenza virus died by day 10 after the infection, regardless of *Rb*. LPS administration. Additional administration of the *Rb*. LPS to mice infected with the influenza virus at a dose of 10^2 $TCID_{50}$ increased their mortality (*Fig. 3*). The curves of weight changes revealed that introduction of the *Rb*. LPS into healthy animals did not affect their condition and weight (*Fig. 4*). Mice infected with $10–10^2$ $TCID_{50}$ of the virus continued to gain weight throughout the experiment. Infection with doses of $10^3–10^5$ $TCID_{50}$ significantly affected the condition of the animals, causing significant inflammation and rapid weight loss. Additional administration of the *Rb*. LPS to infected animals led to even greater weight loss (*Fig. 4*).

The administration of the *Rb*. LPS to the control mice and infection with a dose of 10 $TCID_{50}$ of the H1N1 influenza virus, followed by the administration of the *Rb*. LPS, did not affect the survival rate of the animals until the end of the experiment (day 12). In the group of mice infected with the influenza virus at a dose of 300 $TCID_{50}$, 14% of the mice survived until the end of the experiment; additional administration of the *Rb*. LPS increased mortality in mice (*Fig. 5*). An analysis of weight change curves showed that the administration of the *Rb*. LPS to healthy mice did not affect the condition and weight of the control animals. Mice infected with 10 $TCID_{50}$ of the H1N1 virus showed no signs of disease and began rapidly gaining weight on the 3rd day after infection, until the end of the experiment (day 12). Additional administration of the *Rb*. LPS to

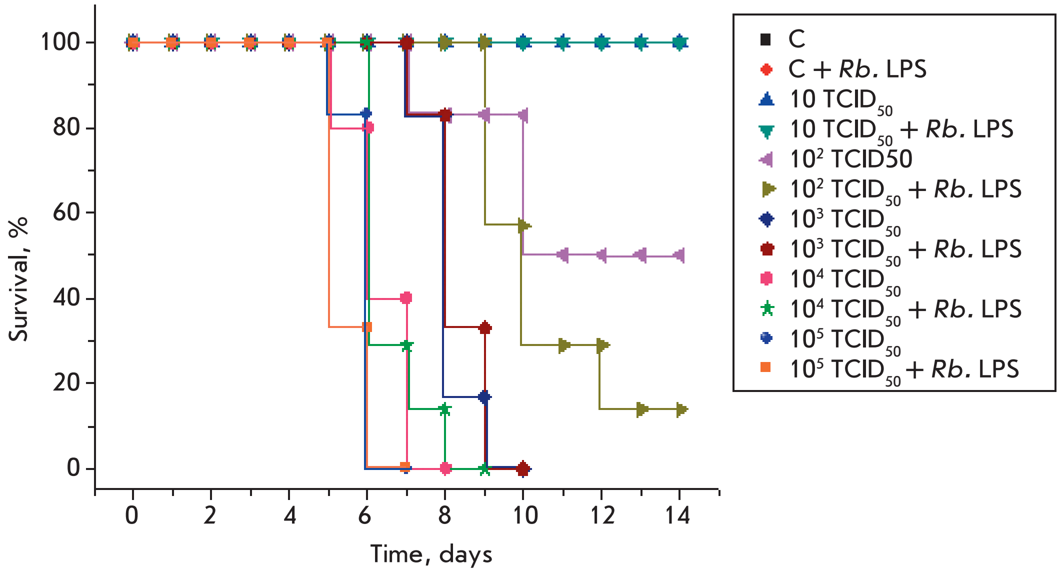

Fig. 3. Survival of mice in response to the administration of the *Rb.* LPS, A/chicken/Kurgan/5/2005 (H5N1) influenza virus, and both factors simultaneously

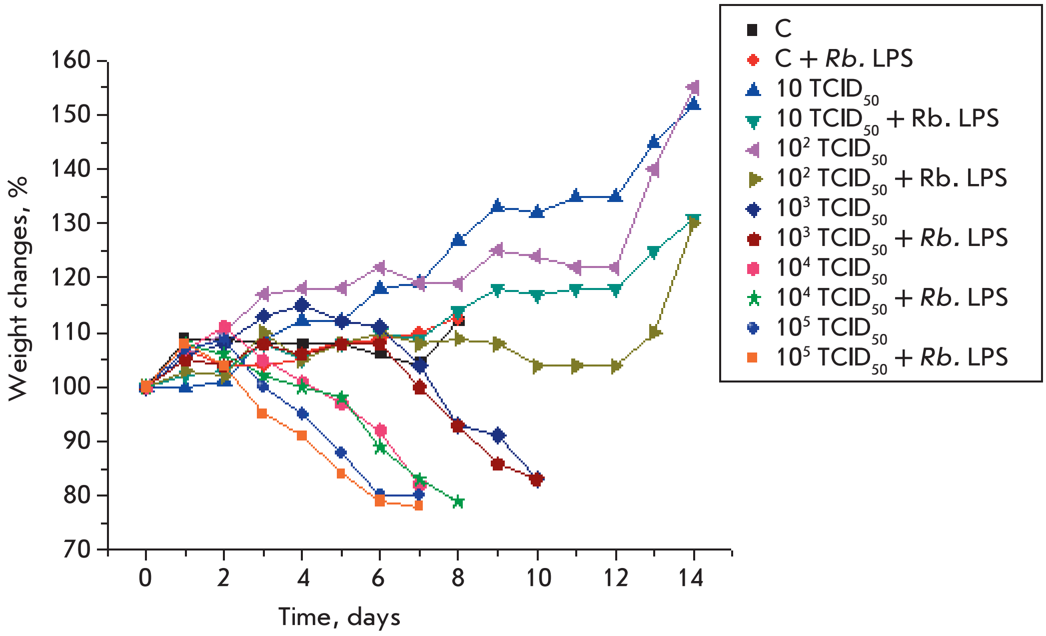

Fig. 4. Weight changes in mice in response to the administration of the *Rb.* LPS, A/chicken/Kurgan/5/2005 (H5N1) influenza virus, and both factors simultaneously

the animals infected with the virus at this dose led to a decrease in the animals' weight after day 7 of the experiment. Virus infection (300 $TCID_{50}$) markedly affected the condition of the mice, causing significant inflammation and weight loss. The administration of the *Rb.* LPS to infected mice worsened the condition of the animals and led to additional weight loss (*Fig. 6*).

Survival and weight changes in the animals infected with the H5N1 or H1N1 influenza virus revealed the absence of a protective effect on the part of the *Rb.* LPS on mice against a lethal infection (*Fig. 3–6*). Daily (for 5 days) intravenous administration of Eritoran starting 2 days after infection was shown to protect mice from the A/PR/8/34 (H1N1) influenza virus. Protection from DAMPs released from influenza infected and destroyed cells that occurred through the TLR4-dependent mechanism [18]. The virus type determines the response mechanisms of innate immunity to infection. The signaling pathways in an infection caused by different H5N1 and H1N1 virus strains differ and determine the survival rate and pathology of the inflammation [7]. Obviously, the infection in our experiments

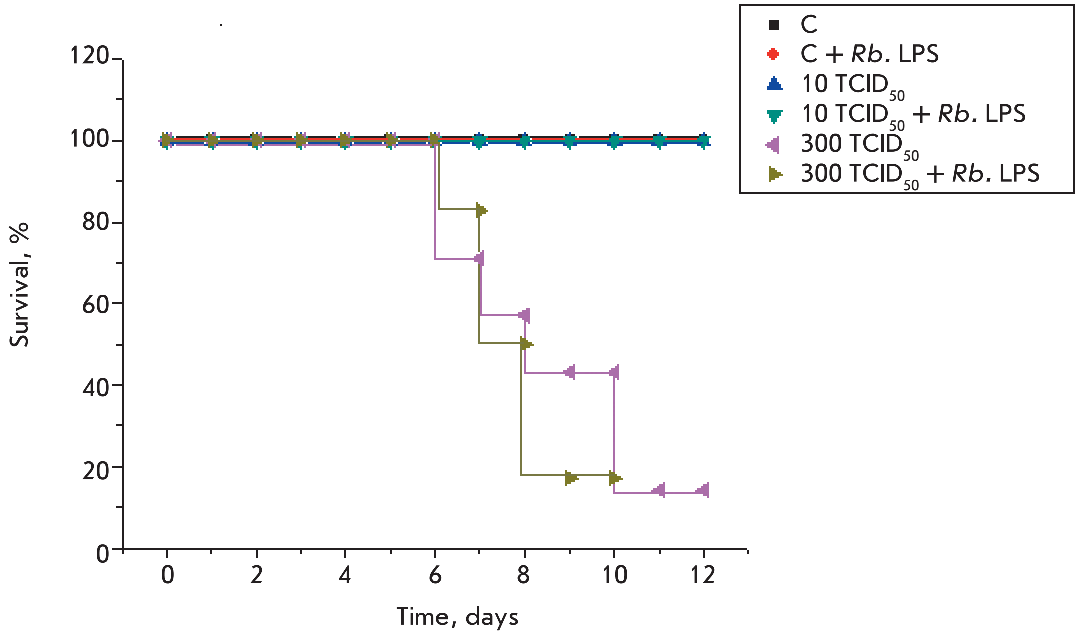

Fig. 5. Survival of mice in response to the administration of the *Rb.* LPS, A/Hamburg/2009 MA (H1N1) influenza virus, and both factors simultaneously

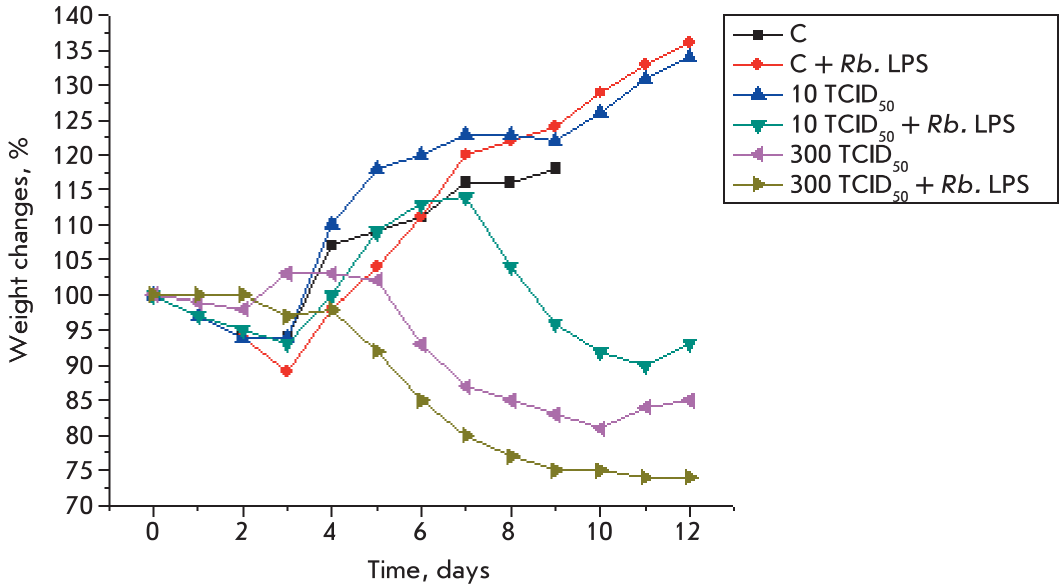

Fig. 6. Weight changes in mice in response to the administration of the *Rb.* LPS, A/Hamburg/2009 MA (H1N1) influenza virus, and both factors simultaneously

develops through molecular mechanisms other than cell activation through the TLR4 pathway. Probably, the administration regiment and *Rb.* LPS concentration used in our experiments were ineffective in protecting against these viral strains.

Signs of viral infection include an increased induction of pro-inflammatory cytokines and chemokines, such as TNF-α, IL-1, IL-6, IL-8 [19], as well as IFN-β and IFN-γ, which have antiviral effects [20, 21].

The administration of the *Rb.* LPS to mice caused a 1.5-fold increase in the TNF-α level in blood serum compared to that in the control mice by day 3, which remained at about the same level until day 5 of the experiment. It should be noted that the serum TNF-α level in the control mice was quite high (74.7 ± 8.7 pg/mL), indicating a sensitized state of the animals. Production of TNF-α in the blood of the influenza-infected mice depended on the virus dose and showed positive dynamics during the experiment. The administration of the *Rb.* LPS to infected mice enhanced TNF-α production in their blood (*Fig. 7A*).

The dynamics of IL-6 synthesis in all experiment variants was similar. The IL-6 level increased significantly (1000- to 2000-fold) by day 4 of the experiment.

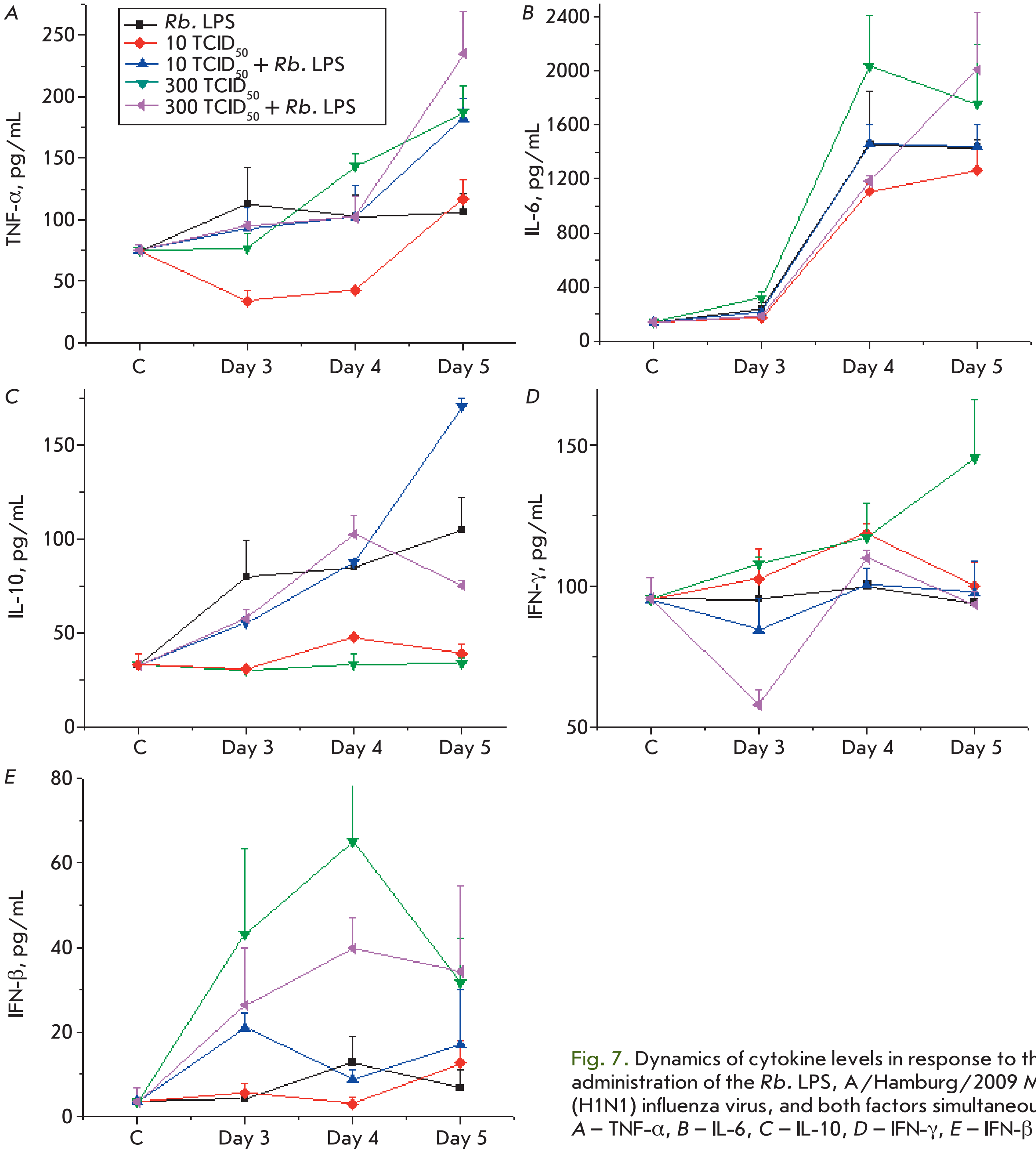

Fig. 7. Dynamics of cytokine levels in response to the administration of the *Rb.* LPS, A/Hamburg/2009 MA (H1N1) influenza virus, and both factors simultaneously. *A* – TNF-α, *B* – IL-6, *C* – IL-10, *D* – IFN-γ, *E* – IFN-β

IL-6 production in the infected mice depended on the virus dose. The IL-6 level in response to the introduction of the *Rb.* LPS was comparable to that in the influenza-infected mice. The administration of the *Rb.* LPS to infected mice slightly increased IL-6 production by day 5 of the experiment (*Fig. 7B*).

These findings demonstrate that a viral infection causes a dose-dependent induction of the synthesis of the pro-inflammatory cytokines TNF-α and IL-6, with the induction increasing with time. These cytokines are produced mainly by monocytes and macrophages in response to both bacteria and viruses, using independent

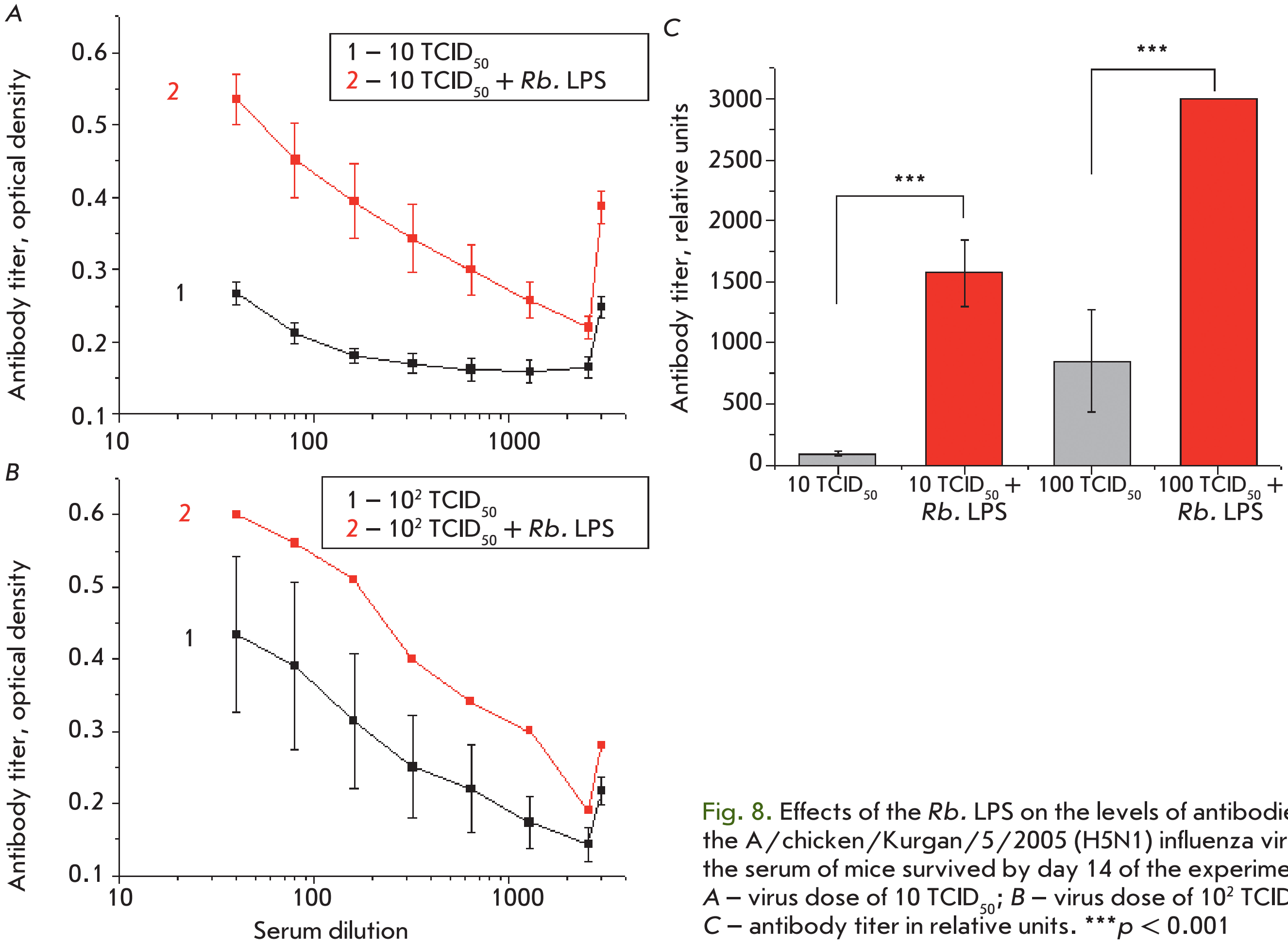

Fig. 8. Effects of the *Rb.* LPS on the levels of antibodies to the A/chicken/Kurgan/5/2005 (H5N1) influenza virus in the serum of mice survived by day 14 of the experiment. *A* – virus dose of 10 $TCID_{50}$; *B* – virus dose of 10^2 $TCID_{50}$; *C* – antibody titer in relative units. $^{***}p < 0.001$

signaling pathways involving different surface and intracellular receptors but the same adapter proteins and transcription factors. The data on the induction of TNF-α and IL-6 synthesis show that the administration of the *Rb.* LPS to influenza-infected mice enhanced the pro-inflammatory response of their immune cells (*Fig. 7A, B*). This worsened the condition of the animals, as evidenced by the data on the survival rate and weight changes (*Fig. 5, 6*).

The administration of the *Rb.* LPS into mice caused an increase in the anti-inflammatory IL-10 cytokine level that exceeded the baseline level 3-fold by day 5. The influenza virus, regardless of the dose, had no effect on the production of the anti-inflammatory IL-10 cytokine. The administration of the *Rb.* LPS into infected mice, regardless of the virus dose, had almost no bearing on the induction of IL-10 synthesis compared to the administration of the *Rb.* LPS alone (*Fig. 7C*). The immunoregulatory cytokine IL-10 is a key component of the system that regulates excessive immune responses by suppressing the expression of pro-inflammatory cytokines such as TNF-α, IL-6, and IL-1 [22, 23]. Levels of IL-10 production in response to LPS are significantly higher than those in a viral infection [24, 25]. The obtained results indicate an increase in the IL-10 level in response to the administration of the *Rb.* LPS into both healthy and influenza-infected mice. This may indicate that the *Rb.* LPS promotes enhanced anti-inflammatory responses by cells (*Fig. 7C*).

These findings indicate a lack of IFN-γ production in response to the administration of the *Rb.* LPS to mice. The influenza virus increases the blood IFN-γ level in mice in a dose-dependent manner. Furthermore, additional administration of the *Rb.* LPS to mice infected with the H1N1 influenza virus reduced IFN-γ production in their blood (*Fig. 7D*).

Having no effect on the production of IFN-γ, the *Rb.* LPS caused a 4-fold increase in the IFN-β production compared to the control level by day 4 of the experiment. On day 5, the IFN-β level had decreased to its

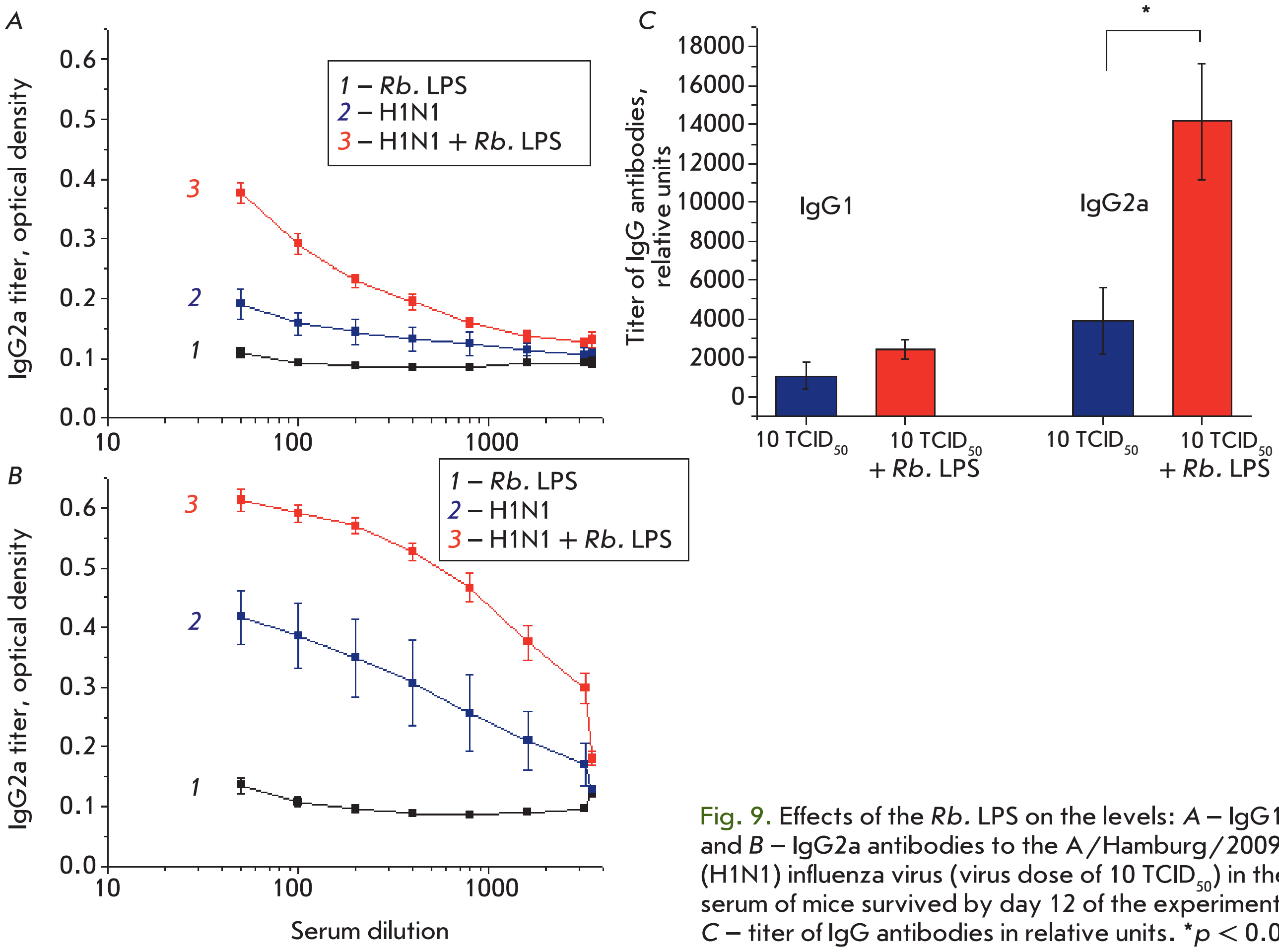

Fig. 9. Effects of the *Rb.* LPS on the levels: *A* – IgG1 and *B* – IgG2a antibodies to the A/Hamburg/2009 MA (H1N1) influenza virus (virus dose of 10 $TCID_{50}$) in the serum of mice survived by day 12 of the experiment. *C* – titer of IgG antibodies in relative units. $*p < 0.05$

baseline value. In response to a H1N1 virus infection at a dose of 10 $TCID_{50}$, the IFN-β level increased 3-fold by day 5 of the experiment. The influenza virus at a dose of 300 $TCID_{50}$ significantly increased the induction of IFN-β (16-fold), compared to the baseline value by day 4. The administration of the *Rb.* LPS to mice infected with 10 $TCID_{50}$ and 300 $TCID_{50}$ of the influenza virus enhanced or decreased, respectively, the cytokine level, compared to that in mice infected with the influenza virus alone (*Fig. 7E*).

These results demonstrated that the levels of IFN-γ and IFN-β synthesized in response to the used *Rb.* LPS administration schedule were insufficient for an effective antiviral protection against the virus strains under study.

IFN-β, a component of the influenza vaccine, acts as a powerful adjuvant and helps induce the synthesis of IgG2a and IgA, providing protection against infection. Production of IgG2a antibodies, which is characteristic of the response to a viral infection, has a protective and neutralizing effect against influenza viruses. Expression of type I IFN and generation of IgG2a antibodies in a viral infection are interrelated events of biological significance for subsequent protective immunity [26].

The action of existing vaccines against an influenza virus infection is based mainly on the induction of neutralizing antibody synthesis in response to viral HA [27]. Determination of the level of H5N1 virus HA antibodies in mouse serum revealed that the higher the infective virus dose, the higher the titer of serum antibodies in the infected animals. Additional administration of the *Rb.* LPS to H5N1-infected mice resulted in a significant increase in the antibody titer ($p < 0.001$) in blood serum (*Fig. 8*).

Determination of IgG1 and IgG2a antibody levels in response to the H1N1 virus infection showed that IgG2a titers were significantly higher than the IgG1 titers in all the groups of animals. Introduction of the *Rb.* LPS statistically significantly increased the serum IgG2a level compared to influenza-infected mice without additional administration of the *Rb.* LPS ($p < 0.05$) (*Fig. 9*).

The innate immune response is crucial in the fight against viruses and plays a key role in the induction and regulation of adaptive immune responses. For this reason, TLR ligands are considered as potential adjuvants for inclusion in vaccines. Simultaneous delivery of a TLR ligand and an antigen of interest is believed to be more effective than vaccination with a mixture of an adjuvant and an antigen [28, 29].

Our findings demonstrate that the administration of the *Rb*. LPS to mice promotes IFN-β production (*Fig. 7E*) or controls the blood IFN-β level in mice infected with various doses of the influenza virus. IFN-β promotes antibody production by acquired immunity cells [26]. Our findings also demonstrate that additional administration of the *Rb*. LPS leads to the production of antibodies in the blood of animals infected with the influenza A virus (*Fig. 8, 9*).

CONCLUSION

Our study has demonstrated that the nontoxic natural *Rb*. LPS promotes the production of the immunomodulatory cytokine IFN-β both in healthy mice and in animals infected with influenza A/chicken/Kurgan/5/2005 (H5N1) and A/Hamburg/2009 MA (H1N1) strains and also promotes the production of antibodies to the HA of these strains in the blood of infected animals. ●

REFERENCES

1. Pebody R., Warburton F., Ellis J., Andrews N., Potts A., Cottrell S., Johnston J., Reynolds A., Gunson R., Thompson C., et al. // Euro Surveill. 2016. V. 21. № 13. P. 30179.
2. McLean H.Q., Thompson M.G., Sundaram M.E., Kieke B.A., Gaglani M., Murthy K., Piedra P.A., Zimmerman R.K., Nowalk M.P., Raviotta J.M., et al. // J. Infect. Dis. 2015. V. 211. № 10. P. 1529–1540.
3. Finberg R.W., Wang J.P., Kurt-Jones E.A. // Rev. Med. Virol. 2007. V. 17. № 1. P. 35–43.
4. Kawai T., Akira S. // Immunity. 2011. V. 34. № 5. P. 637–650.
5. Yang H., Antoine D.J., Andersson U., Tracey K.J. // J. Leukoc. Biol. 2013. V. 93. № 6. P. 865–873.
6 Sakabe S., Iwatsuki-Horimoto K., Takano R., Nidom C.A., Le M.Q., Nagamura-Inoue T., Horimoto T., Yamashita N., Kawaoka Y. // J. Gen. Virol. 2011. V. 92. № 6. P. 1428–1434.
7. Leung Y.H., Nicholls J.M., Ho C.K., Sia S.F., Mok C.K., Valkenburg S.A., Cheung P., Hui K.P., Chan R.W., Guan Y., et al. // J. Gen. Virol. 2014. V. 95. № 9. P. 1870–1879.
8. Shirey K.A., Lai W., Scott A.J., Lipsky M., Mistry P., Pletneva L.M., Karp C.L., McAlees J., Gioannini T.L., Weiss J., et al. // Nature. 2013. V. 497. № 7450. P. 498–502.
9. Wang H., Bloom O., Zhang M., Vishnubhakat J.M., Ombrellino M., Che J., Frazier A., Yang H., Ivanova S., Borovikova L., et al. // Science. 1999. V. 285. № 5425. P. 248–251.
10. Alleva L.M., Budd A.C., Clark I.A. // J. Immunol. 2008. V. 181. № 2. P. 1454–1459.
11. Liu Q., Zhou Y., Yang Z. // Cell Mol. Immunol. 2016. V. 13. № 1. P. 3–10.
12. Prokhorenko I.R., Grachev S.V., Zubova S.V. Patent for invention RU № 2392309 of 20.06.2010.
13. Kabanov D.S., Serov D.A., Zubova S.V., Grachev S.V., Prokhorenko I.R. // Biochemistry (Moscow). 2016. V. 81. № 3. P. 275–283.
14. Warren H.S., Fitting C., Hoff E., Adib-Conquy M., Beasley-Topliffe L., Tesini B., Liang X., Valentine C., Hellman J., Hayden D., Cavaillon J.M. // J. Infect. Dis. 2010. V. 201. № 2. P. 223–232.
15. Munford R.S. // J. Infect. Dis. 2010. V. 201. № 2. P. 175–177.
16. Makhneva Z.K., Vishnevetskaya T.A., Prokhorenko I.R. // Prikladnaya Biokhimiya i Mikrobiologiya. 1996. V. 32. № 4. P. 444-447.
17. Order of the Ministry of Health of the Russian Federation No. 267 of 19.06.2003 «Rules of Laboratory Practice in the Russian Federation».
18. Shirey K.A., Lai W., Patel M.C., Pletneva L.M., Pang C., Kurt-Jones E., Lipsky M., Roger T., Calandra T., Tracey K.J., et al. // Mucosal. Immunology. 2016. V. 9. № 5. P. 1173–1182.
19. Mogensen T.H., Paludan S.R. // Microbiol. Mol. Biol. Rev. 2001. V. 65. № 1. P. 131–150.
20. Lai C., Wang X., Yang P. // Clin. Microbial. 2014. V. 3. № 3. P. 147–149.
21. Betakova T., Kostrabova A., Lachova V., Turianova L. // Curr. Pharm. Des. 2017. V. 23. № 18. P. 2616–2622.
22. Williams L., Bradley L., Smith A., Foxwell B. // J. Immunol. 2004. V. 172. № 1. P. 567–576.
23. Saraiva M., O'Garra A. // Nat. Rev. Immunol. 2010. V. 10. № 3. P. 170–181.
24. Yu X., Zhang X., Zhao B., Wang J., Zhu Z., Teng Z., Shao J., Shen J., Gao Y., Yuan Z., Wu F. // PloS One. 2011. V. 6. № 12. P. e28680.
25. Blok D.C., van der Sluijs K.F., Florquin S., de Boer O.J., van't Veer C., de Vos A.F., van der Poll T. // PloS One. 2013. V. 8. № 3. P. e58191.
26. Proietti E., Bracci L., Puzelli S., Di Pucchio T., Sestili P., De Vincenzi E., Venditti M., Capone I., Seif I., De Maeyeret E., et al. // J. Immunol. 2002. V. 169. № 1. P. 375–383.
27. Cox R.J. // Hum. Vaccin. Immunother. 2013. V. 9. № 2. P. 405–408.
28. Blander J.M., Medzhitov R. // Science. 2004. V. 304. P. 1014–1018.
29. Blander J.M. // Trends Immunol. 2007. V. 28. № 1. P. 19–25.

The Structural and Immunological Properties of Chimeric Proteins Containing HIV-1 MPER Sites

A. P. Rudometov[1*], N. B. Rudometova[1], D. N. Shcherbakov[1,4], A. A. Lomzov[2,3], O. N. Kaplina[1], N. S. Shcherbakova[1], A. A. Ilyichev[1], A. Yu. Bakulina[1,3], L. I. Karpenko[1]
[1]State Research Center of Virology and Biotechnology "Vector", Koltsovo, Novosibirsk region, 630559, Russia
[2]Institute of Chemical Biology and Fundamental Medicine SB RAS, Ac. Lavrentieva Ave. 8, Novosibirsk, 630090, Russia
[3]Novosibirsk State University, Pirogova Str. 1, Novosibirsk, 630090, Russia
[4]Altai State University, Lenin Ave. 61, Barnaul, 656049, Russia
*E-mail: andrei692@mail.ru

Received May 28, 2019; in final form, August 7, 2019
DOI: 10.32607/20758251-2019-11-3-56-65

Copyright © 2019 National Research University Higher School of Economics. This is an open access article distributed under the Creative Commons Attribution License,which permits unrestricted use, distribution, and reproduction in any medium, provided the original work is properly cited.

ABSTRACT **The human immunodeficiency virus (HIV-1) poses a serious risk to global public health. The development of a safe and effective vaccine could stop the HIV/AIDS pandemic. Much of the research focused on HIV-1 prevention through vaccination is aimed at developing immunogens and immunization strategies to induce the formation of antibodies with neutralizing activity against a broad range of HIV-1 isolates (bNAbs). The objective of this study was to develop immunogens capable of targeting an immune response to MPER, one of the regions of bNAb binding in Env. Two immunogens carrying MPER fragments on their scaffolds (protein YkuJ *Bacillus subtilis* and artificial polypeptide TBI) were constructed. Circular dichroism spectroscopy was used to show that the secondary structure of the immunogens was consistent with their theoretical models. The antigenic structure of the MPER-TBI and YkuJ-MPER proteins was characterized using bNAbs that recognize HIV-1 MPER (2F5, 4E10, and 10E8). The rabbit model made it possible to show the immunogenicity of the constructed recombinant proteins. The resulting serum was found to be cross-reactive with immunogens carrying MPER. The constructs designed and characterized in this study can be used for targeting the humoral immune response to MPER, which is known to be one of the sites of HIV-1 vulnerability.**

KEYWORDS **HIV-1, neutralizing antibody epitopes, recombinant immunogens, bNAbs, MPER.**

ABBREVIATIONS **HIV-1 – human immunodeficiency virus type 1; bNAbs – broadly neutralizing antibodies; BSA – bovine serum albumin; MPER – membrane-proximal external region; mAb – monoclonal antibody; PBS – phosphate buffered saline.**

INTRODUCTION

A safe and effective anti-HIV-1 vaccine is needed to stop the HIV/AIDS pandemic [1, 2]. The discovery of antibodies that exhibit neutralizing activity against a broad range of HIV-1 isolates (broadly neutralizing antibodies, bNAbs) has created hope that such a type of vaccine would be created [3, 4]. It has been found that passive administration of isolated bNAbs or their combination can completely protect animal models against the HIV infection [5, 6]. Although bNAbs appear in the body during the natural course of the HIV infection, inducing the production of these antibodies through vaccination is quite challenging and still needs a solution [7]. There currently are several trends in the development of immunogens capable of inducing the production of bNAbs [4, 8, 9]. One such trends is to insert conserved HIV-1 regions (sites of HIV-1 vulnerability), the targets of broadly neutralizing antibodies, into scaffold proteins [10, 11].

The membrane-proximal external region (MPER) of gp41, which plays a key role in the fusion between the viral and cellular membranes, is one of the sites of HIV-1 vulnerability [12]. There exist a number of bNAbs targeted at this epitope: 2F5, 4E10, Z13, Z13e1, m66.6, CH12, 10E8 and DH511.2 [13, 14].

A series of attempts were previously made to develop immunogens that can induce the production of bNAbs that target MPER [15]. However, only a few of these immunogens proved capable of inducing the production of neutralizing antibodies (characterized by a low effectiveness and limited neutralization breadth) [16, 17]. There can be various reasons for that outcome, including the autoreactivity of anti-MPER antibodies [18], the changes in the conformation of the MPER domain as the virus penetrates the cell [14], and the complexation between the lipid membrane and anti-MPER antibodies [19]. Furthermore, the high hydrophobicity of MPER [20] and the steric hindrance imposed by the gp120 fragment [21] make it weakly immunogenic.

This study aimed at developing and characterizing recombinant immunogens, YkuJ-MPER and MPER-TBI, capable of targeting the immune response at MPER, the site of HIV-1 vulnerability.

EXPERIMENTAL

Monoclonal antibodies, bacterial strains, and enzymes

MAbs 4E10 (No. 10091), 10E8 (No. 12294), and 2F5 (No. 1475) were provided by the NIH AIDS Research and Reference Reagent Program (USA). The *Escherichia coli* BL21(DE3) pLysS strain (Invitrogen) was provided by the Department of Microorganism Collections, State Research Center of Virology and Biotechnology "Vector," Federal Service for the Surveillance of Consumer Rights Protection and Human Welfare (Koltsovo, Russia). The restriction endonucleases XbaI, FauNDI, Sfr274I, EcoRI, Zsp2I, KpnI, and T4 DNA ligase were purchased from SibEnzyme (Novosibirsk, Russia).

Constructing the gene encoding the chimeric protein YkuJ-MPER

In order to choose a scaffold protein for YkuJ, we searched through the Structural Classification of Proteins (SCOP) database. The amino acid sequence homology between YkuJ and human proteins was analyzed using the UniProt database and the BLAST software in order to estimate the likelihood of an autoimmune response. When designing the chimeric protein YkuJ-MPER, the N- and C-termini of the selected scaffold protein were substituted for HIV-1 MPER fragments.

The gene encoding the chimeric protein YkuJ–MPER was synthesized by Evrogen (Moscow, Russia) and cloned into the pET21a plasmid vector (Novagen) at the restriction sites FauNDI and Sfr274I.

Constructing the gene encoding MPER-TBI polypeptide

MPER-TBI immunogen was constructed by substituting the C- and N-terminal domains of TBI_tag polypeptide [22] for the fragments corresponding to MPER in YkuJ-MPER. The resulting oligonucleotide duplexes encoding the ELLELDKWASLANWFIITN-LLWLIK and IALLLDAWASLWNWFDITNWLWYI sequences and carrying adhesive terminal domains similar to those formed as a plasmid vector is treated with the restriction endonucleases EcoRI and Zsp2I, or KpnI and Sfr274I, respectively, were synthesized by Evrogen (Moscow, Russia). The oligonucleotide duplexes were cloned at unique sites into pET-TBI_tag recombinant plasmid encoding TBI_tag polypeptide. The first oligonucleotide duplex was cloned at the EcoRI and Zsp2I sites; the env (255–266) fragment within TBI_tag was substituted. The second oligonucleotide duplex was cloned at the KpnI and Sfr274I sites; the fragments gag (351–361), gag (211–305), and gag (99–109) of TBI_tag polypeptide were substituted. Hence, the recombinant plasmid pET-MPER-TBI was obtained. The structures of the target plasmids pET-YkuJ-MPER and pET-MPER-TBI were confirmed by sequencing at the Genomics Core Facility, Siberian Branch of Russian Academy of Sciences (Novosibirsk, Russia).

Building models of interaction between YkuJ-MPER and the Fab fragments of the 10E8, 2F5, and 4E10 antibodies

The models were built using the Modeller and PyMOL software. The PyMOL software was used to combine the structure of YkuJ from PDB (2FFG) and the structure of MPER fragments from the MPER complexes with Fab fragments of the antibodies 2F5 (2PR4), 4E10 (2FX8) or 10E8 (4G6F). The result of this combination was employed as a template for homology modeling in the Modeller software. Next, the respective structures of the MPER complexes with Fab fragments of the antibodies were superposed onto the resulting models in the PyMOL software in order to test whether YkuJ-MPER could bind to monoclonal antibodies.

Production and purification of the recombinant proteins YkuJ-MPER and MPER-TBI

Bacterial strains producing the proteins YkuJ-MPER and MPER-TBI were obtained by transformation of BL21 competent *E. coli* cells with the pET-YkuJ-MPER and pET-MPER-TBI plasmids and then cultured according to the procedure described in [22]. Chimeric proteins were purified by metal-chelate affinity chromatography on a Ni-NTA column (Qiagen, Germany) according to the manufacturer's protocol. Refolding of the purified proteins was carried out by dialysis against PBS (four buffer changes with decreasing urea concentration (6, 4, 2, 1 M)); the final dialysis stage was conducted against normal saline. The purification degree of the target protein was assessed by PAGE (15%), followed by fixation and staining with Coomassie G-250. Quantitative assay of the protein content was performed by spectrophotometric measurements of the concentration at 280 nm (NanoDrop-2000, Thermo Fisher Scientific).

Predicting the secondary structure of MPER-TBI

The secondary structure of immunogen MPER-TBI was predicted using the PSSfinder algorithm (GeneSilico Metaserver) [23].

Circular dichroism spectroscopy

The circular dichroism (CD) spectra of the proteins YkuJ-MPER and MPER-TBI were recorded in normal saline at 25°C using a thermostated 1-mm cuvette on a J-600 spectropolarimeter (JASCO, Japan). All the spectra were measured at a wavelength range of 195–260 nm, with a step of 1 nm, and they were averaged after three measurements. Sample concentrations in normal saline were normalized to the same optical density at $\lambda = 214$ nm.

In order to determine the percentages of α-helices, β-sheets, turns, and the disordered structures, we minimized the difference between the theoretical and experimental curves. The theoretical curves were calculated as a linear combination of the basis spectra of various components of the secondary structures taken from the CCA+ software [24].

Dot blot assay

Dot blot assay was conducted using the SNAP i.d. system (Millipore, USA) according to the previously described procedure [22]. The proteins YkuJ-MPER and MPER-TBI, obtained as a series of two-fold dilutions (2 μl each; initial concentration, 0.2 mg/ml), were applied onto a nitrocellulose membrane (Amersham, Austria). MAbs 4E10, 10E8, and 2F5 (1 : 10,000 dilution in PBS, 1% BSA) were used as primary antibodies. Rabbit anti-human IgG secondary antibodies (Sigma, USA) conjugated to alkaline phosphatase (1 : 5,000 dilution in PBS, 1% BSA) were used as secondary antibodies. The immune complex was visualized by adding the NBT/BCIP stock solution (Sigma, USA).

Collecting and analyzing serum samples from the animals immunized with the proteins YkuJ-MPER and MPER-TBI

Four-month-old female chinchilla rabbits (weight, 1.6–2 kg) were used in the experiments. The animals were housed in individual cages (vivarium of the State Research Center of Virology and Biotechnology "Vector," Federal Service for Surveillance of Consumer Rights Protection and Human Welfare), were fed a standard diet, and had unrestricted access to food and water. The experiments were approved at a meeting of the Bioethics Committee of the State Research Center of Virology and Biotechnology "Vector" (protocol No. 3 dated April 25, 2018) and conducted in compliance with the ethical principles laid out in EU directives (86/609/EEC) and the Declaration of Helsinki.

The animals were randomly assigned into two groups (three rabbits per group). Each animal received four injections of protein products on days 1, 14, 28, and 42. At the first immunization, the rabbits were subcutaneously injected with 500 μg of YkuJ-MPER or MPER-TBI supplemented with complete Freund's adjuvant. At the second immunization, the animals received 500 μg of the sample supplemented with complete Freund's adjuvant; at the following immunizations, they received 800 μg of the sample without the adjuvant. Blood samples were collected prior to each immunization and 2 weeks after the last immunization and used to isolate serum samples.

Enzyme-linked immunosorbent assay

The specific activities of the serum samples from the rabbits immunized with the proteins YkuJ-MPER and MPER-TBI were assessed by ELISA according to the procedure described in [22]. The proteins YkuJ-MPER and MPER-TBI (5 μg/ml) were sorbed onto the wells of a 96-well plate (Greiner Bio-One, Germany). Serum samples were added in a series of five-fold dilutions. Horseradish peroxidase-conjugated goat anti-rabbit IgG secondary antibodies (Sigma, USA) (1 : 10,000 dilution in PBS) were then added. The plate was washed, and a TMB substrate solution (Amresco, USA) was added. The optical density at 450 nm was measured on an ELISA reader (Model 680 Microplate reader, Bio-Rad, USA). All the experiments were conducted in three replicates. When determining the serum titer, the maximum dilution was the one with an optical density (OD) twofold higher than the OD value of the negative control (at the same dilution). The diagrams were plotted using the GraphPad Prism 6.0 software.

Analyzing the serum samples to detect antibodies specific to HIV-1 proteins

The analysis was conducted using a New Lav Blot I test kit (Bio-Rad, France), in compliance with the manufacturer's protocol. Goat anti-rabbit IgG secondary antibodies (1 : 5,000 dilution in PBS) conjugated to alkaline phosphatase (Sigma, USA) were used as a conjugate for the rabbit serum samples. The immune complexes were visualized by adding a NBT/BCIP stock solution (Sigma, USA).

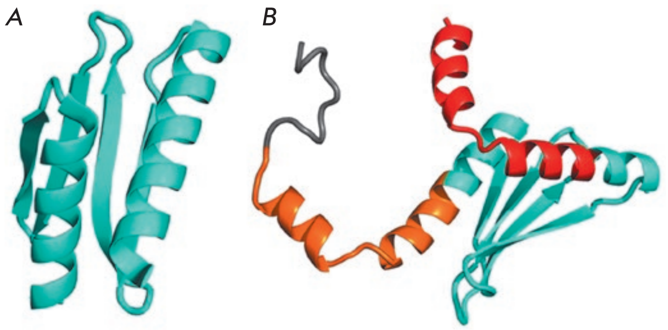

Fig. 1. *A* – The structure of the protein YkuJ, PDB ID 2FFG; *B* – the model of the chimeric protein YkuJ-MPER. For illustrative purposes, the frame of the original protein is shown in cyan; the MPER regions inserted at the N- and C-termini are shown in red and brown, respectively; the histidine tag is shown in gray

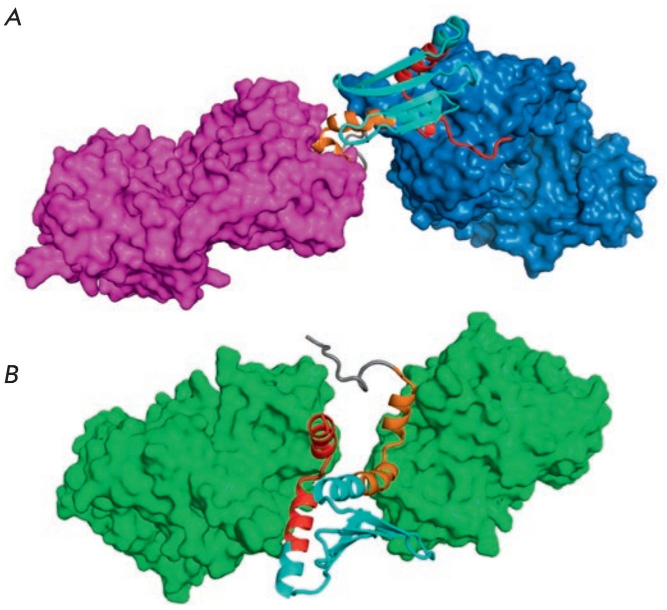

Fig. 2. The model of the interactions of YkuJ with the Fab fragments of mAbs 2F5 and 4E10 (*A*) and with 10E8 (*B*). *A* – The Fab fragments of antibody 2F5 are shown in purple; the Fab fragments of antibody 4E10 are shown in blue; *B* – The Fab fragments of antibody 10E8 are shown in green. The models were built using the PyMOL software

RESULTS

Designing proteins carrying HIV-1 MPER

Two scaffold proteins varying in their spatial structures were used to ensure MPER presentation to the immune system. The scaffolds are supposed to ensure the conformational mobility of MPER, be nontoxic, soluble and small-sized, and not elicit an autoimmune response.

Having searched through the Structural Classification of Proteins (SCOP) database, we chose the scaffold protein YkuJ from *Bacillus subtilis* (*Fig. 1A*). The core of this protein consists of antiparallel β-strands that form a rigid scaffold. The terminal regions are helical, corresponding to the conformation of epitopes in mAbs 4E10 and 10E8. It is reasonable to expect the protein YkuJ to be safe, since *B. subtilis* is pathogenic for neither animals nor humans. In order to eliminate the possible autoimmune responses to YkuJ, we searched for its homologues in the human protein database using the BLAST software. No significant matches between the amino acid sequence of this protein and those of the human proteins were revealed; therefore, it is unlikely that the protein YkuJ will induce an autoimmune response.

When designing the chimeric protein YkuJ-MPER, the N- and C-termini of the scaffold protein were substituted for fragments of the consensus sequence of subtype B HIV-1 MPER; the numbering corresponds to the HXB2 strain: $_{659}$ELLELDKWASLWNWFDITNWLWYIK$_{683}$. Meanwhile, when YkuJ residues that are crucial for maintaining the spatial structure of the scaffold protein overlapped with the sequence being inserted, they were left intact. The core of the scaffold protein was also left unaltered so that the original structure of YkuJ was preserved to the maximum possible extent. The YkuJ-MPER structure contains all the amino acid residues of MPER that are critical in binding bNAbs 10E8, 4E10, and 2F5. Six histidine residues were added to the C-terminus to enable purification of the recombinant protein by metal-chelate affinity chromatography. The size of the final construct, YkuJ-MPER, is 119 amino acid residues; its molecular weight is 14.2 kDa (*Fig. 1B*). The amino acid sequence of YkuJ-MPER (the fragments belonging to MPER are shown in bold and underlined): M**ELLELDKWASL**A**NWF**I**ITN**L**LW**L**IK**TAEAANEPMQRYFEVNGEKICSVKYFEKNQTFELTVFQKGEKPNTYPFDNIDMVSIEIA**LL**L**LD**A**WASLWNWFDITNWLWYI**HHHHHH.

Molecular modeling revealed that the MPER domains at the ends of the chimeric protein YkuJ-MPER could acquire the conformations that are typical of the epitopes of the known monoclonal antibodies targeting this region: 2F5 and Z13 (conformation without a regular secondary structure), 4E10 and 10E8 (the α-helical conformation); two antibodies can simultaneously bind to two domains of the molecule (*Fig. 2*). The molecular modeling of the spatial structure of the chimeric protein also demonstrated that the 6 × His-tag does not impede binding between antibodies and YkuJ-MPER (*Fig. 2*).

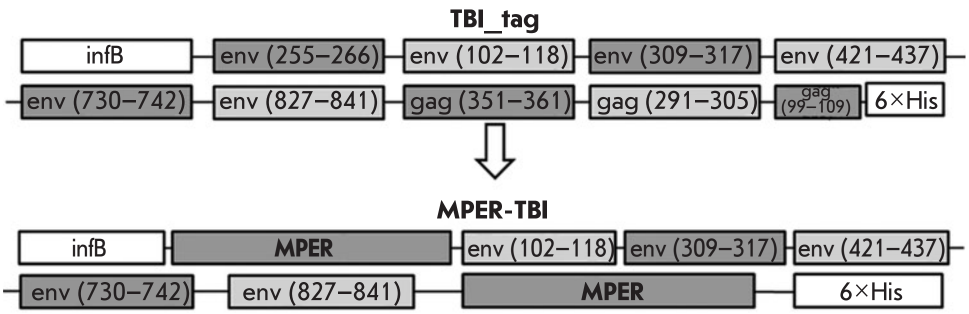

Fig. 3. A schematic presentation of the structure of the immunogens TBI_tag and MPER-TBI. B-cell epitopes are shown on a dark background; Th-epitopes are shown on a light background. InfB is a fragment of the *E. coli* transcription activator protein, InfB; 6 × His – six histidine amino acid residues; MPER – parts of the membrane-proximal external region of HIV-1

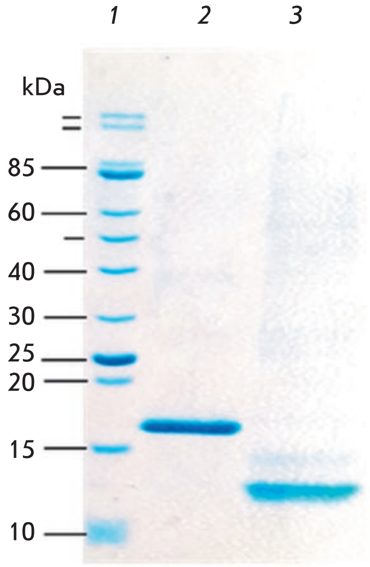

Fig. 4. Electrophoregram of the proteins MPER-TBI (*2*) and YkuJ-MPER (*3*); *1* – molecular weight marker

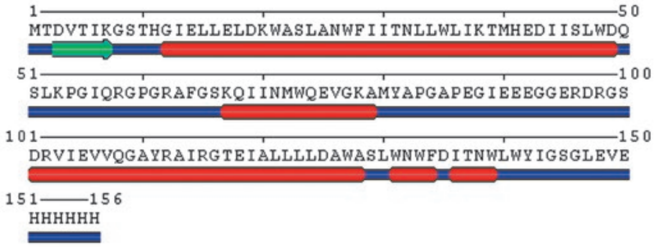

Fig. 5. Amino acid sequence and the secondary structure of the MPER-TBI protein. The unordered areas are shown in blue; the α-helices are shown in red; and β-sheets are shown in green. The PSSfinder prediction method was used

When designing the gene encoding YkuJ-MPER, the unique restriction sites (FauNDI, Bpu14I, Bsa29I, and Sfr274I) flanking the MPER domains were added to the nucleotide sequence so that this protein could be used as a platform to construct immunogens carrying other antigenic determinants of HIV-1 or other infectious agents. The synthesized *YkuJ-MPER* gene was cloned into the plasmid vector pET21a.

The optimized variant of polypeptide TBI, TBI_tag [22], was used as the second scaffold. As a component of the CombiHIVvac candidate vaccine, TBI has passed phase I clinical trials and proved immunogenic and safe [25]. The difference between TBI_tag and TBI was that the codon composition in the original polypeptide was optimized to ensure its efficient expression in *E. coli*. In addition, the fragment encoding 20 amino acid residues of the RecA protein from *Proteus mirabilis* was substituted for the sequence encoding a fragment (7 amino acids) of the *E. coli* transcription activator protein InfB. In this study, the terminal fragments of TBI_tag were substituted for HIV-1 MPER domains similar to those included in YkuJ-MPER. The designed polypeptide was named MPER-TBI (156 amino acid residues, 17.8 kDa). *Figure 3* shows the block diagrams of the proteins TBI_tag and MPER-TBI.

The gene encoding polypeptide MPER-TBI was cloned into the plasmid vector pET21a in the reading frame with a sequence encoding six His residues.

Synthesis and analysis of the properties of the recombinant proteins YkuJ-MPER and MPER-TBI

The proteins YkuJ-MPER and MPER-TBI were synthesized and purified by metal-chelate affinity chromatography. The degree of protein purity was assessed by PAGE (15%) (*Fig. 4*). Additional purification and refolding of the proteins was carried out by dialysis against buffers with a decreasing urea concentration. The degree of protein purity in the final protein products was ≥ 90%.

Predicting the secondary structure of MPER-TBI

The secondary structure of the protein MPER-TBI predicted using the PSSfinder software and its amino acid sequence are shown in *Fig. 5*. According to the predictions, MPER-TBI has a predominantly α-helical structure; the percentage of α-helices is 56%.

Circular dichroism spectroscopy of YkuJ-MPER and MPER-TBI

The fraction of secondary structure elements of the antigens YkuJ-MPER and MPER-TBI were determined experimentally by circular dichroism spectroscopy. The percentages of secondary structural elements of the immunogens according to the CD spectra measured in normal saline are listed in *Table*.

According to the model shown in *Fig. 1B*, the ratio between the secondary structural elements in YkuJ-MPER with terminal regions corresponding to the epitopes of 10E8 is as follows: 45% of α-helices and 24% of β-strands. The findings obtained by circular dichroism spectroscopy were consistent with this model in terms of the percentage of β-strands, while the experimentally determined percentage of α-helices was lower.

The predicted model of the secondary structure of MPER-TBI (*Fig. 5*) showing that the percentage of α-helices is 56% slightly differs from the CD data, since MPER-TBI contains 68% of α-helices and no β-strands, according to these findings.

Dot blot assay of the proteins

Dot blot assay with mAbs 10E8, 4E10, and 2F5 was conducted to analyze the antigenic properties of the epitopes of bNAbs 4E10, 10E8, and 2F5 within MPER in the proteins YkuJ-MPER and MPER-TBI (*Fig. 6*). The protein TBI_tag containing no epitopes of these antibodies was used as a control. It was confirmed that mAbs 10E8, 4E10, and 2F5 interact with the proteins YkuJ-MPER and MPER-TBI, but they do not interact with the control.

Immunogenicity analysis of the proteins

Immunogenicity analysis was conducted on rabbits. Two groups of the animals were immunized with purified products based on the protein YkuJ-MPER or MPER-TBI (see the EXPERIMENTAL section). The specific activities of the serum samples were studied by ELISA by comparing the values to the control samples (serum collected from the rabbits prior to immunization). It was shown that the blood serum samples in both groups of immunized animals contained antibodies specific to the immunogens under study. After the fourth immunization, antibody titers in the serum samples of the rabbits immunized with MPER-TBI and YkuJ-MPER were 1 : 1,000,000 and 1 : 3,000,000, respectively (*Fig. 7*). In both groups, the titers increased from the first to the third immunization. The ELISA signal from the preimmune serum samples was comparable to the background level.

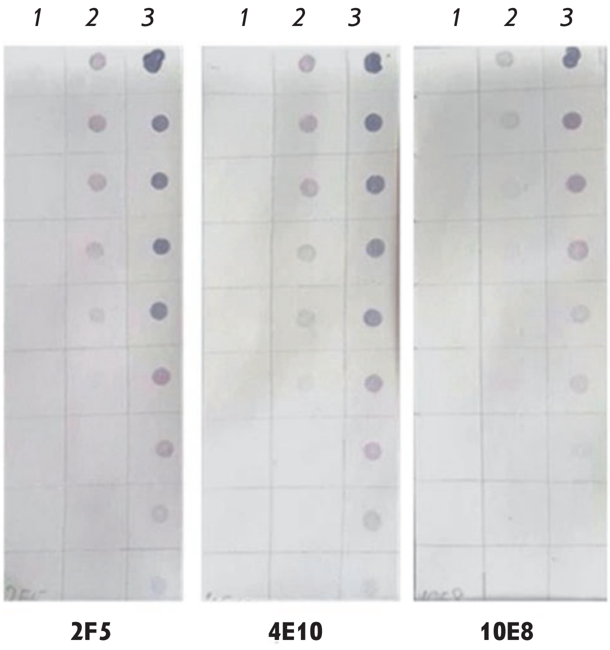

Fig. 6. Dot blot assay: *1* – TBI_tag (control); *2* – MPER-TBI; *3* –YkuJ-MPER; 2F5, 4E10 and 10E8 – mAbs. Two-fold dilutions of the corresponding proteins are applied from top to bottom

Analysis of the cross-immunogenicity of the proteins

The ability of the serum samples to bind to the "foreign" antigen (in other words, whether serum samples

Secondary structural elements of the proteins YkuJ-MPER and MPER-TBI

Structure	Sample			
	YkuJ-MPER		MPER-TBI	
	Theoretical calculations, %	CD spectroscopy in normal saline, %	Theoretical calculations, %	CD spectroscopy in normal saline, %
α-helices	45	26	56	68
β-strands	24	26	3	0
Turn I	–	5	–	5
Turn II	–	0	–	0
Unordered structures	31	43	41	27

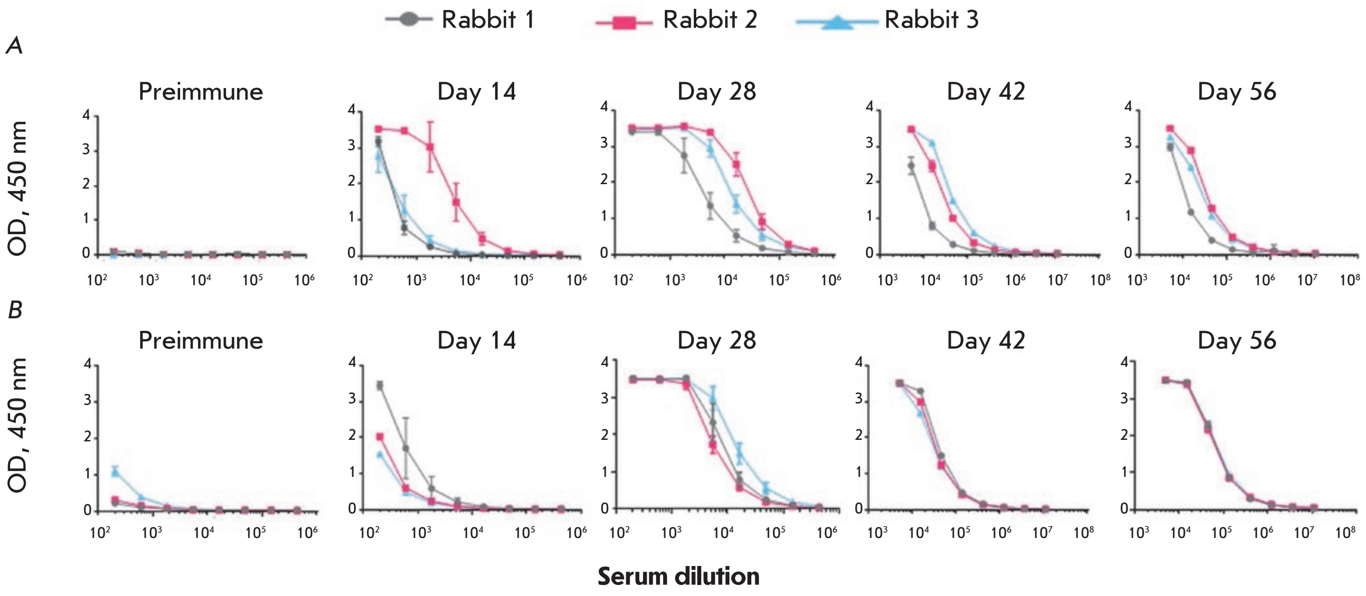

Fig. 7. ELISA results of serum samples from the rabbits immunized with MPER-TBI or YkuJ-MPER. A is a group of rabbits immunized with MPER-TBI: the protein MPER-TBI is sorbed as an antigen. B is a group of rabbits immunized with YkuJ-MPER: the protein YkuJ-MPER is sorbed as an antigen. The OD value (450 nm) is plotted on the Y axis; serum dilutions are plotted on the X axis. The data in the diagrams are presented as the mean value and standard deviation

from the animals immunized with MPER-TBI can react with protein YkuJ-MPER, while serum samples from the animals immunized with YkuJ-MPER can react with protein MPER-TBI) was tested by ELISA (*Figs. 8* and *9*, respectively). It was demonstrated that serum samples from the animals could cross-react with the respective antigens. Upon immunization with MPER-TBI, the titers of the antibodies produced in response to the antigen YkuJ-MPER in serum samples from all animals in the group were 1 : 400,000 (*Fig. 8*). The titers of the antibodies produced in response to the antigen MPER-TBI in the serum samples from animals immunized with YkuJ-MPER were 1 : 1000,000 (*Fig. 9*).

Specificity analysis of the serum samples from the immunized animals

The New Lav Blot I test kit was used to study whether the serum samples contained antibodies specific to HIV-1 proteins. It was found that the serum samples collected from the rabbits immunized both with MPER-TBI and with YkuJ-MPER contained antibodies against the proteins gp160 and gp41 (*Fig. 10*). The serum samples from the animals immunized with MPER-TBI additionally recognized gp120.

DISCUSSION

The membrane-proximal external region of HIV-1 is considered to be among the most promising targets for which to develop immunogens inducing the formation of bNAbs [14]. Nevertheless, there have been no successful attempts in efforts to create an immunogen that could ensure the reliable formation of bNAbs specific to this target [18, 19]. In order to enhance efficiency in the presentation of MPER epitopes to the immune system, they can be incorporated into the scaffolds obtained using the rational design method. The consecutive immunization ('prime-boost') strategy using these constructs would make it possible to increase the immune response to the incorporated epitopes [26–28].

In this study, we have designed two immunogens based on scaffold proteins of different spatial organizations. Their application in the prime-boost immunization strategy can prevent an untoward immune response to the scaffold. The globular protein YkuJ from *B. subtilis* having a known tertiary structure and the earlier characterized artificial polypeptide TBI_tag were used as scaffolds.

Experimental identification of the secondary structures of the immunogens in normal saline by circular dichroism spectroscopy yielded results that showed agreement with the theoretically predicted structures. It turned out that the structure of MPER-TBI was predominantly α-helical, which is consistent with its secondary structure predicted using the PSSfinder method. The number of β-strands in YkuJ-MPER agrees with the constructed model of spatial structure, while the percentage of α-helices is smaller than that

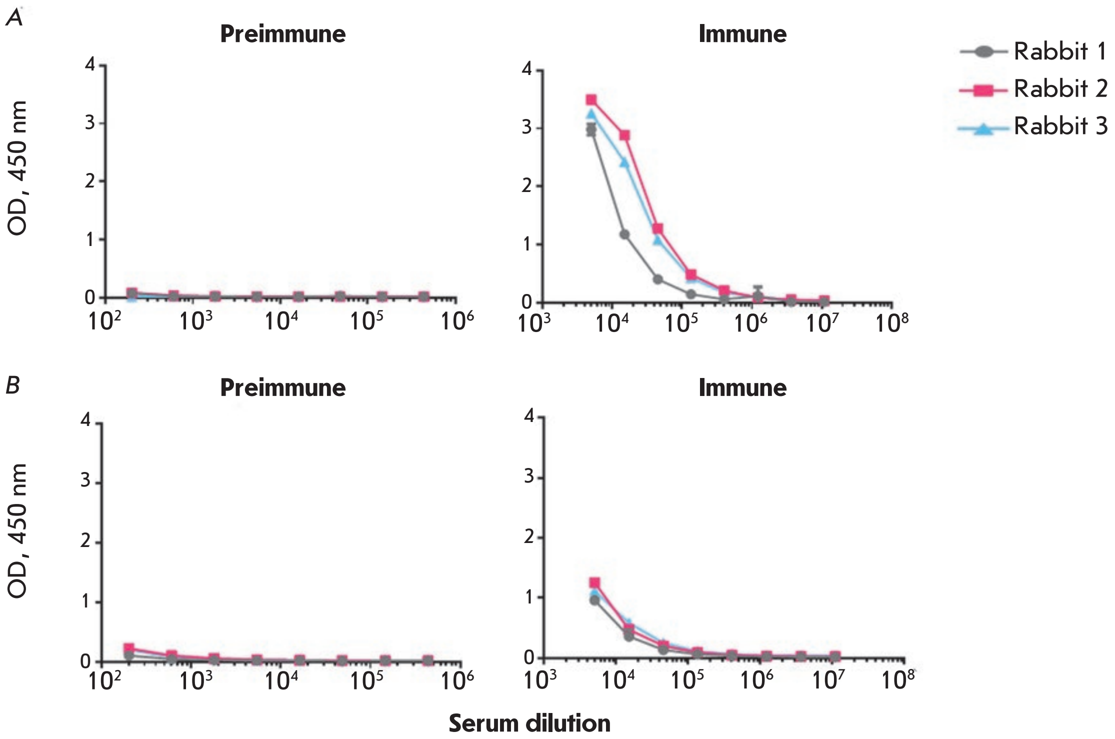

Fig. 8. ELISA results of serum samples from the rabbits immunized with MPER-TBI. *A* – the protein MPER-TBI is sorbed as an antigen; *B* – the protein YkuJ-MPER is sorbed as an antigen. Preimmune is the serum of the intact animals. Immune is the serum of the animals after the 4th immunization

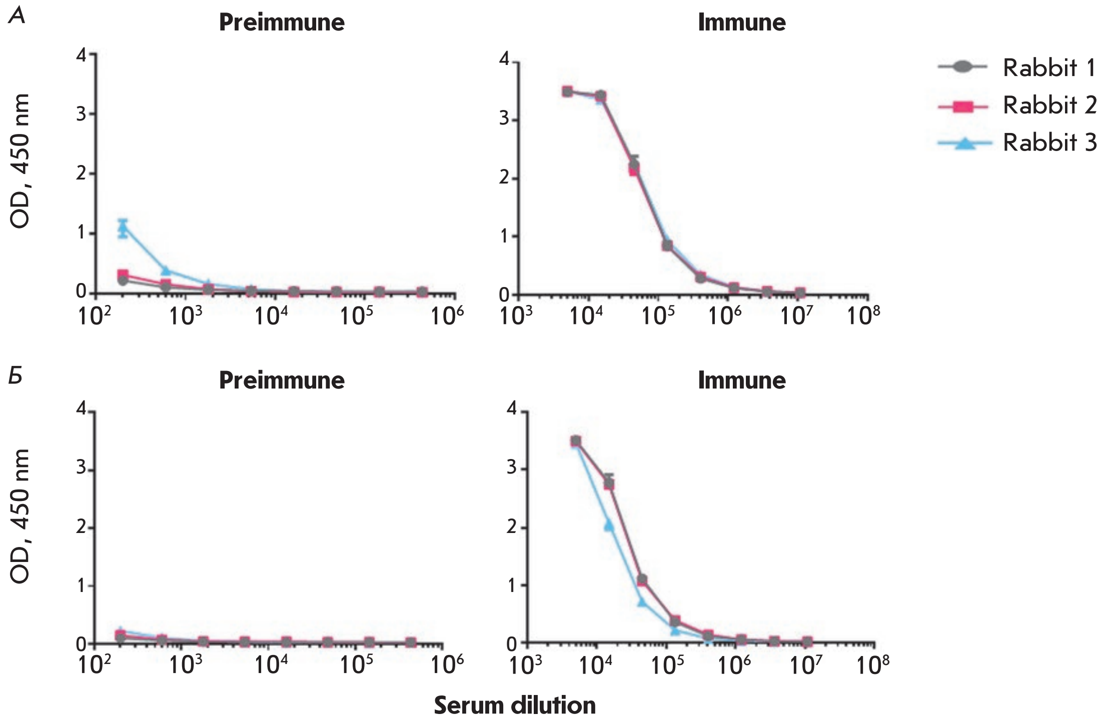

Fig. 9. ELISA results of serum samples from rabbits immunized with YkuJ-MPER. *A* – the protein YkuJ-MPER is sorbed as an antigen; *B* – the protein MPER-TBI is sorbed as an antigen. Preimmune is the serum of the intact animals. Immune is the serum of the animals after the 4th immunization

in the model where both inserted MPER fragments have a α-helical conformation that corresponds to the epitope of antibody 10E8. This fact indicates that the central β-sheet of YkuJ-MPER remains stable, while the inserted epitopes are flexible (as was expected).

Both immunogens were soluble under physiological conditions. Hydrophobicity is one of the known problems related to MPER as an immunogen [20]. Expectedly, our constructs made it possible to overcome this problem.

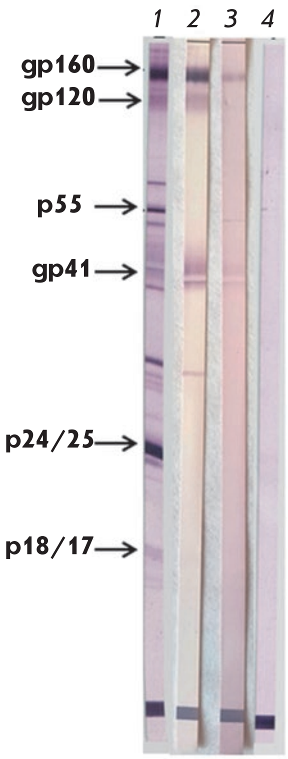

Fig. 10. Analysis of blood serum samples from animals immunized with the proteins MPER-TBI and YkuJ-MPER with a New Lav Blot I western blot kit. *1* – positive control from the New Lav Blot I kit; *2* – serum of rabbits immunized with MPER-TBI; *3* – serum of rabbits immunized with YkuJ-MPER; *4* – preimmune serum of rabbits

The results of dot-blot assay demonstrated that YkuJ-MPER and MPER-TBI could specifically interact with mAbs 4E10 and 10E8, which bind to MPER in the α-helical conformation, and with antibody 2F5, which binds to MPER in the conformation without a regular secondary structure [14]. This result indirectly attests to the conformational mobility of the inserted MPER fragment. We have not experimentally tested how many antibody molecules can bind to a single molecule of the protein YkuJ-MPER, but the models demonstrate the possibility for two antibodies to be bound simultaneously. It was also assumed that MPER-TBI could simultaneously bind two antibodies, since its structure is appreciably mobile. This hypothesis also requires experimental verification.

Immunization of laboratory animals with purified protein drug products demonstrated that the rabbit's organism produces specific antibodies whose titers increase as early as after the first immunization. Furthermore, it was found that antibodies formed as a result of immunization with YkuJ-MPER interact with MPER-TBI, and vice versa. Since, with the exception of the histidine tag (6×His-tag), YkuJ-MPER and MPER-TBI have no common fragments except for the MPER region, it is fair to say that these constructs induce the formation of anti-MPER antibodies.

The New Lav Blot I kit was used to demonstrate that the antibody formed after the immunization of the animals with YkuJ-MPER or MPER-TBI interacts with the sorbed HIV proteins (namely, with gp41 and gp160) (*Fig. 10*). Furthermore, MPER-TBI induces the formation of antibodies that recognize the gp120 protein, owing to the fact that the scaffold protein TBI_tag contains fragments of HIV-1 gp120 (env 102–118, env 309–317, and env 421–437).

CONCLUSIONS

Two immunogens capable of inducing the formation of anti-MPER antibodies have been developed in this study. One of these immunogens is based on the protein YkuJ, which has never been used as a carrier platform for viral epitopes; the second immunogen is based on the TBI immunogen that has been previously well studied. It was demonstrated that chimeric proteins interact with bNAbs targeting HIV-1 MPER. The results of cross-verification of the immunogenic properties of YkuJ-MPER and MPER-TBI and the immunoblot analysis with HIV-1 proteins show that both constructs can ensure the formation of anti-MPER antibodies in immunized animals. A preliminary study of the structural features of the developed immunogens was carried out. The results of this study and the chimeric proteins (YkuJ-MPER and MPER-TBI) could lay the groundwork for the development of immunogens capable of targeting the humoral immune response at the sites of HIV-1 vulnerability. ●

This study was supported by the Russian Foundation for Basic Research (project No. 18-34-00314).

REFERENCES

1. Eisinger R.W., Fauci A.S. // Emerg. Infect. Dis. 2018. V. 24. № 3. P. 413–416.
2. Durova O.M., Vorobiev I.I., Smirnov I.V., Reshetnyak A.V., Telegin G.B., Shamborant O.G., Orlova N.A., Genkin D.D., Bacon A., Ponomarenko N.A., et al. // Mol. Immunol. 2009. V. 47. № 1. P. 87–95.
3. Huang J., Kang B.H., Pancera M., Lee J. H., Tong T., Feng Y., Imamichi H., Georgiev I.S., Chuang G., Druz A., et al. // Nature. 2014. V. 515. № 7525. P. 138–142.
4. Sok D., Burton D.R. // Nat. Immunol. 2018. V. 19. № 11. P. 1179–1188.
5. Hessell A.J., Rakasz E.G., Tehrani D.M., Huber M., Weisgrau K.L., Landucci G., Forthal D.N., Koff W.C., Poignard P., Watkins D.I., et al. // J. Virol. 2010. V. 84. № 3. P. 1302–1313.
6. Pegu A., Hessell A.J., Mascola J.R., Haigwood N.L. // Immunol. Rev. 2017. V. 275. № 1. P. 296–312.
7. Subbaraman H., Schanz M., Trkola A. // Retrovirilogy. 2018. V. 15. № 1. P. 1–14.

8. Vzorov A.N., Uryvaev L.V. // Mol. Biol. 2017. V. 51. № 6. P. 819–829.
9. Saunders K.O., Verkoczy L.K., Jiang C., Zhang J., Parks R., Chen H., Housman M., Bouton-Verville H., Shen X., Trama A.M., et al. // Cell. Rep. 2017. V. 21. № 13. P. 3681–3690.
10. Haynes B.F., Moody M.A., Alam M., Bonsignori M., Verkoczy L., Ferrari G., Gao F., Tomaras G.D., Liao H., Kelsoe G. // J. Allergy Clin. Immunol. 2014. V. 134. № 1. P. 3–10.
11. Shcherbakov D.N., Bakulina A.Y., Karpenko L.I., Ilyichev A.A. // Acta Naturae. 2015. V. 7. № 4. P. 11–21.
12. Montero M., Houten N.E., Wang X., Scott J.K. // Microbiol. Mol. Biol. Rev. 2008. V. 72. № 1. P. 54–84.
13. Williams L.D., Ofek G., Schätzle S., McDaniel J.R., Lu X., Nicely N.I., Wu L., Lougheed C.S., Bradley T., Louder M.K., et al. // Sci. Immunol. 2017. V. 2. № 7. P. eaal2200.
14. Liu H., Su X., Si L., Lu L., Jiang S. // Protein Cell. 2018. V. 9. № 7. P. 1–20.
15. Venditto V.J., Wieczorek L., Molnar S., Teque F., Landucci G., Watson D.S., Forthal D., Polonis V.R., Levy J.A., Szoka F.C. // J. Clin. Vaccine Immunol. 2014. V. 21. № 8. P. 1086–1093.
16. Ye L., Wen Z., Dong K., Wang X., Bu Z., Zhang H., Compans R.W., Yang C. // PLoS One. 2011. V. 6. № 5. P. 1–12.
17. Correia B.E., Ban Y.E., Holmes M.A., Xu H., Ellingson K., Kraft Z., Carrico C., Boni E., Sather D.N., Zenobia C., et al. // Structure. 2010. V. 18. № 9. P. 1116–1126.
18. Kelsoe G., Haynes B.F. // Immunol. Rev. 2017. V. 275. № 1. P. 79–88.
19. Irimia A., Serra A.M., Sarkar A., Jacak R., Kalyuzhniy O., Sok D., Saye-Francisco K.L., Schiffner T., Tingle R., Kubitz M., et al. // PLoS Pathog. 2017. V. 13. № 2. P. 1–20.
20. Scholz C., Schaarschmidt P., Engel A.M., Andres H., Schmitt U., Faatz E., Balbach J., Schmid F.X. // J. Mol. Biol. 2005. V. 345. № 5. P. 1229–1241.
21. Kim M., Song L., Moon J., Sun Z.Y., Bershteyn A., Hanson M., Cain D., Goka S., Kelsoe G., Wagner G., et al. // J. Biol. Chem. 2013. V. 288. № 44. P. 31888–31901.
22. Rudometov A.P., Andreeva N.B., Chikaev A.N., Shcherbakova N.S., Kaplina O.N., Karpenko L.I. // Siberian Scientific Medical Journal. 2018. V. 8. № 4. P. 37–43.
23. Kozlowski L.P., Bujnicki J.M. // BMC Bioinformatics. 2012. V. 13. № 1. P. 1–11.
24. Perczel A., Hollósi M., Tusnády G., Fasman G.D. // Protein Eng. 1991. V. 4. № 6. P. 669–679.
25. Karpenko L.I., Bazhan S.I., Bogryantseva M.P., Ryndyuk N.N., Ginko Z.I., Kuzubov V.I., Lebedev L.R., Kaplina O.N., Reguzova A.Y., Ryzhikov A.B., et al. // Russ. J. Bioorgan. Chem. 2016. V. 42. № 2. P. 170–182.
26. Rathore U., Kesavardhana S., Mallajosyula V.V., Varadarajan R. // Biochim. Biophys. Acta. 2014. V. 1844. № 11. P. 1891–1906.
27. Zolla-Pazner S., Kong X., Xunqing J., Cardozo T., Nádas A., Cohen S., Totrov M., Seaman M.S., Wang Sh., Lu Sh. // J. Virol. 2011. V. 85. № 19. P. 9887–9898.
28. Xu K., Acharya P., Kong R., Cheng C., Chuang G.Y., Liu K., Louder M.K., O'Dell S., Rawi R., Sastry M., et al. // Nat. Med. 2018. V. 4. № 6. P. 857–867.

Long Noncoding RNA LL35/Falcor Regulates Expression of Transcription Factor Foxa2 in Hepatocytes in Normal and Fibrotic Mouse Liver

O. V. Sergeeva[1*], S. A. Korinfskaya[1], I. I. Kurochkin[1], T. S. Zatsepin[1,2]
[1]Skolkovo Institute of Science and Technology, Bolshoy Blvd. 30, bldg. 1, Moscow, 121205, Russia
[2]Department of Chemistry, Lomonosov Moscow State University, Leninsikie gory 1, bldg. 3, Moscow, 119991, Russia
[*]E-mail: o.sergeeva@skoltech.ru

Received April 22, 2019; in final form, June 20, 2019
DOI: 10.32607/20758251-2019-11-3-66-74

Copyright © 2019 National Research University Higher School of Economics. This is an open access article distributed under the Creative Commons Attribution License,which permits unrestricted use, distribution, and reproduction in any medium, provided the original work is properly cited.

ABSTRACT **Long noncoding RNAs (lncRNA) play important roles in the regulation of transcription, splicing, translation, and other processes in the cell. Human and mouse lncRNA (DEANR1 and LL35/Falcor, respectively) located in the genomic environment in close proximity to the Foxa2 transcription factor were discovered earlier. In this work, tissue-specific expression of LL35/Falcor lncRNA has been shown in mouse liver and lungs. The use of antisense oligonucleotides allowed us to achieve LL35/Falcor lncRNA downregulation by 90%. As a result, the level of Foxa2 mRNA and protein dropped, which confirms the involvement of LL35/Falcor lncRNA in the regulation of transcription factor Foxa2. We have shown a decrease in the expression of LL35 lncRNA in liver fibrosis, which correlates with the previously published data for mRNA Foxa2. Thus, lncRNA LL35 regulates Foxa2 expression in the liver not only in normal conditions, but also during development of fibrosis, which allows one to consider lncRNA a biomarker of this pathological process.**

KEYWORDS **non-coding RNA, transcription factor Foxa2, regulation, liver.**

ABBREVIATIONS **lncRNA – long non-coding RNA; ASO – antisense oligonucleotides.**

INTRODUCTION

Analysis of the human transcriptome demonstrated that less than 2% of the genome encodes proteins, while noncoding RNA genes prevail among the remaining 98%. Among the variety of noncoding RNAs, short (less than 200 nucleotides in length) and long RNAs (more than 200 nucleotides) can be distinguished [1]. Long noncoding RNAs (lncRNAs) perform regulatory functions in all major cellular processes. They participate in the regulation of transcription both locally (*in cis*) and remotely (*in trans*), having an impact on such regulatory elements as promoters and enhancers, as well as the chromatin structure and RNA polymerase activity [2]. LncRNAs can participate in the regulation of translation [3] and alternative splicing by recruiting protein factors [4], serve as “molecular sponges” for miRNAs, and regulate their level of free form in the cell [5]. LncRNAs are also often expressed in tissue-specific manner and/or transcribed only in certain conditions. An uncontrolled increase of lncRNAs transcription, such as MALAT-1, HOTAIR, H19, and HULC, stimulates the development of oncological diseases [6].

The number of characterized functionally important long noncoding RNAs increases every year. However, their mechanisms of action remain unknown for the most part. Despite the fact that cell culture studies allow us to describe the molecular mechanisms of lncRNA action, the use of animal models provides a more general and consistent approach to the study of lncRNA functions. However, the low homology between lncRNAs even amongst closely related species complicates such studies and, in some cases, the homology is observed only at the level of the secondary structure. The search for functional analogues of human lncRNAs in mice also allows us to expand the conditions for a functional study of lncRNAs by using various mouse disease models.

It has been previously shown that human lncRNA DEANR1 regulates the proliferation and promotes the apoptosis of choriocarcinoma cells [7], it influences the

Notch signaling pathway [8], and serves as a potential biomarker for a number of cancers such as choriocarcinoma [9], gastric [10], pancreas [11] and colon [12] cancers, as well as several types of lung cancer [13]. The DEANR1 lncRNA gene is located in close proximity to the Foxa2 transcription factor gene in the human genome. DEANR1 is involved in the regulation of Foxa2 during the differentiation of human pancreatic endoderm cells [14]. The authors proposed a mechanism for the activation of *Foxa2* transcription through the recruitment of Smad2/3 proteins to its promoter by DEANR1. Foxa2 is essential for liver development from the endoderm [15] and serves as a transcriptional activator of the liver-specific genes that encode albumin and transferrin. Foxa2 also plays an important role in glucose homeostasis in the liver [16]. An analysis of the genomic environment of *Foxa2* in the mouse genome revealed a potential functional analogue of DEANR1: LL35/Falcor lncRNA (hereinafter referred to as LL35) [17]. Knockout of the gene encoding LL35 lncRNA leads to a decrease in the level of Foxa2 mRNA by 25-30% in the mouse lung epithelium and does not result in a pronounced phenotype in the development of embryo lungs. However, LL35 plays an important role in the regulation of Foxa2 in response to additional exposure, such as lung damage [18]. In this work, LL35 lncRNA has been characterized: we established its tissue-specific expression in mouse organs and demonstrated its intracellular localization. We compared different approaches to lncRNA knockdown, achieved LL35 lncRNA knockdown, and demonstrated the involvement of Foxa2 transcription factor in mouse hepatocytes. Also, we revealed a drop in the level of LL35 lncRNA in liver fibrosis.

EXPERIMENTAL

Cell lines

AML12 mouse hepatocytes (ATCC, USA) were cultured in a DMEM/F12 medium supplemented with 10% fetal bovine serum at 37°C and 5% CO_2.

Isolation of nuclear and cytoplasmic cell fractions

AML12 cells (~1 × 10^6) were grown under standard conditions, then they were removed from the substrate using a 0.25% trypsin solution in 0.5 mM EDTA, washed with phosphate buffer (10 mM sodium phosphate, 100 mM sodium chloride, pH 7.4), followed by centrifugation at 500 *g* for 5 min. The pellet was resuspended in CE buffer (20 mM HEPES (pH 7.4), 1.5 mM $MgCl_2$, 10% glycerol, 0.05% NP-40) containing protease inhibitors; incubated on ice for 10 min; and centrifuged at 1,700 *g* and 4°C for 5 min. The supernatant fraction contained the cytoplasmic cell extract. The pellet was resuspended in NE buffer (20 mM HEPES (pH 7.4), 1.5 mM $MgCl_2$, 10% glycerol, 0.05% NP-40, 500 mM NaCl) containing protease inhibitors; incubated on ice for 10 min; and centrifuged at 1,700 *g* for 5 min at 4°C. The supernatant fraction contained the nuclear cell extract. Total RNA was isolated from the separated extracts using the Trizol reagent (Invitrogen, USA) according to the manufacturer's protocol.

RT-qPCR

Total RNA was isolated from mouse organs or AML12 cells using the Trizol reagent (Invitrogen, USA) according to the manufacturer's protocol. Next, ~1 μg of total RNA was treated with DNase I (Thermo Scientific, USA) according to the manufacturer's instructions in order to remove residual genomic DNA. Reverse transcription was performed using a Maxima First Strand cDNA synthesis kit (Thermo Scientific, USA). The reaction mixture was 3x diluted with water, and qPCR was performed using a PowerUp SYBR Green Master Mix reagent kit (Applied Biosystems, USA) according to the manufacturer's protocol (0.3 μM primer mixture, 0.2 μg of cDNA). For the amplification of LL35 lncRNA, two sets of primers were selected which were further used in all experiments (*table*). The reaction products were analyzed by 1% agarose gel electrophoresis in TAE buffer (40 mM Tris-acetate, 1 mM EDTA, pH 7.6). For RT-PCR of the isolated cell fractions, the level of target RNA in the nuclear fraction was normalized to the level of U2 snRNA and the level of target RNA in the cytoplasmic fraction was normalized to Gapdh mRNA.

Transfection of AML12 cells with siRNAs and antisense oligonucleotides

Small interfering RNAs (siRNA) and antisense oligonucleotides (ASO) (*table*) were synthesized using the phosphoramidite method and purified by ion exchange chromatography. Oligonucleotide purity was confirmed by LC-MS. AML12 cells (~1 × 10^5) were transfected with siRNA or ASO at concentrations of 10 and 5 nM, respectively, using the Lipofectamine-RNAiMAX reagent (Invitrogen) according to the manufacturer's instructions. Small interfering RNA and ASO for luciferase gene were used as a control (*table*). To obtain the siRNA and ASO mixtures, the components were mixed in an equimolar ratio. Small interfering RNA: No. 1: 1+2+3+6; No. 2: 1+3+2; No. 3: 1+3+6; No. 4: 1+3+6; No. 5: 2+3+6. ASO: No. 1: 3+4+7+8+14; No. 2: 3+7+14; No. 3: 3+4+14; No. 4: 3+14. Total RNA was isolated 24 h after transfection using the Trizol reagent (Invitrogen, USA) according to the manufacturer's protocol. Knockdown efficiency was analyzed by RT-qPCR.

Primers for RT-qPCR, siRNA, and ASO used in the study

Primer	Nucleotide sequence, 5’→3’
LL35-1-F	*TTTGGCCAAGGGAGAAAGCTCAGA*
LL35-1-R	*ACGGTGCCTGTAACTTACCTGAAG*
LL35-2-F	*GCTCGGTTTGAGCTCAAATAAATG*
LL35-2-R	*CAGAGGCTCTAGCCACGATGGAG*
Gapdh-F	*TGCACCACCAACTGCTTAGC*
Gapdh-R	*GGATGCAGGGATGATG*
U2-F	*GAAGTAGGAGTTGGAATAGGA*
U2-R	*ACCGTTCCTGGAGGTA*
Foxa2-F	*TATGCTGGGAGCCGTGAAGATGG*
Foxa2-R	*GCGTTCATGTTGCTCACGGAAGAG*
siRNA 1	cucAAAGuuuAGAGuucAu*T*s*T* AUGAACUCuAAACUUUGAG*T*s*T*
siRNA 2	uAAcuuAccuGAAGAGGAA*T*s*T* UUCCUCUUcAGGuAAGUuA*T*s*T*
siRNA 3	cuGAAuuAGAGAAAcAAcu*T*s*T* AGUUGUUUCUCuAAUUcAG*T*s*T*
siRNA 4	GucAGuAAAcAAccGAAAA*T*s*T* UUUUCGGUUGUUuACUGAC*T*s*T*
siRNA 5	GuGGAAuAAuGuuAAGcuu*T*s*T* AAGCUuAAcAUuAUUCcAC*T*s*T*
siRNA 6	cAAcAuGAuGGcAAGGuAu*T*s*T* AuACCUUGCcAUcAUGUUG*T*s*T*
siRNA 7	uGGuGuGGAAuAAuGuuAA*T*s*T* UuAAcAUuAUUCcAcACcA*T*s*T*
siRNA 8	GGuccuAAAuGGuuGAAGA*T*s*T* UCUUcAACcAUUuAGGACC*T*s*T*
siRNA 9	AuGGcAAGGuAuGAAccAA*T*s*T* UUGGUUcAuACCUUGCcAU*T*s*T*
siRNA 10	cuAAAuGGuuGAAGAAcAc*T*s*T* GUGUUCUUcAACcAUUuAG*T*s*T*
Control siRNA	cuUaCgCuGaGuAcUuCgATCGAAGTA*T*s*T* UCgAaGuAcUcAgCgUaAg*T*s*T*
ASO 1	gsgsgsasus*CsCsTsGsGsAsAsAsAsAsAsAs*asgsasasu
ASO 2	gsasgsusus*GsGsAsAsAsGsUsGsAsAs*cscscsasu
ASO 3	ususgscscs*AsTsCsAsTsGsTsTsGsT*sascscsusg
ASO 4	cscscscsus*CsTsCsAsGsTsGsCsTs*Gsgsasascsc
ASO 5	csasgscsas*TsAsTsCsAsGsCsCsAsAsGs*csuscsusg
ASO 6	gsasusasgs*GsTsCsAsGsGsGsCsAsGsGsAs*ususcscsu
ASO 7	ususasgsgs*TsGsGsCsAsGsTsTsCsAs*gsgsasgsa
ASO 8	gsuscsgsgs*TsAsTsCsAsGsTsTsGsCs*asgsasgsa
ASO 9	asasgsasas*AsAsGsAsTsCsTsTsCsAs*tsgsgsgsu
ASO 10	gsgststsgs*TsTsTsAsCsTsGsAsCsTsTs*tsgststststsa
ASO 11	csasasgsas*TsAsTsCsGsAsTsCsAsGsCsGs*ususasusa
ASO 12	asasususus*GsCsTsGsAsAsGsTsGsTs*gsascsgsu
ASO 13	usgsasgsgscs*CsCsAsGsTsCsAsGsTsCsCsCs*usgscsusasc
ASO 14	usgsususgsus*AsCsCsTsGsGsCsCsAsGsTs*csasgscsusgsc
Control ASO	tscsgsasasgs*TsAsCsTsCsAsGs*csgstsasasg

Note. Capital letters indicate ribonucleotides, capital italics denote 2′-deoxynucleotides, lowercase letters indicate 2′-*O*-methylribonucleotides, s – phosphorothioate groups.

Western blot

The AML12 cells (~1×10^6) were lysed in RIPA buffer (Thermo Scientific, USA) containing 1 mM DTT, 0.05% Triton X-100, 0.2 mM phenylmethylsulfonyl fluoride, protease and phosphatases inhibitors. The concentration of proteins in lysates was determined by spectrophotometry using the Bradford reagent (Thermo Scientific, USA). For further analysis, a lysate containing 40 μg of the protein, preliminarily denatured at 95°C for 5 min, was used. The proteins were separated in 10% PAGE in Tris-glycine buffer (pH 8.3), and then they were transferred to a PVDF membrane (Millipore) at a voltage of 70 V for 1 h. Next, the membrane was incubated with a 5% BSA solution for 1 h, and then with a solution of specific antibodies. The antibodies against Foxa2 (ab108422 Abcam, USA) and actin (ab179467 Abcam, USA) proteins, horseradish peroxidase conjugates with antibodies against rabbit and mouse immunoglobulins (ab6721 and ab6728 Abcam, USA) were used. Secondary antibodies were visualized on the membranes by chemiluminescence using a Pierce ECL kit (Thermo Scientific, USA) according to the manufacturer's protocol.

Statistical analysis of the experimental data

All the diagrams are based on at least three independent experiments. Statistical data processing was performed using the GraphPad Prism software (version 6.0) with a two-sample *t*-test, as well as a two-way ANOVA analysis of variance or repeated-measures ANOVA and Sidak *t*-test. The data were considered statistically significant at $P < 0.05$.

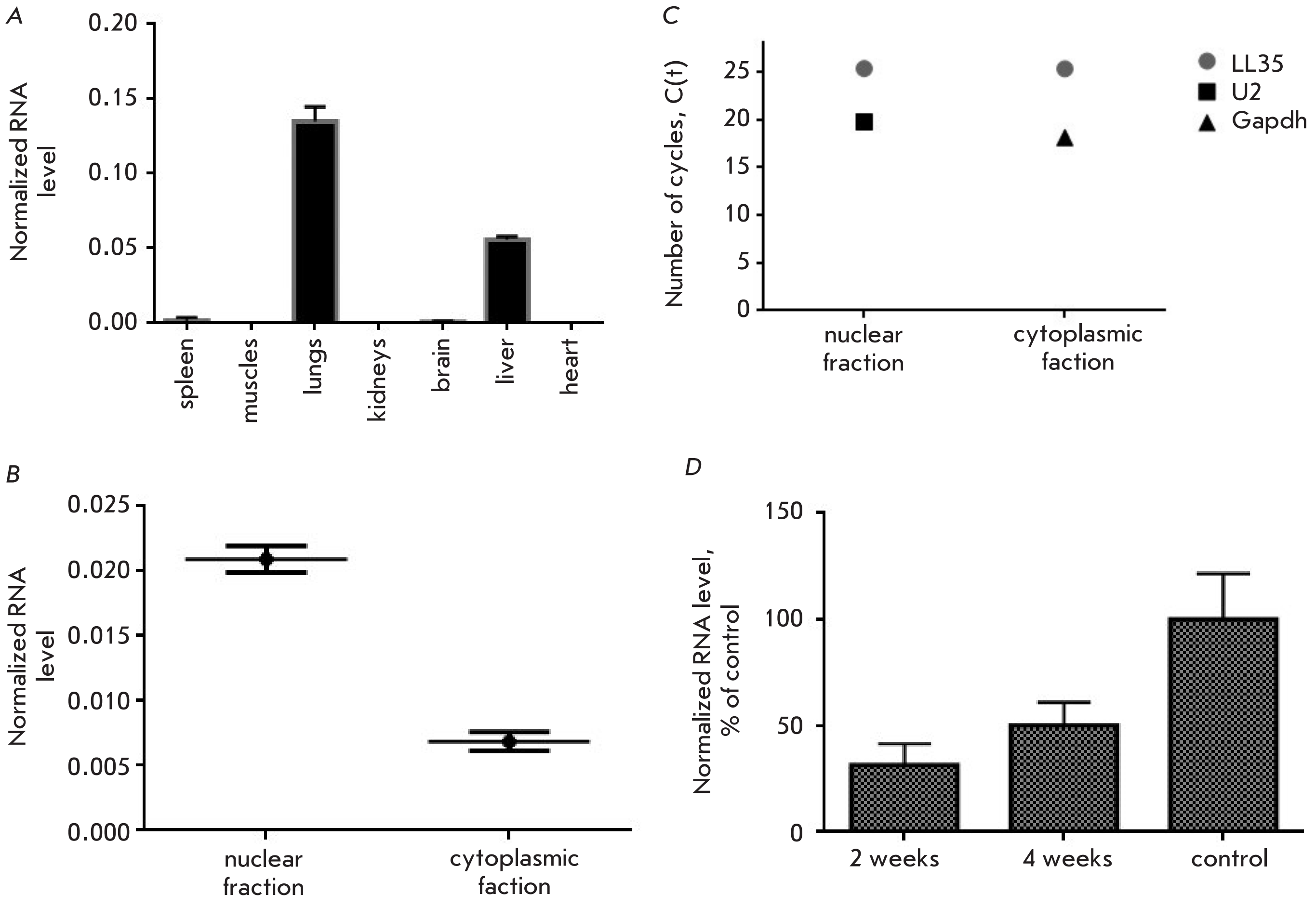

Fig. 1. A) Quantification of LL35 lncRNA in mouse organs (control – Gapdh mRNA); B) Determination of the cellular localization of LL35 in AML12 hepatocytes (controls – U2 RNA for the nuclear fraction, Gapdh mRNA for the cytoplasmic fraction); C) Comparison of LL35 RNA distribution between the nuclear and cytoplasmic fractions of AML12 cells using U2 and Gapdh RNAs as a reference; D) Quantification of LL35 lncRNA in the samples of mouse liver with CCl_4-induced fibrosis at weeks 2 and 4 (control – Gapdh mRNA)

Prediction of LL35 lncRNA secondary structure

To propose secondary structure of the LL35 lncRNAs, the ViennaRNA software package (http://rna.tbi.univie.ac.at/) was used. It predicts secondary RNA structures with minimal free energy taking into account the probability of base pair formation for RNA.

RESULTS

Determination of the LL35 lncRNA expression level in mouse organs and AML12 liver cells

According to NCBI database, the LL35 lncRNA gene (*9020622O22Rik*) is located 2,500 nucleotides downstream of the Foxa2 transcription factor gene and encodes 38 annotated transcripts, the majority of which share the same exons (the first and the last two ones) (https://www.ncbi.nlm.nih.gov/gene/?term=9030622O22Rik). Analysis of the expression level of exons common to all transcripts was used to determine the level of LL35 lncRNA in the mouse organs. Tissue-specific expression and the highest abundance of LL35 lncRNA were shown for lungs and the liver (*Fig. 1A*). To determine the localization of LL35 lncRNA in normal liver AML12 cells, nuclear and cytoplasmic cell fractions were isolated for further analysis by RT-qPCR. LL35 lncRNA is predominantly located in the cell nucleus: only ~20% of the total RNA is located in the cytoplasm (*Fig. 1B*). Moreover, the level of LL35 RNA in the nucleus is only 1.3 times lower than that of U2 snRNA, which is an indication of a high transcription level for lncRNA (*Fig. 1C*).

It has been previously shown that the level of the transcription factor Foxa2 mRNA decreases in liver fibrosis, while a deletion of this factor predisposes one to the development of fibrosis [19]. We noted a up to 70% decrease in LL35 lncRNA in mouse liver two weeks after fibrosis induction with carbon tetrachloride, followed by partial restoration of lncRNA levels up to 60% of their base level four weeks after induction (*Fig. 1D*).

Selection of the conditions for LL35 lncRNA knockdown in AML12 cells

At the first stage of the study, we used RNA interference to knockdown LL35 RNA *in vitro*. The sequence of LL35 RNA was analyzed, and possible siRNA binding sites, as well as sequences found in other RNAs of the mouse transcriptome, were excluded. Afterwards, 10 siRNAs specific to LL35 RNA and containing 2'-*O*-methyl pyrimidine nucleotides and phosphorothioates groups for increasing the stability to intracellular nucleases were designed and synthesized. The efficiency in LL35 knockdown by individual siRNAs did not exceed 40% (*Fig. 2A*). In order to improve that knockdown efficiency, siRNA combinations (three to four siRNAs in the mixture) were tested. In this case, knockdown achieved approximately 60% of the base LL35 RNA level (*Fig. 2B*). One of the possible explanations for such a low efficiency of the siRNAs can be the predominant nuclear localization of LL35 lncRNA and the absence of active nucleus ↔ cytoplasm transport.

Taking into account the nuclear localization of LL35 lncRNA, antisense oligonucleotides (ASO) were chosen as an alternative approach to knockdown LL35 lncRNA. A model of the secondary structure of LL35 lncRNA was obtained using the ViennaRNA software for the design of ASO (*Fig. 2C*) [20]. Fourteen antisense oligonucleotides complementary to the helixes in the predicted RNA structure were selected. ASO 3, 4, 7, 8, 13, and 14 showed a higher efficiency for LL35 lncRNA knockdown (*Fig. 2D*) than individual siRNAs and their combinations. The use of ASO combination No. 1 allowed us to reduce the level of LL35 lncRNA expression to 90% of the basal level. Therefore, this combination was selected for further studies (*Fig. 2E*).

LL35 lncRNA is involved in the regulation of the Foxa2 transcription factor in AML12 mouse hepatocytes

Previously, analysis of the transcriptome of human embryonic stem cells at the differentiation stage revealed a correlation between changes in the expression of both DEANR1 lncRNA and Foxa2 mRNA. A possible mechanism for the activation of the transcription of Foxa2 through Smad2/3 transcription modulators that directly interact with DEANR1 has been proposed [14]. The level of Foxa2 mRNA decreases by 20% of the basal mRNA level (*Fig. 3B*) upon knockdown of the functional analogue of DEANR1, LL35 lncRNA, in mouse hepatocytes (*Fig. 3A*). The level of the Foxa2 protein is reduced by 30% (*Fig. 3C*).

DISCUSSION

The Foxa2 transcription factor is an important regulator of endoderm differentiation into various types of tissues. In an adult liver, Foxa2 is required for normal functioning of the organ and acts as one of the main regulators of the transcription of the liver-specific genes encoding key participants in the lipid metabolism and ketogenesis [16]. The important role of Foxa2 in regulating liver organogenesis should be also noted [21]. In genome, human lncRNA DEANR1 and mouse lncRNA LL35 are located in close proximity to the Foxa2 gene. A mechanism has been proposed for the regulation of the Foxa2 by human lncRNA DEANR1 in embryonic stem cells [14]. The genomic localization of the LL35 lncRNA gene suggests that LL35 lncRNA, which can be involved in the regulation of the transcription factor Foxa2, performs similar functions.

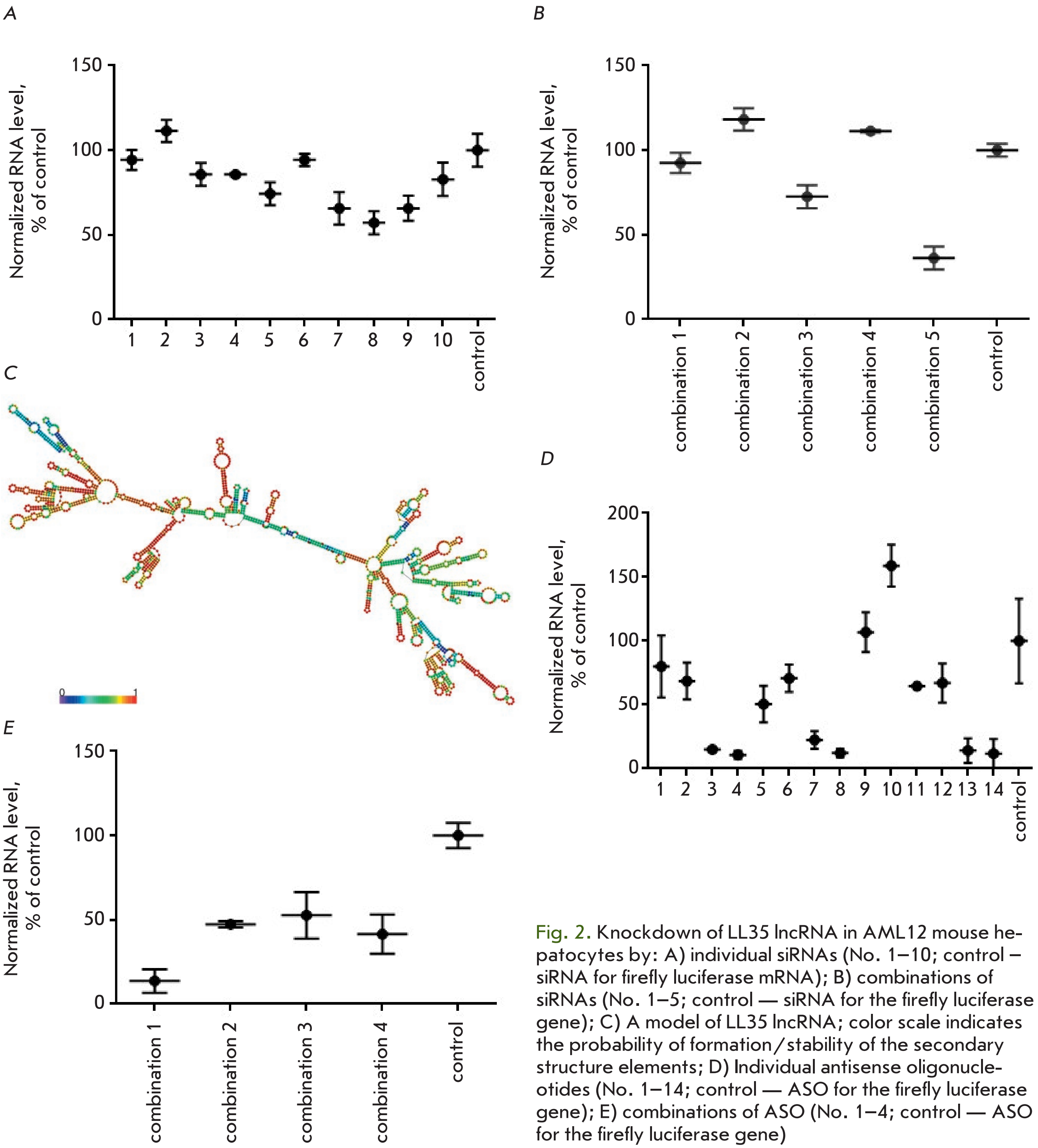

Fig. 2. Knockdown of LL35 lncRNA in AML12 mouse hepatocytes by: A) individual siRNAs (No. 1–10; control – siRNA for firefly luciferase mRNA); B) combinations of siRNAs (No. 1–5; control — siRNA for the firefly luciferase gene); C) A model of LL35 lncRNA; color scale indicates the probability of formation/stability of the secondary structure elements; D) Individual antisense oligonucleotides (No. 1–14; control — ASO for the firefly luciferase gene); E) combinations of ASO (No. 1–4; control — ASO for the firefly luciferase gene)

According to the data in the NCBI database, the hierarchy of abundance of human DEANR1 lncRNA is as follows: in the liver, then the stomach, then in the lungs, pancreas, and intestines (https://www.ncbi.nlm.nih.gov/gene/140828). Analysis of the level of a potential functional analogue of DEANR–LL35 RNA–in mouse organs revealed its tissue-specific expression in the lungs and liver, which is slightly different from the expression of human DEANR1 RNA. It is possible that there are differences in the func-

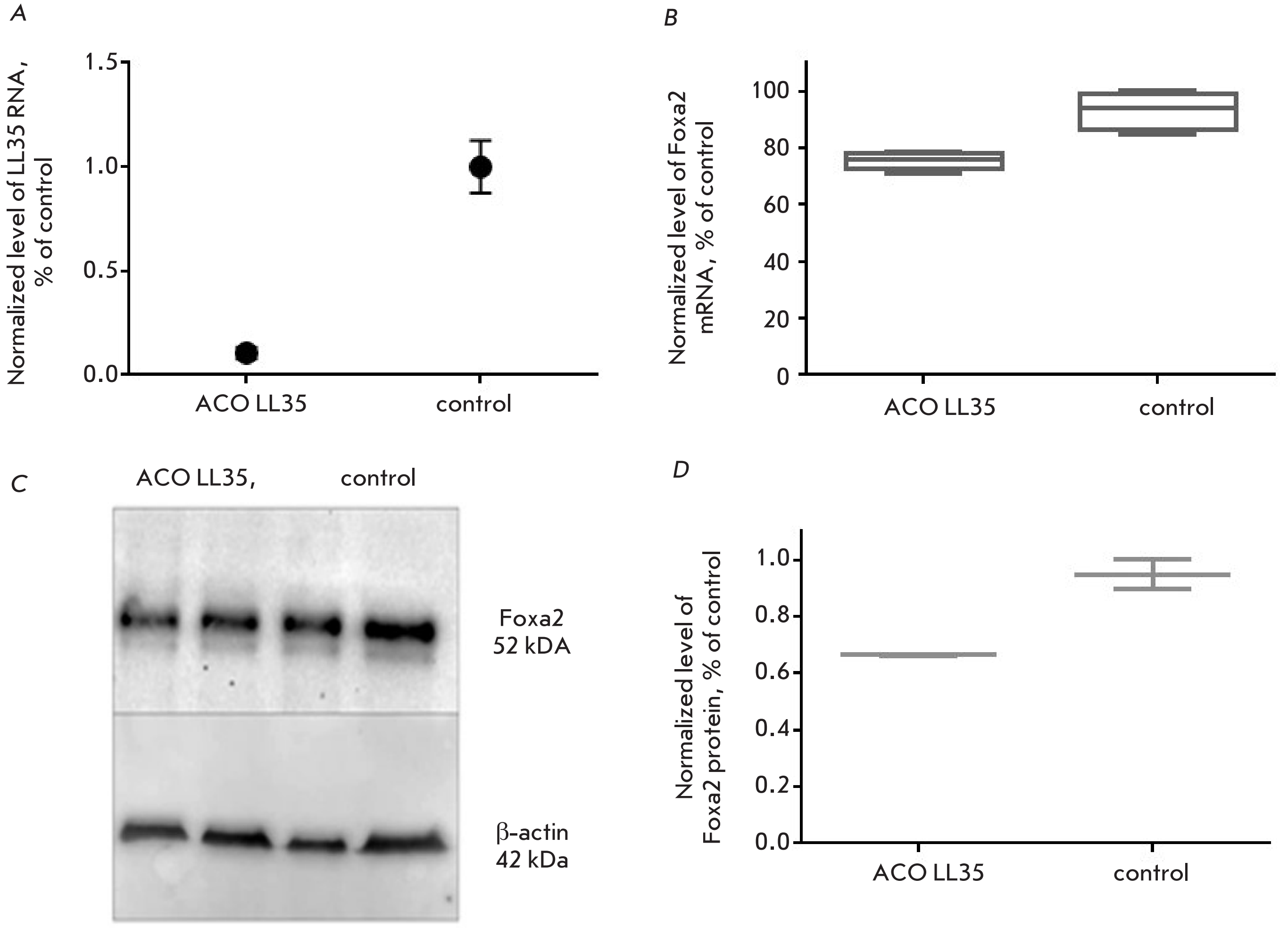

Fig. 3. A) Efficacy of LL35 lncRNA knockdown in AML12 mouse hepatocytes with ASO mix No. 1; B) knockdown of LL35 RNA results in downregulation of the transcription factor Foxa2 mRNA; C), D) Analysis of the Foxa2 protein level under conditions of LL35 RNA knockdown (control — β-actin)

tion of DEANR1 and LL35 in some organs. Therefore, we selected the liver as our object of further studies, since both lncRNAs are highly abundant in the liver.

We have shown that, in mouse hepatocytes, LL35 lncRNA, as well as human DEANR1 lncRNA, is located mainly in the nucleus. The use of antisense oligonucleotides is considered to be the optimal approach to knockdown and study of the function of lncRNAs that have targets localized in the nucleus. However, siRNA can be also used in case of active nucleus ↔ cytoplasm transport. Small interfering RNAs are advantageous for *in vivo* studies, because they are effective at lower doses and provide a longer suppression of the target expression while minimizing hepatotoxicity. Having compared the two approaches, we have chosen ASOs, which knockdown LL35 lncRNA with higher efficiency. However, the use of individual ASO to suppress LL35 lncRNA can result in the preservation of the functionally active part of lncRNA. In order to increase the probability of inactivation of the functional center of LL35 lncRNA, the efficiency of LL35 knockdown by various ASO combinations was tested. Using this approach, we were able to achieve a 90% knockdown of LL35 lncRNA in mouse hepatocytes. Knockdown of the lncRNA in AML12 mouse hepatocytes resulted in a 20% decrease of Foxa2 mRNA and 30% decrease of the Foxa2 protein. The obtained data are in good agreement with the published ones on the changes in the Foxa2 level in mouse lung cells in embryonic knockout of the LL35 lncRNA gene. We suggest a similar mechanism of regulation for the transcription factor Foxa2 through recruitment of Smad2/3 proteins to the *Foxa2* promoter region resulting in transcription activation [14]. One can also assume that, in an adult healthy liver, LL35 lncRNA is involved in maintenance of normal liver function by regulating the activation of Foxa2 and its targets, depending on external signals.

LncRNA functions and the molecular mechanisms they are involved in are studied mainly *in vitro*, which complicates determination of their role in the development of various diseases. The optimal approach to solving this problem is studying lncRNA functions *in vivo*. It has been previously shown that, in liver fibrosis, the transcription factor Foxa2 is suppressed, which results in stress to the endoplasmic reticulum and leads to the death of hepatocytes [19, 22]. The level of Foxa2 also decreases in hepatic injuries of various etiologies [22]. The decrease in the LL35 lncRNA level detected in liver samples with induced fibrosis is consistent with previously published data on a decrease in the level of Foxa2 mRNA, which also confirms the existence of the regulation. Moreover, the expression level of LL35 lncRNA on the second and fourth week after fibrosis induction is consistent with the proliferative activity of hepatocytes during liver regeneration in fibrotic damage [23].

CONCLUSION

Based on the data obtained, as well as previously published data, we can conclude that mouse LL35 lncRNA is a functional analogue of human lncRNA DEANR1. In the present work, tissue-specific expression of LL35 lncRNA has been demonstrated in the liver and lungs. Nuclear localization was established for liver cells, and efficient knockdown of LL35 lncRNA expression by ASO was demonstrated for the first time. A decrease in the level of LL35 RNA results in a decrease in the level of Foxa2 mRNA and protein in liver cells. For the first time, a decrease in the level of LL35 lncRNAs in liver fibrosis was determined, which indicates the potential of further studies of lncRNA *in vivo*. Based on the obtained results, one can assume that LL35 lncRNA is involved in the molecular mechanisms of endoplasmic reticulum stress in hepatocytes, which occurs in liver fibrosis. On the other hand, LL35 lncRNA can also contribute to fibrosis *via* interaction with Smad2/3 transcription modulators in stellate cells [14]. For example, LFAR1 lncRNA regulates the level and degree of phosphorylation of Smad2/3 proteins, which, in turn, causes their translocation to the nucleus and activates the expression of a number of genes, including those involved in the synthesis of type I collagen [24]. All these hypotheses require further confirmation, while the possibility of targeted *in vivo* delivery of the proposed antisense oligonucleotides to liver cells allows one to study LL35 lncRNA in various mouse models of liver diseases [25]. ●

The authors would like to thank Y. V. Kotelevtsev (Skolkovo Institute of Science and Technology) for the provided samples of mouse liver with induced fibrosis; A.N. Malyavko and O.A. Dontsova (M.V. Lomonosov Moscow State University) for valuable advice.

The work was supported by the Russian Science Foundation (grant No. 17-74-10140).

REFERENCES

1. Al-Tobasei R., Paneru B., Salem M. // PLoS One. 2016. V. 11. № 2. P. e0148940.
2. Long Y., Wang X., Youmans D.T., Cech T.R. // Sci. Adv. 2017. V. 3. № 9. P. eaao2110.
3. Dykes I.M., Emanueli C. // Genom. Proteom. Bioinf. 2017. V. 15. № 3. P. 177–186.
4. Tripathi V., Ellis J.D., Shen Z., Song D.Y., Pan Q., Watt A.T., Freier S.M., Bennett C.F., Sharma A., Bubulya P.A., et al. // Mol. Cell. 2010. V. 39. № 6. P. 925–938.
5. Militello G., Weirick T., John D., Döring C., Dimmeler S., Uchida S. // Brief. Bioinform. 2017. V. 18. № 5. P. 780–788.
6. Smekalova E.M., Kotelevtsev Y.V., Leboeuf D., Shcherbinina E.Y., Fefilova A.S., Zatsepin T.S., Koteliansky V. // Biochimie. 2016. V. 131. P. 159–172.
7. Wang Y., Xue K., Guan Y., Jin Y., Liu S., Wang Y., Liu S., Wang L., Han L. // Oncol. Res. 2017. V. 25. № 5. P. 733–742.
8. Zhang H.-F., Li W., Han Y.-D. // Cancer Biomark. Sect. Dis. Markers. 2018. V. 21. № 3. P. 575–582.
9. Wang Y., Xue K., Guan Y., Jin Y., Liu S., Wang Y., Liu S., Wang L., Han L. // Oncol. Res. 2017. V. 25. № 5. P. 733–742.
10. Fan Y., Wang Y.-F., Su H.-F., Fang N., Zou C., Li W.-F., Fei Z.-H. // J. Hematol. Oncol. 2016. V. 9. № 1. P. 57–72.
11. Müller S., Raulefs S., Bruns P., Afonso-Grunz F., Plötner A., Thermann R., Jäger C., Schlitter A.M., Kong B., Regel I., et al. // Mol. Cancer. 2015. V. 14. P. 94–112.
12. Wang Z.K., Yang L., Wu L.L., Mao H., Zhou Y.H., Zhang P.F., Dai G.H. // Braz. J. Med. Biol. Res. 2017. V. 51. № 2. P. e6793.
13. Liu Y., Xiao N., Xu S.-F. // Eur. Rev. Med. Pharmacol. Sci. 2017. V. 21. № 24. P. 5691–5695.
14. Jiang W., Liu Y., Liu R., Zhang K., Zhang Y. // Cell Rep. 2015. V. 11. № 1. P. 137–148.
15. Lee C.S., Friedman J.R., Fulmer J.T., Kaestner K.H. // Nature. 2005. V. 435. № 7044. P. 944–947.
16. Wolfrum C., Asilmaz E., Luca E., Friedman J.M., Stoffel M. // Nature. 2004. V. 432. № 7020. P. 1027–1032.
17. Herriges M.J., Swarr D.T., Morley M.P., Rathi K.S., Peng

T., Stewart K.M., Morrisey E.E. // Genes Dev. 2014. V. 28. № 12. P. 1363–1379.
18. Swarr D.T., Herriges M., Li S., Morley M., Fernandes S., Sridharan A., Zhou S., Garcia B.A., Stewart K., Morrisey E.E. // Genes. Dev. 2019. V. 33. № 11–12. P. 656–668..
19. Wang W., Yao L.-J., Shen W., Ding K., Shi P.-M., Chen F., He J., Ding J., Zhang X., Xie W.-F. // Sci. Rep. 2017. V. 7. № 1. P. 15532–15547.
20. Lorenz R., Bernhart S.H., Höner zu Siederdissen C., Tafer H., Flamm C., Stadler P.F., Hofacker I.L. // Algorithms Mol. Biol. 2011. V. 6. P. 26–40.
21. Lee C.S., Friedman J.R., Fulmer J.T., Kaestner K.H. // Nature. 2005. V. 435. № 7044. P. 944–947.
22. Wang K. // Cell. Signal. 2015. V. 27. № 4. P. 729–738.
23. Koyama Y., Brenner D.A. // J. Clin. Invest. 2017. V. 127. № 1. P. 55–64.
24. Peng H., Wan L.-Y., Liang J., Zhang Y.-Q., Ai W.-B., Wu J.-F. // Cell Biosci. 2018. V. 8. P. 63–71.
25. Crooke S.T., Witztum J.L., Bennett C.F., Baker B.F. // Cell Metab. 2018. V. 27. № 4. P. 714–739.

Surgical Simulation of a Posttraumatic Spinal Cord Glial Scar in Rats

G. B. Telegin[1*], A. N. Minakov[1], A. S. Chernov[1], V. N. Manskikh[3], D. S. Asyutin[2], N. A. Konovalov[2], A. G. Gabibov[4]
[1]Branch of Shemyakin and Ovchinnikov Institute of Bioorganic Chemistry of the Russian Academy of Sciences, Prospect Nauki 6, Pushchino, 142290, Russia
[2]N.N. Burdenko National Scientific and Practical Center for Neurosurgery, RF Health Ministry, 4th Tverskaya-Yamskaya Str. 16, Moscow, 125047, Russia
[3]M.V. Lomonosov Moscow State University, Leninskie Gory 1, Moscow, 119991, Russia
[4]Shemyakin-Ovchinnikov Institute of bioorganic chemistry, GSP-7, Miklukho-Maklaya Str. 16/10, Moscow, 117997, Russia
[*]E-mail: telegin@bibch.ru

Received June 24, 2019; in final form, August 02, 2019
DOI: 10.32607/20758251-2019-11-3-75-81

Copyright © 2019 National Research University Higher School of Economics. This is an open access article distributed under the Creative Commons Attribution License,which permits unrestricted use, distribution, and reproduction in any medium, provided the original work is properly cited.

ABSTRACT **We developed and verified an original, minimally invasive method for surgical simulation of a posttraumatic spinal cord glial scar in rats. The model is intended for use as a biological platform for testing the stimulation of regenerative processes in the central nervous system. Unification of the model enables one to achieve versatility both for implantation techniques and for the development of system-action approaches. Faced with a standard structural defect of the spinal cord, researchers will have the unique opportunity to test *in vivo* promising methods for spinal function recovery in the posttraumatic period. We developed anesthetic support, surgical tactics, and a set of rehabilitation measures for the chronic postoperative period. Experimental exposure effects were preliminarily assessed *in vivo* using a standard technique for recording the motor activity of rats in the postoperative period of spinal cord injury. Our final conclusions were drawn based on an analysis of histological sections of the rat spinal cord glial scar in three mutually perpendicular planes.**

KEYWORDS **surgical simulation, laboratory rat, spinal cord injury, glial scar, axonal regeneration, cryoapplication, unilateral hemilaminectomy.**

ABBREVIATIONS **SC – spinal cord; SCI – spinal cord injury; 3Rs – principles (Reduce, Refine, Replace) for performing more humane animal research; BBB scale – a scale (Basso, Beattie, Bresnahan) to evaluate locomotor recovery in rats with spinal cord injury; SPF – specified pathogen free.**

INTRODUCTION

Spinal cord injury (SCI) is one of the main causes of disability [1], which is associated with the inevitable formation of a glial scar in the posttraumatic period, which prevents regenerative axonal growth and nerve impulses. Clinically, SCI is accompanied by a serious functional deficit, which may lead to irreversible paralysis of body areas distal to the injury. Several weeks after injury, 30% of patients develop posttraumatic syringomyelia, which reduces their neurological status [2].

The prospects for treating patients with spinal cord injuries will depend on the success of experimental studies based on the use of appropriate animal models. According to 3R principles, smaller animals are preferred for biomodeling. However, in the case of biomodeling on the spinal cord, which is associated with surgical intervention, minimization of the animal size faces obvious limitations due to the need for a sufficient amount of a simulated posttraumatic scar which allows for its use in the development of methods for spinal function recovery. The use of small rodents is considered most suitable for the modeling of SCI thanks to the common pathophysiology between the injury and clinical practice [3, 4]. Based on all these described conditions, species preference for use as an animal model was given to laboratory rats.

The most common SCI models in rats are closed SC injuries – compression-simulating impaction and contusion-simulating bruise. However, these models are difficult to reproduce, and they cannot be used to study spinal cord regeneration in structural injuries [3].

Our research team developed an approach to the modeling of SCI that uses an original cryoapplicator. The proposed innovative method for the modeling of a standard glial scar by means of cryoapplication is based on research by Vasiliev S.A. *et al.* on the cryodestruction of the spinal cord [5, 6], as well as on methods of nerve cryoanalgesia [7].

EXPERIMENTAL

To optimally visualize and identify the anatomical structures and ensure sufficient space for the surgical procedure, we used large, 320–358 g, male SD rats with the SPF status. The animals were kept under standard conditions at the Animal Breeding Facility of the Branch of the Institute of Bioorganic Chemistry (BIBCh). All manipulations with the animals were approved by the Institutional Animal Care and Use Committee at BIBCh.

A total of 26 animals were used in experiments testing the use of cryotechnologies in the modeling of a structural defect of the spinal cord in rats: 14 rats were used at the stages of mastering of the experimental methodology, including development of a cryoconductor design, choice of the spinal cord cooling exposure, and access control, and 12 rats were involved at the stage of verification of the selected method for low-temperature exposure (local cryoapplication).

Preoperative preparation and anesthetic support

The animals were placed in cages with clean bedding and water 24 h before surgery. Surgery was performed under general isoflurane inhalation anesthesia; premedication was not used.

Surgical approach

A standard microsurgical tool kit was used to make a 2-cm median incision in the skin, subcutaneous fascia, and adipose tissue in the projection of the intersection of the vertebral column with the costal arch of the animal (*Fig. 1B*). The spinous process of the last thoracic vertebra T13 was identified cranial to the convergence of the posterior spinal muscle aponeuroses (*musculus erector spinae*) to spinous lumbar processes (*Fig. 1A*). The spinous process and posterior arch of the approach vertebra were skeletonized under visual control using a binocular operating microscope (Optika, Italy) (*Fig. 1C*). Hemostasis was provided with a thermocautery (FTS, England). The spinous process was resected to ensure sufficient operative space. Unilateral hemilaminectomy was performed using an original technique, by means of a portable dental micromotor. We used end-paramedian perforation by a 1.0-mm diamond burr at 30,000 rpm (*Fig. 1D*). In this case, the dura mater was not involved, which was confirmed by the absence of a CSF leak. After completion of laminectomy, the approach area was washed with physiological saline, the excess of which was synchronously removed by vacuum suction (Millipore, Germany).

Surgical procedure

The spinal cords in all animals in the experimental group were locally cooled by applying a cryoconductor through the dura mater (*Fig. 1D, E*). The conductor diameter in the area of contact with biological substrate tissue was 0.8 mm; the material was copper; the distance from the source of the cold (liquid nitrogen) in the original device was 9 cm; the exposure time for application was 1 min; the conductor temperature in the contact area was 20°C.

The animals in the control group (four rats) underwent a surgical approach to the spinal cord similar to that in the experimental rats, but without local cooling.

Wound closure

Tissues were closed in layers using Prolene 6/0 atraumatic nonabsorbable monofilament material (Ethicon, USA).

Single application of microporous aluminum suspension (Vetoquinol, France) was used to protect the surgical wound surface.

Temperature mode

During surgery, the animals were fixed on an operating table with a temperature of 38°C to compensate for the hypothermia developed upon anesthesia. Immediately after surgery and until full recovery from anesthesia, the animals were placed in a cage mounted on an electrically heated table and fed oxygen-enriched air.

Postoperative monitoring

The follow-up period in the experiment was 30 days. The developed surgery protocol and clinical monitoring regimen yielded a 100% survival rate of rats.

To prevent wound infection and because of the significant extent of the surgical injury and the chronic period of postoperative follow-up, preventive antibiotic therapy was performed through an intramuscular injection of Baytril (enrofloxacin, 25 mg/mL) at a dose of 10 mg/kg once a day, for 10 days.

Fig. 1. Development of the surgical approach: A – anatomical 3D-reconstruction; B – topographic landmarks, C – dissection and resection of the spinous process, D –unilateral hemilaminectomy, E – cryoprobe, F – local cooling of the spinal cord

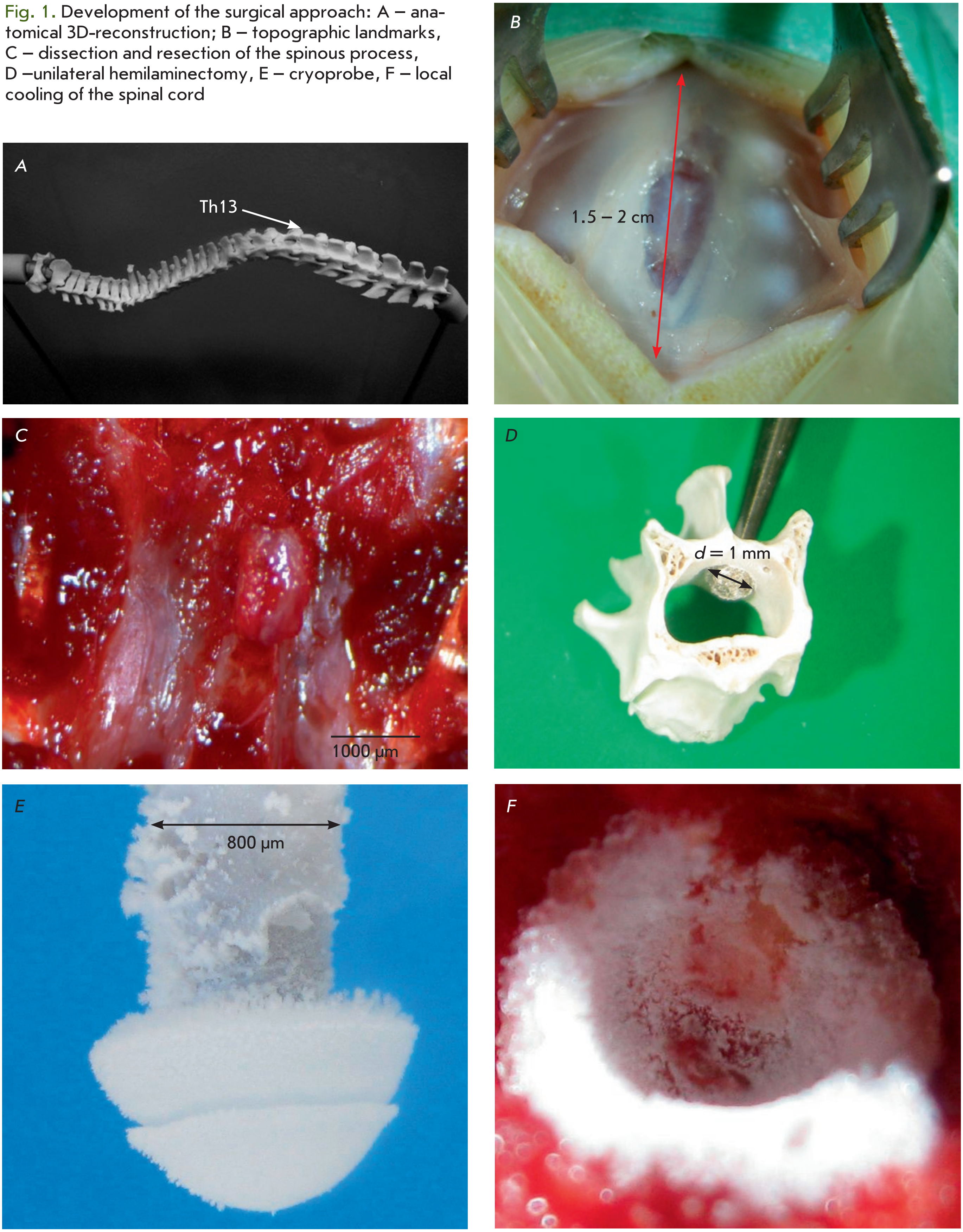

For postoperative analgesia, the rats were treated with Norocarp (carprofen) at a dose of 10 mg/kg of live weight once a day, for 4–6 days.

For re-hydration immediately after surgery, the animals were subcutaneously injected with 5 mL of a physiological sodium chloride solution preheated to 38°C.

Throughout the chronic experiment, the operated animals were evaluated for appearance, unprovoked behavior, respiratory rate, feed and water consumption, bodily functions, nest building, response to hands, mucous membrane color, skin turgor, surgical wound condition, body weight changes, body temperature (rectal), and motor and sensitive functions of pelvic limbs and tail.

Assessment of locomotor activity

The effect of the experimental procedure on the locomotor activity of the rats was tested “in open field,” according to the 21-point BBB scale, which is traditionally used in the simulation of spinal cord injury [8].

Morphological examination

The spinal cord was isolated from the spinal canal (within the T12–L1 vertebrae) by transecting the lateral walls of the posterior vertebral arches using a burr, which ensured maximum preservation of the posterior spinal cord surface at the site of impact. The ostensible site of cold exposure was macroscopically identified by a light brown spot on the tissue, which was about 3/4 of the spinal cord diameter. Samples were fixed in a 10% formalin solution in phosphate buffer (pH 7.4) for 24 h. After fixation, the samples were dehydrated in isopropyl alcohol (Isoprep, Biovitrum), embedded in paraffin, sliced in 5-μm sections on a rotational microtome (RM2245, Leica), and stained with hematoxylin and eosin according to routine protocols [9].

To comprehensively assess the morphological features of the injury, we prepared serial sections in three mutually perpendicular planes: sagittal (to evaluate the depth and longitudinal extent of the defect), frontal (area in the contact spot plane), and segmental (transverse defect size relative to the spinal cord diameter). The sections with a maximum defect area were selected for morphological measurements in each plane. The topography of the affected spinal cord structures was determined according to the data of [10].

Sample images and morphometric procedures were produced with an Axioscope A1 microscope and a MRc 5 camera using the AxioVision 3.0 software (Carl Zeiss, Germany). The obtained data were processed using the SigmaPlot statistic (v. 13.0) software package.

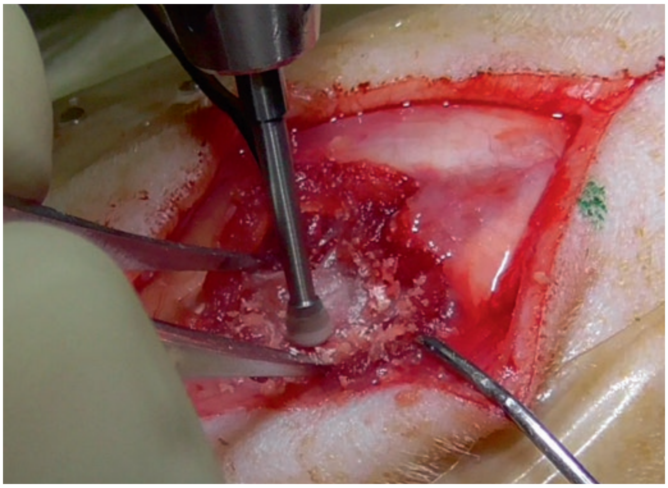

Fig. 2. Hemilaminectomy of the T13 posterior arch in a rat, using a dental burr

RESULTS AND DISCUSSION

Surgical approach development

The investigation of spinal function recovery requires the modeling of a posttraumatic glial scar – standard and minimal in volume. In contrast to the mainly mechanical contusion impacts on the spinal cord used to simulate spinal cord injury, we modeled the glial scar using an original technique of local low-temperature spinal cord injury. The idea’s prototype was the experiment of using cryotechnologies for cryoanalgesia of peripheral nerves and cryodestruction of central nervous system tissue [5–7].

To ensure the most correct interpretation of the results obtained in the model of the posttraumatic spinal cord glial scar during the development of methods for spinal function recovery, we chose a unilateral spinal cord impact which enabled the use of clinical and pathomorphological changes to the intact state as a control.

Due to the need to standardize the spinal cord approach level, we attempted original approaches, such as using the topography of the convergence of the posterior spinal muscle aponeuroses as an intraoperative landmark of the last thoracic vertebra from the side of the operational action vector (*Fig. 1B*) and using the dura mater as a damper for direct cold effect on the spinal cord. It should be noted that intraoperative navigation may be significantly complicated in younger animals, which are smaller in size, as well as in rats with dark pigmentation (e.g., the Dark Agouti line) because the posterior spinal muscle aponeuroses involved in the lumbar spinous processes look much less contrasting than those in large albino rats.

Therefore, the technique for applying a cryoconductor to the spinal cord enables maximal localization of the low-temperature exposure site and minimization of nonspecific concussive organ damage during surgery. An indicator of structural preservation of the spinal cord during unilateral hemilaminectomy performed by end perforation was a lack of CSF leaks. Animals with iatrogenic durotomy were excluded from the experiment. A transosseous approach to the spinal cord was performed using a dental burr (*Fig. 2*).

Clinical monitoring indicators

According to the BBB scale [9], monoplegia was observed on the exposure side in most rats with a simulated posttraumatic scar of the spinal cord, which lasted for 21 days. The animals in the experimental group had a medium level of locomotor dysfunction (2.3 points of the BBB scale), while in the control group lacking cold exposure complete recovery of the motor activity was observed 5 days after surgery.

Current SCI models cause significant urinary system dysfunctions in rats, which is a serious drawback [11]. It is necessary to manually empty the bladder of the animals several times a day after injury to avoid bladder rupture and infectious inflammation [12, 13]. Our model had no such drawback thanks to the minimal surgical injury. After injury, the animals retained their ability to naturally empty their bladder and intestines during the entire follow-up period despite the persistent monoplegia. The ability to urinate independently and defecate is the key to life support in the chronic postoperative period; it prevents the development of distress in rats and a nonspecific injury to the spinal cord when stimulating natural movements by palpation on the walls of the intestines and bladder through the abdominal wall of the animal.

Histological findings

According to the spinal cord histological data, an identical histological pattern was observed in all animals on the 30th day after cryodestruction (*Fig. 3*). At the defect center, there was a cavity filled with cell debris and macrophage-like cells. The cavity was partially lined with elements of a maturating gliomesodermal scar, which were more pronounced on the meningeal side and formed cords and commissures. Most of the wall, including areas adjacent to the scar tissue, was represented by fibrous and vacuolated neuropil that gradually transformed into intact nervous tissue. In the vacuolization area, there were no neurons but there were cells of unclear morphology with signs of

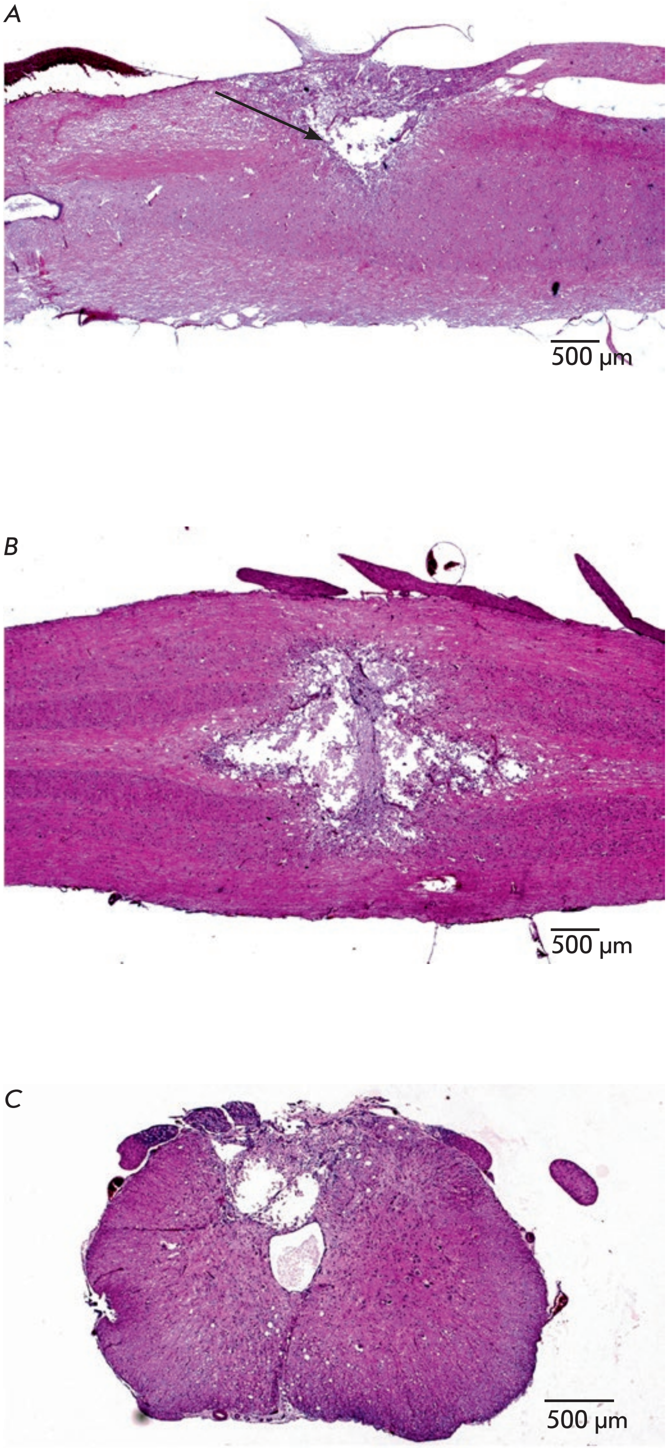

Fig. 3. Typical histological pattern of spinal cord cryodestruction on day 30 after the proposed surgical procedure: *A* – sagittal section (the walls of a crater-shaped defect are depicted by arrows). *B* – frontal section (the structural defect cavity is clearly visible); *C* – segmental section (the structural defect cavity is clearly visible). H&E staining, ×25 magnification

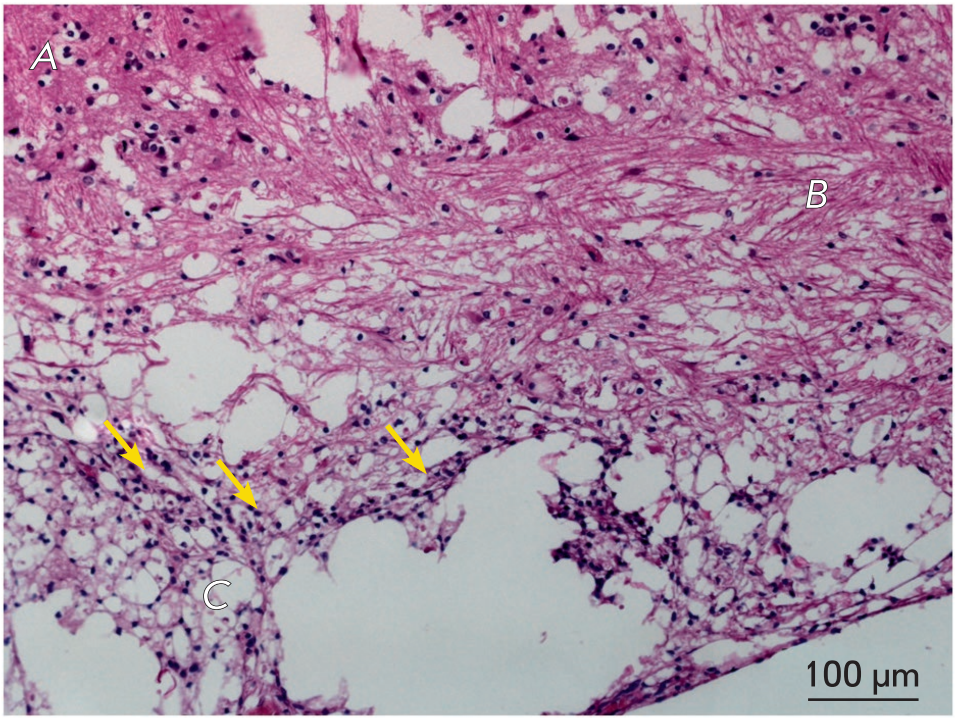

Fig. 4. Morphology of the affected spinal cord area during hemilaminectomy (×200). *A* – intact tissue; *B* – reactive changes (neuropil rarefaction); *C* – necrosis area, arrows indicate cells of inflammatory infiltrate (lymphocytes or microglial elements)

apoptosis (karyorrhexis and karyopyknosis of nuclei). There was no acute exudative inflammation in the defect area, but there was moderate infiltration by lymphocytes and microglial elements. The total injury area was 3.6 ± 0.25 mm^2 (n = 6) in the sagittal plane (*Fig. 3A*), 3.2 ± 0.36 mm^2 (n = 4) in the frontal section (*Fig. 3B*), and 1.1 ± 0.1 mm^2 (n = 4) in the cross section (*Fig. 3C*). In all cases of experimental exposure, the posterior horns of gray matter and the adjacent lateral funiculi in the *tractus pyramidalis et tractus dorsolateralis* area were structurally altered.

It should be noted that in the control group, where only hemilaminectomy was performed, a gliomezodermal-like scar was found in the approach area (*Fig. 4*). This fact may be associated with technical errors inherent to the approach technique, but it is also an indication of how much the spinal cord is sensitive to any outside influence.

Further optimization of the local spinal cord cooling technology will involve improvements to the original cryoconductor design and optimization of low-temperature exposure conditions. Detailed studies on animal models related to the improvement of surgical techniques and use of innovative laser-optical technologies and other techniques will bring practicing surgeons closer to solving the problem of functional recovery of the spinal cord in the posttraumatic period [14–16].

CONCLUSION

This study substantiated, developed, and verified a method for the simulation of a posttraumatic spinal cord glial scar in rats. Exact adherence to the established anatomical landmarks, as well as the use of original tools and methods of local cold exposure of the spinal cord, enabled the unification of the simulated object. According to the clinical and histological data harvested, the proposed technique indicates the creation of an adequate animal model of posttraumatic spinal cord scar. ●

Data obtained using animals from the unique scientific unit "Biomodel" BIBCh RAS.

REFERENCES

1. Nas K., Yazmalar L., Şah V., Aydın A., Öneş K. // World J. Orthop. 2015. V. 18. № 6 (1). P. 8–16.
2. Falci S.P., Indeck C., Lammertse D.P. // J. Neurosurg. Spine. 2009. V. 11. P. 445–446.
3. Minakov A.N., Chernov A.S., Asutin D.S., Konovalov N.A., Telegin G.B. // Acta Naturae. 2018. V. 10. № 3 (38). P. 4–10.
4. Minakov A., Chernov A., Sirotkin A., Asutin D., Konovalov N., Telegin G. // Lab. Animals. 2019. V. 53(1S). P. 130.
5. Vasiliev S.A., Krylov V.V., Pesnya-Prasolov S.B., Zuev A.A., Levin R.S., Pavlov V.N., Zhidkov I.L., Khovrin V.V., Fedorov D.N., Vetsheva N.N. // Neurosurgery. 2010. № 4. P. 58–64.
6. Vasiliev S.A., Pesnya-Prasolov S.B., Kungurtsev S.V., Pavlov V.N. // Clin. Exp. Surg. Petrovsky J. 2015. № 1. P. 15–21.

7. Ilfeld B.M., Gabriel R.A., Trescot A.M. // Br. J. Anaesth. 2017. V. 119. № 4. P. 703–706.
8. Bispo dos Santos G., Cristante A.F., Marcon R.M., Inácio de Souza F., Pessoa de Barros Filho T.E., Damasceno M.L. // Acta Ortop. Bras. 2011. V. 19. № 2. P. 87–91.
9. Trofimenko A.I., Chitanava T.V., Dzhopua M.A., Kade A.Kh., Egiev I.K., Chechelyan V.N., Sergeeva Y.A. // Modern Problems Sci. Edu. 2017. № 3. P. 22–31.
10. Nozdrachev A.D., Polyakov E.L. Rat anatomy. Saint-Petersburg: Lan, 2001. 464 P.
11. Krishna V., Andrews H., Jin X., Yu J., Varma A., Wen X., Kindy M.A. // J. Vis. Exp. 2013. V. 78. e50111, doi: 10.3791/50111.
12. David B.T., Steward O. // Exp Neurol. 2010. V. 226. № 1. P. 128–135. doi: 10.1016/j.expneurol.2010.08.014.
13. Wada N., Shimizu T., Takai S., Shimizu N., Kanai A.J., Tyagi P., Kakizaki H., Yoshimura N. // Neurourol. Urodyn. 2017. V. 36. № 5. P. 1301–1305. doi: 10.1002/nau.23120.
14. Marcol W., Slusarczyk W., Gzik M., Larysz-Brysz M., Bobrowski M., Grynkiewicz-Bylina B., Rosicka P., Kalita K., Węglarz W., Barski J.J. // J. Reconstr. Microsurg. 2012. V. 28. № 8. P. 561–568.
15. Kuzmina A.G., Baranov K.K., Gorbatova N.E., Kurilov V.P., Kuzmin G.P., Sirotkin A.A., Tikhonevich O.V., Zolotov S.A. // J. Appl. Spectroscopy. 2016. V. 83. № 6–16. P. 708.
16. Bogachouk A.P., Storozheva Z.I., Telegin G.B., Chernov A.S., Proshin A.T., Sherstnev V.V., Zolotarev Yu.A., Lipkin V.M. // Acta Naturae. 2017. V. 9. № 3(34). P. 64–70.

The Catalytic Mechanisms of the Reactions between Tryptophan Indole-Lyase and Nonstandard Substrates: The Role of the Ionic State of the Catalytic Group Accepting the C_α Proton of the Substrate

N. G. Faleev[1*], M. A. Tsvetikova[1], O. I. Gogoleva[1], V. V. Kulikova[2], S. V. Revtovich[2], K. A. Kochetkov[1,3]
[1]Nesmeyanov Institute of Organoelement Compounds, Russian Academy of Sciences, Vavilova Str. 28, Moscow, 119991, Russia
[2]Engelhardt Institute of Molecular Biology, Russian Academy of Sciences, Vavilova Str. 32, Moscow, 119991, Russia
[3]Mendeleev University of Chemical Technology, Miusskaya Sq. 9, Moscow, 125047, Russia
[*]E-mail: ngfal@ineos.ac.ru

Received April 24, 2019; in final form, July 23, 2019
DOI: 10.32607/20758251-2019-11-3-82-88

Copyright © 2019 National Research University Higher School of Economics. This is an open access article distributed under the Creative Commons Attribution License,which permits unrestricted use, distribution, and reproduction in any medium, provided the original work is properly cited.

ABSTRACT **In the reaction between tryptophan indole-lyase (TIL) and a substrate containing a bad leaving group (L-serine), general acid catalysis is required for the group's elimination. During this stage, the proton originally bound to the C_α atom of the substrate is transferred to the leaving group, which is eliminated as a water molecule. As a result, the basic group that had accepted the C_α proton at the previous stage has to be involved in the catalytic stage following the elimination in its basic form. On the other hand, when the substrate contains a good leaving group (β-chloro-L-alanine), general acid catalysis is not needed at the elimination stage and cannot be implemented, because there are no functional groups in enzymes whose acidity is strong enough to protonate the elimination of a base as weak as Cl^- anion. Consequently, the group that had accepted the C_α proton does not lose its additional proton during the elimination stage and should take part in the subsequent stage in its acidic (not basic) form. To shed light on the mechanistic consequences of the changes in the ionic state of this group, we have considered the pH dependencies of the main kinetic parameters for the reactions of TIL with L-serine and β-chloro-L-alanine and the kinetic isotope effects brought about by replacement of the ordinary water used as a solvent with ^2H_2O. We have found that in the reaction between TIL and β-chloro-L-alanine, the aminoacrylate hydrolysis stage is sensitive to the solvent isotope effect, while in the reaction with *L*-serine it is not. We have concluded that in the first reaction, the functional group containing an additional proton fulfills a definite catalytic function, whereas in the reaction with *L*-serine, when the additional proton is absent, the mechanism of hydrolysis of the aminoacrylate intermediate should be fundamentally different. Possible mechanisms were considered.**

KEYWORDS **tryptophan indole-lyase, mechanism, kinetics, L-serine, β-chloro-L-alanine.**

ABBREVIATIONS **TIL – tryptophan indole-lyase; PLP – pyridoxal-5'-phosphate; SOPC – S-*o*-nitrophenyl-L-cysteine; LDH – lactate dehydrogenase; NADH – nicotinamide-adenine dinucleotide; SKIE – solvent kinetic isotope effect.**

INTRODUCTION

In studies focused on enzymic mechanisms, the basic notion frequently taken into account is that completion of any stage of the process creates favorable chemical and conformational prerequisites for the subsequent stages [1]. In this context, the mechanisms of enzymes displaying broad substrate specificities are of considerable interest, since some situations arising in the active site depending on the chemical nature of the substrate may violate the aforementioned principle. Tryptophan indole-lyase (TIL), also known as tryptophanase (EC 4.1.99.1), is a pyridoxal-5'-phosphate (PLP)-dependent enzyme catalyzing the reversible α,β-elimination of L-tryptophan with the formation of indole and ammonium pyruvate.

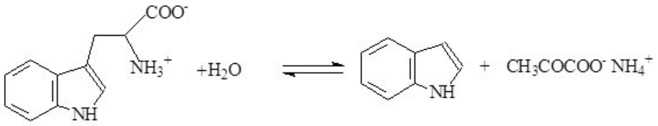

The other substrates of TIL are tryptophan analogs substituted at various positions of the indole ring [2, 3], benzimidazole analogs of tryptophan [4], as well as amino acids containing suitable leaving groups at the β-carbon atom, including S-(o-nitrophenyl)-L-cysteine (SOPC) [5], S-alkyl-L-cysteine analogs [6], β-chloro-L-alanine [5], and L-serine [6] and O-acyl-L-serines [7].

The three-dimensional structure was established by X-ray analysis for TIL from *Escherichia coli* [8–10] and for the enzyme from *Proteus vulgaris* [11]. The catalytic mechanism of TIL was studied in detail in [12–16]; the role of specific residues in the mechanism of TIL was elucidated in [17–20].

Scheme shows the catalytic mechanism of TIL with its natural substrate, L-tryptophan, which is in agreement with the known X-ray and kinetic data. The key stages in this mechanism involve the abstraction of the α-proton of external aldimine under the action of the side amino group of the lysine 270 residue, and subsequent elimination of the side indole group assisted by proton transfer from phenol hydroxyl of the tyrosine 74 residue to the 3-position of the leaving indole group. According to the data reported in [16], proton transfer and breaking of the C–C bond proceed almost simultaneously. It was determined in [21] that enzymic decomposition of L-tryptophan is accompanied by a considerable intramolecular transfer of the C_α proton of the substrate to the 3-position of the indole that has been formed. Since the lysine 270 and tyrosine 74 residues are far apart from each other and are located on opposite sides of the cofactor plane, direct transfer of a proton between them seems improbable. Therefore, the observed intramolecular transfer [21] might be a result of the existence of a chain of hydrogen bonds between several residues, which renders the observed transfer possible. Convincing X-ray evidence of the existence of such a

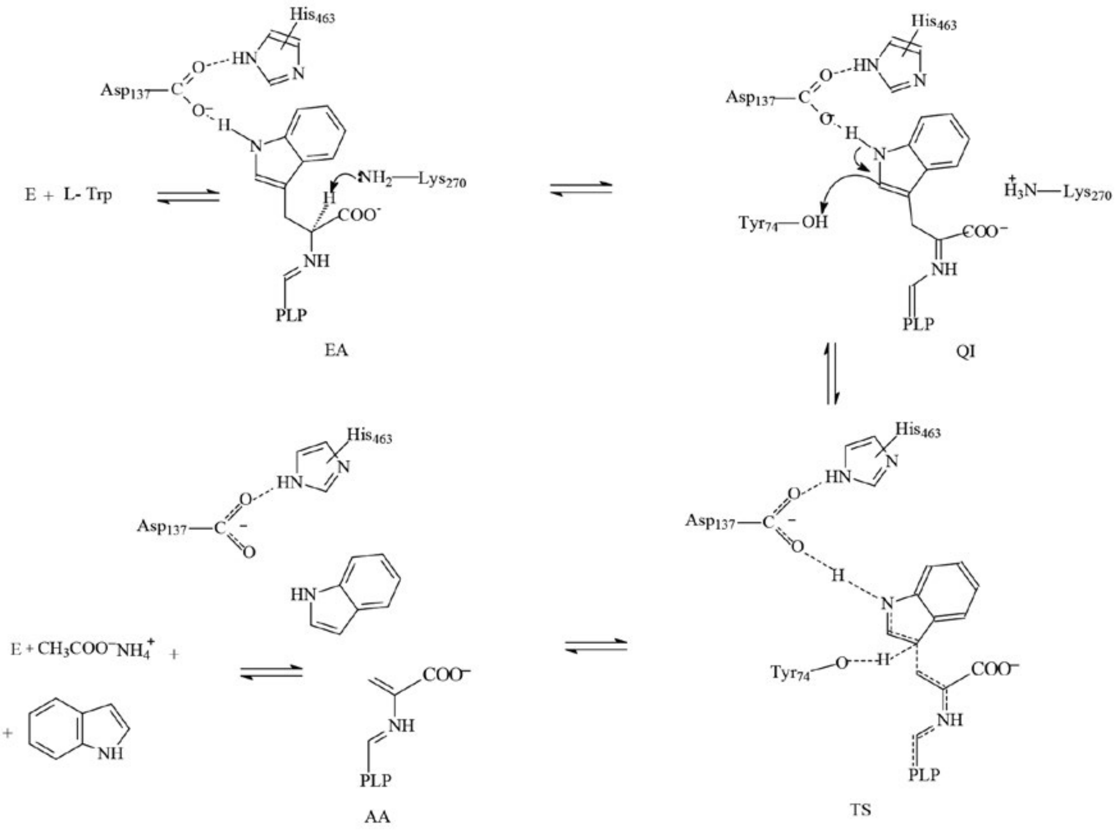

Scheme The principal mechanism of the reaction between TIL and *L*-tryptophan, which is consistent with [12–18]. E – internal aldimine; EA – external aldimine; QI – quinonoid intermediate; TS – transition state; and AA – aminoacrylate chain was presented in [20]. In α,β-elimination reactions with substrates containing bad leaving groups (e.g., L-serine), general acid catalysis is required at the stage of the leavinggroup elimination. During this stage, formal transfer of a proton (either directly or through the chain of hydrogen bonds) from the C_α position of the substrate to the leaving group takes place; the latter is eliminated in the form of the respective conjugated acid. As a result, the base that has originally accepted the α-proton should appear as the respective conjugated base once the leaving group has been eliminated. β-Chloro-L-alanine is known to be a good substrate for α,β- and α,γ-eliminating lyases. In the reactions with this substrate, the role of the leaving group is played by a chlorine anion. No general acid catalysis is needed with such a leaving group; in this case, it cannot even be implemented, since the enzymes carry no functional groups whose acidities are strong enough for the acids to give away their protons to a base as weak as the chlorine anion. Consequently, the catalytic group that had originally accepted the α-proton from the substrate should appear in its acidic, rather than basic, form at the following stage. We believe that it is of considerable interest what mechanistic consequences the change in the ionic state of this group has. Two possibilities seem plausible: (1) the emergence of a new acidic group in the pH profile of kinetic parameters, which is associated with the necessity of a transition of the group that has accepted the α-proton into its basic form; (2) changes in the mechanism of the stage(s) following the elimination brought about by the changes in the ionic state of the aforementioned catalytic group. In the present work, we attempted to shed light on this question by considering the pH dependencies of the main kinetic parameters of the reactions of TIL from *Escherichia coli* with L-serine and β-chloro-L-alanine, as well as the kinetic isotope effects resulting from the replacement of ordinary water, as a solvent, for ^2H_2O.

EXPERIMENTAL

The reagents used in this work were purchased from Sigma-Aldrich. The isotopic purity of ^2H_2O was 99%.

Enzyme

Tryptophan indole-lyase was isolated from *E. coli* JM101 cells containing plasmid pMD6 with the *E. coli tna*A gene, as described in [22]. Enzyme concentrations were estimated from the absorbance of the holoenzyme at 278 nm ($A_{1\%}$ = 9.19) [23] using a subunit molar mass of 52 kDa [24].

The activity of TIL was determined using S-o-nitrophenyl-L-cysteine (SOPC) as a substrate. The reaction mixture contained 0.6 mmol SOPC, the enzyme, 0.12 M potassium phosphate buffer (pH 7.8), 3 mM dithiothreitol, 0.06 mM PLP, and 10% glycerol. Activity was measured at 30°C according to the decline in SOPC absorbance at 370 nm (ε = -1860 $M^{-1}min^{-1}$). One unit of activity was assumed equal to the amount of enzyme catalyzing the decomposition of one micromole of SOPC per minute under standard conditions. SOPC was synthesized as described in [25].

Table. The solvent isotope effect on the kinetic parameters of the TIL reactions with L-serine and β-chloro-*L*-alanine

Substrate	Parameter	SIE
L-serine	V/*K*	3.5 ± 0.5
L-serine	V	0.8 ± 0.2
β-chloro-*L*-alanine	V/*K*	2.2 ± 0.5
β-chloro-*L*-alanine	V	3.6 ± 1.2

Steady-state kinetic measurements were performed at 30°C using the lactatedehydrogenase (LDH) coupled assay. Reaction mixtures contained 0.2 mM NADH, 8 units of LDH, and 0.2 μM TIL in 0.1 M potassium phosphate or borate buffer solutions in the presence of 0.1mM PLP at various pH and substrate concentrations. The reaction rates were determined at 30°C according to the decline in absorbance of NADH at 340 nm (ε = - 6220 $M^{-1}cm^{-1}$).

Determination of the solvent kinetic isotope effect (SKIE)

The potassium phosphate buffer solution (20 ml, pH 8.2) was evaporated to dryness in vacuum. The residue was vacuum-dried over $CaCl_2$ and dissolved in 20 ml of ^2H_2O. The obtained buffer solution was used for kinetic studies under conditions analogous to those described earlier for solutions in water.

Comparing the kinetic parameters for the reactions in water and ^2H_2O allowed us to collect the data presented in *Table*. The steady-state kinetic data were analyzed using the Cleland's FORTRAN programs [26].

RESULTS AND DISCUSSION

In the present work, we have studied the pH dependencies of the main kinetic parameters for the reactions of TIL with L-serine and β-chloro-L-alanine. The results were compared with the literature data for the reaction of TIL with its natural substrate, L-tryptophan [13]. For this reaction, the pH dependence of V/*K* can be described by equation (1) with two pKs equal to 7.6 and 6.0.

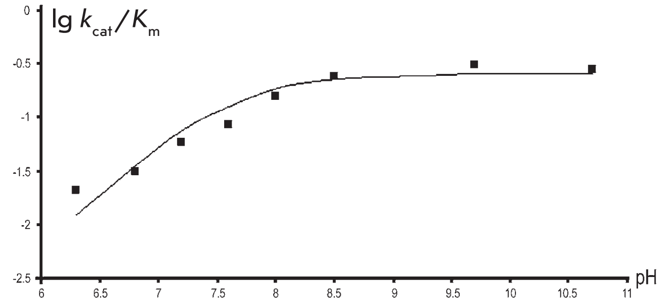

Fig. 1. The pH dependence of V/K for the reaction between TIL and *L*-serine. The points denote the experimentally determined values obtained by data-fitting to the Michaelis–Menten equation, while the curve was plotted by fitting the resulting values using Eq. (2) where $pK_a = 7.6$

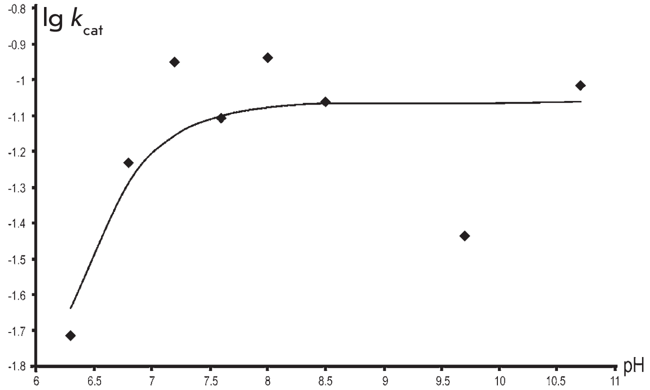

Fig. 2. The pH dependence of V for the reaction between TIL and L-serine. The points are the experimentally determined values obtained by fitting the data to the Michaelis–Menten equation, while the curve was plotted by fitting the resulting values using Eq. (1), where $pK_a = pK_b = 6.3$

$$\frac{k_{cat}}{K_m} = \frac{C}{1 + \frac{H}{K_a} + \frac{H^2}{K^1{}_a K^2{}_a}}, \qquad (1)$$

where $pK_a = 7.6 \pm 0.09$, $K_b = 6.0 \pm 0.2$.

The value of 7.6 can be ascribed to the amino group of the Lys270 residue, which is responsible for the abstraction of the C_α proton of the external aldimine, whereas the p*K* equal to 6.0 can be ascribed to the side group of Asp137 interacting with nitrogen of the indole moiety at the stage of substrate binding [15, 17], which leads to activation of the indole group as a leaving group.

We have shown that pH dependence of V/*K* for the reaction with L-serine (*Fig. 1*) could be described by equation (2) with one p*K* equal to 7.6.

$$\frac{k_{cat}}{K_m} = \frac{C}{\left(1 + \frac{H}{K_a}\right)}, \qquad (2)$$

where $pK_a = 7.6 \pm 0.1$.

A conclusion can be drawn that ionization of the acidic group of Asp137, which takes part in the activation of the leaving indole group in the reaction with the natural substrate, is not reflected in the pH dependence for the reaction with L-serine. We may assume that serine conformation in the active site is analogous to that of tryptophan in the sense that the position of hydroxylic oxygen strictly corresponds to the position of the C_γ atom of the indole ring. In this case, according to the X-ray data [20], hydroxylic oxygen of L-serine should be located in close proximity to the phenol group of the Tyr74 residue, which is connected to the amino group of the Lys270 residue by a chain of hydrogen bonds [20]. In the course of α,β-elimination, a proton from the ammonium group of Lys270 is transferred to Tyr74 through the chain of hydrogen bonds. The Tyr74 residue donates its own proton to the hydroxylic group of serine, which is eliminated as water. The ionic states of all the participants in this process, except for Lys270, remain unchanged, and the whole process may be considered a formal transfer of a proton from Lys270 to the leaving group. It seems probable that, in the pH range under study, the phenol group of the Tyr74 residue remains in its acidic form, which is needed for the reaction to proceed. This explains the absence of the respective p*K* in the pH dependence.

Figure 2 shows the pH dependence of k_{cat} for the reaction of TIL with L-serine, which can be described by an equation with two similar p*K*s (Eq. (1), where $pK_a = pK_b = 6.3 \pm 0.1$). At the same time, it was established for the reaction of TIL with L-tryptophan [13] that k_{cat} is independent of pH, thus providing evidence for a protonation mechanism in which the substrate binds only to the correctly protonated enzyme form. As a result, the enzyme–substrate complex forms, being inaccessible to protons from the environment. It seems probable that in the reaction with L-serine containing a small side group, the latter occupies less space in the active site. Therefore, hydroxonium cations from the external solvent are able to penetrate into the enzyme–substrate complex and protonate certain functional groups, thus making the reaction impossible. We have shown that for the reaction of TIL with β-chloro-L-alanine the pH dependence of V/*K* (*Fig. 3*) is virtually identical to a similar dependence for the reaction with L-serine. It can be described by an equa-

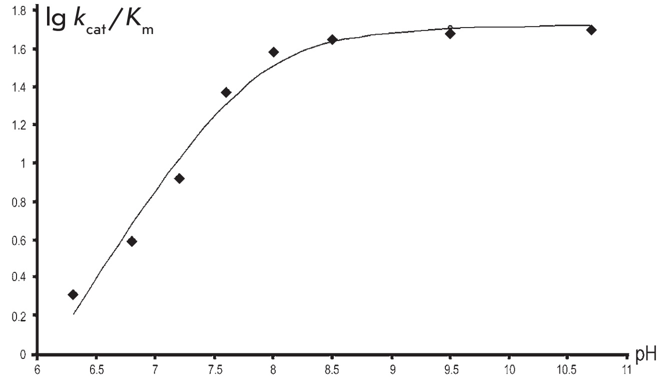

Fig. 3. The pH dependence of V/K for the reaction between TIL and β-chloro-L-alanine. The points are the experimentally determined values obtained by data-fitting to the Michaeli–Menten equation, while the curve was plotted by fitting the resulting values using Eq. (2), where $pK_a = 7.8$

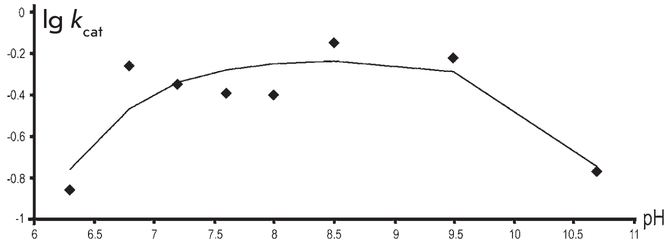

Fig. 4. The pH dependence of V for the reaction between TIL and β-chloro-L-alanine. The points are the experimentally determined values obtained by data-fitting to the Michaelis–Menten equation, while the curve was plotted by fitting the resulting values using Eq. (3), where $pK_a = 6.7$, $pK_b = 10.3$

tion with one pK_a (Eq. (2)) equal to 7.8 ± 0.1. Meanwhile, the pH dependence of V has a fundamentally different, bell-shaped appearance (Fig. 4) and can be described by Eq. (3):

$$k_{cat} = \frac{C}{\left(1 + \frac{H}{K_a} + \frac{K_b}{H}\right)}, \tag{3}$$

where $pK_a = 6.7 \pm 0.2$; $pK_b = 10.3 \pm 0.2$.

As it was mentioned above, the reaction with β-chloro-L-alanine is most likely to proceed without activation of the leaving group, which is eliminated as a chlorine anion. As a consequence, the situation in the active site immediately after the elimination of Cl^- should fundamentally differ from that in the reaction with L-serine, because the proton originally bound to the α-carbon atom of the substrate in the reaction of β-chloro-L-alanine remains in the active site, while it is withdrawn from the active site together with the leaving group in the reaction with L-serine. We may assume that the pK_b value = 10.3, which was observed in the pH profile of V for the reaction of β-chloro-L-alanine, reflects the acidic dissociation of exactly this additional proton in the enzyme–substrate complex. The observed *decrease* in V can be associated with a given catalytic function fulfilled by the respective *acidic* group during chemical transformations following the elimination of the chlorine anion.

In order to conduct a detailed study of the roles played by various elementary stages in the mechanisms of reactions with nonstandard substrates, we examined the kinetics of the reactions of TIL with β-chloro-L-alanine and L-serine in water and ^2H_2O in the optimal pH range and determined the solvent isotope effects on the main kinetic parameters. These results are presented in *Table*. Unlike in the reaction with a natural substrate, reactions of TIL with L-serine and with β-chloro-L-alanine proceed only in the direction of substrate decomposition, but not their synthesis. Thus, the α,β-elimination yielding an aminoacrylate intermediate in the active site is irreversible in this reaction. Taking this fact into account, we considered the mechanisms of both reactions under the following kinetic scheme (scheme 2):

$$E + S \overset{K_S}{\rightleftharpoons} ES \underset{k_r}{\overset{k_f}{\rightleftharpoons}} EQ \xrightarrow{k_e} EA \xrightarrow{k_h} P,$$

where E is the internal aldimine, ES is the external aldimine, EQ is the quinonoid intermediate, EA is the aminoacrylate complex, and P is the reaction product (pyruvate).

For the presented kinetic scheme, the main kinetic parameters are described by Eqs. (4) and (5).

$$\frac{k_{cat}}{K_m} = \frac{k_e k_f}{K_s (k_e + k_r)}, \tag{4}$$

$$k_{cat} = \frac{k_h k_e k_f}{k_h (k_f + k_e + k_r) + k_e k_f}. \tag{5}$$

One can see that the solvent isotope effect on V/K for the reaction between TIL and L-serine is equal to 3.5 (see *Table*). Among the constants in Eq. (4), k_e is not isotope-sensitive if the abstraction of the C_α proton under the action of the Lys270 amino group occurs directly. On the contrary, the k_r value should be isotope-sensitive because this constant refers to the return of

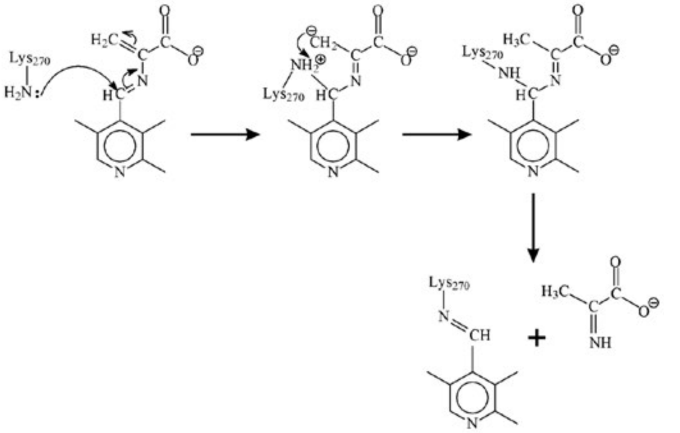

Fig. 5. The possible scheme of aminoacrylate hydrolysis in the reaction between TIL and L-serine

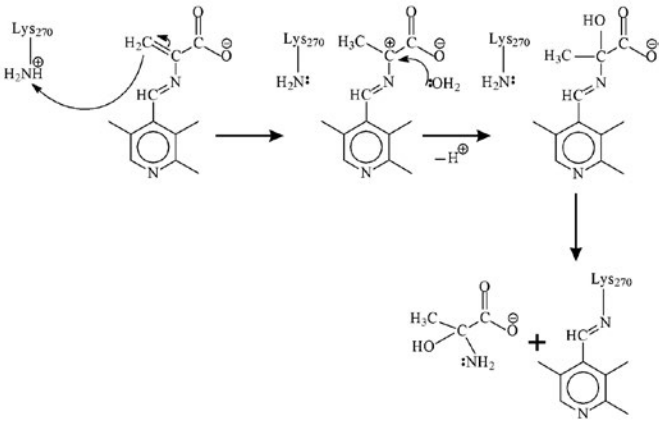

Fig. 6. The possible scheme of aminoacrylate hydrolysis in the reaction between TIL and β-chloro-L-alanine

a proton to the C_α atom of the quinonoid intermediate under the action of the ammonium group of Lys270, which contains at least two deuterons in ^2H_2O, and even three deuterons if isotopic exchange with the solvent proceeds sufficiently fast. However, as it follows from Eq. (4), this effect should accelerate the reaction in ^2H_2O, whereas in fact we observed that it slowed down. Hence, a conclusion can be drawn that elimination of the leaving hydroxylic group is the only stage determining the observed solvent isotope effect, since it assumes that a proton is transferred from Lys270 to Tyr74 through the chain of hydrogen bonds, and then to the hydroxylic oxygen. When ordinary water used as a solvent is replaced with ^2H_2O, all the protons involved in this transfer are exchanged for deuterons and the process is expected to slow down. It follows from the data presented in *Table* that the solvent isotope effect on V within the experimental error does not differ from unity. This probably results from the fact that a new constant, $k_{h,}$ appears in Eq. (5) describing k_{cat}; Eq. (4) did not contain this constant. It determines the rate of aminoacrylate hydrolysis. It is evident that when $k_h (k_f + k_t + k_r) << k_e k_f$, the k_{cat} value should be equal to the k_h ($k_{cat} \sim k_h$) value. The k_h constant is apparently rate-limiting; on the other hand, it is insensitive to the solvent isotope effect. In the case of the TIL reaction with β-chloro-L-alanine, the elimination of the leaving group should not be accompanied by proton transfer to the chlorine anion being eliminated. Consequently, the stage described by the k_e constant should not be isotope-sensitive. Everything that has been said about the k_f and k_r constants in the reaction with L-serine should also be true for the reaction with β-chloro-L-alanine. Therefore, it seems reasonable to suggest that there is no solvent isotope effect on the V/*K* parameter. However, an isotope effect equal to 2.2 is in fact observed. A plausible explanation is that the stage of C_α-proton abstraction (k_f) may proceed not directly but through a water molecule (or molecules), which is expected to reduce k_f when the solvent is changed from water to ^2H_2O. A similar phenomenon can also take place in the reaction with L-serine. In this case, the solvent isotope effect on V/*K*, observed for this reaction, can be associated not only with the stage of aminoacrylate formation.

For the reaction with β-chloro-L-alanine, the solvent isotope effect on parameter V is equal to 3.6 (see *Table*). Therefore, the emergence of the rate of aminoacrylate hydrolysis (k_h) in Eq. (5) considerably increases the isotope effect, contrary to its decline in the L-serine reaction. It is fair to conclude that aminoacrylate hydrolysis is an isotope-sensitive stage in the reaction with β-chloro-L-alanine; the hydrolysis mechanism differs significantly from that in the reaction with L-serine. In the reaction with L-serine, the amino group of Lys270 exists in its basic form at the stage of aminoacrylate hydrolysis. The attack of the lysine amino group at the aldimine double bond of the aminoacrylate intermediate is probably the rate-limiting stage of hydrolysis (see *Fig. 5*). Since no transfer of protons that could be exchanged for deuterons accompanies the limiting stage, the hydrolysis should be insensitive to solvent replacement. On the other hand, in the reaction with β-chloro-L-alanine, a similar limiting stage cannot be implemented because the side amino group of Lys270 is present in its acidic---ammonium---form containing the additional proton. The ammonium group can donate this additional proton to the methylene group of aminoacrylate, most probably through the chain of hydrogen bonds (see *Fig. 6*). Since the protons of the ammonium group and those participating in the chain of hydrogen bonds can undergo isotopic exchange with the solvent, aminoacrylate hydrolysis should be an isotope-sensitive stage, which was actually observed.

CONCLUSIONS

Hence, the results of our work show that the changes in the nucleophilic nature of the leaving group in TIL substrates may alter not only the mechanism of elimination of the leaving group, but also the mechanism of the subsequent stage of aminoacrylate hydrolysis. ●

This work was supported by the Russian Foundation for Basic Research (grant No. 16-04-00947). Spectral characterization and elemental analysis were performed with the financial support from the Ministry of Science and Higher Education of the Russian Federation using the facilities of the Center for Molecule Composition Studies of the A.N. Nesmeyanov Institute of Organoelement Compounds, Russian Academy of Sciences.

REFERENCES

1. Ivanov V.I., Karpeisky M.Ya. // Adv. Enzymol. Relat. Areas Mol. Biol. 1969. V. 32. P. 21–53.
2. Lee M., Phillips R.S. // Bio. Med. Chem. 1995. V. 3. № 2. P. 195–205.
3. Faleev N.G., Gogoleva O.I., Dementieva I.S., Zakomirdina L.N., Belikov V.M. // Biochem. Mol. Biol. Int. 1994. V. 34. № 1. P. 209–216.
4. Harris A.P., Phillips R.S. // FEBS J. 2013. V. 280. № 8. P. 1807–1817.
5. Suelter C.H., Wang J., Snell E.E. // FEBS Lett. 1976. V. 66. № 2. P. 230–232.
6. Watanabe T., Snell E.E. // J. Biochem. (Tokyo) 1977. V. 82. № 3. P. 733–745.
7. Phillips R.S. // Arch. Biochem. Biophys. 1987. V. 256. № 1. P. 302–310.
8. Dementieva I.S., Zakomirdina L.N., Sinitzina N.I., Antson A.A., Wilson K.S., Isupov M.N., Lebedev A.A., Harutyunyan E.H. // J. Mol. Biol. 1994. V. 235. № 2. P. 783–785.
9. Kogan A., Gdalevsky G.Y., Kohen-Luria R., Parola A.H., Golggur Y. //Acta Cryst. D60. Pt 11. P. 2073–2075.
10. Tsesin N., Kogan A., Gdalevsky G., Himanen J.-P., Cohen-Luria R., Parola A., Goldgur Y., Almog O. // Acta Cryst. D. Biol. Cryst. 2007. V. 63. Pt. 9. P. 969–974.
11. Isupov M.N., Antson A.A., Dodson E.J., Dodson G.G., Dementieva I.S., Zakomyrdina L.N., Wilson K.S., Dauter Z., Lebedev A.A., Harutynyan E.H. // J. Mol. Biol. 1998. V. 276. № 3. P. 603–623.
12. Phillips R.S., Miles E.W., Cohen L.A. // Biochemistry. 1984. V. 23. № 25. P. 6228–6234.
13. Kiik D.M., Phillips R.S. // Biochemistry. 1988. V. 27. № 19. P. 7339–7344.
14. Phillips R.S. // J. Am. Chem. Soc. 1989. V. 111. № 2. P. 727–730.
15. Phillips R.S. // Biochemistry.1991. V. 30. № 24. P. 5927–5934.
16. Phillips R.S., Sundararaju B., Faleev N.G. // J. Amer. Chem. Soc. 2000. V. 122. № 6. P. 1008–1014.
17. Demidkina T.V., Antson A.A., Faleev N.G., Phillips R.S., Zakomirdina L.N. // Mol. Biol. 2009. V. 43. № 2. P. 269–283.
18. Demidkina T.V., Zakomirdina L.N., Kulikova V.V., Dementieva I.S., Faleev N.G., Ronda L., Mozzarelli A., Gollnick P.D., Phillips R.S. // Biochemistry. 2003. V. 42. № 38. P. 11161– 11169.
19. Kulikova V.V., Zakomirdina L.N., Bazhuina N.P., Dementieva I.S., Faleev N.G., Gollnick P.D., Demidkina T.V. // Biochemistry (Moscow). 2003. V. 68. № 11. P. 1181–1188.
20. Phillips R.S., Buisman A.A., Choi S., Hussaini A., Wood Z.A. // Acta Crystallogr. D Struct. Biol. 2018. V. 74(Pt 8). P. 748–759. doi: 10.1107/S2059798318003352.
21. Vederas J.C., Schleicher E., Tsai M.D., Floss H.G. // J. Biol. Chem. 1978. V. 253. № 15. P. 5330–5334.
22. Phillips R.S., Gollnick P.D. // J. Biol. Chem. 1989. V. 264. № 18. P. 10627–10632.
23. Dua R.K., Taylor E.W., Phillips R.S. // J. Amer. Chem. Soc. 1993. V. 115. № 4. P. 1264–1270.
24. Kagamiyama H., Wada H., Matsubara H., Snell E.E. // J. Biol. Chem. 1972. V. 247. № 5. P. 1571–1575.
25. Phillips R.S., Ravichandran K., von Tersch R.L. // Enz. Microb. Technol. 1989. V. 11. № 2. P. 80–83.
26. Cleland W.W. // Methods Enzymol. 1979. V. 63. P. 103–138.

An Abnormally High Closing Potential of the OMPF Porin Channel from *Yersinia Ruckeri*: The Role of Charged Residues and Intramolecular Bonds

D. K. Chistyulin[1*#], O. D. Novikova[1], E. A. Zelepuga[1*], V. A. Khomenko[1], G. N. Likhatskaya[1], O. Yu. Portnyagina[1], Y. N. Antonenko[2]
[1]Elyakov Pacific Institute of Bioorganic Chemistry, Far Eastern Branch, Russian Academy of Sciences, Prospect 100 let Vladivostoku 159, Vladivostok, 690022, Russia
[2]Belozersky Institute of Physico-Chemical Biology, Lomonosov Moscow State University, Leninskie Gory 1/40, Moscow, 119991, Russia
[*]E-mail: cdk27@mail.ru, zel@piboc.dvo.ru
[#]Equally contributed

Received April 11, 2019; in final form, May 17, 2019
DOI: 10.32607/20758251-2019-11-3-89-98

Copyright © 2019 National Research University Higher School of Economics. This is an open access article distributed under the Creative Commons Attribution License,which permits unrestricted use, distribution, and reproduction in any medium, provided the original work is properly cited.

ABSTRACT **Electrophysiological experiments on bilayer lipid membranes showed that the isolated outer membrane major porin of *Yersinia ruckeri* (YrOmpF) exhibits activity typical of porins from Gram-negative bacteria, forming channels with a mean conductance of 230 pS (in 0.1 M KCl) and slight asymmetry with respect to the applied voltage. Under acidic conditions (up to pH = 3.0), there was no significant decrease in the total conductance of the YrOmpF channel reconstituted into the bilayer. The studied channel significantly differed from the porins of other bacteria by high values of its critical closing potential (Vc): Vc = 232 mV at pH = 7.0 and Vc = 164 mV at pH = 5.0. A theoretical model of the YrOmpF spatial structure was used for the analysis of the charge distribution in the mouth and inside the channel to explain these properties and quantitatively assess the bonds between the amino acid residues in the L3 loop and on the inner wall of the barrel. The parameters of YrOmpF were compared with those of the classical OmpF porin from *E. coli*. The results of electrophysiological experiments and theoretical analysis are discussed in terms of the mechanism for voltage-dependent closing of porin channels.**

KEYWORDS ***Yersinia ruckeri*, pore-forming proteins, bilayer lipid membranes, voltage-dependent gating.**

ABBREVIATIONS **YrOmpF – *Yersinia ruckeri* OmpF porin; EcOmpF – *Escherichia coli* OmpF porin; Vc – critical voltage; OM – outer membrane; AA – amino acid; MD – molecular dynamics; BLM – bilayer lipid membrane; octyl-POE – *n*-octylpolyoxyethylene; DPhPC – 1,2-diphytanoyl-sn-glycero-3-phosphocholine.**

INTRODUCTION

Yersinia ruckeri is a Gram-negative bacterium that causes yersiniosis in fish, mainly in salmonids. Like other yersinia, this pathogen is able to survive and maintain virulence in various environmental conditions and in a wide temperature range. *Y. ruckeri* causes outbreaks of the disease in aquaculture fish, which leads to large economic losses each year [1–4].

Porins, along with lipopolysaccharide, are known to be a quantitatively dominant component of the outer membrane (OM) of Gram-negative bacteria and to play a crucial role in the adaptation of microorganisms to changing environmental conditions. Like transmembrane proteins, they form a system of channels for the passive transport of low-molecular-weight hydrophilic compounds through the bacterial OM. The main functional unit of porins is a homotrimer [5, 6]. The protein monomer is an ellipsoid beta-folded cylinder (barrel) consisting of antiparallel beta strands connected by segments (external loops) with an alpha-helical or disordered structure. The inner part of the porin monomer channel is the hydrophilic surface of the beta-barrel, and the outer part is formed by adjacent parts of the loops (the pore mouth and vestibule region). The pore vestibule is in immediate contact with a fragment of the adjacent barrel's loop L2 that is directed away from "its" monomer. In the channel center, there is the longest loop L3 that, unlike the others extending outside the barrel, is inserted into the middle of the pore, thereby limiting its size and forming a narrowing, the so-called constriction zone or pore eyelet. The barrel wall consists mainly of positively charged amino acid (AA) residues; on the contrary, the L3 loop contains a large number of acidic AA residues. The spatial configuration of charged AA residues is such that an electrostatic field is generated inside the channel and underlies the channel's selectivity for the charges of penetrating ions and hydrophilic compounds [7].

Electrophysiological experiments performed on nonspecific porins from *Escherichia coli* have demonstrated that the OmpF protein channel occurs in an open state most of the time, ensuring the entry of ions and hydrophilic molecules into the cell. However, most porins can switch to a stable, closed state; e.g., upon increasing medium acidity and/or under an applied external voltage (voltage-dependent closure) [8–14].

With regard to the biological function of these channel properties, various hypotheses are put forward. In particular, this may be due to the closing of the channels of improperly incorporated proteins and may also be the protective (as the medium pH decreases) or even regulatory transport function of porins (e.g., in proteins with a very low critical channel closure voltage, Vc) [15, 16]. However, all the proposed explanations are not sufficiently convincing and, perhaps, this property may be considered only as an unusual artifact [17].

Various suggestions for the mechanism of voltage-dependent closure of porin channels (gating mechanism) have been proposed. Based on molecular dynamics (MD) data, a model of a movable loop L3 whose displacement leads to channel blockage was proposed as a possible gating mechanism [18]. However, because this loop has many interactions with the barrel wall (salt bridges, hydrogen bond network), this idea seems unlikely. In addition, the closing of the channel is not accompanied by significant changes in the loop's position: there are no noticeable differences in this property in *E. coli* OmpF whose L3 loop is modified with disulfide bridges [19, 20]. This fact indicates that a potential cause of channel blockage may be local changes in the tertiary structure of some L3 loop fragments. MD studies of perturbations have suggested that at least part of loop L3 from *R. capsulatus* porin is flexible [21]. This part may well correspond to the region immediately following the conserved PEFGG sequence motif found in OmpF from *Escherichia coli*. Indeed, replacement of two glycine residues in PEFGG led to a change in the functional properties of the channel [22]. It is worth noting that the hypotheses explaining the voltage-dependent closing of the channels of the pore-forming proteins, as well as the facts underlying those hypotheses, are quite contradictory. For example, the charged AA residues located inside the barrel and generating the electrostatic field are known to strongly affect the Vc value. Moreover, the replacement of negatively and positively charged residues with neutral ones has a different effect on porins of different types. For example, PhoE from *E. coli*, which is selective for negative ions, decreases Vc in response to a substitution of acidic residues in the L3 loop by neutral ones, while cation-selective OmpF from *E. coli* increases Vc. On the contrary, substitution of basic residues in the barrel increases Vc in PhoE and decreases Vc in OmpF [23].

However, based on the hypothesis of a flexible loop L3, the inconsistency of experimental facts may be explained by a dual role of charged AA residues. On the one hand, these residues are involved, through hydrogen and ionic bonds, with neighboring AA residues in the channel tertiary structure formation and, therefore, in the stabilization of the channel open state. On the other hand, they are sensors of the electric field and promote the transition of the channel to a closed state. In this case, their sensitivity to changes in the membrane potential, in combination with localization in the long and rather mobile L3 loop, may cause conformational changes in the L3 loop. This is explained by the fact that the transport of molecules through the pore is accompanied by a redistribution of water molecules (or counterions) inside the channel and a related reorientation of the side chains of AA residues in the channel. As a result, there may be local displacements within the L3 loop, which could lead to closure of the pore [13, 24].

In this work, we characterized the electrophysiological properties of the porin channels OmpF from the OM of *Y. ruckeri* (YrOmpF) and OmpF from *E. coli* (EcOmpF) using artificial bilayer lipid membranes (BLMs); namely, we determined single channel conductance for these proteins and critical closing potentials in neutral and slightly acidic media. We also investigated the changes in the total conductance of the channels during stepwise changes in the medium pH to a pH of 3.0. We used spatial models of YrOmpF and EcOmpF for a comparative analysis of the charged AA distribution in the mouth, vestibule, and inside the channel of both proteins, as well as for a quantitative assessment of the intramolecular bonds within the L3 loop. Given the decisive importance of these data for characterizing the functional properties of porin channels, this comparison was of particular interest, because the OmpF porin from *Y. ruckeri* differs in its number of acidic AA residues in the L3 loop from the classical OmpF porin of *E. coli*. The calculated data enabled the identification of a more rigid L3 loop conformation in YrOmpF, which obviously affects the open state stability of its channel and underlies the higher Vc value.

EXPERIMENTAL

Microorganisms

Y. ruckeri (strain KMM 821) was used in the study. Microorganisms were cultured in 2×YT medium at 6 °C as described in [25] and were harvested at the logarithmic growth phase. Then, the cell suspension was centrifuged at 5,000 g and the resulting pellet was washed twice with physiological saline.

Preparation of peptidoglycan-associated protein fractions and isolation and purification of YrOmpF porin

Y. ruckeri bacteria were destroyed by ultrasound using a disintegrator (UZDN-2T, Russia) at 44 MHz (10 times for 1 min with a 1–2 min break to cool the mixture) in an ice bath. Undisrupted cells were removed by centrifugation at 5,000 g for 10 min, and the supernatant was centrifuged at 20,000 g for 1 h. The resulting crude membrane fraction in the form of a pellet was treated with 0.5% nonionic detergent *n*-octyl-polyoxyethylene (POE) in 10 mM phosphate buffer pH 8.5 (buffer A), according to the Garavito procedure [26]. The target protein in the extracts was determined by denaturing polyacrylamide gel electrophoresis (SDS-PAGE) [27]. Fractions containing maximum amounts of oligomeric YrOmpF were pooled and purified by ion exchange chromatography on DEAE-Sepharose CL 6B; the protein was eluted with buffer A containing 0.1% Zwittergent 3-14, using a 0.137–0.5 M NaCl gradient. Homogeneous electrophoretically pure YrOmpF was eluted with 0.4 M NaCl, which was confirmed by SDS-PAGE. This sample was used in the electrophysiological experiments.

Electrophysiological experiments

BLMs were prepared according to the Mueller–Rudin technique [28] from a diphytanoylphosphatidyl choline (DPhPC) solution in *n*-heptane (5 mg/mL) in Teflon cells separated by a septum with 1-mm holes for the total current and 0.25-mm holes for single channels. The aqueous phase contained 0.1 or 1 M KCl in the following buffer: 10 mM Tris-HCl, 10 mM MES, and 10 mM beta-alanine (pH 7.0, 5.0, and 2.8). The ion current was detected by a pair of Ag/AgCl electrodes in voltage detection mode. The electrode on the *cis* membrane side was grounded, and that on the *trans* side was connected to a BC-525C amplifier (Warner Instrunments, USA). Measurements were carried out at room temperature. A protein solution was added to the *cis* side of the cell, and, by raising the voltage to 200 mV, channels were inserted. The total current through the BLM was recorded at a YrOmpF concentration of 50–500 ng/mL; single protein channels were obtained at a concentration of 5–20 ng/mL. Changes in the current through the BLM were recorded in the presence of the protein dissolved in neutral or acidic buffer at various membrane potential values (50 to 150 mV).

Theoretical analysis of intramolecular bonds

To generate a theoretical model of the spatial *Y. ruckeri* OmpF structure, we used the AA sequence of porin E2FHC9 from the Uniprot database [29]; the atomic coordinates of *E. coli* OmpF porin (PDB ID 2OMF) were used as a prototype. Homologous models were generated using the MOE software as described previously [30]. The models were optimized with the MOE 2018.0101 program and Amber10:EHT force field [31]. According to the Ramachandran map, about 96.4% of residues in the generated models of the YrOmpF and EcOmpF channels occurred in a favorable conformation and 3.6% of residues were in an allowable conformation. This indicated that these models might be used for further investigation. The energy contribution of intramolecular non-covalent interactions to the porin structure formation was analyzed and evaluated using the MOE 2018.0101 program [31]. The geometric and physicochemical parameters of the pore's interior were estimated using a distant MOLE online resource [32].

RESULTS AND DISCUSSION

Electrophysiological properties of YrOmpF in neutral and acidic media

Figure 1 shows changes in the total electrical conductance of a planar DPhPC bilayer membrane under a voltage of ± 50 mV in the presence of YrOmpF or EcOmpF at various pH values. The current fluctuations (initial parts of the curves) illustrate an active stepwise increase in the membrane conductance upon addition of porins at a concentration of 100 ng/mL into the aqueous phase (buffer pH 7.0). This effect, characteristic of Gram-negative bacterial porins, reflects the incorporation of functionally active protein trimers.

To evaluate the potential effect of medium acidity on the functional activity of YrOmpF reconstituted in the lipid bilayer, the aqueous phase in both parts of the cell was sequentially acidified to pH 5.0 and 3.0 during the experiment. The current recordings shown in *Fig. 1B* (second and third segments) demonstrate that as the medium pH decreases, the membrane conductance increases. In this case, the single channel conductance does not change, which means that this effect illustrates a sharp activation of protein incorporation into the membrane.

At a medium pH of 3.0 (the third curve segment), the total conductance of the YrOmpF channel sharply decreases and then gradually recovers. Current recordings under these conditions are characterized by

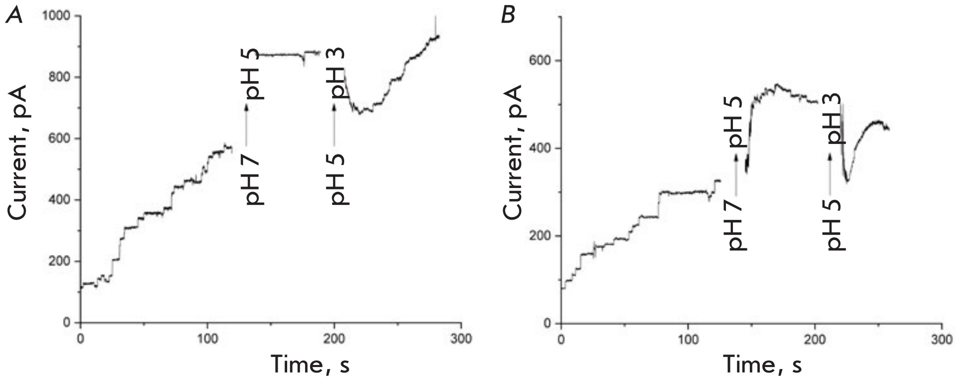

Fig. 1. Channel conductance of *Y. ruckeri* OmpF (YrOmpF) and *E. coli* OmpF (EcOmpF) porins when changing pH from 7.0 to 3.0. Aqueous phase: 0.1M KCl, 10 mM Tris-HCl, 10 mM MES, 10 mM beta-alanine, 100 ng/mL protein. Voltage, 50 mV. *A* – EcOmpF; *B* – YrOmpF

increased noise, which is typical of porin channels in an extremely acidic medium and is associated with fast opening/closing of channels.

It should be noted that we did not observe a decrease in the total channel conductance during short-term incubation (for minutes) of the protein at low pHs. However, long-term incubation of the protein in buffer at pH 3.0 before incorporation into the BLM led to a loss in the functional activity of YrOmpF, which was not restored even after neutralization of the medium (data not shown). Probably, at extremely acidic medium pHs, the studied porin molecules undergo significant conformational changes disabling porins to form conducting channels in the membrane. Obviously, the lipid environment protects the protein from similar changes in the spatial structure and facilitates the stabilization of their functionally active conformation, which leads to preservation of the functional activity of most of the incorporated channels.

To investigate the effect of pH on the conductance of a single YrOmpF channel and its asymmetry, the protein (10 ng/mL) was inserted into the membrane in buffer at pH 7.0 in 0.1 M KCl then the buffer was acidified in both cells simultaneously. During this experiment, the porin channel was found to have a small conductance asymmetry (12%), which remained during medium acidification to pH 5.0. The channel conductance during acidification increased by 2% (n = 4), on average. It should be noted that a similar channel asymmetry was also observed for the *E. coli* OmpF porin [14].

The conductance histograms of single YrOmpF and EcOmpF channels in neutral and acidic media (*Fig. 2*) were obtained in 0.1 M KCl. Protein samples pre-incubated in buffer solutions with different pHs (7.0 and 5.0) were added to the *cis* side of the cell to a final concentration of 100 ng/mL, and a voltage of 50 to 150 mV was applied. During the experiment, hundreds of insertional steps of the studied proteins were analyzed.

Inserted into the model DPhPC membrane both in neutral and acidic media, YrOmpF was shown to form a pore population heterogeneous in conductance. At pH 7.0 in 0.1 M KCl, the largest number of channels had a conductance of about 230 pS (*Fig. 2A*); in this case, the histogram contains minor multiple conductance peaks, which are obviously associated with protein trimer aggregates (460 and 690 pS). As the medium pH decreased to 5.0 (*Fig. 2B*), the conductance heterogeneity of YrOmpF channels increased even more. Additional peaks appeared on the histogram, and the proportion of channels with major multiple conductance also increased.

Compared to YrOmpF, the EcOmpF channel is characterized by a less heterogeneous pore population with a peak of 276 pS at pH 7.0 and 285 pS at pH 5.0. However, in an acidic medium, a wider distribution of channel conductance and EcOmpF protein is observed.

Previously, we demonstrated that the *Yersinia* porins, especially nonpathogenic ones [33], were characterized by a wide range of channel conductance levels compared to *E. coli* OmpF. In the case of YrOmpF, this may be due to the fact that this porin is a wild-type protein obtained from the membrane using the nonionic POE detergent that more gently affects the porin conformation upon release than the ionic SDS detergent. For this reason, protein trimer associates with a higher conductance may remain in the YrOmpF sample. The described pH-dependent changes in the functional properties of YrOmpF were also observed in the OmpF channels from *Y. pseudotuberculosis* (YpOmpF). We found that the protein occurred predominantly as a trimer in the aqueous solution at pH 7.0 and as a monomer at pH 3.0 [34]. The main disturbances in the spatial organization of YpOmpF in an acidic medium are associated with a decrease in the beta-barrel packing density and the changes in the microenvironment of the aromatic chromophores in the protein molecule. At low pHs, changes in the electrostatic potential on the protein surface are accompanied by significant struc-

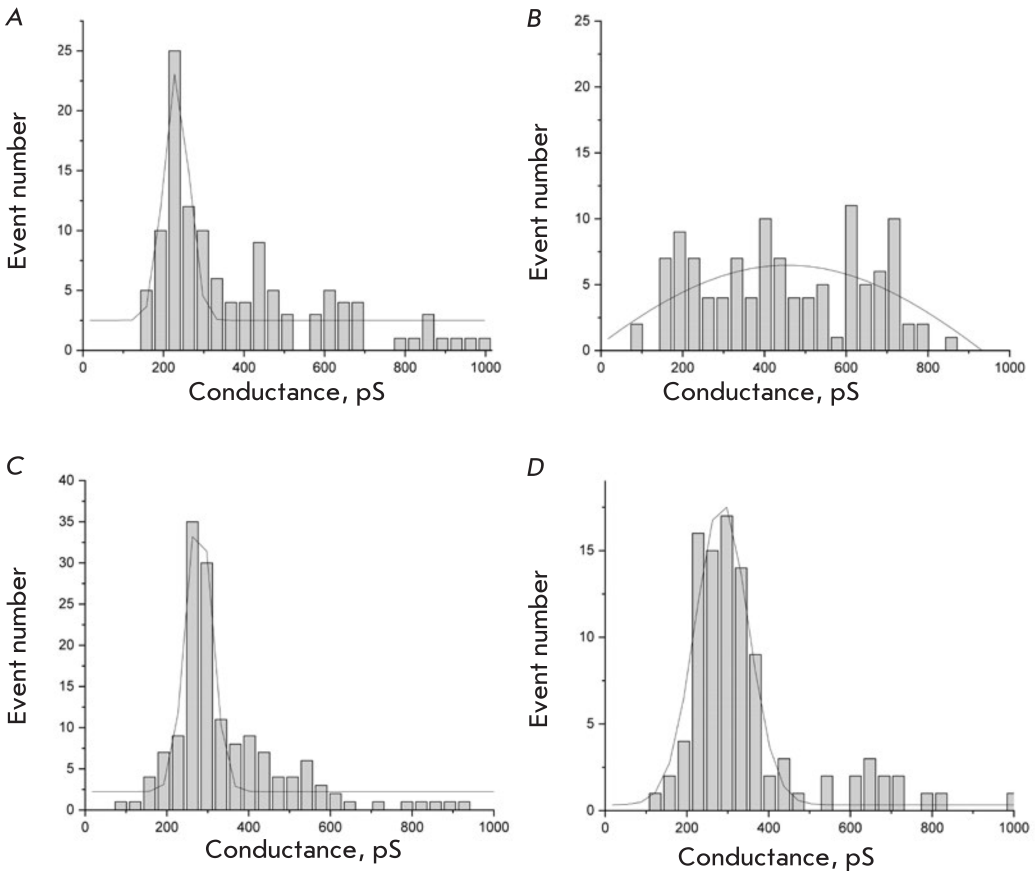

Fig. 2. Distribution of single channel conductance of YrOmpF and EcOmpF in a DPhPC BLM. The proteins were reconstituted at neutral pH = 7.0 (*A*) and acidic pH = 5.0 (*B*). Aqueous phase: 0.1M KCl, 10 mM Tris-HCl, 10 mM MES, 10 mM beta-alanine, 100 ng/mL protein. Voltage, 50–150 mV

tural rearrangements, which leads to dissociation of porin trimers into monomers [34]. In addition, we showed earlier that both molecular protein forms (trimer and monomer) had high affinity for the membrane, but only binding of trimers led to porin channel formation in the lipid bilayer [35].

Therefore, the experimental data obtained for YrOmpF and EcOmpF and the results of earlier studies of a closely related porin of the pseudotuberculosis microbe suggest that extremely low pHs lead to irreversible changes in the ability of the studied porins to incorporate into the model membrane to form channels. However, these conditions do not reduce the conductance of pre-inserted channels. Therefore, the tendency of porin channels to close at lower pH is unlikely to play a significant role in the regulation of ion fluxes through the bacterial membrane.

Potential-dependent closing of YrOmpF channels

One of the properties of pore-forming protein channels from Gram-negative bacteria is their ability to switch to a closed state as the voltage applied to the membrane is increased. This closing is stepwise and reflects sequential closure of monomer channels in the protein trimer.

Because YrOmpF channels had a weak tendency to close, and high membrane potentials (more than 220 mV) often led to significant activation of channel incorporation, recording of classical current–voltage characteristics posed certain experimental difficulties. Therefore, the ability of YrOmpF channels for voltage-dependent closure was studied in single channels. For this purpose, a 5 ng/mL YrOmpF sample was added to the cell *cis* side, and the membrane potential was increased to 250 mV, awaiting a single channel insertion event. Then, the voltage was reduced to 100 mV and increased stepwise at a rate of 10 mV/min. The voltage causing stable closure of at least one monomer was considered the critical closing voltage (Vc). Similarly, 10 YrOmpF channels were analyzed at pH 7.0 and 15 channels at pH 5.0, which enabled to measure the Vc value under these conditions. We also used this technique for measuring Vc of the EcOmpF channels. The obtained values are given in *Table*.

Typical current recordings illustrating the difference in the closing voltage of the channels of the two

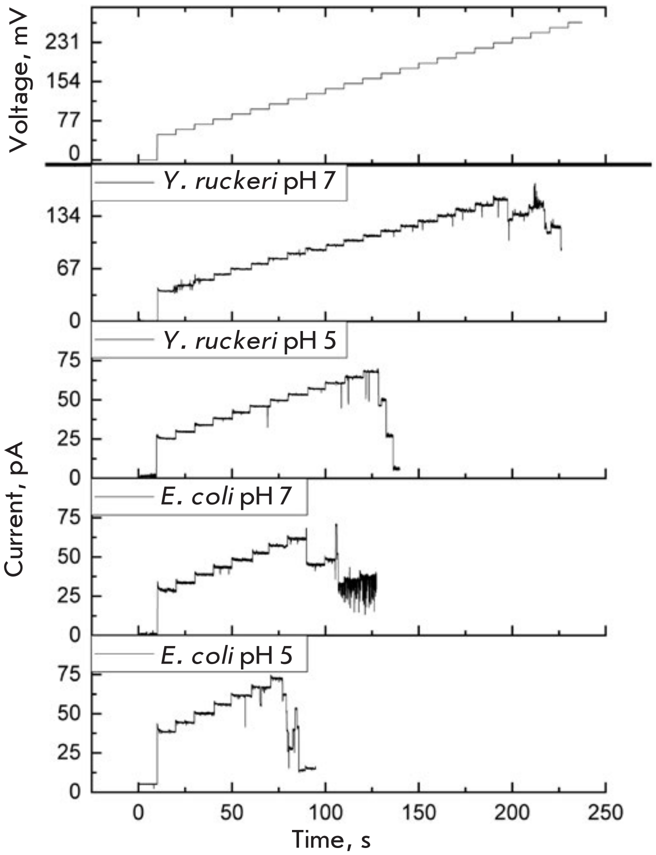

Fig. 3. Conductance of YrOmpF and EcOmpF porin channels during a stepwise increase in the membrane potential. Aqueous phase: 0.1M KCl, 10 mM Tris-HCl, 10 mM MES, 10 mM beta-alanine, 10 ng/mL protein. Voltage, 0, 50, –250 mV

Critical closing potential of the studied porins

Porin	Vc, mV	
	pH 7.0	pH 5.0
E. coli OmpF	124 ± 6 ($n = 10$)	103 ± 10 ($n = 15$)
Y. ruckeri OmpF	232 ± 7 ($n = 10$)	164 ± 8 ($n = 15$)

proteins are shown in *Fig. 3* (not all channels in the given records are single).

During the experiment, YrOmpF channels were found to have unusually high critical closing potentials compared to those of EcOmpF channels (*Table*). In addition, this characteristic of the YrOmpF channels was found to depend on medium acidity because lowering of the electrolyte pH to 5.0 led to a decrease in Vc. Thus, the pH dependence of channel conductance for the studied protein is similar to that for the *E. coli* OmpF channels [36]. The Vc values obtained for the EcOmpF sample used in this study also correspond to the data of [36].

The functional characteristics of porin channels are known to be controlled mainly by the structure of their constriction region, where the beta-barrel diameter decreases significantly [7]. An unusual organization of the pore constriction region with two oppositely charged semirings situated across each other in a restricted space generates an intense electrostatic field in the pore, which controls solute flow through the channel and determines the pore activity of a given protein.

The cationic cluster on the inner wall of the *E. coli* OmpF barrel is formed by three arginine residues (Arg42, Arg82, and Arg132) that are flanked by a lysine residue (Lys16). A positively charged cluster is present inside the OmpF barrel of *Yersinia* porins, like in *E. coli* OmpF as was shown earlier [37]. In YrOmpF, this arginine cluster is represented by three residues (Arg37, Arg76, and Arg127). However, the acidic residue Glu117 (present in *E. coli* OmpF) in a highly conserved PEFGG porin region of the loop L3 [38] is replaced by neutral Val111 as in other *Yersinia*. In addition, this loop in YrOmpF lacks another charged residue: Asp127 (in *E. coli* OmpF) is replaced by Asn122. As a result, instead of six acidic residues in the L3 loop of *E. coli* OmpF, YrOmpF contains only four residues, whose charge can change in an acidic medium.

Replacement of charged residues in the L3 loop and in opposite segments of the beta-barrel in the AA sequence of *E. coli* OmpF is known to lead to significant Vc variations. For example, higher Vc values were obtained for *E. coli* OmpF mutants with acidic residues in the L3 loop replaced by neutral ones [23]. Therefore, the structural differences in the functionally important sites of the L3 loop, revealed by a comparative analysis of the AA sequences of YrOmpF and OmpF from *E. coli*, may be responsible for the differences in the Vc values of these two proteins.

Analysis of intramolecular interactions based on theoretical porin models

To explain the higher experimental Vc value of *Y. ruckeri* OmpF porin compared to that of classical *E. coli* OmpF, we used a comparative analysis of the charge distribution at the mouth, entrance, and inside the pore in a theoretical model of the spatial structure of these two proteins, which was generated by homologous modeling.

Alignment of the AA sequences of the studied proteins revealed that the primary structure of the barrel in their molecules has a high degree of homology, but that the external loops differ in the length

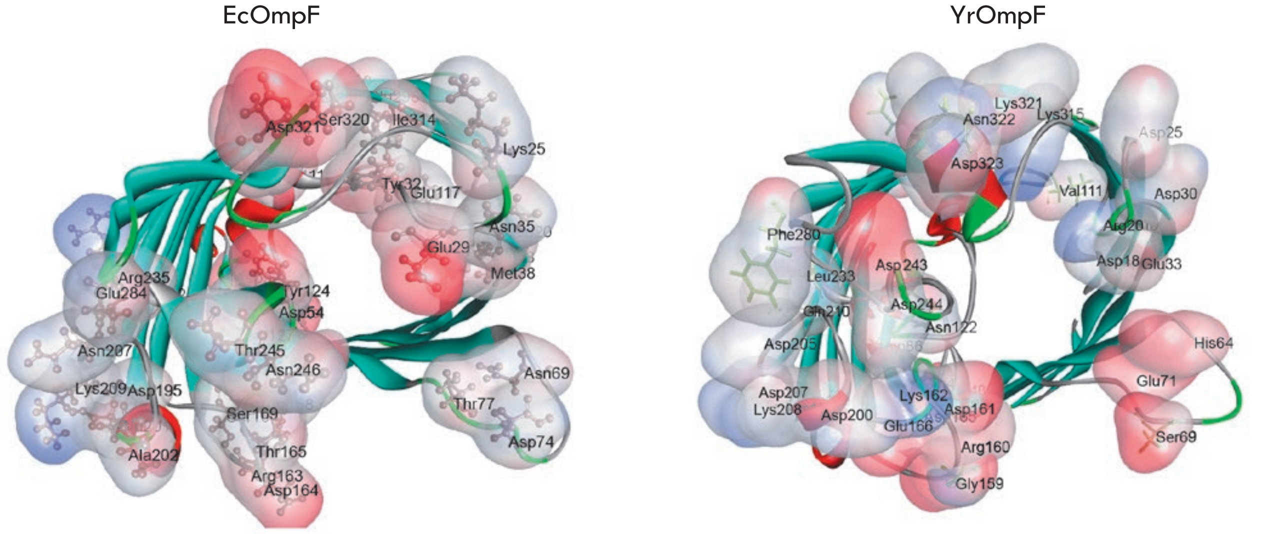

Fig. 4. Distribution of basic and acidic amino acid residues in the variable regions of the porins.
The protein structures are shown as a monomer ribbon diagram. Variable amino acid residues are shown as translucent surfaces and colored according to their charge: basic AAs are shown in blue; acidic AAs are shown in red. Amino acid side chains in EcOmpF and YrOmpF are shown as balls-and-sticks or sticks, respectively

and AA composition. Here, there are both inclusions of additional residues and deletions. For example, loop L1 in YrOmpF is shorter by two residues, and loops L4 and L8 contain two and four additional residues, respectively, compared to the same loops in EcOmpF. In addition to the differences in the number of AA residues in the loops forming the channel entrance, the number of basic residues in this region of the EcOmpF molecule was found to be noticeably smaller than that in YrOmpF (data not shown).

A detailed MOLE-based analysis of the charge distribution revealed significant differences in the number and localization of basic and acidic AA residues both in the external loop region and inside the pore of the studied proteins (*Figs. 4* and *5*). For example, the channel entrance region in EcOmpF contains a greater amount of acidic AA residues (*Fig. 4*), so this region is charged more negatively than that in YrOmpF. However, the external vestibule and constriction zone of the EcOmpF channel contain more basic AA residues and, therefore, have a stronger positive charge than YrOmpF (*Fig. 5*).

In addition, despite a comparable pore length (38.9 Å for YrOmpF and 38.4 Å for EcOmpF), the studied porins significantly differ in their charge distribution in the inner part of their channels. For example, the interior of EcOmpF is characterized by a finer structural organization in terms of alternating positively and negatively charged residues along the pore, while the inner surface of the YrOmpF channel contains longer charged areas (*Fig. 5*).

These facts may be one of the causes for the differences in the closing potential of the studied proteins. It is known that Omp-Pst1 and Omp-Pst2 porins from *Providencia stuartii*, which have close structural similarity but significantly differ in their charge distribution patterns along channel walls and, respectively, in the strength of electrostatic interactions inside the pore, not only possess opposite ion selectivity, but also significantly differ in their closing potential [16].

On the other hand, the degree of conformational mobility of the L3 loop is known to be controlled by the network of hydrogen bonds and salt bridges located between the top and base of L3 and the adjacent barrel wall [39]. It is the strength of these bonds that affects the porin channel sensitivity to the membrane potential [16]. Therefore, the features of intramolecular interactions associated with L3 may play a significant role not only in the pore conductance, but also in the voltage-gated switching of the channel on/off. As mentioned above, the hypothesis of a "flexible" L3 loop is the most plausible among existing explanations for voltage-gating of porin channels. Due to its capacity for significant fluctuations, this loop can change its spatial orientation under voltage applied to the membrane, which switches off the ion flow. If this hypothesis is true, then the difference in the closing potential between YrOmpF and EcOmpF porins should depend

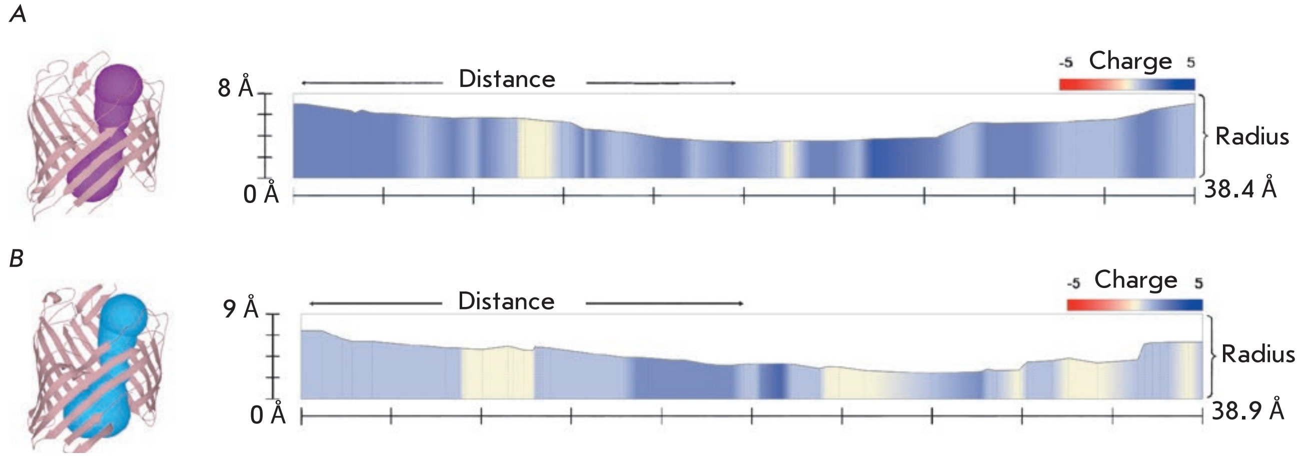

Fig. 5. Geometrical characteristics (length, radius) and charge distribution in the pore interior. *A* – EcOmpF; *B* – YrOmpF.The spatial structures of monomeric porins are shown on the left

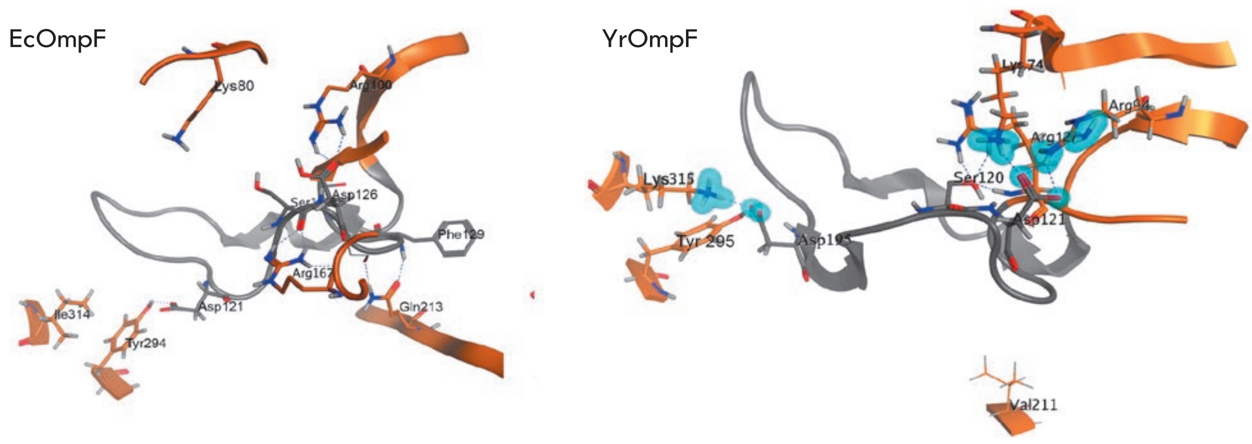

Fig. 6. Intramolecular non-covalent interactions of functionally important amino acid residues in loop L3 in YrOmpF and EcOmpF porins. Protein secondary-structure elements are shown as ribbons; functionally important amino acid residues are shown as sticks. Elements of loop L3 are shown in grey; β-strands and other loops are shown in brown. Hydrogen bonds are shown as blue dotted lines; ionic interactions are shown as blue contours

on the degree of conformation stability of the L3 loop. In both proteins, this is controlled by the contacts and bonds that exist between specific AA residues in the L3 loop and residues in other loops and the barrel wall.

An analysis of the intramolecular interactions between the residues of the L3 loop in the studied porins revealed that the total interaction number varies significantly. For example, the position of this loop in EcOmpF is stabilized by 23 non-covalent interactions with a total energy contribution of −63.8 kcal/mol, while the L3 loop conformation in YrOmpF is controlled by 35 interactions whose energy is −131.6 kcal/mol.

According to the calculated data, there are hydrogen bonds in the *E. coli* porin between the variable residues Arg167 (Val163 in YrOmpF) and Gln213 (Ala215 in YrOmpF) localized in the L4 loop and β10 strand, respectively, and the conserved residues Ser125 (Ser120 in YrOmpF) and Phe129 (Phe123 in YrOmpF) in the L3 loop (*Fig. 6*). Their presence leads to a side chain conformation of the conserved residue Asp126 in EcOmpF, which prevents the formation of both salt bridges (with Lys80 side chains) and additional hydrogen bonds with Arg100 (only two hydrogen bonds are formed). However, the conserved residue Asp121 in the L3 loop of YrOmpF, which corresponds to Asp126 in EcOmpF, forms five salt bridges and four hydrogen bonds with Arg94 in the β5 strand (corresponds to Arg100 in EcOmpF) with a total contribution of about −17.563 kcal/mol. In addition, there is another hydrogen bond between Asp121 and Lys74 in the β4 strand of *Y. ruckeri* porin (Lys80 in EcOmpF) with a contribution of −13.8 kcal/mol (*Fig. 6*).

In another part of the L3 loop, replacement of Ile314 (in EcOmpF) with Lys315 (in YrOmpF) changes the interaction pattern of the conserved Asp115 residue (corresponds to Asp121 in EcOmpF) in the L3 loop of YrOmpF porin. Therefore, in addition to the interactions between Asp115 and Tyr295 (−38.27 kcal/mol) conservative for these porins, Asp115 in YrOmpF forms a network of energy-intensive hydrogen bonds and ionic interactions (−10, −6.355, and −2.652 kcal/mol) with the Lys315 side chain in the β15 strand, which are absent in EcOmpF (*Fig. 6*).

Therefore, the calculated data indicate that the L3 loop of YrOmpF has a more stable conformation.

CONCLUSION

Our electrophysiological experiments revealed an abnormally high critical closing potential of the OmpF channel from *Y. ruckeri* compared to that of the *E. coli* porin. A theoretical analysis of the charge distribution in regions of the spatial porin structure which are important for channel conductance and a quantitative assessment of the intramolecular bonds inside the YrOmpF and EcOmpF pores revealed significant differences in polar interactions between the AA residues of the L3 loop and the barrel. The conformational mobility of the L3 loop in YrOmpF is much more restricted, which may create a need to apply an additional (compared to *E. coli* porin) potential in order to switch the YrOmpF channel to a closed state.

The obtained results contribute to the investigation of the molecular mechanisms of channel conductance in nonspecific porins from Gram-negative bacteria. These proteins are of interest, as biological nanopores, for use in nanotechnology and nanomedicine. The basis for this is their ability to change conductivity in response to any external factor and/or an analyte. In this regard, a detailed investigation of the structural basis for the functioning of pore-forming proteins will lead to a more meaningful approach to the design of biological sensors with the desired properties. ●

This work was financially supported in part by the Russian Foundation for Basic Research (No. 19-03-00318).

REFERENCES

1. Ross A.J., Rucker R.R., Ewing W.H. // Can. J. Microbiol. 1966. V. 12. № 4. P. 763–770.
2. Rucker R.R. // Bull. Off Int. Epizoot. 1966. V. 65. № 5. P. 825–830.
3. Hunter V.A., Knittel M.D., Fryer J. L. // J. Fish Dis. 1980. V. 3. № 6. P. 467–472.
4. Coqet L., Cosette P., Junter G.A., Beucher E., Saiter J.M., Jouenne T. // Colloids and Surfaces B. 2002. V. 26. P. 373–378.
5. Nikaido H. // J. Biol. Chem. 1994. V. 269. № 6. P. 3905–3908.
6. Koebnik R., Locher K.P., van Gelder P. // Mol. Microbiol. 2000. V. 37. № 2. P. 239–253.
7. Cowan S.W., Schirmer T., Rummel G., Steiert M., Ghosh R., Pauptit R.A., Jansonius J.N., Rosenbusch J.P. // Nature. 1992. V. 358. № 6389. P. 727–733.
8. Xu G., Shi B., McGroarty E.J., Ti Tien H. // Biochim. Biophys. Acta – Biomembranes. 1986. V. 862. № 1. P. 57–64.
9. Lakey J.H., Pattus F. // Eur. J. Biochem. 1989. V. 186. № 1–2. P. 303–308.
10. Morgan H., Lonsdale J.T., Alder G. // Biochim. Biophys. Acta – Biomembranes. 1990. V. 1021. P. 175–181.
11. Todt J.C., McGroarty E.J. // Biochem. Biophys. Res. Commun. 1992. V. 189. № 3. P. 1498–1502.
12. Jones C.M., Taylor D.M. // Thin Solid Films. 1996. V. 284–285. P. 748–751.
13. Delcour A.H. // FEMS Microbiol. Lett. 1997. V. 151. № 2. P. 115–123.
14. Nestorovich E.M., Rostovtseva T.K., Bezrukov S.M. // Biophys. J. 2003. V. 85. № 6. P. 3718–3729.
15. Nikaido H. // Microbiol. Mol. Biol. Rev. 2003. V. 67. № 4. P. 593–656.
16. Song W., Bajaj H., Nasrallah C., Jiang H., Winterhalter M., Colletier J.-P., Xu Y. // PLoS Comput. Biol. 2015. V. 11. № 5. P. e1004255.
17. Sen K., Hellman J., Nikaido H. // J. Biol. Chem. 1988. V. 263. № 3. P. 1182–1187.
18. Watanabe M., Rosenbusch J.P., Schirmer T., Karplus M. // Biophys. J. 1997. V. 72. № 5. P. 2094–2102.
19. Phale P.S., Schirmer T., Prilipov A., Lou K.L., Hardmeyer A., Rosenbusch J.P. // Proc. Natl. Acad. Sci. USA. 1997. V. 94. № 13. P. 6741–6745.
20. Bainbridge G., Mobasheri H., Armstrong G.A., Lea E.J., Lakey J.H. // J. Mol. Biol. 1998. V. 275. № 2. P. 171–176.
21. Soares C.M., Björkstén J., Tapia O. // Protein Eng. 1995. V. 8. № 1. P. 5–12.
22. van Gelder P., Saint N., Boxtel R., Rosenbusch J.P., Tommassen J. // Protein Eng. 1997. V. 10. № 6. P. 699–706.
23. van Gelder P., Saint N., Phale P., Eppens E.F., Prilipov A., van Boxtel R., Rosenbusch J.P., Tommassen J. // J. Mol. Biol. 1997. V. 269. № 4. P. 468–472.
24. Eppens E.F., Saint N., van Gelder P., van Boxtel R., Tommassen J. // FEBS Lett. 1997. V. 415. № 3. P. 317–320.
25. Chistyulin D.K., Novikova O.D., Portnyagina O.Yu., Khomenko V.A., Vakorina T.I., Kim N.Yu., Isaeva M.P., Likhatskaya G.N., Solov'eva T.F. // Biochemistry. (Mosc) Suppl. Ser. A Membr. Cell Biol. 2012. V. 6. №. 3. P. 235–242.
26. Garavito R.M., Rosenbusch J.P. // Methods Enzymol. 1986. V. 125. P. 309–328.
27. Laemmli U.K. // Nature. 1970. V. 227. № 5259. P. 680–685.
28. Mueller P., Rudin D.O., Ti Tien H., Wescott W.O. // Nature. 1962. V. 194. P. 979–980.

29. Stenkova A.M., Isaeva M.P., Shubin F.N., Rasskazov V.A., Rakin A.V. PLoS One. 2011. V. 6. № 5. P. e20546.
30. Likhatskaya G.N., Chistyulin D.K., Kim N.Yu., Khomenko V.A., Portnyagina O.Yu., Solov'eva T.F., Novikova O.D. // Biophysics. 2016. V.61. № 6. P. 1088–1097.
31. Chemical ComputingGroup (CCG) http://www.chemcomp.com) [Molecular Operating Environment (MOE)], 2013.08; Chemical Computing Group ULC, 1010 SherbookeSt. West, Suite #910, Montreal, QC, Canada, H3A 2R7, 2018.
32. Pravda L., Sehnal D., Toušek D., Navrátilová V., Bazgier V., Berka K., Svobodová Vařeková R., Koča J., Otyepka M. // Nucl. Acids Res. 2018. V. 46. № W1. P. W368–W373.
33. Vostrikova O.P., Kim N.Yu., Likhatskaya G.N., Guzev K.V., Vakorina T.I., Khomenko V.A., Novikova O.D., Solov'eva T.F. // Russ. J. Bioorg. Chem. 2006. V. 32. № 4. P. 371–383.
34. Novikova O.D., Kim N.Yu., Luk'yanov P.A., Likhatskaya G.N., Emelyanenko V.I., Solov'eva, T.F. // Biochemistry. (Mosc) Suppl. Ser. A Membr. Cell Biol. 2007. V. 24. № 2. P. 159–168.
35. Rokitskaya T.I., Kotova E.A., Naberezhnykh G.A., Khomenko V.A., Gorbach V.I., Firsov A.M., Zelepuga E.A., Antonenko Yu.N., Novikova O.D. // Biochim. Biophys. Acta – Biomembranes. 2016. V. 1858. № 4. P. 883–891.
36. Saint N., Lou K.L., Widmer C., Luckey M., Schirmer T., Rosenbusch J.P. // J. Biol. Chem. 1996. V. 271. № 34. P. 20676–20680.
37. Likhatskaya G.N., Solov'eva T.F., Novikova O.D., Issaeva M.P., Gusev K.V., Kryzhko I.B., Trifonov E.V., Nurminski E.A. // J. Biomol. Struct. Dyn. 2005. V. 23. № 2. P. 163–174.
38. Jeanteur D., Lakey J.H., Pattus F. // Mol. Microbiol. 1991. V. 5. № 9. P. 2153–2164.
39. Karshikoff A., Spassov V., Cowan S.W., Ladenstein R., Schirmer T. // J. Mol. Biol. 1994. V. 240. № 4. P. 372–384.

A Unique Prototypic Device for Radiation Therapy: The p53-Independent Antiproliferative Effect of Neutron Radiation

D. I. Yurkov[1], S. V. Syromukov[1], V. V. Tatarskiy[2,3], E. S. Ivanova[2], A. I. Khamidullina[3], M. A. Yastrebova[3], V. I. Sysoev[1], R. V. Dobrov[1], A. V. Belousov[4,5], V. N. Morozov[1,4], M. A. Kolyvanova[4], G. A. Krusanov[4,6], V. I. Zverev[1], A. A. Shtil[2,3*]
[1]N.L. Dukhov All-Russia Research Institute of Automatics, Sushchevskaya Str. 22, Moscow, 127055, Russia
[2]Blokhin National Medical Center of Oncology, Kashirskoye Sh. 24, Moscow, 115478, Russia
[3]Institute of Gene Biology, Russian Academy of Sciences, Vavilova Str. 34/5, Moscow, 119334, Russia
[4]A.I. Burnasyan Federal Medical Biophysical Center, Marshala Novikova Str. 23, Moscow, 123098, Russia
[5]Moscow State University, Department of Physics, Leninskie Gory Str. 1, bldg. 2, Moscow, 119234, Russia
[6]D.V. Skobeltsyn Institute of Nuclear Physics at Moscow State University, Leninskie Gory Str. 1, bldg. 2, Moscow, 119234, Russia
*E-mail: shtilaa@yahoo.com

Received April 9, 2019; in final form, June 18, 2019
DOI: 10.32607/20758251-2019-11-3-99-102

Copyright © 2019 National Research University Higher School of Economics. This is an open access article distributed under the Creative Commons Attribution License,which permits unrestricted use, distribution, and reproduction in any medium, provided the original work is properly cited.

ABSTRACT **Radiation therapy with heavy particles including neutrons, an otherwise therapeutically perspective because of its high tissue penetration and efficient tumor damage, is currently limited by the lack of adequate equipment. An NG-24 generator (140 kg, 42 × 110 cm, ~10^{11} particles/s, > 14 MeV) has been designed and engineered to replace the huge and environmentally harmful neutron reactors, cyclotrons, and accelerators with a compact, portable, safe, and potent source of high-energy neutrons. We demonstrate that the neutron beam produced by NG-24 causes a significant antiproliferative effect on human tumor cell lines regardless of the status of the anti-apoptotic p53 protein. Phosphorylation of histone 2A and increased amounts of p21, cyclin D, and phospho-p53 were detectable in HCT116 colon carcinoma cells (wild-type p53) irradiated with 4 Gy several days post-treatment, accompanied by G2/M phase arrest. These treatments dramatically reduced the ability of single cells to form colonies. In the HCT116p53KO subline (p53 -/-), the G2/M arrest was independent of the aforementioned mechanisms. Hence, the NG-24 generator is a source of a powerful, therapeutically relevant neutron flux that triggers a p53-independent antiproliferative response in tumor cells.**

KEYWORDS **fast neutrons, neutron generators, tumor cells, DNA damage, cell death.**

INTRODUCTION

Photons with an energy range of 30 keV–25 MeV are routinely used in the conventional radiation therapy of tumors. However, heavy particles (in particular, neutrons with energy > 1 MeV; fast neutrons)) are more effective than photons. Due to its high linear energy transfer and relative biological effectiveness (RBE), fast neutron therapy of radioresistant tumors has an advantage over photon beam radiation therapy [1]. Fast neutrons can be used in combination with photon beam therapy. Despite their therapeutic potential, the clinical use of neutrons remains limited, partly because of a lack of adequate equipment. The cyclotrons, nuclear reactors, and accelerators currently in use worldwide [1, 2] are huge stationary devices that are difficult to operate and maintain.

Fast neutron generators can be an alternative. An NG-24 generator designed at the N.L. Dukhov All-Russia Research Institute of Automatics is a compact, portable, and safe device with a therapeutically suf-

Table. Parameters of the NG-24 neutron source

D-T neutron flux, particles/s	~10^{11}
Neutron energy, MeV	>14
Time resource, h	500
Dimensions, mm	420 × 1100
Weight, kg	140
Electric supply	50/60 Hz, 220 V, 1200 W
Body	Grounded

ficient particle flux [3]. The characteristics of the NG-24 generator are shown in *Table*. Because of its small dimensions, NG-24 can be mounted both on a gantry and on a robotic manipulator. A tritium-saturated target to which a deuterium ion beam accelerated in the electric field is focused serves as a source of irradiation. The nuclear reaction ^{3}H(d,n) generates 14–15 MeV neutrons. Due to a big reaction cross section (5 barn at 107 keV), one can obtain a flux of >10^{11} neutrons/s [4, 5]. Theoretical calculations and experiments showed that the neutron energy (14.71–14.87 MeV) was practically linearly dependent on the accelerating voltage [6, 7].

In this study, we evaluated the ability of a neutron beam produced by NG-24 to induce therapeutically relevant effects in cultured human tumor cells.

EXPERIMENTAL

The dose absorbed by the cell monolayer was assessed according to the particle flux by computer simulation using the Geant4 software [8] (Physicslist QGSP_BIC_HP for neutrons with energy < 20 MeV). The calculated coefficient of neutron flux conversion into the dose absorbed by the cell monolayer was 5.7×10^{-13} Gy/neutron. Non-homogeneity of the neutron flux across the monolayer was ± 15%.

The reagents were purchased from PanEco (Russia), except when specified otherwise. The HCT116 colon cancer (wild type p53) and MCF7 human breast cancer (caspase-3 deletion) cell lines were purchased from the American Type Culture Collection. The HCT116p53KO subline with an inactivated p53 protein has been generated in the B. Vogelstein's laboratory [9]. The cells (50% monolayer) in 25-cm^2 cell culture flasks were irradiated with 14 MeV neutrons. For colony formation, 1,000 irradiated cells were plated onto a 100-mm Petri dish in 20 ml of a Dulbecco modified Eagle's medium supplemented with 10% fetal calf serum (HyClone, USA), 2 mM *L*-glutamine, 100 U/ml penicillin, and 100 μg/ml streptomycin, and incubated at 37°C, 5% CO_2 for 14 days. The colonies were fixed with methanol and stained with methyl violet. For flow cytometry and immunoblotting, the irradiated cells were incubated in the aforementioned medium for 1–4 days. The antibodies were purchased from Cell Signaling (USA). The protocols have been published in our earlier papers [10–12].

RESULTS AND DISCUSSION

Irradiation of HCT116 cells with a single dose of 2 Gy significantly reduced the proliferation rate of the cells; only small individual colonies (≤ 6 cells) were detected after 3 Gy (*Figure A*). Two days post-irradiation, the cells accumulated in the G2/M phase. This arrest was observed for at least 4 days (*Fig. B*; note the increased percentage of polyploid cells, a hallmark of altered mitosis). These data indicated that DNA damage was the major mechanism of cell response to the neutron irradiation generated by NG-24. Indeed, after 4 h, the percentage of cells with phosphorylated H2A histone, a marker of DNA double-strand breaks, increased from 10% in untreated cells to > 70% in the cells exposed to 4 Gy. This effect persisted for at least 24 h after irradiation.

Importantly, the effects of neutron irradiation on HCT116 cells were reproduced for the isogenic subline HCT116p53KO. This subline with inactivated pro-apoptotic p53 is resistant to a number of DNA-damaging anticancer drugs [10]. Therefore, p53 is not needed for the antiproliferative activity of neutrons. The described effects were also observed in a MCF7 breast cancer cell line (caspase-3 deletion). Hence, antiproliferative potency is revealed in cells of different tissue origins; individual nonfunctional mechanisms of cell death, which may limit the therapeutic effects in other situations, do not impede the antitumor efficacy of the neutrons.

The molecular events in cells with the wild type and inactivated p53 were different. The accumulation of p21, the protein known to halt cell cycle progression in response to DNA damage, and activation of cyclin D1 driving the G1-S transition were detected only in HCT116 cells but not in the HCT116p53KO subline (4 Gy; *Figure B*). Therefore, the increased p53, p21, and cyclin D1 levels contributed to G2/M arrest in HCT116 cells, while other mechanisms are responsible for the same cell cycle arrest in the case of non-functional p53. These mechanisms need to be elucidated, and the final outcome of neutron irradiation (apoptosis, mitotic catastrophe, senescence, etc.) has to be determined.

Hence, the NG-24 neutron generator produces a neutron flux that is sufficient for inducing molecular and phenotypic changes at doses and time intervals relevant to those used in radiation therapy. Therefore, one may expect that the generator can be used in therapeutic applications. Meanwhile, neutron radiation requires special measures for patient safety.

The damage to non-tumor cells caused by neutrons is a crucial issue. Taking into account the dependence between antitumor efficacy and radiation parameters, the lack of information about the biological mechanisms of neutron irradiation, as well as the challenges associated with accurate quantification of the neutron-absorbed dose, there is little sense in comparing the responses of tumor and non-tumor cells. Experimental studies are complicated by the inability of non-transformed cells to form colonies and by the challenges related to long-term culture.

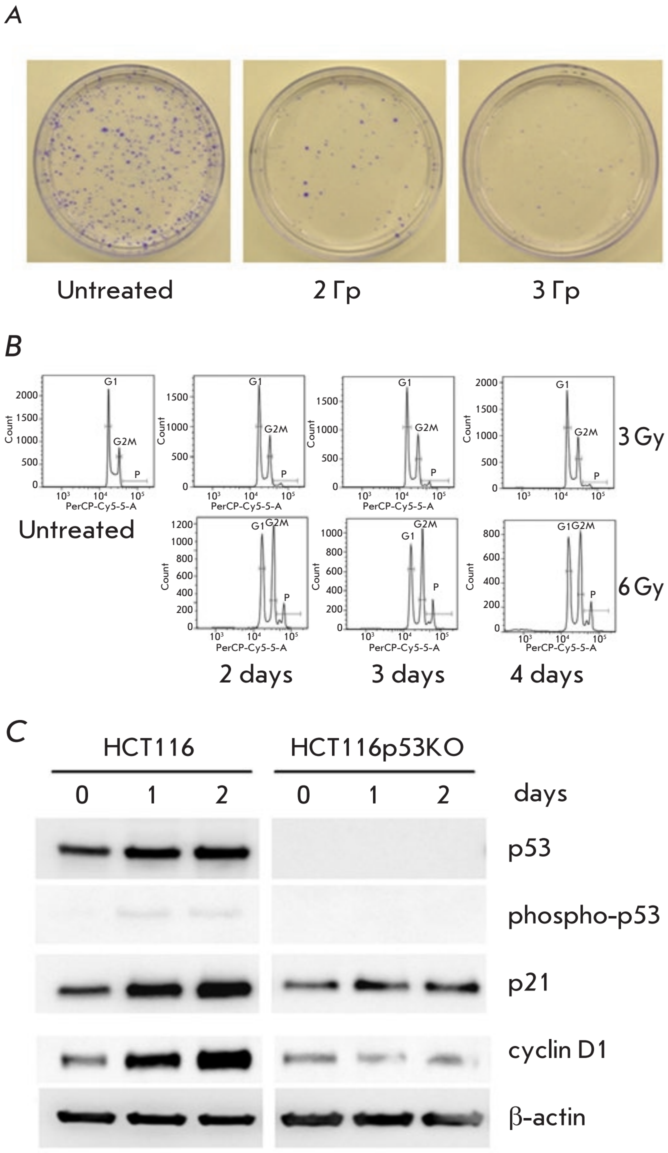

Molecular mechanisms of the response of HCT116 and HCT116p53KO cells to irradiation with fast neutrons. *A* – colony formation; *B* – cell cycle distribution (flow cytometry; P – polyploids); *C* – immunoblotting. The results of at least three replicates are shown

The conformity of neutron radiation is ensured by proper technical solutions. Modern radiotherapy tools allow one to significantly reduce or avoid the damage to surrounding tissues due to the possibilities offered by treatment planning (calculating the radiation-absorbed dose in the tumor and peritumoral tissue). Since the dose produced by neutrons on the surface (skin) is higher than that inside the tumor (the absorbed dose decreases twofold at a depth of 5–6 cm), the therapy employs multiple field irradiations. The dose accumulates in the tumor as the patient's body is irradiated at different angles. It is possible to reduce the specific surface dose, while the therapeutically effective dose in the tumor is retained. Multileaf collimators are used for an accurate shaping of the tumor. As the radiation source is rotated around the patient's body, the collimator leaves move to generate a field for each radiation angle. Irradiation may require many collimator leaf positions. Furthermore, the RBE of neutrons increases with a decrease of neutron energy. It is expected that RBE inside the tissue, where the neutrons are slowed down, will be higher compared to that on the skin. However, taking into account the complexity of measuring the RBE value, this question needs further investigation.

This communication demonstrated that the experimental NG-24 neutron generator produces a neutron flux with biological parameters that are acceptable for antitumor radiotherapy. The problem to be solved next is the design of a therapeutic prototype that would combine the high antitumor efficacy of neutron radiation with radiation therapy conformity and meet the requirements for the safety of patients and personnel.

CONCLUSIONS

This safe and compact NG-24 neutron generator produces a fast neutron flux which allows one to deliver a radiation dose sufficient for inducing a pronounced antiproliferative response in tumor cells. Loss of DNA integrity and delayed cell cycle progression in response to neutron irradiation are detectable regardless of the status of the pro-apoptotic protein p53. These findings suggest that fast neutrons efficiently eliminate tumor cells in which individual molecular mechanisms that control the cell death/survival balance are not functioning. ●

This work was supported by the Ministry of Education and Science of the Russian Federation (Agreement with the Institute of Gene Biology, Russian Academy of Sciences, No. 14.W03.31.002).

REFERENCES

1. Specht H.M., Neff T., Reuschel W., Wagner F.M., Kampfer S., Wilkens J.J., Petry W., Combs S.E. // Front. Oncol. 2015. V. 5. P. 262.
2. Valcović V. 14 MeV neutrons: Physics and applications. Boca Raton: CRC Press, Taylor and Francis Group, 2015. 516 p.
3. Syromukov S.V., Stepnov V.V. Generator neytronov. – Poleznaya model' dlya patenta RF №166092 ot 03.06.2016
4. Syromukov S.V., Stepnov V.V., Dobrov R.V., Sysoev V.I., Mel'nik A.V., Bogatikov K.V., Starostin A.N., Letichevskii R.D. // Atomic Energy. 2015. V. 119. P. 68–71.
5. Sevast'yanov V.D., Kovalenko O.I., Orlov A.V., Shibaev R.M., Obudovskii S.Yu., Portnov B.D., Batyunin A.V., Kashchuk Yu.A. // Measur. Tech. 2016. V. 59. P. 994–1001.
6. Syromukov S.V. // Atomic Energy. 2018. V. 123. P. 267–274.
7. Lityaev V.M., Ulyanenko S.E., Koryakin S.N., Brovin A.I., Syromukov S.V., Bogolyubov E.P., Ryzhova V.I., Gorbushin N.G. Apparat dlya distancionnoy neytronnoy terapii. – Patent RF №2526244 ot 28.08.2013
8. Agostinelli S., Allison J., Amako K., Apostolakis J., Araujo H., Arce P., Asai M., Axen D., Banerjee S., Barrand G., et al. // Nucl. Instrum. Meth. Phys. Res. Section A. 2003. V. 506. P. 250–303.
9. Bunz F., Dutriaux A., Lengauer C., Waldman T., Zhou S., Brown J.P., Sedivy J.M., Kinzler K.W., Vogelstein B. // Science. 1998. V. 282. P. 1497–1501.
10. Tikhomirov A.S., Lin C.Y., Volodina Y.L., Dezhenkova L.G., Tatarskiy V.V., Schols D., Shtil A.A., Kaur P., Chueh P.J., Shchekotikhin A.E. // Eur. J. Med. Chem. 2018. V. 148. P. 128–139.
11. Nadysev G.Y., Tikhomirov A.S., Lin M.-H., Yang Y.-T., Dezhenkova L.G., Chen H.-Y., Kaluzhny D.N., Schols D., Shtil A.A., Shchekotikhin A.E., et al. // Eur. J. Med. Chem. 2018. V. 143. P. 1553–1562.
12. Volodina Y.L., Dezhenkova L.G., Tikhomirov A.S., Tatarskiy V.V., Kaluzhny D.N., Moisenovich A.M., Moisenovich M.M., Isagulieva A.K., Shtil A.A., Tsvetkov V.B., et al. // Eur. J. Med. Chem. 2019. V. 165. P. 31–45.

GUIDELINES FOR AUTHORS 2019

GENERAL RULES

Acta Naturae publishes experimental articles and reviews, as well as articles on topical issues, short reviews, and reports on the subjects of basic and applied life sciences and biotechnology.

The journal *Acta Naturae* is on the list of the leading periodicals of the Higher Attestation Commission of the Russian Ministry of Education and Science. The journal Acta Naturae is indexed in PubMed, Web of Science, Scopus and RCSI databases.

The editors of *Acta Naturae* ask of the authors that they follow certain guidelines listed below. Articles which fail to conform to these guidelines will be rejected without review. The editors will not consider articles whose results have already been published or are being considered by other publications.

The maximum length of a review, together with tables and references, cannot exceed 60,000 characters with spaces (approximately 30 pages, A4 format, 1.5 spacing, Times New Roman font, size 12) and cannot contain more than 16 figures.

Experimental articles should not exceed 30,000 symbols (approximately 15 pages in A4 format, including tables and references). They should contain no more than ten figures.

A short report must include the study's rationale, experimental material, and conclusions. A short report should not exceed 12,000 symbols (8 pages in A4 format including no more than 12 references). It should contain no more than four figures.

The manuscript and the accompanying documents should be sent to the Editorial Board in electronic form:
1) text in Word 2003 for Windows format;
2) the figures in TIFF format;
3) the text of the article and figures in one pdf file;
4) the article's title, the names and initials of the authors, the full name of the organizations, the abstract, keywords, abbreviations, figure captions, and Russian references should be translated to English;
5) the cover letter stating that the submitted manuscript has not been published elsewhere and is not under consideration for publication;
6) the license agreement (the agreement form can be downloaded from the website www.actanaturae.ru).

MANUSCRIPT FORMATTING

The manuscript should be formatted in the following manner:

- Article title. Bold font. The title should not be too long or too short and must be informative. The title should not exceed 100 characters. It should reflect the major result, the essence, and uniqueness of the work, names and initials of the authors.
- The corresponding author, who will also be working with the proofs, should be marked with a footnote *.
- Full name of the scientific organization and its departmental affiliation. If there are two or more scientific organizations involved, they should be linked by digital superscripts with the authors' names. Abstract. The structure of the abstract should be very clear and must reflect the following: it should introduce the reader to the main issue and describe the experimental approach, the possibility of practical use, and the possibility of further research in the field. The average length of an abstract is 20 lines (1,500 characters).
- Keywords (3 – 6). These should include the field of research, methods, experimental subject, and the specifics of the work. List of abbreviations.
- INTRODUCTION
- EXPERIMENTAL PROCEDURES
- RESULTS AND DISCUSSION
- CONCLUSION
  The organizations that funded the work should be listed at the end of this section with grant numbers in parenthesis.
- REFERENCES
  The in-text references should be in brackets, such as [1].

RECOMMENDATIONS ON THE TYPING AND FORMATTING OF THE TEXT

- We recommend the use of Microsoft Word 2003 for Windows text editing software.
- The Times New Roman font should be used. Standard font size is 12.
- The space between the lines is 1.5.
- Using more than one whole space between words is not recommended.
- We do not accept articles with automatic referencing; automatic word hyphenation; or automatic prohibition of hyphenation, listing, automatic indentation, etc.
- We recommend that tables be created using Word software options (Table → Insert Table) or MS Excel. Tables that were created manually (using lots of spaces without boxes) cannot be accepted.
- Initials and last names should always be separated by a whole space; for example, A. A. Ivanov.
- Throughout the text, all dates should appear in the "day.month.year" format, for example 02.05.1991, 26.12.1874, etc.
- There should be no periods after the title of the article, the authors' names, headings and subheadings, figure captions, units (s – second, g – gram, min – minute, h – hour, d – day, deg – degree).
- Periods should be used after footnotes (including those in tables), table comments, abstracts, and abbreviations (mon. – months, y. – years, m. temp. – melting temperature); however, they should not be used in subscripted indexes (T_m – melting temperature; $T_{p.t}$ – temperature of phase transition). One exception is mln – million, which should be used without a period.
- Decimal numbers should always contain a period and not a comma (0.25 and not 0,25).
- The hyphen ("-") is surrounded by two whole spaces, while the "minus," "interval," or "chemical bond" symbols do not require a space.
- The only symbol used for multiplication is "×"; the "×" symbol can only be used if it has a number to its

right. The "·" symbol is used for denoting complex compounds in chemical formulas and also noncovalent complexes (such as DNA·RNA, etc.).

- Formulas must use the letter of the Latin and Greek alphabets.
- Latin genera and species' names should be in italics, while the taxa of higher orders should be in regular font.
- Gene names (except for yeast genes) should be italicized, while names of proteins should be in regular font.
- Names of nucleotides (A, T, G, C, U), amino acids (Arg, Ile, Val, etc.), and phosphonucleotides (ATP, AMP, etc.) should be written with Latin letters in regular font.
- Numeration of bases in nucleic acids and amino acid residues should not be hyphenated (T34, Ala89).
- When choosing units of measurement, SI units are to be used.
- Molecular mass should be in Daltons (Da, KDa, MDa).
- The number of nucleotide pairs should be abbreviated (bp, kbp).
- The number of amino acids should be abbreviated to aa.
- Biochemical terms, such as the names of enzymes, should conform to IUPAC standards.
- The number of term and name abbreviations in the text should be kept to a minimum.
- Repeating the same data in the text, tables, and graphs is not allowed.

GUIDENESS FOR ILLUSTRATIONS

- Figures should be supplied in separate files. Only TIFF is accepted.
- Figures should have a resolution of no less than 300 dpi for color and half-tone images and no less than 500 dpi.
- Files should not have any additional layers.

REVIEW AND PREPARATION OF THE MANUSCRIPT FOR PRINT AND PUBLICATION

Articles are published on a first-come, first-served basis. The members of the editorial board have the right to recommend the expedited publishing of articles which are deemed to be a priority and have received good reviews.

Articles which have been received by the editorial board are assessed by the board members and then sent for external review, if needed. The choice of reviewers is up to the editorial board. The manuscript is sent on to reviewers who are experts in this field of research, and the editorial board makes its decisions based on the reviews of these experts. The article may be accepted as is, sent back for improvements, or rejected.

The editorial board can decide to reject an article if it does not conform to the guidelines set above.

The return of an article to the authors for improvement does not mean that the article has been accepted for publication. After the revised text has been received, a decision is made by the editorial board. The author must return the improved text, together with the responses to all comments. The date of acceptance is the day on which the final version of the article was received by the publisher.

A revised manuscript must be sent back to the publisher a week after the authors have received the comments; if not, the article is considered a resubmission.

E-mail is used at all the stages of communication between the author, editors, publishers, and reviewers, so it is of vital importance that the authors monitor the address that they list in the article and inform the publisher of any changes in due time.

After the layout for the relevant issue of the journal is ready, the publisher sends out PDF files to the authors for a final review.

Changes other than simple corrections in the text, figures, or tables are not allowed at the final review stage. If this is necessary, the issue is resolved by the editorial board.

FORMAT OF REFERENCES

The journal uses a numeric reference system, which means that references are denoted as numbers in the text (in brackets) which refer to the number in the reference list.

For books: the last name and initials of the author, full title of the book, location of publisher, publisher, year in which the work was published, and the volume or issue and the number of pages in the book.

For periodicals: the last name and initials of the author, title of the journal, year in which the work was published, volume, issue, first and last page of the article. Must specify the name of the first 10 authors. Ross M.T., Grafham D.V., Coffey A.J., Scherer S., McLay K., Muzny D., Platzer M., Howell G.R., Burrows C., Bird C.P., et al. // Nature. 2005. V. 434. № 7031. P. 325–337.

References to books which have Russian translations should be accompanied with references to the original material listing the required data.

References to doctoral thesis abstracts must include the last name and initials of the author, the title of the thesis, the location in which the work was performed, and the year of completion.

References to patents must include the last names and initials of the authors, the type of the patent document (the author's rights or patent), the patent number, the name of the country that issued the document, the international invention classification index, and the year of patent issue.

The list of references should be on a separate page. The tables should be on a separate page, and figure captions should also be on a separate page.

The following e-mail addresses can be used to contact the editorial staff: vera.knorre@gmail.com, actanaturae@gmail.com, tel.: (495) 727-38-60, (495) 930-87-07

ActaNaturae

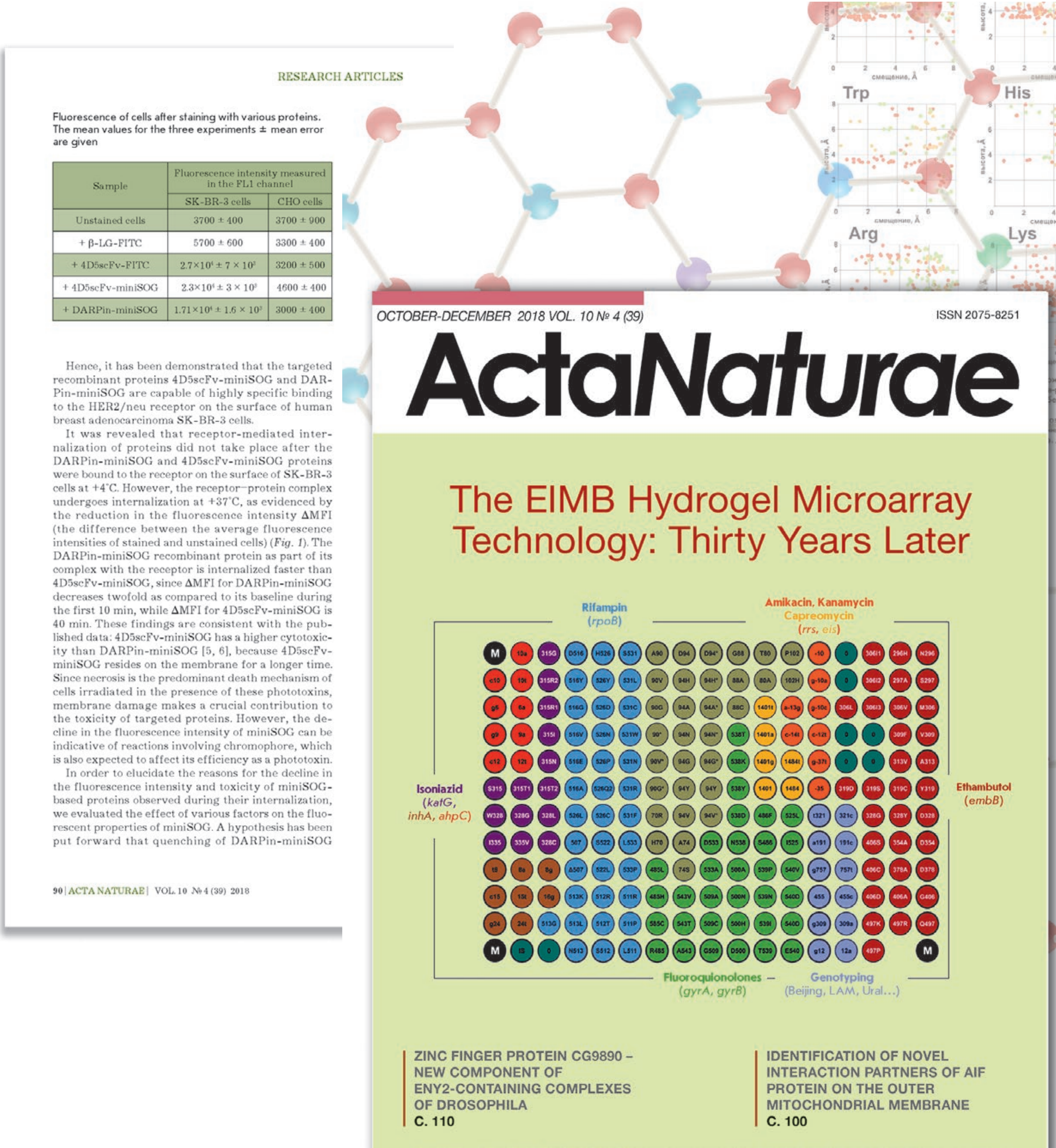

RESEARCH ARTICLES

Fluorescence of cells after staining with various proteins. The mean values for the three experiments ± mean error are given

Sample	Fluorescence intensity measured in the FL1 channel	
	SK-BR-3 cells	CHO cells
Unstained cells	3700 ± 400	3700 ± 900
+ β-LG-FITC	5700 ± 600	3300 ± 400
+ 4D5scFv-FITC	$2.7\times10^4 \pm 7\times10^3$	3200 ± 500
+ 4D5scFv-miniSOG	$2.3\times10^4 \pm 3\times10^3$	4600 ± 400
+ DARPin-miniSOG	$1.71\times10^4 \pm 1.6\times10^3$	3000 ± 400

Hence, it has been demonstrated that the targeted recombinant proteins 4D5scFv-miniSOG and DARPin-miniSOG are capable of highly specific binding to the HER2/neu receptor on the surface of human breast adenocarcinoma SK-BR-3 cells.

It was revealed that receptor-mediated internalization of proteins did not take place after the DARPin-miniSOG and 4D5scFv-miniSOG proteins were bound to the receptor on the surface of SK-BR-3 cells at +4°C. However, the receptor–protein complex undergoes internalization at +37°C, as evidenced by the reduction in the fluorescence intensity ΔMFI (the difference between the average fluorescence intensities of stained and unstained cells) (*Fig. 1*). The DARPin-miniSOG recombinant protein as part of its complex with the receptor is internalized faster than 4D5scFv-miniSOG, since ΔMFI for DARPin-miniSOG decreases twofold as compared to its baseline during the first 10 min, while ΔMFI for 4D5scFv-miniSOG is 40 min. These findings are consistent with the published data: 4D5scFv-miniSOG has a higher cytotoxicity than DARPin-miniSOG [5, 6], because 4D5scFv-miniSOG resides on the membrane for a longer time. Since necrosis is the predominant death mechanism of cells irradiated in the presence of these phototoxins, membrane damage makes a crucial contribution to the toxicity of targeted proteins. However, the decline in the fluorescence intensity of miniSOG can be indicative of reactions involving chromophore, which is also expected to affect its efficiency as a phototoxin.

In order to elucidate the reasons for the decline in the fluorescence intensity of miniSOG-based proteins observed during their internalization, we evaluated the effect of various factors on the fluorescent properties of miniSOG. A hypothesis has been put forward that quenching of DARPin-miniSOG

90 | ACTA NATURAE | VOL. 10 № 4 (39) 2018

OCTOBER-DECEMBER 2018 VOL. 10 № 4 (39)

ISSN 2075-8251

ActaNaturae

The EIMB Hydrogel Microarray Technology: Thirty Years Later

ZINC FINGER PROTEIN CG9890 – NEW COMPONENT OF ENY2-CONTAINING COMPLEXES OF DROSOPHILA
C. 110

IDENTIFICATION OF NOVEL INTERACTION PARTNERS OF AIF PROTEIN ON THE OUTER MITOCHONDRIAL MEMBRANE
C. 100

ActaNaturae

Journal “*Acta Naturae*” is a international journal on life sciences based in Moscow, Russia. Our goal is to present scientific work and discovery in molecular biology, biochemistry, biomedical disciplines and biotechnology. *Acta Naturae* is also a periodical for those who are curious in various aspects of biotechnological business, innovations in pharmaceutical areas, intellectual property protection and social consequences of scientific progress.

Being a totally unique publication in Russia, *Acta Naturae* will be useful to both representatives of fundamental research and experts in applied sciences.

Journal “*Acta Naturae*” is now available in open access in PubMed Central® and eLIBRARY.RU.

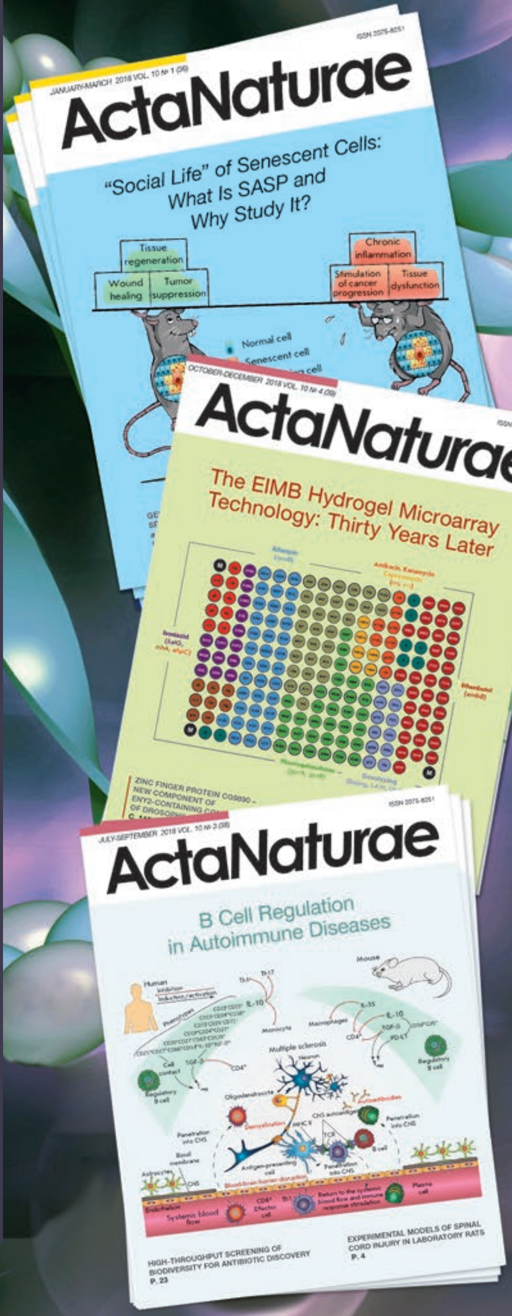

INFORMATION FOR AUTHORS:
if you want to publish in “Acta Naturae”,
please contact us: actanaturae@gmail.com